Universidad de Oviedo

Department of Electrical, Electronics, Computers and Systems Engineering

PhD Thesis

Wind regime characterization, and short-term wind speed and power forecasting using multivariable LSTM and NARX networks in the Andes Mountains, Ecuador

by

Germánico Adán López López

PhD Program in Energy and Process Control

Electrical Current Conversion and Power Systems Research line

January 2023

Universidad de Oviedo

Department of Electrical, Electronics, Computers and
Systems Engineering

PhD Thesis

Wind regime characterization, and short-term wind speed and power forecasting using multivariable LSTM and NARX networks in the Andes Mountains, Ecuador

by

Germánico Adán López López

Dissertation submitted in fulfillment of the requirements for the degree of Doctor of Philosophy in the Energy and Process Control PhD program at the University of Oviedo

Supervisor: PhD. Prof. Pablo Arboleya Arboleya.

January 2023

RESUMEN DEL CONTENIDO DE TESIS DOCTORAL

1.- Título de la Tesis	
Españo: Caracterización del régimen eólico y previsión a corto plazo de la velocidad y la potencia del viento mediante redes multivariables LSTM y NARX en la Cordillera de los Andes, Ecuador	Inglés: Wind regime characterization, and short-term wind speed and power forecasting using multivariable LSTM and NARX networks in the Andes Mountains, Ecuador

2.- Autor	
Nombre: Germánico Adán López López	DNI/**Pasaporte**/NIE:
Programa de Doctorado:Doctorado en Energía y Control de Procesos	
Órgano responsable: Comisión Académica Programa de Doctorado	

RESUMEN (en español)

En los últimos años, la investigación ha revelado que los diseños hidroeléctricos en Ecuador no han considerado adecuadamente la sensibilidad al cambio climático. Además, las condiciones climáticas determinan las variaciones en la generación de electricidad a partir de esta fuente de energía renovable. También, las variaciones en el régimen de lluvias provocan una sequía de julio a octubre por la falta de lluvias. Por lo tanto, disminuiría el caudal de los ríos que alimentan las represas para la generación hidroeléctrica, lo que resultaría en una importante reducción de su capacidad de generación. En años anteriores, la sequía provocó un aumento de la generación térmica con motores diésel, generando millones de toneladas de gases de efecto invernadero que se emitieron a la atmósfera. Para evitar que se presente este inconveniente, es necesario promover el uso de la energía eólica para diversificar la matriz energética ecuatoriana. Esta matriz está compuesta por un 70% de energía hidráulica y un 0,26% de energía eólica. Sin embargo, la integración de la energía eólica en la red eléctrica producida por parques eólicos de alta potencia ubicados en zonas montañosas es una tarea difícil debido a la variabilidad del viento. Además, los Andes ecuatorianos tienen un importante potencial eólico sin explotar debido a su compleja orografía. Actualmente, no existen estudios detallados sobre potencial eólico o predicción de energía eólica en los Andes. En consecuencia, la caracterización del recurso eólico es necesaria. Así como se requieren métodos precisos para predecir la cantidad de energía eólica generada a corto plazo todos los días, lo que se requiere para integrarla a la red eléctrica. El operador de la red necesita el pronóstico de energía por hora para programar los generadores renovables y administrar otros generadores estables para mantener la red equilibrada y la distribución eficiente de energía.

Con el fin de direccionar los desafíos antes mencionados, promover el desarrollo de la energía eólica, evaluar y predecir el potencial eólico y disminuir la necesidad de generadores térmicos, esta tesis describe una metodología para implementar un modelo híbrido basado en modelos de regresión lineal como línea de base para el pronóstico de velocidad de viento (WS), Redes Neuronales Dinámicas. y Redes Neuronales Recurrentes (DNN-RNN) para optimizar la predicción, lo que representa un aporte relevante en este ámbito de investigación. La metodología propuesta permite caracterizar el recurso eólico, pronosticar la velocidad del viento, predecir la energía eólica y estimar los costos de energía con seis horas de anticipación, tanto para invierno como para verano. También favorece la modelización de las características del viento a través del software Ansys Fluent CFD Dinámica Computacional de Fluidos para el posicionamiento de 11 aerogeneradores Goldwind 70/1500 KW para optimizar la Producción Energética Anual (AEP) de un parque eólico hipotético. El modelo propouesto de pronóstico de WS fue entrenado y validado usando datos medidos por dos torres meteorológicas instaladas en el área montañosa de estudio. Los principales hallazgos del estudio indican que el paso del viento entre dos volcanes tiene un alto potencial eólico. Este potencial depende de las variables meteorológicas, la orografía y el efecto acelerador de la velocidad del viento. Estas favorables condiciones hacen posible la instalación de un parque eólico en esta zona con 11 aerogeneradores de alta potencia. Además, el diseño del parque eólico utilizando Ansys CFD mostró que el modelo K-epsilon puede modelar el perfil de las

velocidades del viento y la intensidad de turbulencia (TI) sobre una montaña simulada con gran precisión. Además, la red Memoria de Largo-Corto Plazo (LSTM), debido a su celda de memoria integrada que permite recordar estados previos para predecir valores futuros, alcanzó los valores más bajos de Error Porcentual Absoluto Medio (MAPE) y Raíz del Error cuadrático Medio (RMSE), en comparación con la red Autorregresiva No Lineal con Entrada Exógena (NARX), para predecir la velocidad del viento y la energía eólica en verano a una altura de 80 m Sobre el Nivel del Suelo (AGL), trabajando con velocidades de viento nominales con baja Intensidad de Turbulencia (TI), que permiten la operación continua de viento turbinas a potencia nominal.

RESUMEN (en inglés)

In recent years, research has revealed that hydropower designs in Ecuador have not adequately considered sensitivity to climate change. In addition, climatic conditions determine the variations in electricity generation from this renewable energy source. In addition, variations in rainfall patterns cause a drought from July to October due to the lack of rain. Therefore, it would decrease the flow of the rivers that feed the dams for hydroelectric generation, which would result in a significant reduction of its generating capacity. In previous years, the drought caused an increase in thermal generation with diesel engines, generating millions of tons of greenhouse gases that were emitted into the atmosphere.

To prevent this inconvenience from occurring, it is necessary to promote the use of wind energy to diversify the Ecuadorian energy matrix. This matrix is made up of 70% hydropower and 0.26% wind power. However, the integration of wind energy into the electrical grid produced by high-power wind farms located in mountainous areas is a difficult task due to the variability of the wind. Moreover, the Ecuadorian Andes has significant untapped wind potential due to their complex orography. Currently, there are no detailed studies on wind potential or wind energy prediction in the Andes. As a result, wind resource characterization is necessary. As well as, precise methods are required to predict the amount of wind energy generated in the short term every day, which is done to integrate it into the electrical grid. The grid operator needs the hourly power forecast to schedule and manages renewable generators and other stable generators to keep the grid balanced and power distribution efficient.

In order to address the challenges mentioned above, promote wind energy development, assess wind potential, and diminish the need for thermal generators, this thesis describes a methodology to implement a hybrid model based on linear regression models as a baseline for WS forecasting and Dynamic Neural Networks and Recurrent Neural Networks (DNN-RNN) to optimize prediction, which represents a relevant contribution in this research scope. The proposed methodology allows for wind resource characterization, wind speed forecasting, wind energy prediction, and estimating energy costs six hours in advance, both for winter and summer. It also favors the modeling of wind characteristics through the Ansys Fluent CFD (Computational Fluid Dynamics) software for the positioning of 11 Goldwind 70/1500 KW wind turbines to optimize the AEP (Annual Energy Production) of a hypothetical wind farm. The proposed WS forecasting model was trained and validated using data measured by two meteorological towers installed in the mountainous study area. The study's main findings indicate that the wind passing between two volcanoes has a high wind potential. This potential is dependent on meteorological variables, orography, and the accelerating effect of wind speed. These favorable conditions make it possible to install a wind farm in this area with 11 high-power wind turbines. Furthermore, the wind farm design using Ansys CFD showed that the K-epsilon model can model the profile of wind speeds and Turbulence Intensity (TI) over a simulated mountain with great precision. Moreover, the Long-Short Term Memory (LSTM) network, due to its embedded memory cell that allows remembering previous states to predict future values, reached the lowest values of Mean Absolute Percentage Error (MAPE) and Root Mean Square Error (RMSE) compared with the Nonlinear Autoregressive network with Exogenous input (NARX), to predict wind speed and wind energy in summer at the height of 80 m AGL, working with nominal wind speeds with low Turbulence Intensity (TI), which allow continuous operation of wind turbines at nominal power.

SR. PRESIDENTE DE LA COMISIÓN ACADÉMICA DEL PROGRAMA DE DOCTORADO EN _____

Universidad de Oviedo

Departamento de Ingeniería Eléctrica, Electrónica de
Computadores y Sistemas

Tesis Doctoral

Caracterización del régimen de viento y predicción de velocidad de viento y energía eólica a corto plazo, utilizando redes multivariable LSTM y NARX en la Cordillera de los Andes, Ecuador

Germánico Adán López López

Tesis presentada en cumplimiento de los requisitos para la obtención del grado de Doctor en el programa de Doctorado en Energía y Control de Procesos de la Universidad de Oviedo

Supervisor: PhD. Prof. Pablo Arboleya Arboleya.

Enero 2023

To all my dear family . . . I would like to dedicate this work to my dear family: Olga my mother, Angie, Diego, and David, who, one by one, came into my life during this time and made it all possible.

Acknowledgements

First of all, I want to express my most sincere gratitude to my supervisor, Professor Pablo Arboleya. I want to express my most sincere gratitude for his guidance, for his patience, for his dedication, for all knowledge he has transmitted to me, for recognizing all my efforts, and for constantly feeding my motivation. Thank you for understanding, and for standing with me during my difficult times, and for celebrating every achievement.

In memory of Germánico, my father, and Laura my mother-in-law, for being an example of perseverance, self-improvement, and sacrifice.

Resumen (Spanish)

En los últimos años, la investigación ha revelado que los diseños hidroeléctricos en Ecuador no han considerado adecuadamente la sensibilidad al cambio climático. Además, las condiciones climáticas determinan las variaciones en la generación de electricidad a partir de esta fuente de energía renovable. También, las variaciones en el régimen de lluvias provocan una sequía de julio a octubre por la falta de lluvias. Por lo tanto, disminuiría el caudal de los ríos que alimentan las represas para la generación hidroeléctrica, lo que resultaría en una importante reducción de su capacidad de generación. En años anteriores, la sequía provocó un aumento de la generación térmica con motores diésel, generando millones de toneladas de gases de efecto invernadero que se emitieron a la atmósfera.

Para evitar que se presente este inconveniente, es necesario promover el uso de la energía eólica para diversificar la matriz energética ecuatoriana. Esta matriz está compuesta por un 70% de energía hidráulica y un 0,26% de energía eólica. Sin embargo, la integración de la energía eólica en la red eléctrica producida por parques eólicos de alta potencia ubicados en zonas montañosas es una tarea difícil debido a la variabilidad del viento. Además, los Andes Ecuatorianos tienen un importante potencial eólico sin explotar debido a su orografía compleja. Actualmente, no existen estudios detallados sobre potencial eólico o predicción de energía eólica en los Andes. En consecuencia, la caracterización del recurso eólico es necesaria. Así como se requieren métodos precisos para predecir la cantidad de energía eólica generada a corto plazo todos los días, lo que se requiere para integrarla a la red eléctrica. El operador de la red necesita el pronóstico de energía eólica horaria para programar los generadores renovables, y administrar otros generadores estables para mantener la red equilibrada y la distribución eficiente de energía.

Con el fin de direccionar los desafíos antes mencionados, promover el desarrollo de la energía eólica, evaluar y predecir el potencial eólico, y disminuir la necesidad de generadores térmicos. Esta tesis describe una metodología para implementar un modelo híbrido basado en modelos de regresión lineal como línea de base para el pronóstico de velocidad de viento (WS), Redes Neuronales Dinámicas. y Redes Neuronales Recurentes (DNN-RNN) para optimizar la predicción, lo que representa un aporte relevante en este ámbito de investigación. La metodología propuesta permite caracterizar el recurso eólico, pronosticar la velocidad del viento, predecir la energía eólica y es-

timar los costos de energía con seis horas de anticipación, tanto para invierno como para verano. También favorece la modelización de las características del viento a través del software Ansys Fluent CFD Dinámica Computacional de Fluídos para el posicionamiento de 11 aerogeneradores Goldwind 70/1500 KW para optimizar la Producción Energética Anual (AEP) de un parque eólico hipotético. El modelo propouesto de pronóstico de WS fue entrenado y validado usando datos medidos por dos torres meteorológicas instaladas en el área montañosa de estudio.

Los principales hallazgos del estudio indican que el paso del viento entre dos volcanes tiene un alto potencial eólico. Este potencial depende de las variables meteorológicas, la orografía y el efecto acelerador de la velocidad del viento. Estas favorables condiciones hacen posible la instalación de un parque eólico en esta zona con 11 aerogeneradores de alta potencia. Además, el diseño del parque eólico utilizando Ansys CFD mostró que el modelo K-epsilon puede modelar el perfil de las velocidades del viento y la intensidad de turbulencia (TI) sobre una montaña simulada con gran precisión. Además, la red Memoria de Largo-Corto Plazo (LSTM), debido a su celda de memoria integrada que permite recordar estados previos para predecir valores futuros, alcanzó los valores más bajos de Error Porcentual Absoluto Medio (MAPE) y Raíz del Error cuadrático Medio (RMSE), en comparación con la red Autorregresiva No Lineal con Entrada Exógena (NARX), para predecir la velocidad del viento y la energía eólica en verano a una altura de 80 m Sobre el nivel del suelo (AGL), trabajando con velocidades de viento nominales con baja intensidad de turbulencia (TI), que permiten la operación continua de aerogeneradores a potencia nominal.

Abstract

In recent years, research has revealed that hydropower designs in Ecuador have not adequately considered sensitivity to climate change. Furthermore, climatic conditions determine the variations in electricity generation from this renewable energy source. Moreover, variations in rainfall patterns cause a drought from July to October due to the lack of rain. Therefore, it would decrease the flow of the rivers that feed the dams for hydroelectric generation, which would result in a significant reduction of its generating capacity. In previous years, the drought caused an increase in thermal generation with diesel engines, generating millions of tons of greenhouse gases that were emitted into the atmosphere.

To prevent this inconvenience from occurring, it is necessary to promote the use of wind energy to diversify the Ecuadorian energy matrix. This matrix is made up of 70% hydropower and 0.26% wind power. However, the integration of wind energy into the electrical grid produced by high-power wind farms located in mountainous areas is a difficult task due to the variability of the wind. In addition, the Ecuadorian Andes have significant untapped wind potential due to their complex orography. Currently, there are no detailed studies on wind potential or wind energy prediction in the Andes. As a result, wind resource characterization is necessary. As well as, precise methods are required to predict the amount of wind energy generated in the short term every day, which is done to integrate it into the electrical grid. The grid operator needs the hourly power forecast to schedule and manages renewable generators and other stable generators to keep the grid balanced and power distribution efficient.

In order to address the challenges mentioned above, promote wind energy development, assess wind potential, and diminish the need for thermal generators. This thesis describes a methodology to implement a hybrid model based on linear regression models as a baseline for WS forecasting and Dynamic Neural Networks and Recurrent Neural Networks (DNN-RNN) to optimize prediction and Wind Resource Characterization in the Ecuadorian Andes to install a potential wind farm, which represent a relevant contribution in this research scope. The proposed methodology allows for wind resource characterization, wind speed forecasting, wind energy prediction, and estimating energy costs six hours in advance, both for winter and summer. It also favors the modeling of wind characteristics through the Ansys Computational Fluid Dynamics (CFD software for the positioning of 11 Goldwind 70/1500 KW wind tur-

bines to optimize the Annual Energy Production (AEP) of a hypothetical wind farm. The proposed WS forecasting model was trained and validated using data measured by two meteorological towers installed in the mountainous study area.

The study's main findings indicate that the wind passing between two volcanoes has a high wind potential. This potential is dependent on meteorological variables, orography, and the accelerating effect of wind speed. These favorable conditions make it possible to install a wind farm in this area with 11 high-power wind turbines. Furthermore, the wind farm design using Ansys CFD showed that the K-epsilon model can model the profile of wind speeds and Turbulence Intensity (TI) over a simulated mountain with great precision. Moreover, the Long-Short Term Memory (LSTM) network, due to its embedded memory cell that allows remembering previous states to predict future values, reached the lowest values of Mean Absolute Percentage Error (MAPE) and Root Mean Square Error (RMSE) compared with the Nonlinear Autoregressive network with Exogenous Input (NARX), to predict wind speed and wind energy in summer at the height of 80 m Above Ground Level (AGL), working with nominal wind speeds with low Turbulence Intensity (TI), which allow continuous operation of wind turbines at nominal power.

Acronyms

ABL   Atmospheric Boundary Layer.

AGL   Above Ground Level.

ANN   Artificial Neural Networks.

AR   Auto Regressive.

ARMA   Auto regressive Moving Average.

ASL   Above Sea Level.

BPTT   Back Propagation Through Time.

CDF   Cumulative Density Function.

CONELEC National Electricity Council.

FNN   Feedforward Neural Networks.

DNN   Dynamic Neural Networks.

GEP   Gross Energy Production.

GSR   Global Solar radiation .

LSTM   High Resolution Limited Area Model.

MEER   Ministry of Electricity and Non-Renewable Resour

NAR   Nonlinear Auto Regressive network .

NARX   Nonlinear Auto Regressive network with exogenous

NREL   National Renewable Energy Laboratory .

NWP   Numerical Weather Prediction .

OECD   Organisation for Economic Co-operation and Devel

PDF   Probability Density Function.

RANS   Reynolds Average Navier-Stokes.

RNN   Recurrent Neural Networks.

WASP   Wind Atlas Analysis and Application Program.

WD   Wind Direction.

WECS   Wind Energy Conversion Systems.

WPP   Wind Power Potential.

WRA   Wind Resource Assessment.

WS   Wind Speed .

WSC   Wind Shear Coefficient.

Contents

Chapter 1

Introduction

In the first chapter, a light introduction to the short-term prediction of wind speed and wind power in wind farms is presented, as well as specific objectives proposed in the thesis are described. Finally, the summary of the content of the chapters is indicated.

1.1 Introduction

The global demand for energy coming from fossil fuels had a significant annual growth tendency in 2018 [1]. Fuel combustion produces hazardous emissions that cause environmental damage as global warming [2, 3]. To mitigate this effect and reduce conventional fuel dependence; it is important to use renewable energies available in their different forms. According to OECD, the proportion of renewable energy in the total primary energy supply for 2018 reached a new high of 10.2% [1]. Wind energy has become one of the most relevant forms of renewable energy [4–6]. By the end of 2019, it reached a global installed wind power capacity of 651 GW, with 60.4 GW of newly installed power, with an increase of 10% compared to 2018 [7,8]. It is expected to reach a total installed power of 840 GW by 2022. The global distribution of wind power in 2017 was as follows: Africa 4.52 GW, Asia 228.6 GW, Europe 177.5 GW, North America 150.3 GW, Pacific Region 5.1 GW, Latin America, and Caribbean 17.2 GW [2, 5]. However, it is difficult to integrate renewable generation into the power grid either temporally or spatially [9, 10]. Nowadays, wind energy is considered one of the renewable energy sources more economical and environmentally friendly due to being a fully mature technology for energy use. Wind energy has had rapid growth last two decades [2,4,7]. The growth of wind energy is driven by depletion in operation and maintenance costs, as well as an increase in wind turbine size and reliability [2]. Currently, Vestas WT V236/15MW (See Fig. 1.1) leads the field of largest offshore WTs built to innovate the future of the wind industry [11]. Whereas, the major problem of introducing wind energy into the power grid is the variability and intermittence of

Figure 1.1: Wind turbine offshore Vestas V236/15MW [11]

the wind, which is one of the main barriers faced by power system operators [3, 7]. Accurate forecasting tools are required to solve this problem, directed to the principal objectives of planning wind turbine schedules, cutting down power system operation costs, and reducing its fluctuation [12, 13].

Wind over complex terrain is mainly influenced by land topography and elevation [14]. In this way, wind flow passing over topographical variations, such as mountain tops, ridges, escarpments, and channel pits in mountain ranges, causes wind speed acceleration and turbulence [15, 16]. Wind Turbulence is fluctuations in wind speed on a relatively fast time scale, generally less than ten minutes. It is generated by two main causes: (1) friction of wind speed with the surface of the earth, which causes wind flow disturbance, and (2) thermal effects caused by variations in air temperature and density; which cause vertical movements in the air masses [17, 18]. It should be noted that wind speed increases with height above ground and there is a great wind potential in the mountainous regions. In particular, between the Andes volcanoes Chimborazo 6263 m ASL and Carihuayrazo 5116 m ASL; where wind speed increases its speed and reduces pressure named tunnel effect as is shown in Fig. 5.2 [17, 19, 20].

In recent years, research has revealed that hydroelectric power designs in Ecuador have not appropriately considered climate change sensitivity. " As a result, variations in rainfall patterns, which in turn cause the drought that occurs from October to March next year due to the warm current of El Niño, could reduce the flow of rivers that feed the dams for hydroelectric generation in Ecuador, could have a significant impact on hydroelectric generation capacity. Drought concerns in prior years compelled an increase in heat generation utilizing diesel engines, resulting in millions of tons of greenhouse gas emissions [21].

To prevent the occurrence of this inconvenience, and promote the use of non-conventional renewable energies to diversify the Ecuadorian energy matrix. In March 2014, Resolution CONELEC 001/13/footnotemark[1] was published, which established the goal of establishing the treatment of non-conventional renewable generators in the Ecuadorian electricity sector. generation facilities under the centralized system whose installed power is greater than 10 MW, both in the case of selling the energy generated through preferential rate 1 to the electricity market. On the other hand, ARCONEL regulation 004/15 establishes the criteria and technical requirements for the connection of renewable generators to the transmission and distribution networks to ensure the quality of the electricity service in the generator's influence area and to maintain the voltage and current levels within acceptable ranges.

The community of Mechahuasca located within of the zone of study, was the selected place because of its high wind potential, which requires to be assessed for wind energy applications [21, 22]. Near this location, García et al. [23] studied the influence of sampling rate on wind power density for these communities in the highlands of the Ecuadorian Andes, and proposed a PDF based on the daily Gaussian average of sinusoidal waveforms. Additionally, Ayala et al. [24] estimated the wind energy in the Villonaco wind farm located in complex terrain at a high altitude (2700 m ASL). The results were an annual wind speed of over 10 m/s and a capacity factor of 0.53.

Specifically, the wind energy industry in recent years has used the CFD software for WRA and predictions. The evolution of computational wind engineering makes very attractive the evaluation of wind speed over complex terrain. In fact, significant progress has been made in the CFD application for specific cases of the evaluation of wind flow over escarpments, single and multiple hills, as well as valleys [25]. Many decades ago, CFD emerged as a reliable tool for simulating several engineering problems [26]. It consists in solving a set of Navier-Stokes differential equations, to describe the flow in a particular domain. These equations accompanied by the turbulence models have been able to characterize with acceptable precision the wind behavior on the top of the mountains. In recent studies, Ayala et al. [24] used the Meteodyn CFD tool based on a nonlinear flow model to compare the actual AEP of the Villonaco wind farm with the estimated AEP by Meteodyn. The simulation results indicated that the CFD modeling is adequate for complex terrain, which should be validated by site measurements. Arteaga-López et al, proposed a CFD methodology to improve wind resource assessment for urban environments. The CFD results showed the efficacy of the suggested methodology to implement small wind turbines in urban and rural areas [27]. Tabas et al. [28] analyzed the Windsim CFD software to perform accurate wind power prediction in wind farms over complex terrain. The CFD results showed that Windsim with a proper combination of TI models can predict wind farm performance with great accuracy. In this work, a two-dimensional-2D CFD modeling was carried out using RANS and k-ϵ turbulence model equations to evaluate wind flow characteristics over a location in the Ecuadorian Andes complex terrain and to validate with similar calculated values.

Regardless of studies about wind power assessment in complex terrain in the

Ecuadorian Andes. Nowadays, there is no work on wind speed and power forecasting. Consequently, it appears the need to develop a method to estimate the energy potential of a wind regime in a mountainous region of the Western Ecuadorian Andes. This research will enable us to identify feasible places for wind farm installation considering terrain orography through commercial software Ansys CFD. In addition, to develop an accurate model for short-term wind speed and power forecasting. In order to achieve this objective, the author presents a technique based on single-variable regressive models, such as the persistence model, MA, and ARMA; which serve as the basis for wind speed forecasting; to improve forecasting performance, advanced RNN, such as LSTM networks, as well as NARX models using measured meteorological variables, are employed. This thesis has three main contributions: (1) The proposed model takes wind speed behavior over complex terrain to the next level using the NARX-LSTM networks. (2) The results of the proposed model for wind speed forecasting represent a relevant contribution to scientific research due to no available previous studies in Ecuador and worldwide. (3) This study provides updated data and novel insights into WS and power forecasting over complex terrain very useful for electrical network operators and investors in wind projects.

This thesis is directed to carry out a wind regime characterization and to develop an approach for short-term WS forecasting 6 hours in advance in the western Andes Mountains Range of Ecuador. A hybrid statistical and DNN-RNN model will be used to forecast wind speed. The main reason for conducting this research is related to the need to have an accurate approach to predicting wind speed and power in the Ecuadorian Andes. This study provides updated data and novel insights into WS and power forecasting over complex terrain. This knowledge is very useful for operators of the electrical network and investors in wind projects.

1.2   Background

Selection of input variables and forecasting methods play major roles in influencing the accuracy of wind speed forecasting results [3, 4]. Wind power generation and wind farm planning are heavily dependent on wind speed, so input variables selection has become very relevant in wind speed forecasting [7, 29]. Wind speed and power forecasting are influenced by meteorological variables, such as wind direction, barometric pressure, temperature, humidity, and others. Because wind speed is a key factor in wind power generation and wind farm planning, choosing the input variables has become extremely important [13, 30, 31]. Wind speed is the most important factor in a climate that varies according to geographical position [32, 33]. An ANN model for predicting wind speed based on measurements taken in Hamirpur has been developed by Ramasamy et al. The MAPE and correlation coefficients achieved were 4.55% and 98.5% for predicting the daily wind speed. [34]. A forecasting model for short-term household energy consumption was developed by Becalli et al. [35] using an Elman network and weather variables. As a result of forecasting, the forecasting accuracy was 97.6% and the average error rate was 3.1%.

In the last 20 years, the wind energy sector has experienced rapid growth [2, 4, 7]. Figure 1.1 shows the largest offshore wind turbine Vestas V236/15MW made to date. The wind industry is growing exponentially as wind turbines are becoming more powerful, and reliable, operating at lower costs, and reducing maintenance costs [2]. A major obstacle for system operators in integrating wind power into the electrical grid is the variability and intermittent nature of the wind [3, 7]. In order to solve wind intermittence, accurate forecasting tools are needed, which are mainly aimed at reducing the cost of power system operation cost and reducing the variation of wind turbine schedules [12, 13]. At present, due to the fast spread of wind power generation, worldwide wind speed forecasting techniques have significant great importance for the characterization of wind resources, resource assessment, and forecasting of wind power generation. Because of the complex physics of the atmosphere, wind power is generally characterized by its instability and intermittence when forecasting based on a time horizon [15, 18, 36]. For wind power to be incorporated into the electrical grid, it is required that wind turbines are operated by integrated transmission systems, as well as accurate forecasting tools based on weather forecasts [20, 37]. A major objective of wind speed and power forecasting is to predict wind speed and power with high precision and speed so that they can be incorporated into the power grid [3, 38]. Wind speed and power forecasting, spatial correlation forecasting, regional forecasting, probabilistic forecasting, and offshore forecasting are the five classes of forecasting methods [3]. Various wind speed and power forecasting approaches, including physical, statistical, and artificial intelligence for renewable energy systems have been performed to improve the accuracy of forecasting methodologies [18, 39, 40]. Furthermore, the application of machine learning techniques has enhanced energy efficiency, energy control, and stability in energy demand prediction in renewable energy systems [41]. These techniques have been utilized in the modeling, design, and prediction of energy systems for many years, with rapid development   citeAHMAD2020102052,en12071301. These methods have been used all around the world to assess wind power performance and collect useful data for use in wind power producing systems [42–44].

There are ten types of machine learning algorithms used in wind energy systems, including ANN, MLP, ELM, SVM, WNN, ANFIS, decision trees, deep learning, ensembles, and sophisticated hybrid models [41]. Forecasting and prediction, prediction and control, design optimization, fault detection, and diagnosis are four basic types of ANN models that can be categorized based on the application [4]. In South America, Zucatelli et al. [45] used an ANN approach to create a one-year short-term wind speed forecasting model for Colonia Eulacio, Uruguay. The results revealed good accuracy for the heights evaluated, as well as ideal wind speed forecasts at a reasonable cost of computation. According to recent studies, forecasting accuracy declines over a six-hour time frame, and the MAPE rises to roughly 15%.

Wind speed and wind power modeling and forecasting in complex terrain have gained a lot of interest in recent years because wind speed increases on top of hills and mountains that can be used to generate electricity through wind turbines [20, 39]. For this reason, has been developed many research works dedicated to improving wind

power forecasting performance. The wind power assessment in complex terrain must be done carefully considering morphological features [6,46], and unstable weather regimes to install wind turbines in a mountainous region [3]. FNN was used to predict hourly wind speed in a coastal region with complex topography. To increase ANN accuracy was used a wind vector incorporated variability [47]. Mana et al. [48] proposed two models ANN pure and a hybrid ANN-CFD to forecast wind power in very complex terrain in Italy. The two methods had similar performances. However, the hybrid model showed better performance in low and high wind speed ranges. Tabas et al. [28] analyzed a CFD technique to forecast wind power in complex terrain. It was stated the combined presence of three complex factors: topography, heterogeneous vegetation, and interactions between wind turbine wake.

In order to make a more accurate wind speed forecasting using real data measured in complex terrain located at high altitudes. This study proposes wind speed forecasting with great accuracy by using the NARX network used until now by a few researchers as follows: Cadenas et al. [49] generated a model to forecast short-term wind speed in Mexico by using the NARX model and compared with NAR and persistent models. The results indicated that the NARX model had a performance of 4% over the NAR and 11% over the persistence model. Gao and Er [50] proposed a NARMAX time series model prediction using FNN and RNN as approaches to improve the performance of the NARX model. Hence, comparative studies demonstrated that the FNN approach can flexibly learn complex temporal sequences. Jawad et al. [51] developed a GA-NARX model to predict short-term or medium-term wind power and electrical load. The results showed good accuracy for short-term wind speed forecasting.

In recent studies, according to technological advances in machine learning. Therefore, new deep learning algorithms have been designed and widely used for time series prediction. Among these algorithms, the LSTM networks part of RNN are used for accurate wind speed forecasting results [52]. Liu et al. [53] proposed a deep learning strategy for multistep wind speed forecasting based on EWT to disintegrate original data, LSTM to predict low-frequency data, and Elman networks to predict high-frequency data. The results of the proposed model indicated good forecasting performance. Xie et al. [54] presented a short-term wind speed forecasting model based on ARMA and multi-variable LSTM network by using meteorological variables data in Beijing. The results showed feasibility in forecasting and LSTM superiority over ARMA and simple variable LSTM. These samples of LSTM studies show good feasibility for prediction; as well as consider in this study this algorithm as a good option to improve the wind speed forecasting performance.

From the literature review above, it is observed that have not been reported studies about wind speed forecasting by employing LSTM or NARX models over complex terrain located at high altitudes in the Western Ecuadorian Andes. The present work improves on the previous ones in the fact that it is the first in predicting wind speed at the highest altitude reported so far (4350 m ASL); as well as using RNN and DNN models in place of hybrid models. The LSTM and NARX networks have been developed using measured data instead of climatic models. Furthermore, it is validated by using

DNN instead of hybrid models using wind speed measurements closer to the hub height of high-power wind turbines. From this point of view, this study is unique, and the conclusions obtained from the setup wind speed forecasting method can be helpful for other researchers to forecast wind speed in mountainous terrains at high altitudes.

1.3   Description of the problem

In recent years, research has revealed that hydroelectric power designs in Ecuador have not appropriately considered climate change sensitivity. Furthermore, climatic conditions determine the variations in the electrical generation of this renewable energy source. As a result, variations in rainfall patterns, in turn, causing the drought that occurs from July to October of each year due to the absence of rainfall, could reduce the flow of rivers that feed the dams for hydroelectric generation in Ecuador, could have a significant effect on hydroelectric generation capacity. Drought concerns in prior years compelled an increase in heat generation utilizing diesel engines, resulting in millions of tons of greenhouse gas emissions [21].

To prevent the occurrence of this inconvenience, we need to promote the use of non-conventional alternative energies in order to diversify the Ecuadorian energy matrix, which is made up of 70% hydraulic power. The Resolution CONELEC 001/13/footnote mark [1] of March 2014 established the objective of predicting hourly energy production for each day as renewable non-conventional generators in the Ecuadorian electricity sector for installations in centralized systems with an installed power of more than 10 MW, which is a preferential rate for the sale of electricity produced under the preferential rate [55]. On the other hand, ARCONEL regulation 004/15 defines the criteria and technical requirements for the connection of renewable generators to the transmission and distribution networks. This is to ensure the quality of the electricity service in the generator's influence area and to maintain the voltage and current levels within acceptable ranges.

Ecuador is a privileged country for the exploitation of wind energy, due to many areas with high potentials, such as the Andes Mountains, due to its complex orography. Specifically, one of the main areas with the greatest wind potential in the Highlands is the wind passing between two volcanoes. The Wind Atlas of 2013 provides general information on the wind regime in this zone. However, wind behavior in this zone is specific because of the complex terrain orography. This causes large variations in WS, but until now, this hasn't been assessed in depth to take advantage of this high wind potential for wind speed and power forecasting.

Wind speed behavior in the channel pass shows a wind speed-up effect originating from the venturi effect. The Ecuadorian Wind Atlas at 80 m AGL uses an NWP model and a mesoscale map, which suggests the need to prepare a WRA, short-term WS forecasts, and power forecasts based on ANN models using collected meteorological variables in situ in 2018.

[0.1]Generators that are subject to centralized dispatch must notify CENACE about the forecast of

1.4   Thesis motivation

The main reason has arisen within the context of wind energy prediction, from the critical need to have a tool that can predict short-term wind speed and power over complex terrain with high accuracy, which has been required by electricity companies and system operators, who have assigned significant economic investments in wind farm projects. Furthermore, to generate and contribute original knowledge on wind resource assessment in the Ecuadorian Andes and prediction of wind speed and wind energy using DNN-RNN by highlighting the application of the wind speed forecasting proposed model and modeling of wind characteristics in the study area using the Ansys Fluent CFD software. Therefore, the feasibility of this wind farm project is highly dependent on an accurate assessment and prediction of the wind power potential.

1.5   Thesis outline

The thesis is structured into seven chapters as follows:

- **Chapter 1** presents the thesis objectives, background, and contributions.

- **Chapter 2** introduces wind energy integration into the electrical grid and describes wind characteristics over complex terrain.

- **Chapter 3** describes the current status of wind energy used for electricity generation in Ecuador and worldwide. Also, it shows wind energy integration into the electrical grid.

- **Chapter 4** examines different models used for wind speed and power forecasting. Also, it describes the proposed model.

- **Chapter 5** describes wind speed and power forecasting methodology using the proposed model.

- **Chapter 6** comprises the main results obtained for wind power assessment and modeling of wind characteristics in the Ecuadorian Andes.

- **Chapter 7** presents short-term wind speed forecasting, wind power, and wind energy results using a theoretical wind farm in 2018. In addition, wind farm micro-siting simulation results using Ansys Fluent CFD software are shown.

- The **Appendix** includes the journal publications derived from this research.

---

hourly energy production for each day, within the deadlines established in the Dispatch and Operation Procedures, in order for CENACE to carry out the daily programming.

1.6   Thesis objectives and contributions

According to the motivations described above, there are two primary aims, encompassing other specific objectives:

1. Wind regime characterization over complex terrain in the Ecuadorian Andes in 2018 using the measured meteorological variables. This work has led to a paper published in the Wind Engineering journal. Hence, the research developed has contributed to an article submitted to the Electric Power Systems Research (EPSR) Journal, which is currently under review.

    - Determinate the wind characteristics and wind speed variation with the height change.
    - Select the most compatible wind turbine for the study area.
    - Design a theoretical wind farm in the study area using Ansys Fluent CFD software.
    - Modelate TI and average WS in the study area using Ansys Fluent CFD software.

2. Develop a methodology for a short-term wind speed and power forecasting model over complex terrain in the Ecuadorian Andes. The work developed in this context has contributed to a paper published in the Renewable Energy journal

    - Elaborate the WS forecasting proposed model using linear regression models as a baseline and DNN-RNN models to optimize the wind speed forecasting.
    - Validate the WS forecasting proposed model using the meteorological variables measured in the study area.
    - Predict short-term wind energy in the study area considering predicted wind power.
    - Determine the cost of short-term predicted energy in the study area using NARX and LSTM networks.

The final result has been the design of a model based on statistical models RNN, and DNN.

The case studies will be evaluated for the fulfillment of the specific objectives given, as well as the forecast of power and wind energy, to test the accuracy of the proposed prediction model, and the results obtained will be analyzed and compared to the results of published works. Of course, the outcomes of the suggested model are expected to outperform those of published studies.

1.7   Thesis publications

The following three papers are included in the thesis.

1.7.1 Published papers

Paper 1

A novel probability density function applied to wind characterization in order to evaluate the wind power potential in Tungurahua, Ecuador's Andean region.

Javier García del Valle, Alex Mayorga and Germánico López, Published in Wind Engineering, DOI:10.1177/0309524X18780383, 2018, Publisher SAGE. Quality indexes of the Renewable Energy Journal: CiteScore rank 2021: 2.4, Third Quartile (Q3), 43rd percentile, Subject Area: Energy: Energy Engineering and Power Technology, Energy: Renewable Energy, Sustainability and the Environment, URL: https://www.scopus.com/sourceid/13850. Hence, it has an Impact Factor (IF): 1,8, Citations: Crosfef (1)

Paper 2

Short-term wind speed forecasting over complex terrain using linear regression models and multivariable LSTM and NARX networks in the Andes Mountains, Ecuador

Germánico López and Pablo Arboleya, Published in Renewable Energy (183), $https : //doi.org/10.1016/j.renene.2021.10.070$, January 2022, Publisher: Elsevier. Quality indexes of the Renewable Energy Journal: CiteScore rank 2021: 13.6, First Quartile (Q1), 90th percentile, Subject Area: Energy: Renewable Energy, Sustainability and the Environment, URL: $https : //www.scopus.com/sourceid/27569tabs = 1$ Hence, it has an Impact Factor (IF): of 8,634, Citations: Google Scholar (14), Science Direct (14), considering that the paper was published in January 2022, it is placed in the 94th quartile, according to the PlumX Metrics, URL: $https : //plu.mx/plum/a/?doi = 10.1016/j.renene.2021.10.070theme = plum-sciencedirect-themehideUsage = true$

1.7.2 Submitted paper

Paper 3 Status: In revision

Wind power assessment and wind farm design using Computational Fluid Dynamics in the Andes Mountains, Ecuador

Germánico López, Pablo Arboleya, Diego Núñez, and Andrés Freire submitted to the Energy Conversion and Management Research journal on 2022- Nov- 25.

Chapter 2

Wind energy generation over complex terrain

This chapter describes the wind's origin and its characteristics. Wind over complex terrain is also discussed, as well as the factors that affect wind speed over difficult terrain.

2.1 Introduction to WECS

WECS transforms wind energy into mechanical power. This mechanical energy is transformed into electricity by wind turbines. The energy is then used to do things like pump water, process grains, or move machines in windmills. Windmills with a vertical axis were probably the first wind turbines, dating back to 200 BC in Persia. They had several arms on which they mounted sails to move their arms, which were initially made from reed bundles. The first horizontal-axis windmills appeared in the Mediterranean region in the tenth century. They were designed to harness coastal winds. In Europe, horizontal windmills were first used a few hundred years later [56].

During the late nineteenth century, millions of windmills were built in the United States as the American West was developed. Most of them were utilized to irrigate farmland and ranches. Many European countries were using wind turbine generators to generate power by 1910. Wind energy accounts for about 1% to 2% of the energy that comes from the Sun. This is around 50 to 100 times more energy than all plants on Earth convert into biomass. Wind energy is a commercially viable renewable energy source, with modern wind farms producing power for around $0.05 per kWh. Wind-generated power is still not cost-competitive with coal- or natural-gas-generated electricity for the vast majority of the market, even at that production cost.

During the late nineteenth century, millions of windmills were built in the United States as the American West was developed. Most of them were utilized to irrigate farmland and ranches. Many European countries were using wind turbine generators to generate power by 1910. Wind energy accounts for about 1% to 2% of the energy that comes from the Sun. This is around 50 to 100 times more energy than all plants on Earth convert into biomass. Wind energy is a commercially viable renewable energy source, with modern wind farms providing power for around \$0.05 per kWh. Wind-generated power is still not cost-competitive with coal- or natural-gas-generated electricity for the substantial majority of the market, even at that production cost.

2.2   Wind origin and characteristics

2.2.1   Wind origin

The primary renewable energy resource on Earth comes from the Sun. Pressure shifts over the surface of the Earth brought on by uneven solar radiation heating are what produce global winds. The equator absorbs more solar energy than the poles do at the planet's surface. Depending on the received energy, convective cells develop in the lowest layers of the atmosphere. A straightforward flow model shows that air masses rise near the equator and fall near the poles. The circulation of the atmosphere, which results from unequal heating, is greatly influenced by the effects of the Earth's rotation [57].

Uneven solar radiation heating causes pressure variations across the Earth's surface, which produce global winds. The equator absorbs more solar energy than the poles do at the surface of the globe. As the number of incoming energy changes, convective cells develop in the lower layers of the atmosphere. In a straightforward flow model, air masses rise near the equator and fall at the poles. The circulation of the atmosphere, which results from uneven heating, is significantly influenced by the impacts of the Earth's rotation [57].

The atmospheric pressure field changes due to fluctuations in heat transmission to the Earth's atmosphere, causing air to move from high to low-pressure regions. In the vertical direction, there is a pressure gradient force, which is usually balanced out by the downward gravitational force. As a result, the winds are mainly horizontal in nature, responding to horizontal pressure gradients. Simultaneously, forces work to mix the various temperature and pressure air masses that are dispersed across the Earth's surface. The atmospheric winds are affected by the inertia of the air, the Earth's rotation, and friction with the Earth's surface.

Worldwide wind circulation, as seen in Fig. 2.8, involves large-scale wind patterns that cover the entire planet. These have an impact on the prevailing near-surface winds. It's worth noting that this model is an oversimplification because it ignores the impact of land masses on wind distribution. Air masses movement provides a sideways

push, causing air to circulate anticlockwise in the northern hemisphere and clockwise in the southern hemisphere around areas of low pressure.

2.2.2 Characteristics of wind in time and space

There are many ways in which atmospheric motions vary over time (seconds to months) and over space (centimeters to thousands of kilometers).

2.2.2.1 Temporal variations

In conventional practice, variations in wind speed over time are categorized as follows:

- Inter-annual: Wind speed varies over time and scales more extensively than one year. Their impact can be substantial on long-term wind turbine production as they estimate long-term mean wind at a site to predict interannual variability.

- Annual: Over most of the world, wind speeds vary significantly seasonally or monthly.

- Diurnal: A typical diurnal variation is an increase in wind speed during the day with the wind speeds lowest during the hours from midnight to sunrise.

- Short-term: Wind speed variations include turbulence and gusts over short-time periods. Turbulent fluctuations are typically considered to occur when wind speed changes have a stochastic character and have a period lower than ten minutes [57].

2.2.2.2 Location and wind direction variations

- Local variations The wind speed varies significantly between two sites near each other due to local topographical and ground cover variations.

- Wind direction variations The direction of the wind also varies over the same time scales as the wind speed. During wind turbine design and siting, short-term direction variations are considered a result of the turbulent nature of the wind.

2.2.3 Wind characteristics

Wind resource characteristics can help estimate wind resource potential by considering topics like its global origins.

2.2.3.1   Wind shear profile

Wind shear is defined as the horizontal or vertical variation in WS or WD with a height change in a small portion of the atmosphere [58]. These variations are due to some variables, such as elevation, atmospheric stability, the hour of the day, surface roughness, and terrain shape [20, 57]. Furthermore, it is also known as wind profile [17, 19]. In this work, the vertical wind speed profile was calculated using the power law. Its basic equation is shown in Equation 2.1.

$$\frac{V_2}{V_1} = \left(\frac{Z_2}{Z_1}\right)^{\alpha} \tag{2.1}$$

Where :

V_2 = the projected speed at the desired height h_2

V_1 = the observed speed at the measurement height h_1

α = a non-dimensional power law exponent

The power-law exponent is very variable from 0.1 to 0.35 due to many parameters, such as terrain elevation, the hour of the day, terrain classification, wind speed value, atmospheric stability, and other thermal and mechanical factors [57]. This exponent increases its value during the night hours, causing a stable atmosphere, and decreases during the day hours, originating a neutral and unstable atmosphere [59] α can be calculated from Equation 2.1 as is shown in Equation 2.2. This work was developed while considering a neutral atmosphere.

$$\alpha = \frac{\ln V_2 - \ln V_1}{\ln Z_2 - \ln Z_1} \tag{2.2}$$

2.2.3.2   Wind direction

Wind direction frequency information helps determine the preferred terrain shape and orientations within a wind farm and to optimize the placement of wind turbines [60]. In the context of wind resource assessment and wind power forecasting, directional changes in surface winds have significant relevance [61]. Wind speed and direction change over the same time scales. Seasonal changes may be minor, on the order of 30 degrees, while the average monthly winds may shift 180 degrees in a year. The turbulent nature of the wind causes short-term changes in wind direction. Wind turbine design and placement must account for these short-term fluctuations in wind direction. With changes in wind direction, horizontal axis wind turbines must spin (yaw). Yawing places gyroscopic loads on the turbine construction and puts any yawing mechanisms to the test. Blade loads are affected by crosswinds caused by shifts in wind direction. As a result, short-term changes in wind direction and related motion have an impact on components' fatigue life, such as blade loads and yaw drives [57].

2.2.3.3   Turbulence Intensity

Wind turbulence is the rapid disturbance in the wind speed, direction, and vertical component. Usually, the duration is from ten minutes to one hour, ranging from 0.1 to 0.4. TI is defined in Equation 2.3 and is an influential site characteristic that depends on the surface roughness, thermal behavior, height above the surface, and topographical features [17,57]. High turbulence levels may decrease power output and cause extreme loading on WT components.

$$TI = \frac{\sigma}{V}$$ (2.3)

Where σ is the standard deviation of wind speed, and V is the mean wind speed.

2.2.3.4   Weibull PDF

The Weibull distribution based on k and c parameters has been widely used for short-term and long-term wind data studies to represent the probability of occurrence of mean wind speed throughout one year [17,57,62].

The PDF Weibull is given for Equation 2.4.

$$f(V) = k \left(\frac{k}{c}\right) \left(\frac{V}{c}\right)^{k-1} exp\left[-\left(\frac{V}{c}\right)^{k}\right]$$ (2.4)

Where: k is the shape parameter dimensionless, which describes the wind speed distribution, and c is the scale parameter measured in m/s.

There are numerous approximations to calculate Weibull parameters k and c; one of them is the analytical model based on mean wind speed $\overline{V}$ and standard deviation σ which are shown in Equation 2.5 and Equation 2.6 respectively [37].

For $1 \leq k \text{ ¡ } 10$

$$k = \left(\frac{\sigma v}{\overline{V}}\right)^{-1.086}$$ (2.5)

$$c = \left[\frac{\overline{V}}{\gamma(1 + \frac{1}{k})}\right]$$ (2.6)

Where γ is the gamma function.

The annual mean wind speed $\overline{V}$ expressed in Equation 2.7 can be calculated from Equation 2.4.

$$\overline{V} = c\gamma\left[1 + \frac{1}{k}\right]$$ (2.7)

The CDF is the time interval or probability that WS may be lower or equal to a determined wind speed value. CDF is given in Equation 2.3 [57].

$$F(V) = 1 - exp\left[-\left(\frac{V}{c}\right)^k\right] \qquad (2.8)$$

2.2.3.5 Wind Power Density

The relationship between wind speed and temporal (frequency) distribution at the location determines WPD. Also, it is known as wind energy flux according to Equation 2.9. Furthermore, wind power resources are compared using WPD, which is independent of wind turbine size, according to NREL, and are considered as the quantitative basis of wind standard classification [37].

$$WPD = \left[\frac{P}{A}\right] = \left[\frac{1}{2}\right] * \rho * V^3 (W/m^2) \qquad (2.9)$$

2.2.4 Wind power estimation

This subsection will determine the productivity (both maximum energy potential and machine power output) of a given wind turbine at a given site in which wind speed information is available in either time-series format or summary format.

2.2.4.1 Available wind power

Theoretically, power available from a wind speed stream (V) over a unit rotor area can be calculated using Equation 2.10.

$$Pa = \frac{\rho A V^3}{2} \qquad (2.10)$$

Where:

Pa = Wind turbine active power (W)

ρ = Air density

A = Blades swept area (m^2)

V = Wind speed (m/s)

2.2.4.2 Efficiency in wind power extraction

The Power Coefficient (Cp) measures the efficiency of wind power extraction, which is the proportion of power extracted by the turbine to the overall power of the wind resource as is indicated in Equation 2.11 [63].

$$Cp = \frac{P_{WT}}{P_{Wind}} \tag{2.11}$$

As a result, the WT power capture process is given in Equation 2.12.

$$P_{WT} = \frac{\rho.A.V^3.Cp}{2} \tag{2.12}$$

Where:

P_{WT} = Wind turbine captured power (W)

The maximum extractable power fraction actually has a theoretical upper bound known as the Betz limit. According to Betz's theory, the maximum power coefficient, Cp =16/27 (59 percent), is the highest that a conventional wind turbine can achieve in terms of efficiency [57].

2.2.4.3 WT power curve

Each wind turbine has its own characteristic power curve, and its power output varies as the wind speed increases. In addition, by using a power curve, wind turbine energy production can be predicted without having to consider the details of its various components. Each wind turbine has its own characteristic power curve, and its power output varies as the wind speed increases. In addition, by using a power curve, wind turbine energy production can be predicted without having to consider the details of its various components [57]. Furthermore, power curves show the output of electrical power in relation to hub height and wind speed. A wind turbine generator's performance is influenced by three key points on the velocity scale, as shown in Figure 2.1.

- Cut-in speed: The slowest wind speed that the machine can produce power at. Modern WTs typically have speeds of 3–4 m/s.

- Rated speed: Wind speed at which the electrical generator produces its maximum output. In addition, the ideal wind speed range for wind turbine operation to reach maximum power generated is from 12 to 15 m/s [17, 19].

- Cut-out speed: During wind farm operation, the cut-out wind speed is exceeded 25 m/s in order to protect the wind turbine from overloading.

The following three approaches will be considered to calculate wind power:
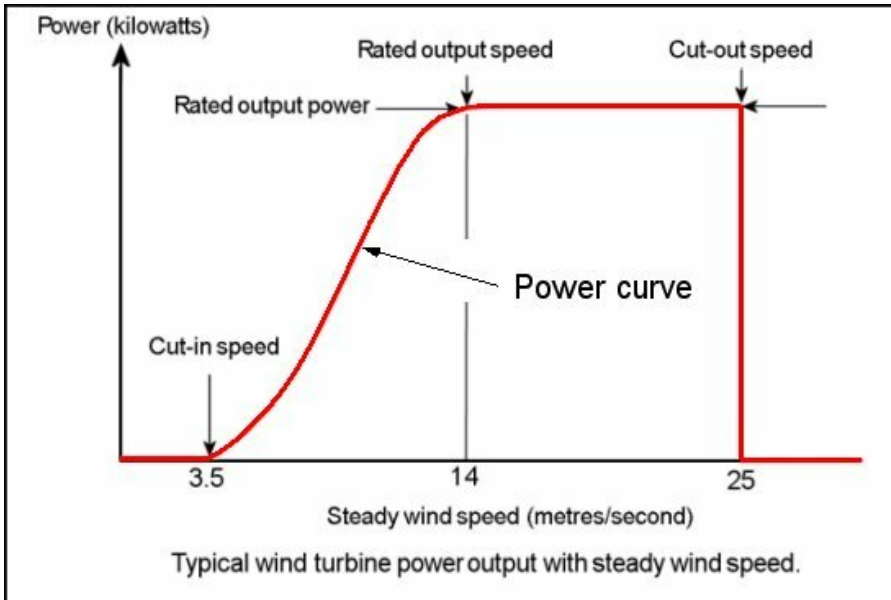
Figure 2.1: WT power curve [64]

- Direct use of data: Using a set of N wind speed readings collected during a time interval $\triangle t$, the following relevant parameters can be calculated: average WS, the standard deviation of WS, average WPD, and average Wind Energy Density.

- Method of bins: This method is also useful for analyzing wind data and predicting turbine productivity. When utilizing this method, a histogram displaying the number of occurrences and bin widths is commonly shown.

- Velocity and power duration curves from data: The velocity duration curve is a graph showing wind speed on the y-axis and the number of hours per year that the wind speed equals or exceeds any certain value on the x-axis.

In a hypothetical example, the three steps required in calculating wind power generation from wind speed are as follows [64]:

- 1. Mesoscale forecast wind speed interpolated to site.

- 2. The turbine power curve is used to determine gross production.

- 3. Subtract the losses associated with wind farms.

In most cases, the power curve established by manufacturers is only available for the desired air density level, so it must be changed to meet the air density at the site [57].

2.2.4.4 AEP and CF

The AEP is composed of gross and net energy production. The gross energy production is considered the wind farm production without losses, as is shown in Equation 2.13.

$$GEP = \sum_{i=1}^{Nd} \sum_{i=1}^{Ns} P_{ijk} F_{ijk} 8760 \qquad (2.13)$$

Where Nd is the number of direction steps, and Ns is wind speed bins, P_{ijk} is the wind power output for each direction from sector i, to wind speed, bin j, F_{ijk} is the frequency of occurrence of wind speed.

Furthermore, wind resource assessment is influenced by the estimation of wind power losses. Consequently, annual net energy production is estimated considering the following losses: plant availability (2-4%), electrical losses (2-4%), turbine performance (1.5-5%), environmental (1-3%), and curtailment (1-3%). Other losses, such as the site climate and the project location, were considered to be 12% [37].

The CF prediction of a wind farm using data from a measurement campaign is considered a complicated work [65]. In this work, the CF is estimated for one year according to Equation 2.14.

$$CF = \frac{actualenergyproduction}{energyatratedspeed} . 100 \qquad (2.14)$$

2.2.5 Complex terrain effect on wind characteristics

Terrain influences on wind flow decrease with height above ground level until they vanish completely at the altitude where the wind blows horizontally without changing direction.

2.2.5.1 Horizontal wind speed-up effect

A wind flow crossing a hill has to squeeze through a narrow passage. While the same amount of air must be moved through at a faster speed (mass-conservative), the terrain has the effect of increasing the wind speed as is shown in Fig. 2.2. The density of streamlines determines the wind speed; the denser the streamlines, the faster the wind, assuming attached flow near the surface [57]. A relative horizontal fractional speedup, $\triangle$ u, is defined as shown in Equation 2.15.

$$\triangle \mu = \frac{\mu o - \mu}{\mu} \qquad (2.15)$$

Where: μo = On top of the hill, it represents the horizontal wind speed

μ = Over the terrain upstream of the hill, it represents the horizontal wind speed.
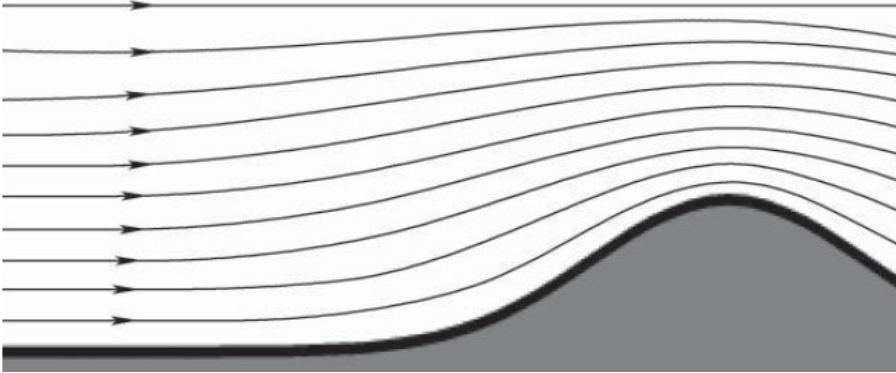
Figure 2.2: Wind streams flow over an idealized hill [57]

2.2.5.2   Vertical wind speed-up effect

Maximum vertical wind speed-up occurs at altitudes below and above l, where the wind profile exhibits a distinct linear trend. But above l, the wind speed seems to increase with height at a consistent rate. A 2L-height intersection is produced by extrapolating the upstream and hilltop wind profiles. Fig. 2.3 provides definitions for the two characteristic length scales, with L denoting the height at which the maximum speed-up effect is found and l denoting the half-width of the hill's middle [57]. However,
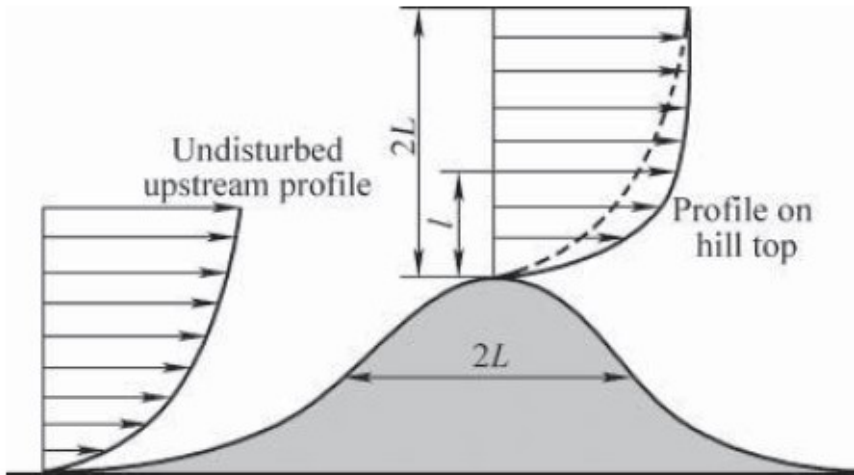
Figure 2.3: An idealized hilltop has undisturbed upstream wind profiles and a hill-top wind profile [57]

for steeper slopes, the flow tends to become detached, resulting in flow separation,

where arrows represent wind direction; dashed lines the virtual surface (see Fig. 2.4). The separated flow layer generates vortex shapes, forming a virtual surface for the flow above, which by and large remains laminar. In neutrally stratified air conditions, it is commonly considered that flow separation occurs when the upstream slope or lee slope exceeds 22° or 17°, respectively. This is the case of the virtual slopes, which is the basis for terrain categorization from flat where there is no flow separation to extremely complex with flow separation [14,57]. Furthermore, Correa Radunz et al. [66] evaluated the effects of atmospheric stability on the power performance of two wind farms located over complex terrain. Consequently, performance variations are most likely the result of atmospheric stability and flow patterns on the leeward side and windward slope rather than in the wake. If the dimensions of the hill perpendicular to the wind direction are
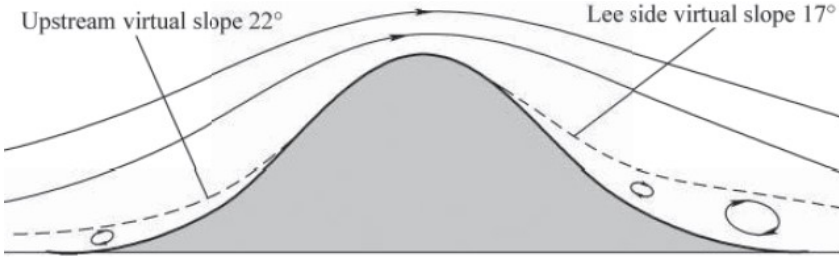
Figure 2.4: Flow separation indicated by vortexes creates the virtual surface [57]

significantly greater than L, then it may be considered a long and gentle ridge, and the flow may be regarded as two-dimensional. Equation 2.16 and Equation 2.17 are used for fractional speed-up and l, respectively.

$$\triangle \mu \simeq 2\frac{h}{L} \tag{2.16}$$

$$l \simeq 0.3Zo \left(\frac{L}{Zo}\right)^{0.67} \tag{2.17}$$

2.2.5.3   Hill effect

The main characteristic of the flow over a hill or mountain chain is the acceleration of the wind speed over the summit. A boundary layer over the crest can be separated into two layers. Above the inner layer where frictional forces dominate over inertial forces is the outer layer where the inertial forces dominate. Maximum fractional speed-up occurs at the boundary between the inner and outer layers. Commonly, wind turbines with hub heights over 100 m are located in the outer layer as is indicated in Fig. 2.5 [14].
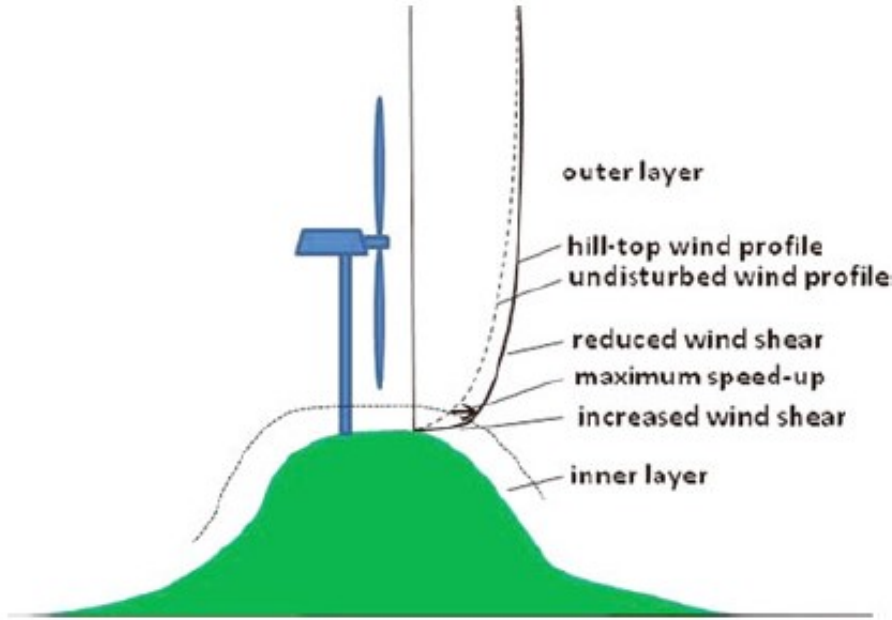
Figure 2.5: The principal characteristic of wind speed conditions over a ridge [14]

2.2.5.4   Tunnel effect

On the windy side of a building or between mountains, the air becomes compressed, and its speed increases, as is indicated in Fig. 2.6 [20]. The placement of a wind turbine in a natural wind tunnel is another way to achieve higher wind speeds than those found in the surrounding areas [57]. Furthermore, wind speed in narrow valleys is typically lower or negative wind shear, and there is less turbulence than the wind speed in an open valley. This shows how geographic features can influence wind speed at hub height, such as terrain or surface cover [67]. Moreover, the speed-up in a mountain pass varies significantly depending on the incoming wind direction.

2.2.6   Winds over complex terrain

Forecasting wind speed can be much more challenging in locations with steep or uneven terrain than in flat ones. The orography of the complex terrain on the western range is what causes mountain and valley breezes, which are similar to anabatic and katabatic winds but smaller in scale [14, 17, 19]. Mountains produce three types of thermally driven secondary circulation systems that alter the vertical structure of the mountainous ABL under simple large-scale pressure gradients and mainly cloudless skies: slope winds, mountain winds, and valley winds, as depicted in Fig. 2.7. Addi-
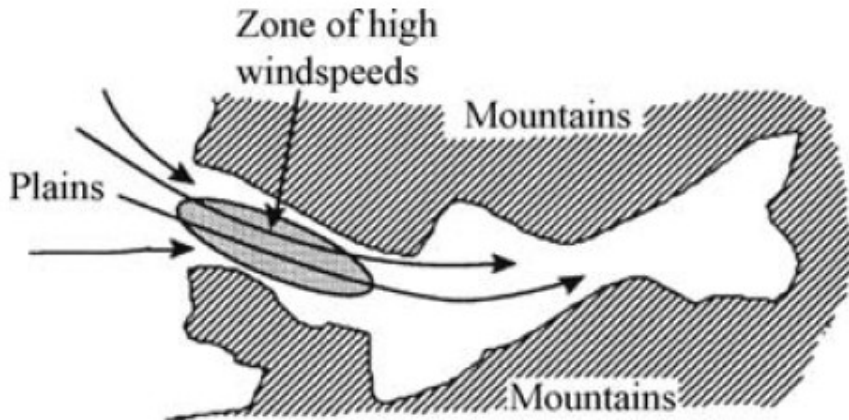
Figure 2.6: Wind speeds increased by mountains channeling prevailing winds [57]

tionally, Lubitz [68] points out that the speed-up in a mountain pass changes greatly depending on the direction of the oncoming wind.

In addition, a diurnally fluctuating wind system between mountain ranges and the nearby plains resembles land-sea wind systems. The three occurrences have a one-day time scale, but they each occur on a different spatial scale. The range of the slope wind scale is a few meters to a kilometer. On a geographical scale ranging from a few hundred meters to a few hundred kilometers, the lengths of valleys, mountains, and valley winds are revealed.

The evening flow consists of dense air forming on slopes draining into the valley (downslope, drainage, or katabatic winds) and air pooling at the valley's bottom being channeled to a nearby plane (down-valley winds). Topographic obstacles, valley geometry, and hydraulic control at the valley mouth all influence the amount of pooling that occurs in a valley. During the day, anabatic winds occur when the wind consists of upvalley and upslope air flows, propelled upward by buoyancy forces [14]. Moreover, the speed-up in a mountain pass varies significantly depending on the incoming wind direction [68].

2.2.7   Complex terrain classification

The height variations of terrain strongly influence the wind profile, as it is the surface of the atmosphere. We categorize terrain according to orography to estimate the suitability and uncertainty of various wind flow models. As shown in Fig. 2.8, the attached flow will tend to become detached from the ground, and flow separation will occur on steeper slopes. Within the separate layer of flow, virtual surfaces are generated, which serve as a base for the flow above, which is largely laminar. Modeling
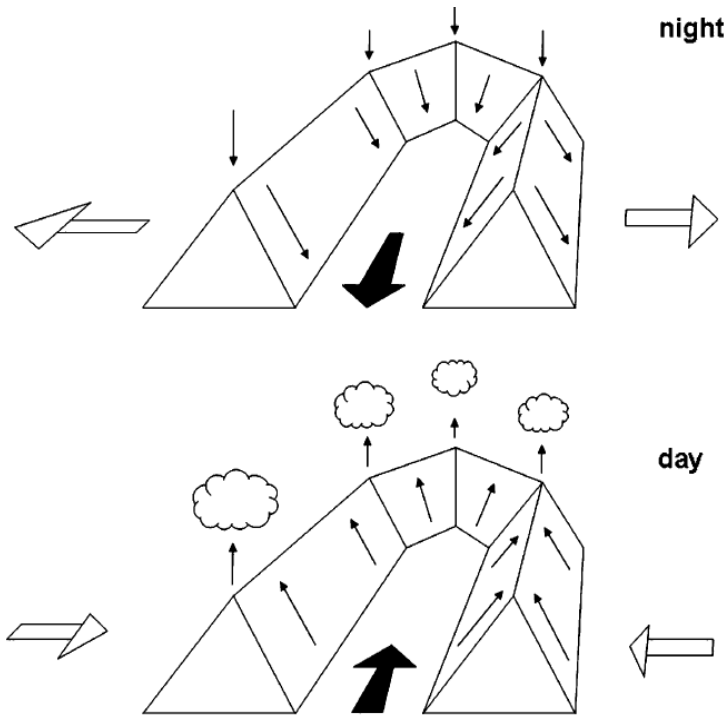
Figure 2.7: Local and regional wind systems over mountains at night-time (top) and at daytime (below) [14]

wind flow and assessing wind resources become tremendously more difficult when there is a separation that no longer follows linear laws.

As a result, the possibility of flow separation forms the basis for categorizing topography, ranging from basic (no flow separation) to exceedingly complex (flow separation). When the upstream slope is larger than 22° and the lee slope is greater than 17° under neutrally stratified air circumstances, such as the virtual slopes given in Fig. 2.8, flow separation is usually recognized. Because wind can blow from any direction in nature, 17 degrees slope is often used as a threshold between simple and complex. The terrain classification is carried out considering the main terrain characteristics as follows:

- Simple flat Category I: Winds near the surface are solely changed by roughness changes and shielding impediments terrain.

- Simple hilly Category II: Terrain is a flat, gentle-sloped hills landscape. The hills' typical horizontal dimensions are a few Km. In addition to roughness and obstacles, hills also accelerate winds near the surface.

- Complex hilly Category III: Terrain is hilly and complex. Furthermore, the hills
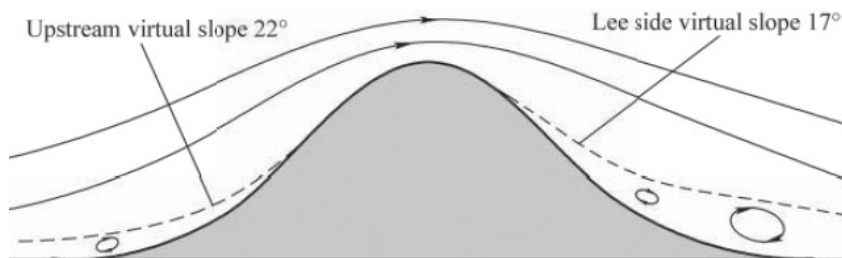
Figure 2.8: Steeper slopes [14]

are typically no larger than a few kilometers in height; where flow separation can no longer be considered empty, and flow modeling, becomes more complicated, with too many unknowns to be ignored. In these instances, linearized flow models tend to overstate the orographic speed-up effect, requiring the use of three-dimensional flow models to hind the winds. Despite the fact that linear models like WASP are incapable of reliability by calculating winds in complex terrain, some suggest that adjustments can be made to obtain more acceptable results.

- Extremely complex mountains Category IV: Most wind flow models, if not all, cannot account for the complex terrain, which includes both high mountains and deep valleys. The wind climate may be dominated by thermally induced valley winds. A change in the pattern of the boundary layer of the atmosphere is also possible [57].

2.3   Factors affecting wind speed

2.3.1   Temperature

A wind farm's operating environment is greatly influenced by the air temperature. This atmospheric variable is used to calculate air density, which has an impact on power generation estimation [19]. If the atmosphere is modeled as a dry ideal gas, the relationship between a change in pressure and elevation is given by Equation 2.18.

$$\partial P = -\rho g \partial z \tag{2.18}$$

The negative sign arises from the tradition that height z is measured positively upward, and pressure p is measured positively downward in the positive z direction. For an ideal gas closed system of unit mass undergoing a quasi-static change of state,

the first law of thermodynamics is as given in Equation 2.19.

$$\partial q = \partial u + p\partial v = \partial h - v\partial p = Cpres\partial T - \frac{1}{\rho}\partial p \tag{2.19}$$

where T is the temperature, q is the amount of heat transferred, u is the internal energy, h is the enthalpy, v is the volume, and Cpres is the constant pressure specific heat.

Equation 2.18 becomes ∂ q = 0 for an adiabatic process to obtain Equation 2.20.

$$Cpres\partial T = \frac{1}{\rho}\partial p \tag{2.20}$$

Under adiabatic conditions, the change in temperature is constant if the changes in g and Cpres with elevation are assumed to be negligible, as is shown in Equation 2.21.

$$\left(\frac{\partial T}{\partial z}\right)_{Adiabatic} = -\frac{0.098°C}{m} \tag{2.21}$$

According to conventional nomenclature, the atmospheric lapse rate G is equal to the inverse of the temperature gradient in the atmosphere. Consequently, Equation 2.22 gives us the adiabatic dry lapse rate [57].

$$\ulcorner = -\left(\frac{\partial T}{\partial z}\right)_{Adiabatic} \approx \frac{1°C}{100m} \tag{2.22}$$

The dry adiabatic lapse rate measures the stability of the atmosphere. In the middle latitudes, the atmospheric lapse rate typically decreases linearly with elevation up to about 10,000 m [57] as is shown in Equation 2.23.

$$\left(\frac{\partial T}{\partial z}\right)_{Standard} = -\frac{(216.7 - 288)°C}{10800m} = -\frac{0.0066°C}{100m} \tag{2.23}$$

The temperature profile declines with increasing height near the ground before sunrise and then reverses after sunrise. Air near the ground is heated, causing a gradient in temperature close to the earth's surface. Up until Z_i (called the inversion height), the temperature gradient for the air near the Earth's surface increases [57].

2.3.1.1   Thermal stratification of the atmosphere

Air parcels rise adiabatically as a result of the decrease in atmospheric pressure, causing the inner energy of the fluid element to expand. The fluid element's temperature decreases due to this expansion. During neutral conditions, the temperature of the new environment where the air parcel moves is unchanged, and no force is pushing it further upward or downward. In addition, to compensate for cooling due to adiabatic

expansion, the potential temperature related to the vanishing temperature gradient is also increased. Furthermore, the pressure decreases linearly with height in a simplified version [15]. At a height z, the potential temperature Θ is expressed in Equation 2.24.

$$\Theta = T(z) + \lceil z \tag{2.24}$$

Where T indicates absolute temperature and $\lceil$ is the dry adiabatic temperature gradient expressed in Equation 2.25.

$$-\partial z T = \approx 0.01 \frac{K}{m} \tag{2.25}$$

Three different types of thermal stratification can be distinguished using the vertical gradient of potential temperature.

- Neutral stratification $\partial z \theta = 0$, the vertical momentum flux is not affected by vertical temperature stratification.

- Unstable stratification $\partial z \theta < 0$, buoyancy enhances the vertical momentum transport due to temperature stratification e.g. sun radiation on sunny days.

- Stable stratification $\partial z \theta > 0$, in a vertically stratified atmosphere, momentum is dampened by temperature stratification. In most cases, this occurs during clear nights.

The gradient sign only determines whether vertical air parcel movements are enhanced or dampened. In consequence, the power density of thermally driven turbulence is greater than the power density of mechanical turbulence [69].

2.3.2 Air density

This variable is in proportion to air temperature and air pressure, which decreases with height and temperature increases [57]. Wind power output decreases with lower air density values [37]. The air density for the site of the study was calculated using the ideal gas law shown in Equation 2.26.

$$\rho = \frac{P}{RT} (kg/m^3) \tag{2.26}$$

Where P is air pressure expressed in KPa, air temperature in Kelvin degrees, and R is the universal constant for gases (287 KPa/JxKg). International standards assume 288.15 ºK and 101.32 kPa for the sea-level temperature and pressure [57].

Because of the unequal solar heating of the Earth's surface, air pressure gradients never totally vanish. When the air above the surface heats up, it expands and rises, lowering the pressure. When the surface cools, the pressure rises [19]. The hydrostatic

equation (Equation 2.27) describes this decrease in the absence of strong vertical accelerations. In this way, air pressure decreases with height, which causes the air density to decrease [14].

$$\frac{\partial P}{\partial z} = -g\rho = -\frac{gP}{RT} \tag{2.27}$$

The atmospheric pressure is given by p. The vertical coordinate is given by z, Earth's gravity by g, the actual air density given by ρ, the specific gas constant of air R, and the absolute temperature given by T.

2.3.3   Earth´s rotation

The Coriolis effect is caused by observing motion from a rotating reference frame, such as the Earth. At the equator, the Earth's surface moves faster around its axis than at the poles as is indicated in Fig. 2.9. Objects moving freely toward the equator cause the surface below them to speed up toward the east. A surface observer perceives from its perspective the object turning westward. In addition, the combination of temperature gradients and Coriolis forces produce equatorial trade winds and mid-latitude west winds. A relatively humid, warm air mass tends to climb to high altitudes through convection near the equator. Due to the Coriolis effect, air flowing into an area turns westward, producing easterly Trade winds [19].

2.3.4   The wind profile

The relationship between AGL height and horizontal wind speed at that height defines a wind profile. The wind profile has two fundamental characteristics:

- Near the surface, there is no wind, and as one rises in altitude.

- The rate at which the wind changes from being extremely rapid near the surface to significantly slower further up [15].

In studies on wind energy, the vertical profile of wind speed has typically been modeled using two mathematical models or laws, such as logarithmic law and power law.

---

[06]"According to the convention, wind direction can be determined based on the direction where the wind is blowing from. In this way, winds blowing toward the north are described as southerly winds."
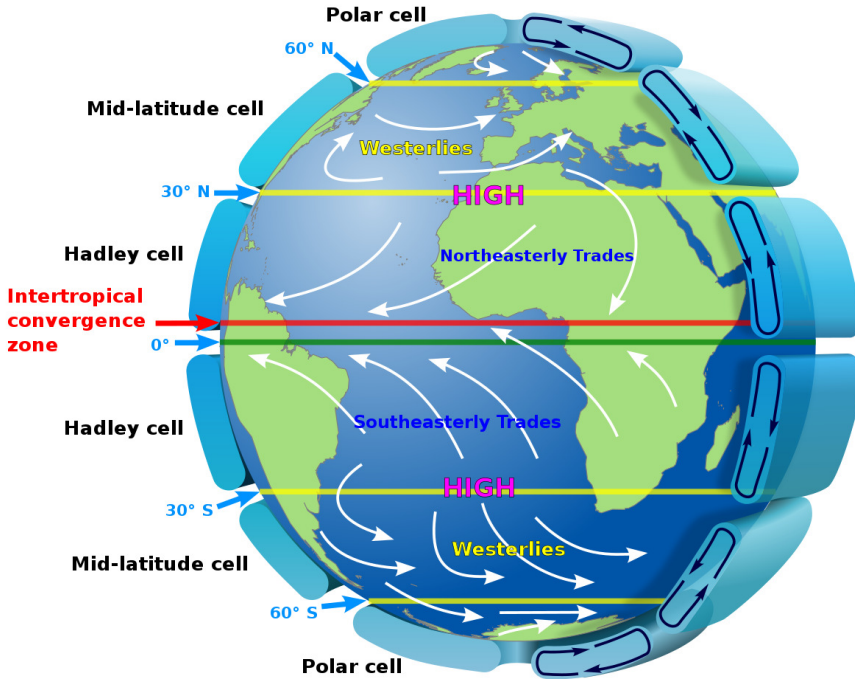
Figure 2.9: Global flow circulation [14]

2.3.4.1 Logarithmic law

A logarithmic wind profile is derived from simple physical considerations applicable to the surface layer, which is described in Equation 2.28.

$$\mu_z = \frac{\mu_*}{k}.ln\frac{Z}{Z_o}; Z \geq Z_o \tag{2.28}$$

Where:

k von Karman's constant equals 0.4

Z Wall height

Z_o Surface roughness length

2.3.4.2 Power law

The logarithmic profile law Equation 2.28, which is based on physical and dimensional reasoning, is sometimes replaced with empirical power law to characterize the vertical wind profile (Equation 2.29).

$$\mu(z) = \mu(Zr) \left(\frac{Z}{Zr}\right)^{\alpha} \tag{2.29}$$

where: Zr = reference height

Z = given height

α = power law exponent or Hellman exponent

The findings of comparing the slope and curvature of the power and logarithmic profiles reveal that the power law has the same slope and curvature as the logarithmic profile, which can only be found in the limit for completely smooth surfaces when the power low exponent tends to zero. As a result, for neutral stratification, it is impossible to create a power law that fits the logarithmic profile over a wider range of heights [14].

2.3.4.3   Roughness class and length

In the ABL lower than 1 Km AGL, wind speeds are affected by friction with the earth's surface. In the wind industry, a difference is made between the terrain roughness, the influence of obstacles and the terrain contour influence also named the orography of the area. The roughness class from the roughness length (Z_o) is the height AGL where the wind speed is theoretically zero. When the wind profile moves towards lower speeds as we approach ground level is often named wind shear. The friction speed is related to the shear stress of the terrain with the density of the fluid and is represented by Equation 2.30

$$\mu_* = \sqrt{\frac{\tau_\omega}{\rho}} \tag{2.30}$$

Where:

μ_* Friction speed

τ_ω Wind shear stress

ρ Air density

Theodore von Kármán stated in 1930 that in a turbulent flow, its mean speed at any point becomes proportional to the logarithm of the distance between any place and the wall [70]. Equation 2.30 represents the average horizontal speed located at the height of z.

The horizontal average velocity μ_z is known as the logarithmic wall law, and only is used for flows that are closer to the wall. This method has been put into practice to estimate the average velocity profile generated in the surface layer, but it is valid up to 150 meters in height as long as there are strong winds.

The term z_o indicates the size of the eddies generated on the surface of the ground when the ground has a greater roughness; the eddies will be directly proportional to

the roughness of the surface. Table 2.1 shows the roughness values of different rough obstacles on uniform study surfaces.

Table 2.1: **Roughness and length for some types of terrain [57]**

Terrain description	Roughness class	Roughness length (m)
Ice or mud	0	0.001
Outdoors, grass, airport lands	0.5	0.24
Agricultural land with scattered buildings	1	0.03
	0.5	0.24
Agricultural land with fences up to 8 meters in height and some houses separated by more than 1 km.	1.5	0.055
Cities, villages, agricultural land with high fences, and forests	3	0.4
Centers of cities with tall buildings	4	1.6

2.4   Wind resource assessment

The most known methodology for WRA includes the following steps:

2.4.1   Preliminary assessment

The preliminary evaluation provides a general notion of how the local wind climate behaves (diurnal, monthly, seasonal, and annual) based on the available wind resource and inputs from local people.

2.4.2   Wind resource assessment site

This stage refers to wind measuring programs used to characterize the wind resource in a specific location or collection of areas where wind power development is being

investigated. For an estimation of WPP, it is mandatory to have wind data for a minimum of one year. Nevertheless, large data measurements are more accurate [71]. The most common goals of this wind measuring scale are to:

- Determine or confirm whether there are adequate wind resources in the area to warrant additional site-specific investigations.

- Compare areas to see where they stand in terms of development potential. Obtain representative data in order to estimate the performance and/or economic viability of specific wind turbines.

- Look for prospective locations for wind turbine installation [60].

2.4.3   Micrositing

Micrositing is the process of determining the precise placement of one or more wind turbines to maximize overall AEP [60, 72]. Each location must meet a number of criteria, including existing wind resources, and distances from other wind turbines nearby [73]. Furthermore, the lifespan of wind turbines is usually 20 years. Nevertheless, within the design parameters of wind conditions, such as mean wind speed, turbulence intensity, inflow angle, and wind shear. In the case of exceeding the design limits, the major components may experience excessive wear and tear, resulting in higher maintenance and operation costs [20]. The purpose of this procedure is to design an efficient wind farm that fulfills the following requirements:

- Productivity. Annual Energy Production should be maximized with this system.

- Durability. The wind farm will approach the end of its expected service life.

- Possibility from a technical standpoint. The wind turbines will be placed in easily accessible areas.

In recent work, Song et al. [74] proposed an approach to optimize wind turbine micrositing using CFD to evaluate wind power variation by changing wind direction. Results showed that by optimizing the position of the turbines in a wind farm, the production of power can be more stable without reducing the yield.

2.5   Wind characteristics modeling using CFD

2.5.1   Mathematical formulation

The Navier-Stokes equations allow us to predict the flow of fluids. These equations are not solvable analytically, except for specific cases, and it is complex to analyze the

fluid behavior. For this reason, numerical and experimental models are used to obtain a solution close to reality.

- Mass or continuity conservation equation according to Equation 2.31

$$\frac{\partial \rho}{\partial t} + \frac{\partial}{\partial x_i}(\rho.U_i) = 0 \tag{2.31}$$

- Equation for the conservation of momentum as is shown in Equation 2.32

$$\rho \left(\frac{\partial \rho}{\partial t} + \frac{\partial}{dx_i}(Ui.U_j) \right) = \frac{\partial P}{\partial t} + \frac{\partial \tau ij}{\partial x_j} \tag{2.32}$$

- Energy conservation equation according to Equation 2.33

$$\rho \left(\frac{\partial E}{\partial t} + \frac{\partial.U_{jH}}{\partial x_j} \right) = \frac{\partial}{\partial t}.(U_i \tau ij) + \frac{\partial}{\partial x_j} + \left(k \frac{\partial T}{\partial x_j} \right) \tag{2.33}$$

Where:

ρ flow density

Components that make up the viscous tensor stress

μ_i Cartesian speed components to direction Xi

μ_j Cartesian speed components to direction Xj

P Fluid pressure

τij Components that make up the viscous tensor stress

E Total energy

H Total enthalpy

k Thermal conductivity coefficient

T Absolute temperature

2.5.1.1 Turbulence model k-ϵ

The discretization techniques and turbulence model selection represent an important function in the simulation accuracy of turbulent airflow [75]. The RANS turbulence selected model contains transport equations that work with mean velocities and scalar variables ϕ, which are turbulent flows, so the Reynolds stress is represented by the Equation 2.34

$$Reynolds stress = \overline{\mu_i \mu_j} \tag{2.34}$$

The turbulent transport equation originates with the addition and subtraction of different terms such as production P_{ij}), which is obtained from the gradient of average velocities. Another term is dissipation ϵ_{ij}, to originate from real-time viscosity acting

on fluctuating speeds. Finally, we have a redistribution term ϕ_{ij}, which facilitates the energy transfer using pressure and fluctuations caused by the fluid current as is shown in Equation 2.35.

$$Netenergy = Producedenergy(P_{ij}) + Redistributedenergy(\epsilon ij) - Dissipatedenergy(\phi ij)$$
$$(2.35)$$

External terms must be considered the convective and diffusive that go from one point to another of the created domain, so this turbulence model is the most practical and used, consisting of two equations that represent the turbulent properties of a flow according to Equation 2.36 [76].

$$C_\mu = \mu_t \rho \frac{k^2}{\epsilon} \qquad (2.36)$$

Where:

C_μ Constant Turbulent kinetic energy

k Dissipation rate of turbulent kinetic energy

μ_t Turbulent viscosity

The equations of the described model are

• Kinetic turbulence according to Equation 2.37

$$\frac{\partial}{\partial t}(\rho k) + \frac{\partial}{\partial x_i}(\rho k \mu_i) = \frac{\partial}{\partial x_j}\left[\left(\mu + \frac{\partial \mu_t}{\partial \sigma_k}.\frac{\partial k}{\partial x_j}\right)\right] + G_k + G_b - \rho_\epsilon - Y_m - S_k \quad (2.37)$$

• Turbulence dissipation as is shown in Equation 2.38

$$\frac{\partial}{\partial t}(\rho \epsilon) + \frac{\partial}{\partial x_i}(\rho \epsilon \mu_i) = \frac{\partial}{\partial x_j}\left[\left(\mu + \frac{\partial \mu_t}{\partial \sigma \epsilon}.\frac{\partial \epsilon}{\partial x_j}\right)\right] + G_1 \epsilon \frac{\partial \epsilon}{k}.(G_k + C_3 \epsilon G m_b) - C_{2\epsilon} \rho \frac{\epsilon^2}{K} + S_\epsilon$$
$$(2.38)$$

Where:

G_k Generation of the kinetic energy of the mean speeds gradients

G_b Kinetic power generation by buoyancy

Y_m Contribution of fluctuating expansion on compressible turbulence

$C_{1\epsilon}, C_{2\epsilon}, C_{3\epsilon}, \sigma_t$ Experimental constants

μ_t Turbulent viscosity

σ_k Prandtl number as a function of k

σ_ϵ Prandtl number as a function of ϵ

The diffusivities represented in the expression of molecular and turbulent viscosities of the turbulence model are shown in Equation 2.39, and Equation 2.40.

$$r^k = \mu \frac{\mu_t}{\rho_K} \tag{2.39}$$

$$r^\epsilon = \mu \frac{\mu_t}{\rho_\epsilon} \tag{2.40}$$

The identification constants $C_{1\epsilon}, C_{2\epsilon}, C_\mu, \sigma_k, \sigma_\epsilon$ were defined by Launder and Spalding for standard models [75, 77] and their values are:

$C_{1\epsilon} = 1.44$

$C_{2\epsilon} = 1.92$

$C_\mu = 0.09$

$\sigma_k = 1$

$\sigma_\epsilon = 1.3$

Chapter 3

Wind energy integration into electrical grid

This chapter shows the current state of wind energy for electricity generation in the Ecuadorian context and worldwide. In addition, it demonstrates how wind farms are integrated into electrical power systems and their importance. Further, the most relevant horizons for wind speed prediction are examined, as well as the parameters used for evaluating the level of accuracy of wind speed and power forecasting.

3.1   Current status of wind energy

3.1.1   Overview

Wind energy has progressed to the point that we can confidently state that we are dealing with a clean, cost-competitive, and well-established technology. Starting with a natural, renewable, and non-polluting source, modern wind turbines can produce power at competitive prices when compared to traditional energy sources, allowing wind energy to become the world's fastest-growing energy source. The need to combat global climate change has largely fueled the rise of wind energy, which avoids carbon dioxide emissions while also producing none of the other pollutants associated with fossil fuel or nuclear generation. Because it does not emit damaging gases or produce long-term waste, this type of energy production is more likely to be accepted in society. According to the most recent data, wind power avoided the emission of about 18 million tons of CO_2 into the atmosphere in 2007, compared to what would have been emitted if the electricity had been generated in coal, gas, or fuel thermal power plants. This allowed it to contribute to the Kyoto Protocol's commitments.

3.1.2 Wind energy global

In the last two decades, renewable energies for electricity generation, including wind, solar, biomass, and hydroelectricity, have seen rapid growth. This has helped achieve a more sustainable energy transition with lower fossil fuel consumption and fewer greenhouse gas emissions. Wind energy is a clean and mature technology with rapid growth in the past 20 years [1, 13]. Wind power generation worldwide reached 2020 with a total installed power of 743 GW (onshore and offshore), adding 93 GW in added installations, and showing a record increase of 53% compared to 2019 as is illustrated in Fig. 3.1. Some countries set up new installations around Asia, America, and Europe with a growing tendency to increase wind power generation [78, 79]. A record 8300 TWh of electricity will be generated by renewables in 2021, representing the fastest year-on-year growth since the 1970s. Approximately two-thirds of the growth in renewables will be attributed to solar PV and wind. It is estimated that Chinese wind electricity generation of 141 TWh will represent almost half of the global increase of 17% from 2020 around 275 TWh, followed by the United States, European Union, and Indian renewable electricity, as is shown in Fig. 3.2 [80].In 2020, China, the US, Brazil, the Netherlands, and Germany were the top five markets for brand-new installations. Together, these five markets accounted for 80.6% of global installations in 2018, which is 10% higher than in 2019 [78].
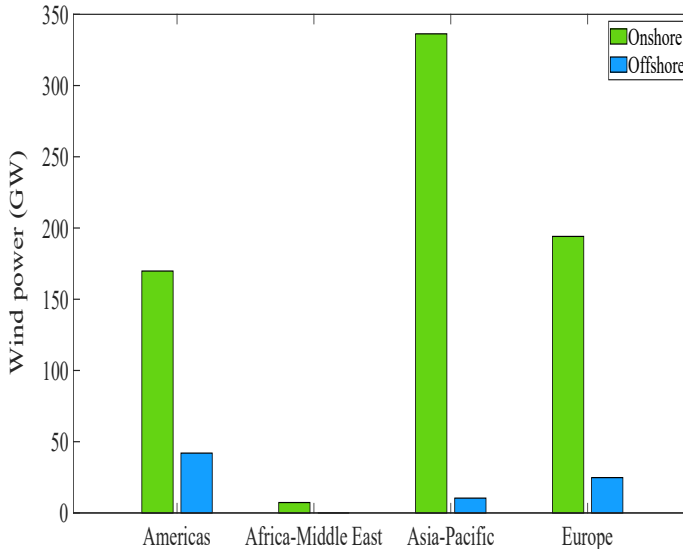
Figure 3.1: Global wind power in 2020 [80]
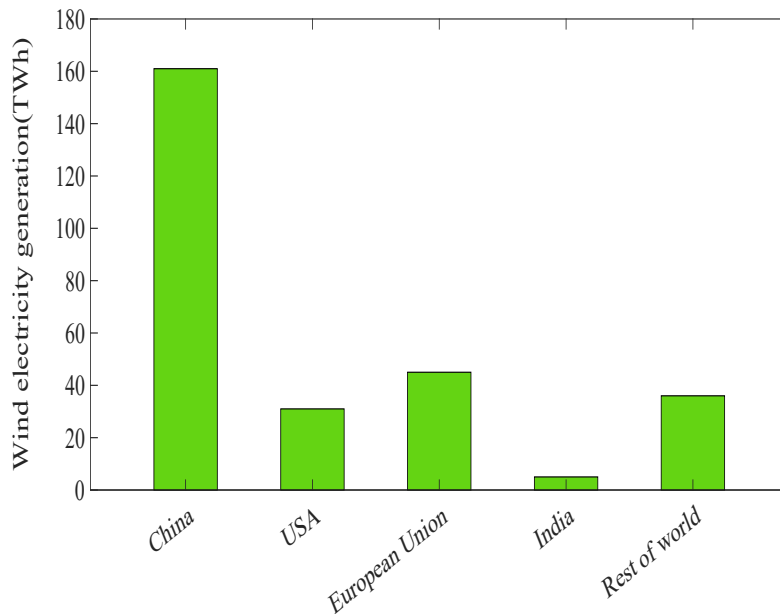
Figure 3.2: Wind electricity generation increase by country and region, 2020-2021 [80]

3.1.3 Wind energy in Latin America

In 2020 Latin America will remain the fourth largest regional market (5%), followed by Africa & Middle East (0.9). In 2020, Brazil had the biggest wind-installed power in this region, around 17.75 GW, which represents 3% of total onshore wind power as is shown in Figure 3.3.

3.1.4 Ecuadorian power matrix

The management of the generation and transmission of the electrical energy systems is provided by the National Interconnected System of Ecuador, where the indicators of the infrastructure of the energy matrix are detailed until the year 2021. The national capacity of the energy matrix is indicated in Table 3.1.

Ecuador's energy matrix is made up of renewable and non-renewable energies, as seen in Fig. 3.4, with hydraulic energy accounting for the biggest share of the matrix. Ecuador is crossed by the Andes mountain range, where many rivers pour onto the Atlantic and Pacific slopes, accounting for a large portion of this energy. Several dams with hydraulic turbines for energy generation have been erected in the channels of these rivers due to the flow and great cascade, lowering the consumption of fossil fuels and
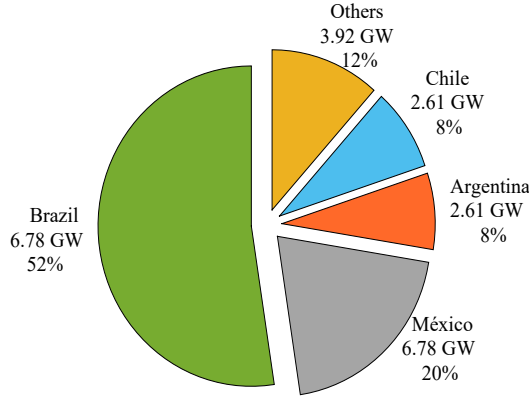
Figure 3.3: Wind installed power in Latin America, 2020-2021 [80]

Table 3.1: **National capacity Electricity generation systems in Ecuador [81]**

System	Renewable (MW)	Non-Renewable (MW)	Total (MW)
NIS	5294.4	2063.5	7357.8
Non-incorporated	13.9	1362.7	1376.6
Total	**5308.3**	**3426.1**	**8734.4**

the emission of hazardous gases to the environment. The contribution of renewable energies to the composition of the energy matrix is minimal due to the high cost of installation, and the cost of generated renewable energy is higher than hydraulic energy.

The national energy production using renewable and non-renewable energy in Ecuador during 2021 reached a value of 28161 GWh as indicated in Fig. 3.5 where it is observed that hydraulic energy reached the highest percentage because this energy has the highest installed power. In contrast, the wind energy generated reached a minimum level due to the small installed power composed of two wind farms.

3.1.5   Wind energy in Ecuador

The change in the energy matrix to increase the use of renewable energy sources is supplemented by the effective use of non-renewable energy sources available in Ecuador, with the goal of drastically reducing the usage of fossil fuels. The plan named "Inventory of Energy Resources of Ecuador for the Purposes of Electricity Production, 2015," which identifies the viable technical potential by kind of source of natural energy was
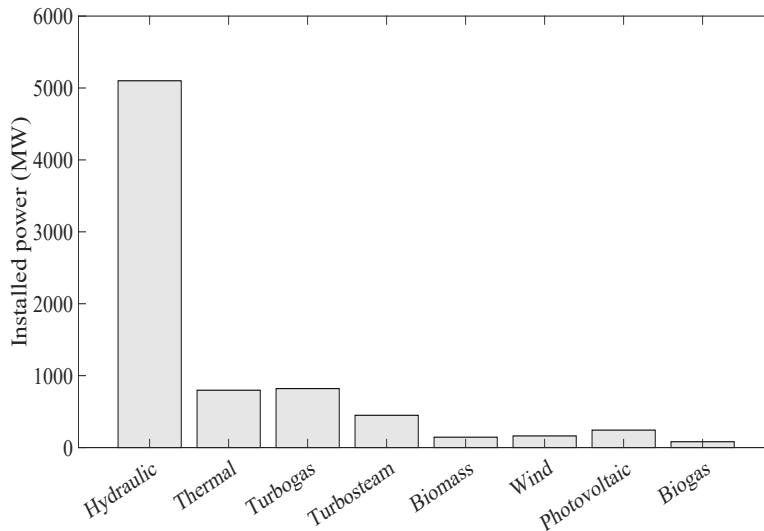
Figure 3.4: Ecuadorian energy matrix composition [81]

used to determine the availability of other energy resources for the Generation Expansion Plan 2018-2027. The resources are classified into five categories: A. Hydraulic resources B. Geothermal resources C. Solar resources D. Wind resources E. Biomass and other energy sources resources

In Ecuador, wind power reached 21.5 MW in 2013, which represents around 0.26% of total installed power systems [22, 82]. Ecuadorian wind power is composed of two wind power investments. The first is the Villonaco wind farm, which is installed at the highest altitude worldwide (2720 m ASL), and holds an installed power of 16.5 MW supplied by 11 WT Goldwind 70/1500 KW each [83]. This wind farm operates under particular conditions, such as an annual mean wind speed of over 10 m/s, low air density around 0.89 kg/m^3, and TI of 0.15 considered as A-class [84]. The second wind farm is located in the Galapagos Islands with a capacity of 4.6 MW [22, 85]. Nowadays, the MEER has approved the construction of the projects to increase wind generation Villonaco II and Villonaco III with an installed power of 110 MW, and Conolophus (14MW) [83].

The wind Atlas published by CONELEC estimates the feasible wind potential at around 884.2 MW. Most wind potential is in the mountainous region of the Andes Highlands [22]. The full wind gross potential in Ecuador is around 1670 MW, and annual wind energy production estimated at 80 m AGL, can reach 2868.98 GWh/year [83].
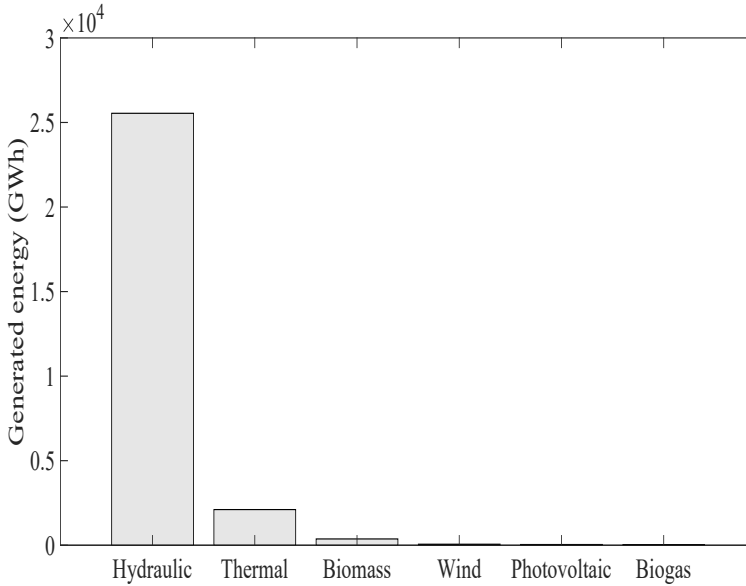
Figure 3.5: National energy production [81]

3.2 Integration of electrical energy of wind origin in the electrical grid

3.2.1 Relevant companies of the Ecuadorian electrical system

The following are the most important firms involved in Ecuador's electrical system:

- MEER: Created to serve the Ecuadorian society through the formulation of the national policy of the electricity sector and the management of projects.

- CONELEC: Designed to regulate the electricity sector and ensure compliance with legal provisions, regulations, and other technical standards for electrification in the country in accordance with the national energy policy [55].

- CELEC: It is characterized as a strategic public service. Its goal is to provide electrical service, which must adhere to the following principles: obligation, generality, uniformity, responsibility, universality, accessibility, regularity, continuity, and quality. CELEC EP's primary activities are as follows: 1. The generation, transmission, distribution, commercialization, import, and export of electrical energy; for which it is authorized to carry out all related activities, including, but not limited to: a. the planning, design, installation, operation, and maintenance of systems that are not part of the National Transmission System. b.

Purchase, sell, exchange, and market energy with distributors, other generation companies, large users, exporters and importers, and engineering works [86].

- CENACE: The National Electricity Operator's (CENACE) mission is to keep the country's energy supply in the best possible condition in terms of safety, quality, economy, and sustainability, as well as to improve the commercial administration of the National Electric Transmission System, and International Electricity Transactions [87].

3.2.2 Effects on the operation of the electrical grid

Technological progress in wind generation leads to the construction of high-power wind turbines, used in wind farms with large installed power, which are generally located in deserted areas with low energy demand. Therefore, wind energy generated must be adjusted at high voltage levels via substations to the transmission and distribution networks [59]. Wind energy integration is difficult due to the wind's variability and randomization, which causes disconnection in low-speed situations or when wind speeds surpass the wind turbine's cut-off speed. As a result of this condition, the other systems contribute more to keep the electrical system balanced.

The main characteristic of wind energy regarding integration into the electrical grid is that it is not programmable because the electrical production cannot be specified in advance due to the following reasons:

- High vulnerability to voltage gaps

- Electric generation with high intermittence

- Impossibility of control of electricity generation

- Lack of certainty in the wind forecast

- Requires reactive power control

The Villonaco wind farm is a significant project of Ecuador's Government that helps to reduce fossil fuel usage and greenhouse gas emissions. At 2720 meters ASL, this wind farm is positioned on the summit line of Villonaco mountain [86]. For this reason, the electrical energy produced at the Villonaco wind farm must be discharged through a substation to the 138 KV distribution network of the national transmission system, as shown in Fig. 3.6.

3.2.3 Importance of short-term wind energy forecasting in wind farms

In electrical power systems, electrical energy cannot be stored on a large scale. As a result, the generation of electrical energy from wind sources must be planned
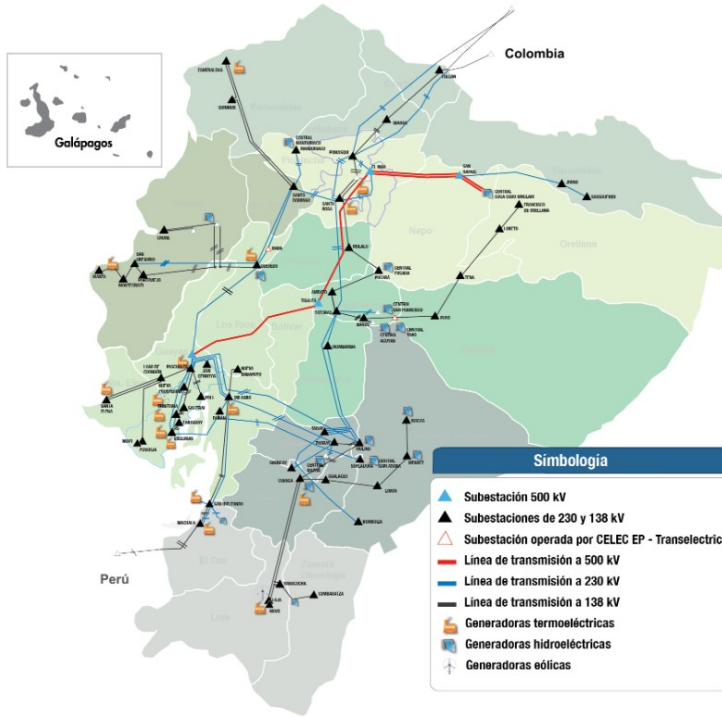
Figure 3.6: National Transmission System [86]

ahead of time, as the electrical power sent to the network cannot be managed fast. It is necessary to manage the hydraulic reserves when the generators fail and are out of service in order to maintain a constant balance between generation and demand. There are three types of reserve regulations:

- Primary: Changing the system frequency by adjusting the speed of the turbine rotors in operation in less than 15 seconds.

- Secondary: It is a power reserve of the generators synchronized with the network, it is used only to correct frequency drops from 15 to 150 seconds. It is activated by the network operator after the primary regulation has been exhausted and to recover it.

- Tertiary: It is a non-spinning reserve available after 30 minutes to 1 hour, to recover the system's spinning reserve [59].

Regarding wind energy prediction in Ecuador, the CONELEC 004/11 regulation named Treatment for energy produced with non-conventional renewable resources involves renewable generation plants with an installed capacity of up to 50 MW. This

Regulation sets preferential prices for energy obtained using renewable resources. Likewise, it establishes a preferential dispatch for energy delivered to the national transmission system. This electrical energy delivered must have the same quality as the energy produced with non-renewable resources. Regarding the energy, the forecast is to be delivered to the National Transmission System, which must inform CENACE of the hourly energy forecast to be produced each day within the established period, in order to carry out the daily generation schedule for the next day.

3.2.4 Forecasting horizons

With respect to forecasting methods by using time horizon, wind power is represented by its instability and intermittence because of the complex physics of the atmosphere [15, 18, 36]. To integrate variable wind energy into the electrical grid are required integrated transmission systems for wind turbine operation and accurate forecasting tools, with weather forecasting included [88–90]. In addition, the expected demand is required in hourly intervals in the energy markets at least one or two days ahead [38]. Wind power forecasting is the estimation of wind conditions based on wind data available, and topographical and meteorological variables of a place [20, 37]. Wind speed and power prediction with great quickness and precision, to integrate into the power system are the principal objectives of wind speed and power forecasting [3, 38]. The classification of wind speed forecasting according to time horizon and its main applications is listed in Table 3.2.

Table 3.2: **Classification of wind speed forecasting [30]**

Categories	Time horizon	Applications
Very short term	Few seconds to 30 minutes	Wind turbine control and load tracking [32]
Short-term	30 minutes to 6 hours	Wind speed forecasting and wind turbines power prediction [13, 91]
Medium-term	6 to 24 hours	Power system management and energy trading [13, 92]
Long-term	1 to 7 days	Wind turbine maintenance program [47, 93]

The forecasting methods are classified into five groups as follows: wind speed and power forecasting, spatial correlation forecasting, regional forecasting, probabilistic forecasting, and offshore forecasting [3]. To increase the accuracy of the forecasting methods have been accomplished various wind speed and power forecasting approaches, including physical, statistical, and artificial intelligence for renewable energy systems [18, 39, 40]. Moreover, the energy efficiency, energy control, and stability in the energy demand prediction in renewable energy systems have been improved with the application of machine learning techniques [41]. These techniques have been used

with quick development from many years ago in modeling, design, and prediction of energy systems [29, 41]. These approaches have been adopted worldwide to evaluate wind power performance and to acquire relevant information for application in wind power generation systems

3.2.5   Forecasting uncertainty

Wind resource estimates present an uncertainty percentage due to many factors, such as wind speed measurements (1.0-2.5%), historical wind records (1.6-4%), future wind resource (1.4-2.2%), wind shear (0.0-6.3%), wind flow modeling (2.0-10%) for a total uncertainty of 3-13% [19]. Wind´s nature and variability cause uncertainty in wind power assessment and forecasting; for this reason, it is difficult to integrate wind energy into the power grid [9, 10]. Jung et al. [94] proposed a Bayesian approach considering uncertainties, such as the limited amount of data, wind speed, air density, surface roughness, and WT performance. In order to estimate the AEP of a site for a hypothetical WT of 3 MW, wind speed data from a nearby weather station is used. The proposed model showed good performance for uncertainty modeling due to the limited amount of data. Rodríguez-Hernández et al. [95] developed a methodology based on a probabilistic model considering different possibilities in the Weibull PDF associated with wind speed to analyze the uncertainty of measurement equipment for wind resource assessment. The developed methodology is indicated to be a useful approach to estimating wind energy production. Baker et al. estimated $\pm$ 10% uncertainty and a confidence level of 90% for wind data collected on-site for one or three years.

Because of the nature and variability of the wind, it is difficult to incorporate wind energy into the power system [9, 10]. A Bayesian strategy taking into account uncertainties, such as the limited data, wind speed, air density, surface roughness, and WT performance was proposed by Jung et al. [3]. Wind speed information from a nearby weather station is used to calculate a site's AEP for a fictitious WT of 3 MW. As a result of the scant amount of data, the proposed model performed well in predicting uncertainty. In order to investigate the uncertainty of measuring equipment for wind resource evaluation, Rodrguez-Hernández et al. [95] created an approach based on a probabilistic model that takes into account several possibilities in the Weibull PDF related to wind speed. It has been determined that the suggested methodology is an effective way of estimating wind energy output. Over on-site wind data gathered for one or three years, Baker et al. [96] estimated a *pm* 10% uncertainty and a confidence level of 90%.

3.2.6   Forecasting verification

The forecasting performance to minimize uncertainty was evaluated by using Equations: 4.1, 4.2, and 4.3 named as Root Mean Square Error (RMSE), MSE, and MAPE respectively [42].

$$RMSE = \sqrt[2]{\frac{1}{n}\sum_{t=1}^{n}(Ws_f - Ws_m)^2} \tag{3.1}$$

$$MSE = \frac{1}{n}\sum_{t=1}^{n}(Ws_f - Ws_m)^2 \tag{3.2}$$

$$MAPE = \frac{1}{n}\sum_{t=1}^{n}\left|\frac{Ws_m - Ws_f}{Ws_m}\right|100 \tag{3.3}$$

In the equations 4.1-4.3 n is the total number of inputs and outputs, Ws_m is measured wind speed,Ws_f is forecasted wind speed.

3.2.7 Conclusions

In this chapter, the state of wind energy in Ecuador and worldwide has been reviewed. It also discusses the problems caused by the integration of wind energy into the electrical network. It should be noted that the main deductions are the following:

- Wind energy is a proven, clean technology that prevents millions of tons of greenhouse gas emissions. It has expanded fast in the last 20 years, reaching a global installed power of 743 GW.

- The fluctuation of the wind makes it difficult to integrate wind energy produced by huge wind farms. As a result, it's critical to forecasting the amount of wind energy that will be generated so that the network operator can manage the hydraulic reserves and keep the generation-demand balance constant at any time.

- Because of the enormous number of rivers that flow from the Andes to the Pacific and Amazon slopes, the Ecuadorian energy matrix contains a higher share of hydraulic energy. The Villonaco onshore wind farm contributes only a tiny amount of wind energy. To compensate for the lack of water flowing in the Andes rivers due to drought, the energy matrix must be diversified to take advantage of the Andes mountains' wind potential.

Chapter 4

Wind speed and power forecasting approaches and proposed model

This chapter presents the most relevant characteristics of short-term prediction models of wind speed and wind energy in wind farms. The following models have been considered: physical, statistical, ANN, and hybrid. A detailed study of the proposed model composed of the following approaches is also carried out: linear regression statistic, DNN, and RNN.

4.1   Physical approach

In physical systems, parameters are determined by detailed physical descriptions of the atmosphere. In most cases, the wind speed provided by the weather service at the wind farm site is converted to the local conditions [97]. Furthermore, the physical approach scales down using a mesoscale or microscale model. Using a look-up table, the mesoscale model can be run for multiple situations when the NWP model is run, providing boundary conditions and initialization for the NWP model. The fundamental distinction between the two is the maximum and minimum domain size and resolution that can be achieved [4]. NWP model makes use of a set of equations that describe fluid flow to forecast weather. Governing equations, numerical methods, and parameterizations of other physical processes are used to convert equations into computer code prior to being run over a domain [15]. The downscaling method necessitates extensive physical descriptions of the wind farms and their environs, including wind farm layout and wind turbine power curve, among other things, and terrain description (orography,

roughness, obstacles, etc.). A calculation of wind power production is made using the refined wind speed data at the hub height of the wind turbines.

In recent years, several physical approaches have been developed for wind speed and power forecasting [98]. The most 4 known approaches are as follows:

- **Prediktor** The Danish Risoe National Laboratory created the Prediktor. It uses the WAsP and the PARK program to account for local conditions using the NWP forecast from the HIRLAM [15].

- **Previento** The Previento is a physical model developed by the University of Oldenburg in Germany, but it uses the Lakel model of the German weather service for its NWP forecast [99].

- **eWind** It is a numerical weather model adjusted with a high-resolution boundary layer model developed by AWS TrueWind Inc. in the USA. It uses the boundary layer model as a numerical weather model to take into account local conditions [100].

- **LocalPred** CENER, Spain's National Renewable Energy Centre, created Local-Pred. It entails adaptive NWP forecast optimization, time series modeling, MM5 mesoscale modeling, and power curve modeling [101].

4.2   Statistical models

A time series model is used to anticipate future wind power or speed in the traditional statistical way. Model identification, model estimate, model diagnostics checking, and forecasting are the four basic processes in the Box-Jenkins approach to creating a mathematical model of the problem. As a reference model, conventional statistical approaches are frequently used. [94]. Another approach to forecasting wind speed is using statistical models that only use historical wind speed series to build their forecasting models [98]. According to conventional statistics, a future wind speed is a linear combination of current and past wind speeds, so they are unable to capture the nonlinear patterns hidden in the wind speed time series [45].

4.2.1   AR model

The most common statistical model for wind speed forecasting is an AR model, which has been widely used in short-term forecasting.

4.2.2   MA model

The moving average measures the trends in a data set.

4.2.3 ARMA model

An ARMA model is used to model and forecast short-term wind speed linear components [102].

4.3 ANN

Wind speed and power forecasting use the ANN as one of the most commonly used statistical approaches. An input layer is followed by one or more hidden layers, then an output layer as is shown in Fig. 4.1. A layer contains artificial neurons, and the neurons in each layer are connected using a connection approach. The training and learning process makes it possible to model the complex non-linear relationship between the input and output layers. The usual neural networks used for forecasting and prediction will be detailed in the subsections below.
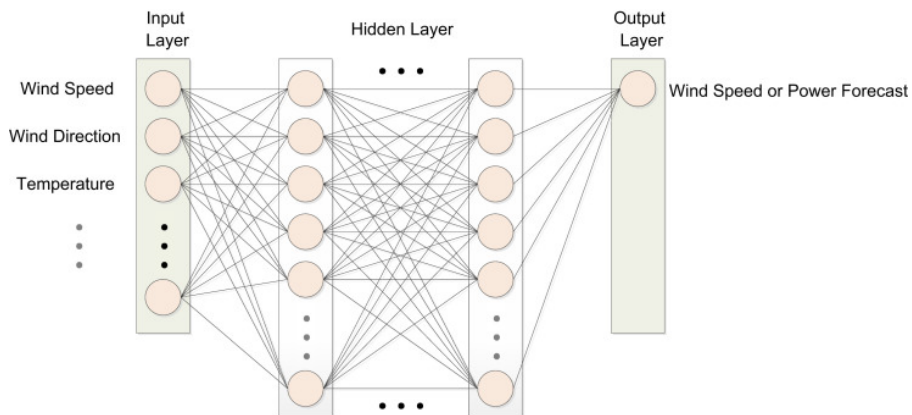
Figure 4.1: Wind speed and power forecasting model using ANN [94]

4.3.1 ANN used for WS and wind power forecasting

4.3.1.1 MLP Network

This network is especially true for the three-layer network layout, in which the input and output layers are directly coupled through a single hidden layer in the middle. The three-layer network structure's intrinsic capacity to perform any conceivable input-output mapping qualifies the MLP network for effective time series forecasting [103].

The following three aspects of the MLP are highlighted:

- Each neuron in the network has a differentiable nonlinear activation function in its model.

- One or more levels are hidden from both the input and output nodes in the network.

- The network has a high degree of connection, with the extent determined by the network's synaptic weights [104].

  This network is especially true for the three-layer network layout, in which the input and output layers are directly coupled through a single hidden layer in the middle. The three-layer network structure's intrinsic capacity to perform any conceivable input-output mapping qualifies the MLP network for effective time series forecasting [103].

4.3.1.2   DNN models

The output of DNN is determined not just by the network's current input but also by the network's current or former inputs, outputs, or states. There are two types of DNN: those with only feedforward connections and those including feedback or recurrent connections. In general, DNNs are more powerful than static networks. DNN may be trained to learn sequential or time-varying patterns since they contain memory. This has applications in various fields, including time series prediction   citeBeale2010.

4.3.1.3   RNN models

The RNN layers correspond to specific locations within a sequence one to one. The timestamp is also known as the sequence position. As a result, instead of incorporating a variable number of inputs into a single input layer, the network comprises a variable number of layers, each with one output corresponding to a single time-stamp   cites Aggarwal2048. Rumelhart et al. proposed a comprehensive framework for training recurrent networks termed backpropagation over time, comparable to the methodology used for training feedforward networks. The algorithm is created by breaking down the network's temporal activity into a layered feedforward that grows with each time step [103].

4.3.2   Deep learning models

Deep Learning is known as a Machine Learning technique that makes use of a deep neural network. The deep neural network is a multi-layer neural network with two or more hidden layers. Previous neural networks could not train their deeper hidden layers and had degraded performance. [46].

4.4   Hybrid models

Hybrid approaches combine different approaches such as physical, ANN, and statistical approaches or combining short-term and medium-term models, and others [97]. At the same time, maintaining the benefits of each approach enhances forecasting accuracy [71].

4.5   Proposed model for short-term WS forecasting

For the design of the proposed model for short-term wind speed forecasting over complex terrain, a hybrid model composed of three types of models were considered, including statistical, DNN, and RNN.

4.6   Statistical models

The statistical models used were the regressive models, such as persistent, AR, MA, and ARMA, to determine a baseline for the prediction to be developed.

4.6.1   Persistence model

According to the persistence model, a prediction can be made by considering that the current time will be equal to the forecasted time [105]. Furthermore, this model has been widely used by researchers in wind power forecasting as a baseline to make comparisons against this model [106]. Moreover, this model has a high performance when the weather variables have a slight variation and the forecasting time does not exceed more than 1 hour [49].

Considering a time series Y_t, knowing its historical data set H_t, forecasting the future values, through a persistence process is given in Equation 4.1. Statistical models like persistent, AR, MA, and ARMA were used to determine a baseline for developing a prediction.

$$H_t = H_t + 1, H_t + 2, ..., H_t + n \qquad (4.1)$$

Specifically, forecasting of the oncoming value will be shown in Equation 4.2

$$H_t = Y_t - n \qquad (4.2)$$

In this study, the wind speed at the moment n will be equal to the wind speed 12 similar hours of the previous day.

4.6.2   Moving Average model

This approach is often used to model univariate time series. In this model, a certain observation is conditioned by the random impulses of the previous observations. In this way, the current observation is defined as the sum of the current pulse and the previous random pulses with a certain weight. The general form of this model is defined in the equation 4.3 [106].

$$Y_t = a_t - \Theta_1 a_t - 1 - \Theta_2 a_t - 2 - \Theta_3 a_t - 3 - ... - \Theta_q a_t - q \qquad (4.3)$$

Where: Y_t is the time series to be described in terms of an unlimited amount of linear a_t; which is the remainder in period t, and $a_t - 1$ the previous values of the error, $(\Theta_1, \Theta_2, ..., \Theta_q)$ are the MA process parameters. Introducing the MA parameter of order q as is shown in Equation 4.4:

$$\theta(B) = 1 - \Theta_1 B - \Theta_2 B^2 - \Theta_3 B^3 - ... - \Theta_q B^q \qquad (4.4)$$

The MA model contains (q+2) unknown parameters to be predicted from the observed values [103]. The compact form of this model is expressed as equation4.5:

$$Y_t = \theta(B)a_t \qquad (4.5)$$

4.6.3   ARMA model

The ARMA model is a practical tool used to express the dynamic behavior of time series. The ARMA model is a practical tool used to express the dynamic behavior of the time series. The estimation of future values of an independent time series through this model is carried out as a combination of past values as well as by random impulses of past observations [106]. Combining the AR and MA models yields this model. Equation 4.6 represents the ARMA model's general form.

The AR and MA models were combined to create this model. Equation 4.6 represents the ARMA model in its generic version.

$$Y_t = \phi_1 Y_t - 1 + \phi_2 Y_t - 2 + ... + \phi_p Y_t - p + a_t - \phi_1 a_t - 1 - \phi_2 a_t - 2 - ... - \phi_q a_t - q \qquad (4.6)$$

Writing again the model as equation 4.7.

$$Y_t = \phi_1 Y_t - 1 + \phi_2 Y_t - 2 + ... + \phi_p Y_t - p + a_t - \phi_1 a_t - 1 - \phi_2 a_t - 2 - ... - \phi_q a_t - q \qquad (4.7)$$

Ordering again as equation 4.8.

$$(1 - \phi_1(B) - \phi_2(B_2^2) - ... - \phi_p(B^p))Y_t = (1 - \Theta_1 B - \Theta B^2 - ... - \Theta_q B^q)a_t \qquad (4.8)$$

The compact form of the ARMA model is written as equation 4.9.

$$\phi(B)Y_t = \theta(B)a_t \tag{4.9}$$

4.7 Dynamic Neural Networks

The DNN replies temporally to an input signal applied from the output as feedback; enabling them to obtain a state representation useful for modeling and forecasting nonlinear systems [104]. In this study, the NARX and LSTM networks are used as forecasters.

4.7.1 NARX network

The NARX model is a type of RNN dynamically driven, with feedback connections enclosing several layers of the network [51, 104, 107]. The basic architecture of the NARX model with one input only is shown in Fig. 4.2; which is based on the static MLP to exploit its mapping capability [49, 104]. The single output or predicted variable $y_{(t+1)}$ is feedback to the network input creating a series-parallel architecture; which is one unit of time ahead of the input u_n. The signal vector to the input layer is composed of two parts: (1) present and past values of the input or exogenous inputs named $u_{(n)}$, $u_{(n-1)}$, ..., $u_{(n-q+1)}$, and (2) delayed values of the output named, $y_{(n)}$, $y_{(n-1)}$, ..., $y_{(n-q+1)}$. The used equation to define the dynamic behavior of the NARX model is shown in Equation 4.10:

$$y_{(n+1)} = F(y_{(n)}, \ldots, y_{(n-q+1)}, u_{(n)}, \ldots, u_{(n-q+1)}) \tag{4.10}$$

Where F is a nonlinear function, n is the number of iterations [104]. In this study, the exogenous variable to be incorporated into the NARX model is wind speed. The representation of this model is shown in equation 4.11, considering Vav as wind speed forecasted used as feedback from output to input layers.

$$y_{(n+1)} = F(y_{(n)}, \ldots, y_{(n-q+1)}, Vav_{(n)}, \ldots, Vav_{(n-q+1)}) \tag{4.11}$$

The general NARX (n_x, N_y) model for prediction considers: on the one hand, y, e, and x as output, noise, and input respectively. On the other hand, n_y, n_e, and n_x as the maximum lags of input, noise, and input in the order given. In addition, F is an unrevealed smooth function; it supposes a mean value of zero for e(t); which is independent of the past value with a finite variance σ^2 as is represented in Equation 4.12 [50].

$$y(t) = F(y(t-1), \ldots, y(t-n_y), x(t-1), \ldots, x(t-n_x)) + e(t) \tag{4.12}$$

The optimum prediction theory is centered around reducing the Mean Square Error
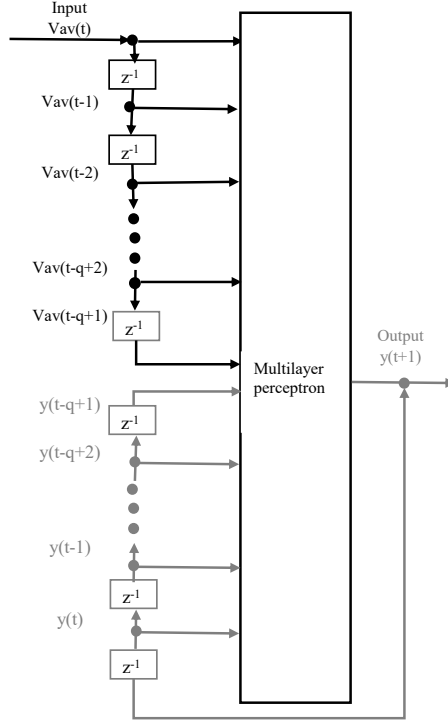
Figure 4.2: NARX model architecture [104]

(MSE) value, considering a finite set of past values dependent on the mean. The lowest
MSE predictor dependent on the mean is given by equation 4.13.

$$\bar{y}(t) = E[y(t) \mid y(t-1), y(t-2), \ldots, y(1)] \qquad (4.13)$$

Supposing the conditions of zero noise and finite variance given in equation 4.10. The
optimal predictor $NARX(n_x, n_y)$ is shown in Equation 4.14.

$$\bar{y}(t) = F[y(t-1), ..., y(t-n_y), x(t-1), x(t-n_x)] \qquad (4.14)$$

4.7.1.1   NARX model learning algorithms

The hidden layer of this network has a tan-sigmoid transfer function, while the
output layer has a linear transfer function. This network is created and trained in an
open loop using true output, which is more accurate and efficient than a closed loop.
Once training has finished, the network may be converted to a closed loop for prediction
mode [107]. This process is developed using a static backpropagation algorithm and
decoupled feedback. To prevent overtraining, the regularization technique is used to

solve the weights and connections problem in the network. By reducing the parameter range, this technique improves performance. In this way, the performance function for training MSE is changed by MSE_{reg} as is shown in Equation 4.15.

$$MSE = \frac{1}{n} \sum_{t=1}^{n} (t_i - t_f)^2 \tag{4.15}$$

Considering Mean Square Weight (MSW) as is indicated in Equation 4.16:

$$MSW = \frac{1}{n} \sum_{j=1}^{n} (W_i)^2 \tag{4.16}$$

The MSE_{reg} is shown Equation 4.17:

$$MSE_{reg} = \xi MSE + (1 - \xi) MSW \tag{4.17}$$

Where t_i is the target, t_f is the predicted value, and ξ performance ratio. As a result of the enhanced performance ratio, the weights and biases of the network are smaller. Furthermore, the network is forced to respond more smoothly and has less chance of overfitting [108].

The main advantage of the NARX model is that is composed of unlike models and computational intelligence at a rational cost [Cadenas2016]. An influential feature of the NARX model is the size of the embedded memory for input and output, as well as the number of neurons in the input layer. Furthermore, its generalization and convergence are better than other networks [51, 108]. Therefore, the NARX network can be used as a predictor, nonlinear filtering, and modeling of nonlinear dynamic systems [107].

4.7.2 NAR network

The NAR network only has one series involved; in this way, the future values of a time series y(t) are predicted from past values. This prediction is known as nonlinear autoregressive [107].

The NARX model can be compared using the NAR network, which is suitable for time series prediction with its delays. The NAR network structure is a combination of MLP with an autoregressive model. In this model, the independent variable y(t) is acquired as a nonlinear function from past d values [49]. The used equation to define the NAR model is shown in Equation 4.18:

$$y(_t) = f(y(_{t-1}), ..., y(_{t-d})) \tag{4.18}$$

The architecture of the NAR model is composed of three layers: input, hidden, and output as is shown in Fig. 4.3. The main characteristics of the hidden layer are

feedback delays, the number of neurons, weights matrix, bias vector, and nonlinear activation function between the hidden layer and output layer for each neuron. Furthermore, the NAR architecture for optimization is reached through trial-and-error testing of the feedback delays and neurons per hidden layer [109]. The algorithm to train NAR networks is Levenberg-Marquardt, approximating Newton's method based on backpropagation with the descendent gradient technique to determine the second derivative order without considering the Hessian matrix. The performance function is the sum of the squares that differ between the real value and the estimated value; this allows for the determination of the gradient as seen in Equation 4.19, and Equation 4.20 estimates the Hessian matrix $nabla2f(x)$.
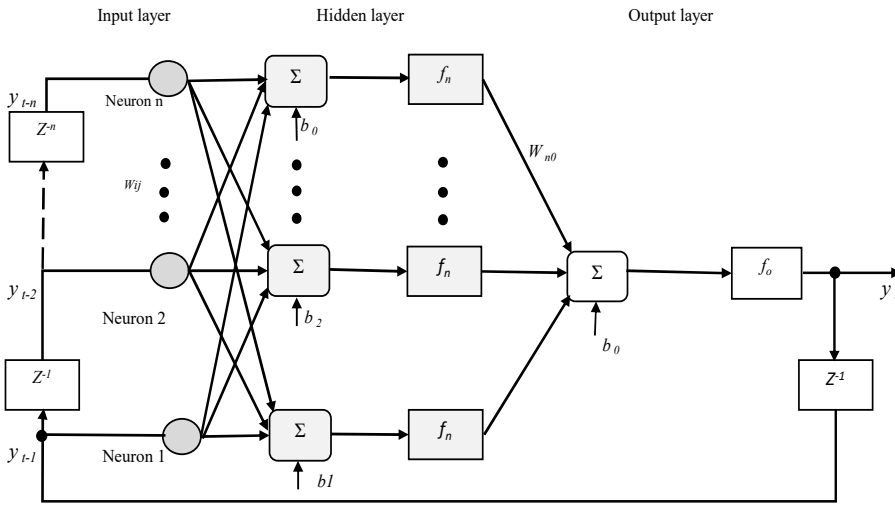
Figure 4.3: NAR model architecture [110]

$$\nabla f(x) = J^T(x)e(x) \tag{4.19}$$

$$\nabla^2 f(x) = J^T(x)J(x) + S(x) \tag{4.20}$$

Where J represents the Jacobian matrix of the first derivatives of the weight and bias vectors of the network error. Additionally, each training step is accompanied by an error vector. According to Equation 4.21, the /cite[Cigizogluetal2005] modification to the Gauss-Newton method assumes S(x) = 0 and uses the following algorithm to estimate the Hessian matrix.

$$\delta(x) = [J^T(x)J(x) + \mu I]^-1 + J^T(x)e(x) \tag{4.21}$$

Where μ is a parameter used to approximate Equation 4.21 to the Gauss-Newton method through an easy modification to the backpropagation algorithm.

4.7.3   NIO network

The NIO network is similar to the NARX model, where there are two series including an input series x(t) and an output series y(t). This model predicts values of y(t) from past values of x(t), with the absence of past values of y(t) [107]. The equation used to define the NIO model is shown in Equation 4.22:

$$y(_t) = f(x(_{t-1}), \dots, x(_{t-d})) \tag{4.22}$$

4.7.4   Deep learning models

4.7.4.1   LSTM network

In terms of long-term and short-term dependency, the LSTM network is a special kind of RNN characterized by its stability and high power. The LSTM is a cell memory to connect previous data to current neurons. This cell can remember the temporal state due to three temporary gates, which can add or delete data to these cells [53]. The problem of vanishing gradient was solved by Hochreiter using a gate control LSTM network [111].

The LSTM network is a unique type of RNN distinguished by its stability and exceptional capacity to address vanishing gradient problems with regard to both long-term and short-term reliance. The LSTM serves as a cell memory to link prior information to active neurons. Three temporary gates that can add or remove data from these cells allow this cell to remember its temporal state [53].

The LSTM network can be trained using a gradient descendent algorithm in combination with BPTT. This algorithm calculates the time required for the optimization process to change the network weight in proportion to the derivative of the error. The procedure to find the direct relationship between the loss function and the network weights is known as unfolding; which is composed of an exact reproduction of the hidden layer of the network for each period to update weights [112]. The LSTM architecture is represented in Fig. 4.4; which is composed of an input gate i_t, a forgetting gate f_t, an output gate O_t, and a memory cell c. The hidden state is h_t at time point t, the network input at time point t is X_t, and the sigmoid activation function is σ [54, 112]
1. The forgetting gate is used to select the information to be discarded or retained in the previous cell m_{t-1} according to Equation 4.23. By entering h_{t-1} and including X_t to the sigmoid function as shown in Equation 4.24; the output cell is designed as c_t [0,1], considering that in zero information will be discarded, and in 1 information will be retained. While W and b are the weights and bias vectors, respectively.

$$f_t = \sigma(W_f[h_{t-1}, X_t] + b_f) \tag{4.23}$$
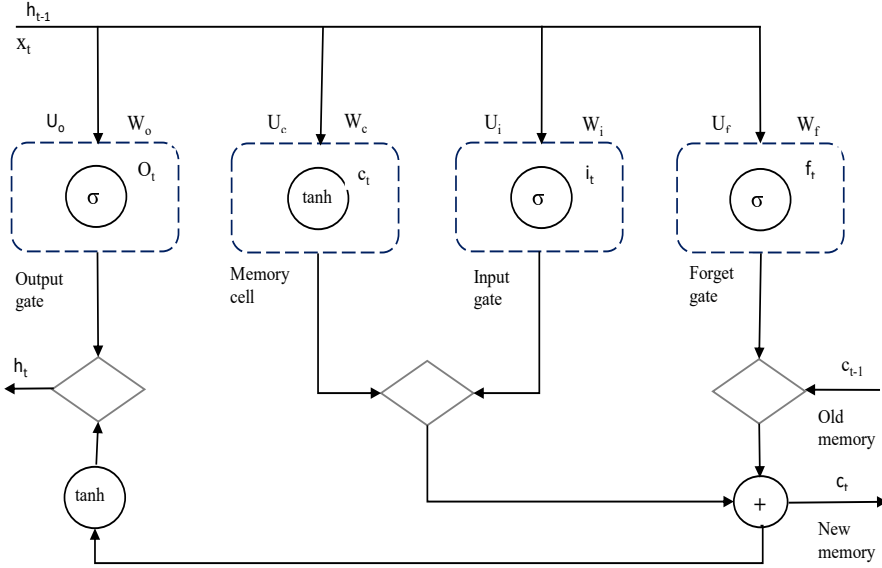
Figure 4.4: LSTM cell memory architecture [54]

$$\sigma_t = \frac{1}{1 - e^- x} \tag{4.24}$$

2. The input gate decides the updated information to be retained in the cell state. By entering into the output h_{t-1} and attaching the present input X_t at time point t into Equation 4.24 (σ function). The generated value [1,0] according to Equation 4.16 in the cell to select the updated information to be retained; the tan h layer accepts simultaneously the selection signal C_t expressed in Equation 4.25 to keep updated the cell state.

$$i_t = \sigma(W_i[h_{t-1}, X_t] + b_i) \tag{4.25}$$
$$c_t = tanh(W_c[h_{t-1}, X_t] + b_c) \tag{4.26}$$

3. The output gate decides the information of the cell state that will be used as output. The previous state of the output h_{t-1} is entered at the last point time t, and attaching the present input x_t to the sigmoid function generates a signal[1,0] named O_t according to Equation 4.27 to decide the number of cells is used as output. The output signal h_t can be obtained by sigmoid and tanh from Equation 4.28.

$$o_t = \sigma(W_o[h_{t-1}, X_t] + b_o) \tag{4.27}$$
$$h_t = O_t.tanh(c_t) \tag{4.28}$$

4.8   Conclusions

The forecasting models described in this chapter represent the most commonly used in forecasting the future values of short-term time series. The proposed model uses statistical, DNN-RNN to predict wind speed, available power, and electrical energy to be produced at a wind farm. The following considerations must be made for all of the prediction models indicated:

- The measured data derived from the meteorological variables and the NWP models must be handled carefully, considering outliers, gusts, and calm winds.

- Since statistical models have a moderate percentage accuracy of the estimated value, they are considered univariate reference models for wind speed forecasting. This is because the results of these models differ significantly from the predicted value.

- In short-term wind speed forecasting, the ANN algorithm is used because it can be used to predict using non-linear systems based on measured meteorological data (multivariate), which results in highly accurate values.

- The components of the proposed model must be compared to the persistent model to determine their accuracy. The statistical model is univariate and serves as a predictor's starting point. The NARX or LSTM multivariable models are used to lower the proportion of error in WS forecasting.

- The NARX dynamic network has feedback between network layers creating a series-parallel for prediction and an open loop for training. It has computational intelligence at a low cost due to its embedded memory. It can be used in the modeling and prediction of dynamic nonlinear systems.

- The LSTM recurrent network is a memory cell. It can remember temporary states by adding or deleting data to its 3 temporary gates. This network is trained using the downward propagation algorithm together with BPTT to calculate the time of the network optimization process.

Chapter 5

Wind speed and power forecasting methodology using the proposed model

This chapter describes the methodology used for WRA, short-term wind speed, and power forecasting considered in the proposed model composed of the following approaches: linear regression models, DNN and RNN networks, and wind farm design using CFD in the Ecuadorian Andes

5.1 Introduction

According to the statement at the beginning of this thesis, the main objective is to design and validate a model to predict wind speed values short-term 6 hours in advance. Due to the complexity of applying a physical model that reproduces the dynamic processes that occur in the atmosphere of complex terrain at high altitude in the Ecuadorian Andes, and taking as a reference the obtained results from the study of the wind regime in that area, it has been chosen as forecaster a hybrid model: statistical-DNN-RNN to reproduce with high accuracy the existing relationships between wind speed behavior and other atmospheric variables measured in the study area. The data from Tower 1 at 30 m AGL were used for the training and validation of the hybrid model. These variables were used as input variables in the selected model. In the same way, were considered the observations in tower 2 at 80 m AGL, whose characteristics were detailed in Chapter 2.

To meet the objectives outlined in the first chapter, the study area in the Ecuadorian Andes is described, then the wind database collected in 2018 is indicated. Finally, the

characteristics of the measurement equipment used are determined. This area of study has been chosen for the following reasons:

- It is a location located within a natural wind pass with strong winds where a wind farm can be built.

- It is relevant to observe the wind behavior over complex terrain at high altitudes away from any effect that could be caused by any external component.

- Because there are wind speed data corresponding to three levels in height, where the existence of vertical variations and the possible repercussion that it could have on the extractable wind energy are evaluated.

- The existing correlation between the two groups of data (30-80m AGL) is very similar, as will be seen later.
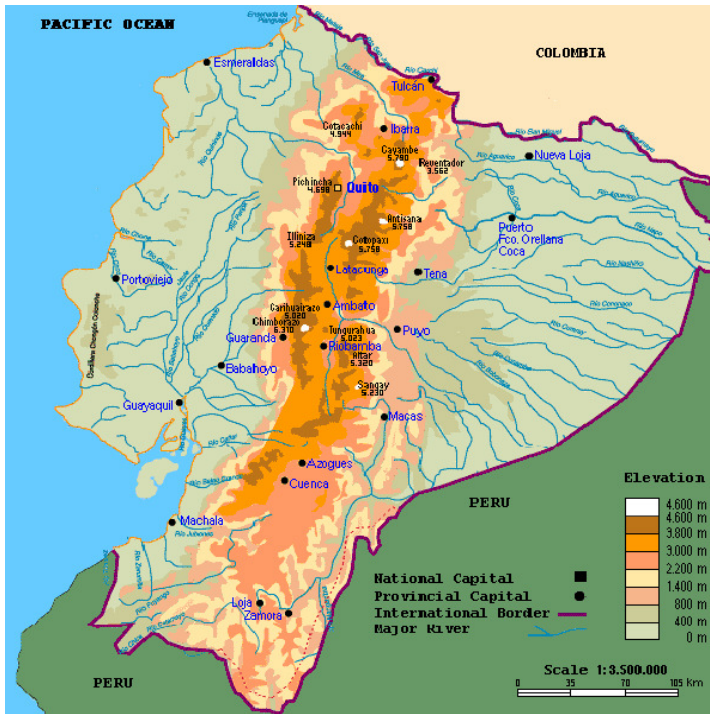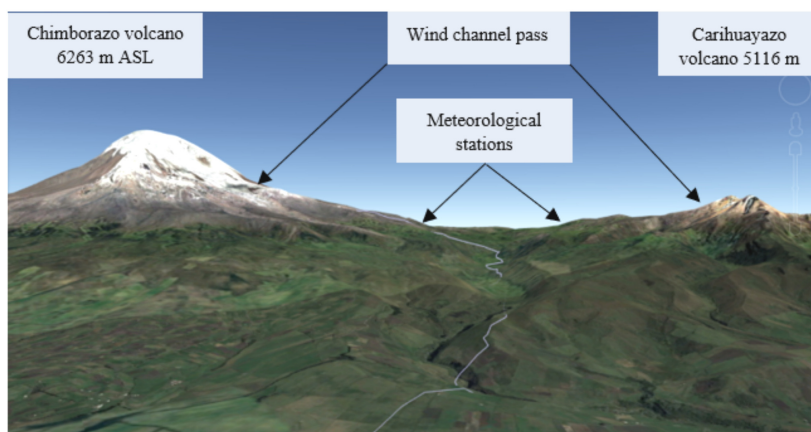
5.2   Area of study

Figure 5.1: Geographic map of Ecuador [113]

1

Fig. 5.1 illustrates that the study area is located in the Sierra region of the Ecuadorian Andes, within the provinces of Tungurahua, Chimborazo, and Bolivar. Furthermore, the study area is located in the Sierra region of the Ecuadorian Andes, among the provinces of Tungurahua, Chimborazo, and Bolívar. Hence, there are few people in this region. The majority of land, which is a natural reserve is owned by the state. According to the Ecuadorian Atlas, El Arenal valley is considered a windy sector within the Ecuadorian Andes [114]. This 10 Km wide valley is located at a natural mountain pass, between the volcanoes Chimborazo (6263 m ASL) and Carihuayrazo (5116 m ASL), as is presented in Fig. 5.2. This wind channel pass causes a wind speed-up effect due to the Venturi effect. This particular site with high wind potential was selected after a preliminary assessment, which is considered the first phase in WRA [60]. Therefore, this site is classified as a region with accelerated wind flow [115]. A preliminary assessment of the wind resource of this particular site was conducted [23], which is considered the first phase of the wind resource assessment.

Figure 5.2: Area of study in the Andes Mountains [116]
2

Ecuador is traversed from North to South in the Sierra region by the Andes Mountains, which are composed of East and West mountain ranges. The topography of the Andes Mountains is characterized by complex terrain at high altitudes, which is composed of hills, plateaus, mountains (3000-4500 m ASL), and volcanoes (¿ 5000 m ASL) [113]. In the mountains, during the day, the sun heats air masses, and hot air rises on the sides of the mountains, creating flow circulation and anabatic winds. Katabatic winds occur at night when air parcels descend on the sides of the moun-

---

02"Reprinted from Renewable Energy, Volume 183, Germánico López and Pablo Arboleya, Short-term wind speed forecasting over complex terrain using linear regression models and multivariable LSTM and NARX networks in the Andes Mountains, Ecuador, Pages 351-368, Copyright 2022, with permission from Elsevier"

tains [14, 15]. There are two predominant climatic stations in this region, which are winter from December to June and summer from July to November [113, 117].

3

Table 5.1: **Geographic coordinates of meteorological stations [118]**

| Parameter	Station 1	Station 2
Latitude	$1°54'S$	$1°54.8'S$
Longitude	$79°15'W$	$78°45.6'W$
Elevation	4260m ASL	4428m ASL

5.3   Equipment and data

The collected data were obtained using sensors mounted on two tubular towers at 30 m and 80 m AGL, respectively, installed in the moorland of the zone of study by international guidelines [119]. Station 1 at a height of 30m AGL was positioned in the community of Mechahuasca, as is shown in Fig. 5.3, and station 2 at a height of 80m AGL was placed close to Chimborazo volcano. Furthermore, this region is suitable for wind power assessment and installation, which does not represent a risk to environmental care [118]. The measured data is formed of 10-minute intervals with average, maximum, minimum, and standard deviation values of the following weather variables:

- AVGTEMP Average air temperature (ºC)

- ATPRES Atmospheric pressure (millibars)

- GSR Global solar radiation (W/m^2)

- WD wind direction (º)

- WSAVG Wind speed average (m/s)

- WSMAX Wind speed maximum (m/s)

- WSMIN Wind speed minimum (m/s)

This study is focused on wind speed and power forecasting, WRA, and wind farm design using CFD in the Ecuadorian Andes. To get this purpose are considered data
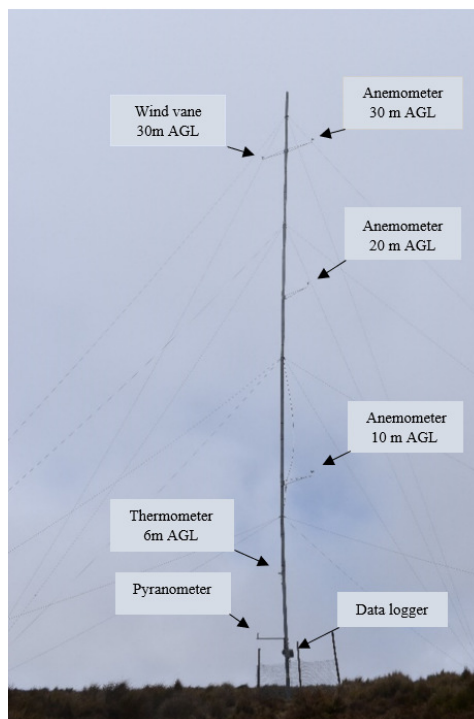
Figure 5.3: Meteorological station 1 in the community Mechahuasca

from two meteorological stations, which are the property of the Technical University of Ambato and the MEER, respectively.

The location of the towers' geographical coordinates is displayed in Table Table 5.1. Given that the set of wind data is a crucial parameter for WRA and that at least one year's worth of wind data is needed to predict WPP [71]. The data was gathered from January 1st to December 31st, 2018. The 40 m-tall-tower was installed on a large plateau. In addition, the tower of 80 m-tall-tower was installed on a round hill in the El Arenal desert close to the Chimborazo volcano. The equipment, sensors, and their characteristics installed on each tower to measure meteorological variables are listed in Table 5.2. One data logger NRG Symphony Plus 3 for each tower, was used to store data in memory during 2018 and to enable remote communication. Readings are averaged at 10-minute intervals. The sampling frequency is 1 Hz [72].

Table 5.2: **Sensors installed on meteorological towers [118]**

Type	Model	Range	Deviation
Anemometer	NRG #40C	$1ms^{-1}$-$96ms^{-1}$	0.5 %
Vane	NRG 200P	0-360°	1%
Barometer	NRG BP20	15KPa-115KPa	1.5%
Thermometer	NRG 110S	-40° to 95.5°C	1.3 %
Pyranometer	LI 200R	400 to 1100 nm	10µV

5.4 Application of proposed forecasting models for wind speed forecasting

The particular application of linear regression and DNN models for wind speed forecasting is directed here.

5.4.1 Linear regression models

5.4.1.1 ARMA or MA model

The forecasting methodology employed using ARMA or MA models is performed in three steps:
1. Model definition: Concerning the election of the (p,q) order of the ARMA model, or q for the MA model, which is designed as a model structure.
2. Model training: Involves the approximation of the model parameters by way of a reduction process known as least squares.
3. Prediction of the next range: Estimation of the oncoming value of the time series based on past values using measured data from one to three days ago.

5.4.2 Dynamic Neural Networks models

The forecasting methodology using DNN is performed in five steps:

5.4.2.1 Data preparation and feature extraction

The data preparation for prediction included five activities such as data collection, data preprocessing, correlation matrix, data normalization, and structuring of data [103]. The data were collected by two meteorological stations over a one-year period and preprocessed to remove noise resulting from malfunctioning sensors. Then, data were validated by using different algorithms [19]. Data normalization of preprocessed data was required to convert data from natural range to operative network range [103].

Structuring of data: Using a multivariable time series for the ANN toolbox, seven variables were arranged as input vectors to the DNN. These input vectors were created with the number of input variables equal to the number of neurons.

Then, the second set of one-time series as output vectors into a second cell array. Eight data sets were arranged as follows: two for winter and two for summer, two per 30m and two for 80 m AGL. Data were collected for each data set for six hours on one day of each month of winter and summer. The output vectors were eight vectors formed by six hours of average wind speed per day of each month for winter and summer, four for each season, and four for each height. The total amount for winter was 36 x 7 = 252 (100%), total amount for summer 36 x 5 = 180.

Inputs and outputs vectors were randomly distributed as follows: 70% for the training set, 15% for validation, and 15% for testing [107]. Data used for training in each season were for winter $252 \times 0.7 = 176.4$ (70.0%), for summer 180 x 0.7 = 126 (70%).
The amount for validation to calculate the error value during training was for winter 252 x 0.15 = 37.8, and for summer 180 x 0.15 = 27. The amount for testing is for winter 252 x 0.15 = 37.8, for summer 180 x 0.15 = 27.

The feature extraction process is considered to be one of the most significant parts of the machine learning process. This is because raw data is converted to information that algorithms can use to eliminate repetition by overfitting. The features were extracted using statistical tools, such as mean, median, standard deviation, and frequency domain [120].

The correlation matrix was based on PCC, which showed the correlation between input variables and output variables. In fact, variables that are not highly correlated can be deleted. PCC is a parametric statistical technique to measure the direction and strength between two variables [121]. This way, we can determine if the points of the two variables have a tendency to be placed in a straight line. PCC is defined as the covariance between x and y divided by the product of the standard deviations of each variable [20]. The equation 5.1 is used to calculate PCC.

$$PCC = \frac{cov(xy)}{\varsigma x \varsigma y} \tag{5.1}$$

where cov is the covariance between variables x and y, ςx is standard deviation of x variable, ς is standard deviation of y variable.

The PCC results between measured weather variables and average wind speed at a height of 80 m AGL in 2018 are shown in Table 5.3, which indicates that WSAVG had a high linear correlation with WSMAX, and WSMIN, while the correlation coefficients with AVGTEMP, ATPRES and GSR are very small, and there is an inverse correlation with WD.

Table 5.3: **PCC results at 80m AGL**

Variables	WS AVG	WS MAX	WS MIN	WD	AVG TEMP	AT PRES	GSR
WSAVG	1	0.96	0.94	-0.47	0	0.29	0.22
WSMAX	0.96	1	0.97	-0.46	0.03	0.28	0.25
WSMIN	0.94	0.97	1	-0.45	0.02	0.28	0.23
WD	-0.47	-0.46	-0.45	1	0.02	-0.19	0.01
AVGTEMP	0.2	0.03	0.02	0.16	1	-0.12	0.72
ATPRES	0.29	0.28	0.28	-0.19	0.16	1	-0.01
GSR	0.22	0.25	0.23	0.01	-0.01	-0.01	1

5.4.2.2   Determination of Network Architecture

In order to achieve this aim, DNN was proposed to predict nonlinear time series for the representation of systems whose internal state changes with time. They are particularly appropriate for modeling nonlinear dynamic systems, generally defined by the state-space [103]. DNN models with feedback, such as NARX and NAR, are suitable for time series prediction/cite[Beale2010]. As part of the network architecture, we conducted the following activities: determination of input nodes required to feed neural networks; this was done according to seven selected variables including WSAVG, VSMAX, WSMIN, WD, AVGTEMP, ATPRES, and GSR. In this way, one neuron per variable is selected. Therefore, the output single node was considered the average wind speed only, as shown in Figure 5.4.

5.4.2.3   Network Training Strategy

During network training for time series forecasting, all main characteristics inserted in the training data of the time series should be known and learned [103]. The input-selected parameters are used to train the DNN, and wind speed is the output. Any of the input values had been used for testing and validation purposes. To prevent overfitting, the input vectors and target vector were randomly divided into three sets as follows: 70%, 15%, and 15% to attribute the data to training, validation, and test of network generalization, respectively. MLP utilizes an algorithm named Levenberg-Marquardt backpropagation to train the network. The performance of the three DNN models was improved by adjusting the number of neurons in the hidden layers and the number of epochs [107].
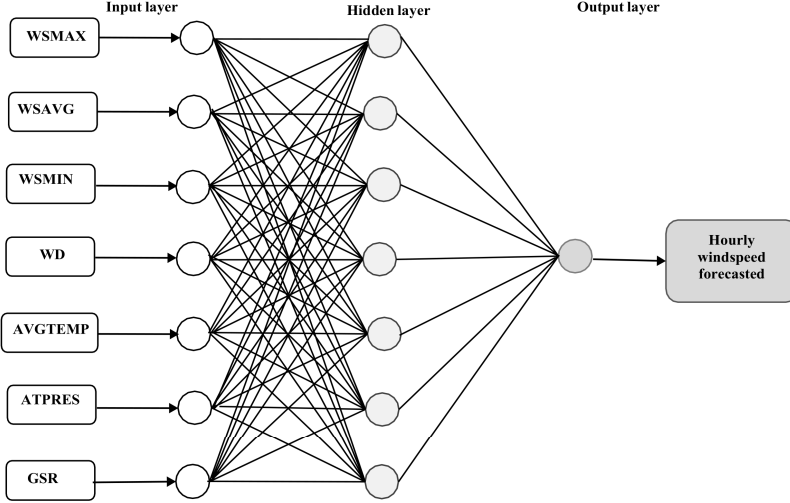
Figure 5.4: Proposed NARX network architecture

5.4.2.4   Network forecasting

Forecasting of the next value was developed by presenting the network with an input vector based on past observations.

5.4.2.5   Error parameters

The forecasting performance to minimize uncertainty was evaluated by using Equations: 5.2, 5.3, and 5.4 named as Root Mean Square Error (RMSE), MSE, and MAPE respectively [42].

$$RMSE = \sqrt[2]{\frac{1}{n}\sum_{t=1}^{n}(Ws_f - Ws_m)^2} \tag{5.2}$$

$$MSE = \frac{1}{n}\sum_{t=1}^{n}(Ws_f - Ws_m)^2 \tag{5.3}$$

$$MAPE = \frac{1}{n}\sum_{t=1}^{n}\left|\frac{Ws_m - Ws_f}{Ws_m}\right|100 \tag{5.4}$$

In the equations 5.2-5.4 n is the total number of inputs and outputs, Ws_m is measured wind speed, Ws_f is forecasted wind speed

5.4.2.6   Software tools

Three kinds of DNN were used with the Neural Network Time Series Toolbox, with a graphic interface in MATLAB R2020b. In the present study, we used three kinds of DNN, such as NARX, NAR, and NIO.

5.4.3   Forecasting using Multivariable LSTM networks

The forecasting process for Multivariable LSTM networks is developed in five stages [54, 122] as follows:

5.4.3.1   Data preprocessing

Multivariable time series means that there are seven meteorological variables for each time step to be used as inputs to LSTM to generate one output, for example. wind speed forecasted. The first step is preparing the measured variables dataset for supervised learning for the LSTM network. Then, a PCC was developed using the seven measured meteorological variables and the data from Table 6.1. The multivariable MV-LSTM method contains four data sets; 12 hours of seven meteorological variables each; one set for Winter, the other for Summer, one for 30 m, and the other for 80 m AGL. The data set was divided into 80% for training and 20% for testing.

5.4.3.2   Data normalization

The seven meteorological variables were measured in different units and required a unique range. Therefore, the selected variables were normalized to have values between zero and one by using the highest and the lowest values of each variable, as shown in Equation 5.5.

$$v_n = \frac{v_i - v_{max}}{v_{max} - v_{min}} \tag{5.5}$$

Where v_n is the normalized value for any variable, v_i is the current value of the variable to be converted, v_{max} is the maximum range for any variable, v_{min} is the minimum range for any variable.

5.4.3.3   Define and fit LSTM model

This step is to create an LSTM regression network and define how many neurons will be used in the hidden layer. The training options must be specified and set up by the solver Adam to optimize performance. The gradient threshold should be set to 1 to prevent the gradient from exploding. The learning rate is set by default to 0.001 and should drop every 5 epochs.

5.4.3.4   LSTM network training and optimization

To perfectly memorize the data sequence, a smaller number of neurons would be used in the hidden layer. The RMSE plots the training report from the standardized data and is employed to measure loss function together with the Adam network performance optimizer. The training and validation loss converge after a certain number of epochs.

5.4.3.5   LSTM network forecasting

The future values of multivariable time series are forecasted one at a time, and the same is updated after each prediction. The last prediction is used as input for each new prediction. The real wind speed forecasted and RMSE are obtained using inverse normalization.

5.4.3.6   LSTM software tools

The simulations were developed using MATLAB R2020b together with the Neural Network Deep Learning Tool.

5.5   Wind characteristics modeling using CFD

5.5.1   Process to create computational domain

It is well-known that the accuracy of CFD simulations relies mainly on the size and shape mesh generated, the boundaries and initial conditions applied, the turbulence model chosen, and the used wall functions [123]. Therefore, it is reasonable to work based on previous research that has worked and shown acceptable results. The following sections show the conditions under which the simulation was carried out. The numerical methods design is developed in three phases to prevent the effects of possible hiding where variables are subordinated as follows [124]:

- In the preprocessing phase, the input data already suitable to be treated are defined by Ansys Fluent, determining the geometry, the domains, the grid, and the selection of the physical and chemical phenomena.

- In the calculation stage, the solution of the algebraic equations resulting from the discretization of the physical model for a volume defined by the numerical grid is performed using 100 iterations.

- In the processing, the visible solution of the calculation is presented, transforming it into a suitable form for its subsequent analysis, data post-processing, and interpretation.

Figure 5.5: Study area located in Chimborazo National Park

The preprocessing phase is developed in three stages as follows:

1. Domain identification

   The computational domain to be created must be large enough to reduce the uncertainties that may be generated in the boundary conditions so that the analysis generates the so-called wake effect. But the domain should not be too large due to can affect the computational simulation time.

   Through the Google Earth software, the location was made using the generate polygon tool and thus finally locating the study area, to generate a kmz format file with the selected study area as is shown in Fig. 5.5. By using the file generated in Google Earth Pro, we proceed to create the contour lines in this Global Mapper software, where you can determine the maximum and minimum height at sea level of the study areas as is shown in Fig. 5.6. With this, pressure output data were obtained with the help of a pressure-height graph, data necessary for the (Boundary Conditions) for further analysis. Global Mapper also allows generating the contour lines in the study areas as presented in Fig. 5.7, which the results were exported in DWG format for the next procedure. Gripphins and Middelton [125] presented a standardization on sinusoidal hills for 2D analysis to represent a parametric function, with a sinusoidal behavior as is shown in Equation 5.6. The post-processing of the contour lines was developed using AutoCAD Civil 3D and then transformed to the surface, performing several procedures. Rhinoceros 6 allowed completing the design and modeling of the surface to de-
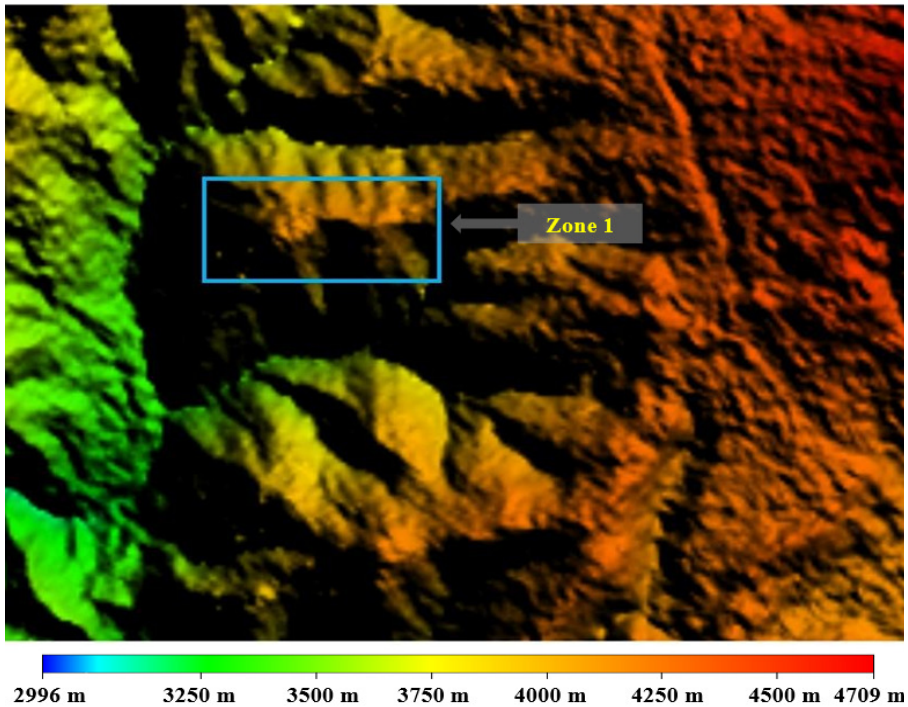
Figure 5.6: Altitude map of the terrain in the study area

termine the number of areas required per area of study as is presented in Fig.5.8. The computational domain was determined, based on the predominant WD from the east, and the diameter of the rotor of the WT Goldwind 70/1500 kW, which diameter is 70 meters, In this way, the length on the X-axis is 28D, on the Y-axis is 14D, and the height of 3D is shown in Fig. 5.9. In the preprocessing of the computational domain of the study area, which is segmented into four surfaces separated 333 meters from each other. This results in a total of 4 contours for the study area as shown in Fig. 5.10.

2. Grid generation The grid process consists of dividing the object of study into several sections, the most relevant within a CFD simulation is the type of mesh since it is where the wind data that already have been defined in its specific coordinates, in the inlet of the computational domain to interpolate the values for each cell until reaching the outlet of the computational domain.

Based on the topological relationship, we started by meshing each of the surfaces. In this method, was created the 2D hybrid meshing of the 4 areas using the Ansys Mechanical meshing tool as indicated in Fig.5.11, which combines structured and unstructured meshing. This allows a better adaptation of the surface to be analyzed. Through the use of skewness in the mesh quality-metric section,
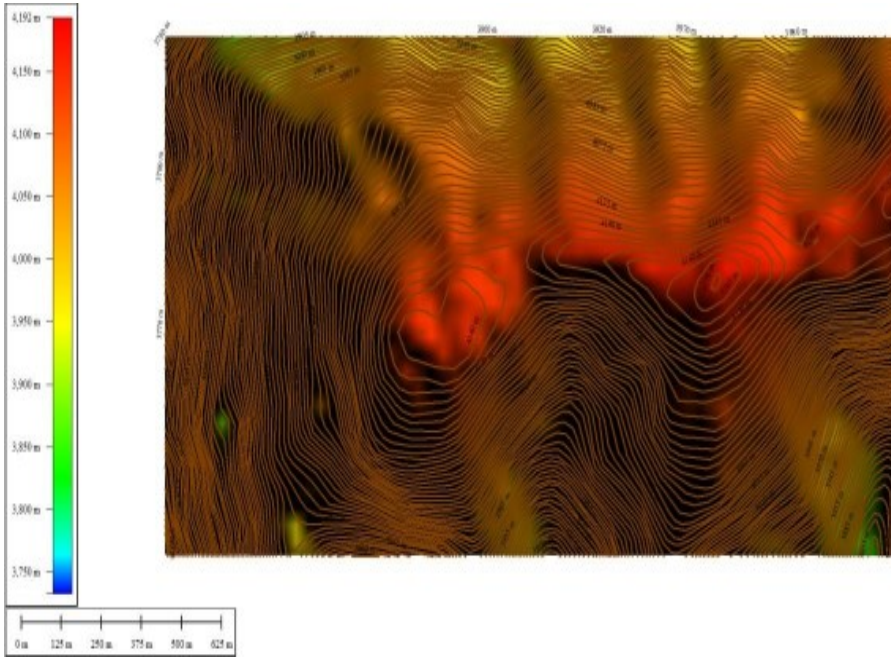
Figure 5.7: Contour lines in Global Mapper Zone 1

meshing asymmetry can be determined if the mesh performed has a high-quality mesh structure through the asymmetry value. Using triangular and quadrilateral shapes to mesh, an equilateral triangle would be the ideal shape for triangular meshes. The same angular and quadrilateral form would be the ideal shape for quadrilateral meshing. This is because highly skewed faces and cells are unacceptable because the equations start to solve assuming the cells are in their correct form. The mesh for study area 1, is excellent for the solution of the equations that describe the model to be analyzed. The average skewness values are in the range of $(0 - 0.25)$ indicating excellent mesh quality.

3. Setting boundary conditions

   Set up:

   It configures general data of the terrain, such as air temperature, air density, space 2D planar, and the elevation of the location wind farm location by considering a stable atmosphere. In addition, the initial wind speed values of the wind speed, roughness class and length, air density, and turbulence models are established, which is the most used for the sites in CFD is the k-ϵ model, which is part of the RANS models of the Navier-Stokes equations.

   Edge conditions:
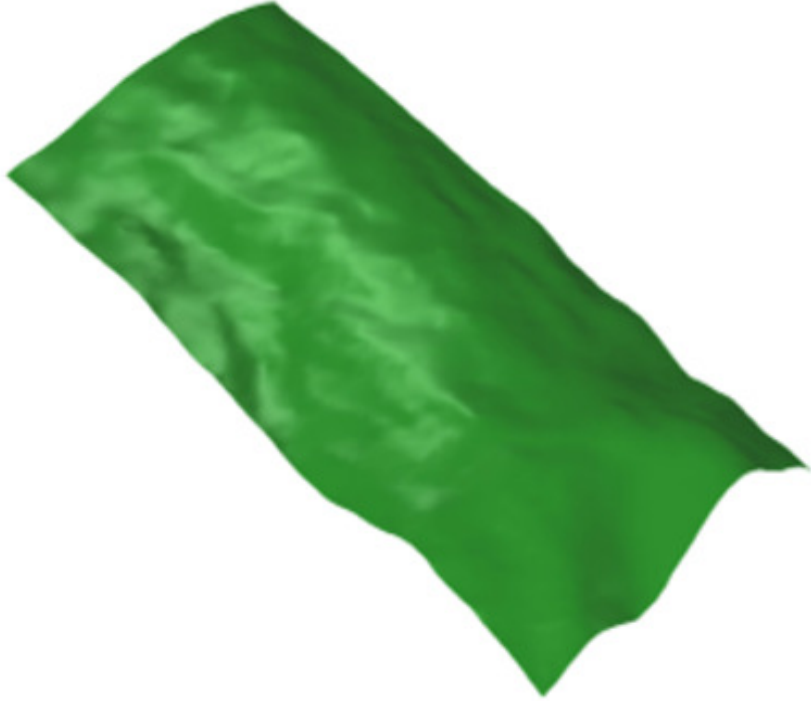
Figure 5.8: Domain surface generated in Rhinoceros 6

Inlet: The inlet was configured to input values of mean wind flow inlet speed and pressure. Also, the calculated monthly values of TI.

Outlet: The outlet was configured so that values of outlet pressure of the wind flow are entered, where the respective calculated value of TI was assigned.

Wall-down: The roughness class of the ground surface was considered, which allows the generation of eddies, thus directly affecting the turbulence and the roughness length. The assigned values are as follows:

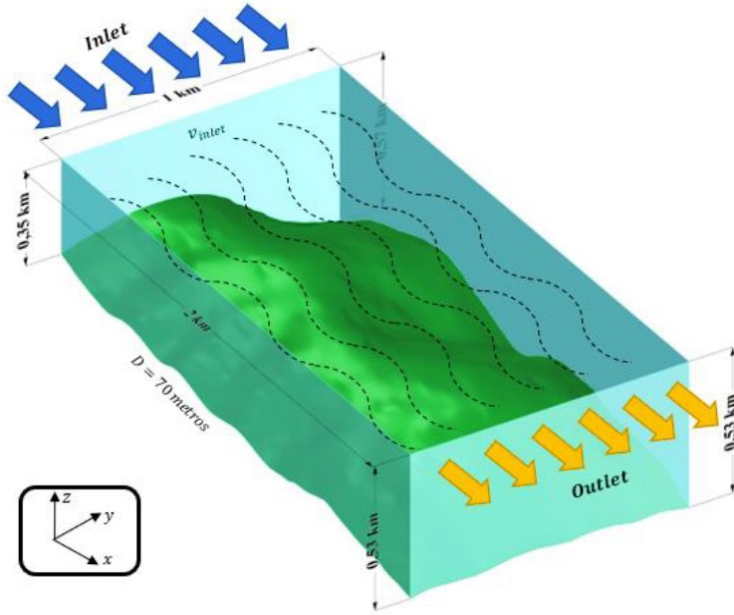Roughness class: 0.5 Landscape with smooth surfaces

Roughness length (Zo): 0.0024 m corresponding to uninhabited areas with grass

Wall-up: This boundary condition represents the atmospheric boundary layer where it does not present roughness by placing zero values.

Trim: It is considered the interior of the study zone. This element of a cell zone determines the type of fluid to be analyzed, by considering air density.

$$Z_s = \left\{ \begin{array}{ll} \frac{H}{2}[1 + cos\frac{Hx}{L}], & -2L < x < 2L \\ 0, & |x| < 2L \end{array} \right\} \tag{5.6}$$
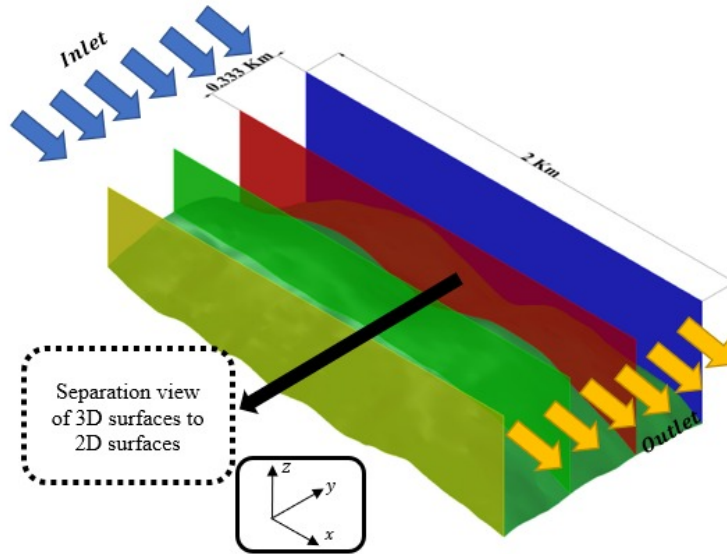
Figure 5.9: Computational domain of Zone 1

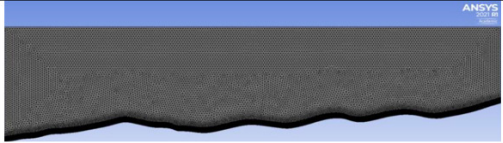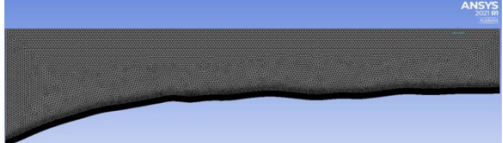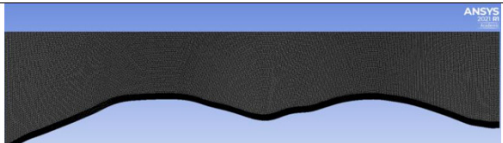Where:

H Hill height

L Hill length
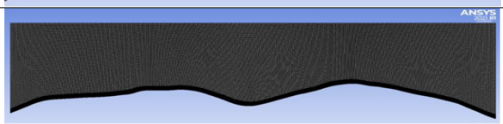
5.5.2   Conclusions

In this chapter, the characteristics of the proposed statistical-DNN-RNN model have been described, as well as the methodology for applying the model to predict short-term wind speed and wind power over complex terrain in the Ecuadorian Andes. Additionally, the Ansys Fluent CFD software can be used to develop wind characteristics modeling. The following aspects should be highlighted.

- The proposed model for short-term wind speed prediction over complex terrain in the Ecuadorian Andes is a hybrid model based on linear regression models as a baseline for prediction. In addition, DNN-RNN networks are used to improve forecasting accuracy.

- A computational domain to represent the size of the mountain is very large. For this reason, the volume of the mountain in 3D was divided into 4 2D sections to efficiently simulate the wind characteristics using the Ansys Fluent CFD software.

Figure 5.10: Division of the 2D computational domains of Zone 1

Area number	Number of nodes	Zone 1 meshing
Area 1	30596	
Area 2	24972	
Area 3	50996	
Area 4	56548	

Figure 5.11: Hybrid meshing in zone 1

Chapter 6

Wind regime characterization and wind characteristics of the Ecuadorian Andes

In this chapter, wind regime characterization results for the study area are reported. Furthermore, a comparison between WPD and CF of the study area against the same parameters of the Villonaco wind farm to select the most suitable WT is developed.

6.1 Wind regime characterization

6.1.1 Preliminary assessment

The Ecuadorian Wind Atlas indicates that wind speed at 80 m AGL is in the range of 10-12 m/s, classified as a moderate breeze, which indicates the presence of strong winds in the study area [114].

6.1.2 Daily and monthly average wind speed

The daily and monthly variation of wind speed average at 30 and 80 m AGL during 2018 from January to December is shown in Fig. 6.1 and Fig. 6.2 respectively. The monthly wind speed analysis indicates two strong seasonal trends. The strongest winds occur from June to September because cold air flows from the East and combines with valley and mountain breezes during this season. Whereas the weakest winds in the winter season are from January to April and from October to December [114, 117].
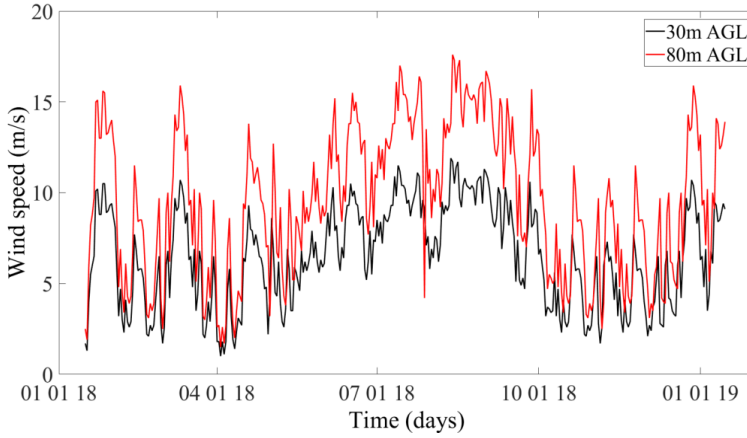
Figure 6.1: Daily wind speed profile for winter and summer in 2018 at 80 m AGL

García et al. [23] observed a similar monthly mean wind speed in the wind data analysis for a nearby location. Strong winds could be feasible for a future wind farm installation with high-power wind turbines and could be a reliable option to forecast short-time wind speeds for power generation. Fig. 6.3 indicates the daily winter and summer wind speed profiles. In the winter profile, there is very low wind speed during the night, which is not recommended for wind turbine operation. During the day, there is a medium wind speed which could be used to forecast wind speed. The summer wind speed profile, however, reaches high wind speed during the day and night; it is useful for predicting wind speed at any time. As a result, summertime wind speed variations exceeded the 10,2 m/s annual mean wind speed value. It should be noted that 12 to 15 m/s of wind speed is the most effective range for wind turbines operating in order to create the most electricity possible [17, 19].

WS was measured in tower 1 at heights of 10, 20, and 30 m AGL and labeled "WS_1", "WS_2", and "WS_3", respectively. For tower 2, the heights are 40, 60, and 80 m AGL and are designated as "WS_4", "WS_5", and "WS_6", respectively. The statistical summary of weather variables is stated in Table 6.1. The percentage of measured values is over 99%, which represents a reliable data set. The mean wind speed measured at six heights from 10 m to 80 m AGL shows an increase in wind speed with height variation, [19] as is shown in Figure 7.1 where WS at 80 m AGL is higher than at 30 m AGL. Moreover, it is observed that WS increases during the summer months due to the influence of the Atlantic equatorial mass composed of the East and Southeast winds that are of greater pressure than the North trade winds [126].

---

[05]"Reprinted from Renewable Energy, Volume 183, Germánico López and Pablo Arboleya, Short-term wind speed forecasting over complex terrain using linear regression models and multivariable LSTM and NARX networks in the Andes Mountains, Ecuador, Pages 351-368, Copyright 2022, with permission from Elsevier"
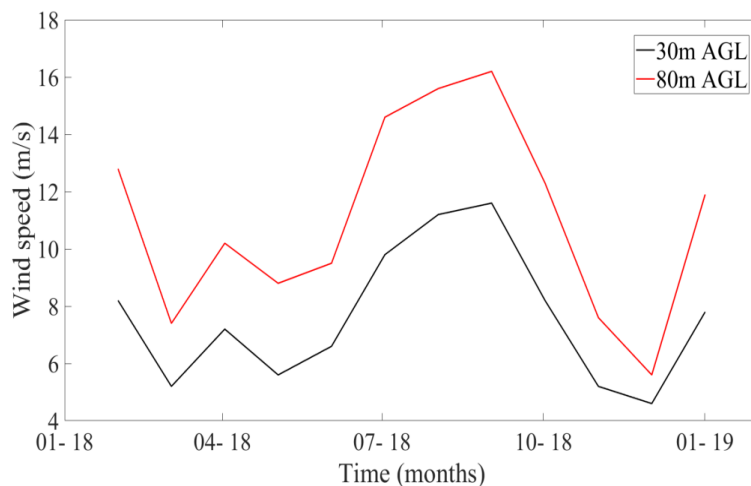
Figure 6.2: Monthly wind speed profile for winter and summer 2018 at 80 m AGL

6.1.3   Wind Power Density

The average WPD was calculated for each month at 80 m AGL based on monthly WS. It observes a WPD increase in summer months in direct proportion to wind speed variation, as is shown in Fig. 6.4.

6.1.4   Wind rose and Weibull probability function

A wind rose diagram is used to display useful information based on wind speed bins /cite [Brower2012]. The wind rose was represented through the software Matlab 2020b by using ten-minute intervals for WS measurements of tower 2, and their corresponding WDs at 80 m AGL are shown in Fig. 6.5. In addition, the predominant wind speed direction at any time is the wind blowing from an azimuth of 90° (East) varying slightly to 105° due to the zone of study being located within a mountain pass between two volcanoes. Furthermore, a similar pattern of wind behavior was found in a nearby location [23]. Moreover, a similar WD was observed in another region of the Ecuadorian Andes [24]. Therefore, the predominant WD is from the East during the summer and winter months.

The Weibull PDF for tower 2 at 80 m AGL is shown in Fig. 6.6, and the estimated wind speed distribution parameters for each tower are presented in Table 6.2; which summarizes the k and c Weibull parameters. Furthermore, the k parameter for both heights is variable due to the influence of the complex topography of the region over eastern winds. Moreover, the annual mean WS is 10.9 m/s. In 2018, the shape parameter k and scale parameter c at 80 m AGL are 1.5 and 11,8 m/s, respectively. Besides,
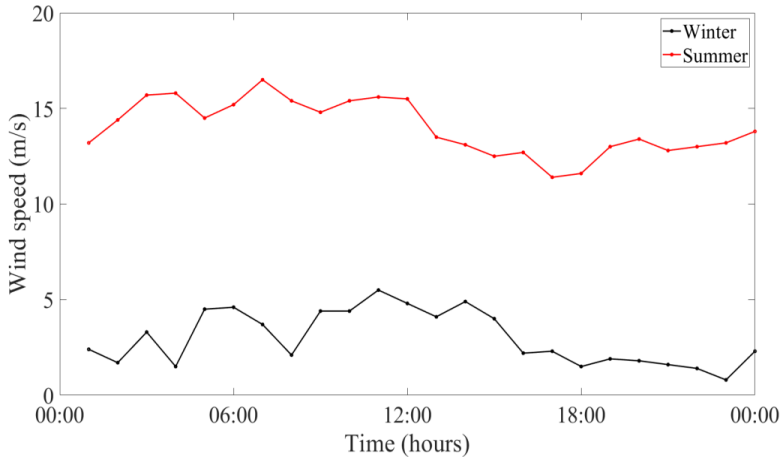
Figure 6.3: Daily wind speed profile for winter and summer 2018 at 80 m AGL

k is considered a lower value, and c is close to the mean WS.

Therefore, according to the results of the Weibull parameters, the area of study has high wind variability with less dispersion concerning the average wind speed and increased availability of wind speed to obtain a large production of wind energy [59]. A similar pattern of Weibull parameters k and c were obtained by Károly Tar [127] to generate monthly average wind speed at different altitudes. In addition, B.K. Gupta [128] attained a variable pattern for k and c monthly values for five locations in India; which is helpful to estimate annual and monthly wind energy production.

Table 6.1: **Weather variables statistics for the zone of study**

Variable	Units	Min	Avg	Max	Percentage
$(WS_1 at 10mAGL)$	m/s	0.2	6.02	23.1	99.68
$(WS_2 at 20mAGL)$	m/s	0.2	6.92	23.5	99.58
$(WS_3 at 30mAGL)$	m/s	0.2	7.02	24.2	99.81
$(WS_4 at 40mAGL)$	m/s	0.2	9.15	41.4	99.86
$(WS_5 at 60mAGL)$	m/s	0.2	10.8	41.5	99.68
$(WS_6 at 80mAGL)$	m/s	0.2	11.02	41.6	99.56
(WPD_1)	W/m^2	0	135	4678	99.4
(WPD_2)	W/m^2	0	250	4990	99.35
(WPD_3)	W/m^2	0	351	5450	99.65
(WPD_4)	W/m^2	0	511	26500	99.61
(WPD_5)	W/m^2	0	584	27482	99.48
(WPD_6)	W/m^2	0	647	28690	99.75
WD (from East)	Degrees	0	90	350	99.45
Temp (3.0 m AGL)	Celsius degrees	-1.5	2.7	9.5	99.7 5
BP	millibars	0	135	746.0	99.75
GSR	W/m^2	606.2	610.9	615.1	98.85
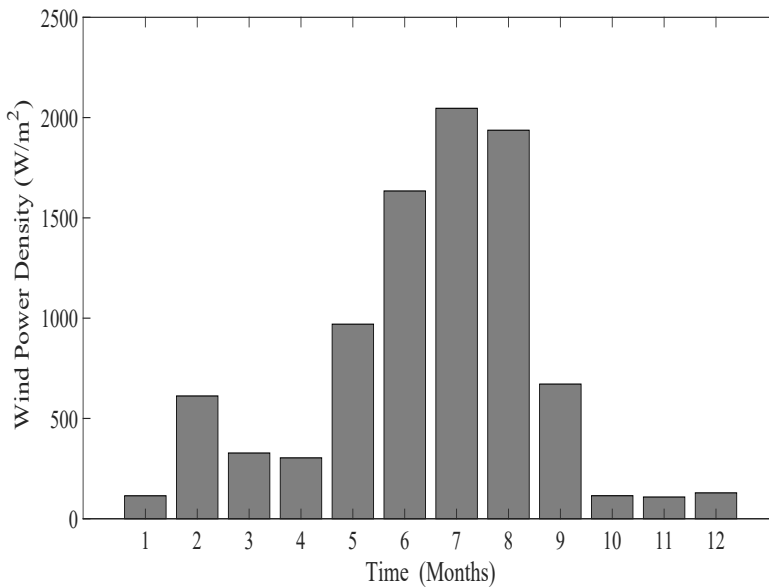
Figure 6.4: Monthly WPD for winter and summer 2018 at 80 m AGL
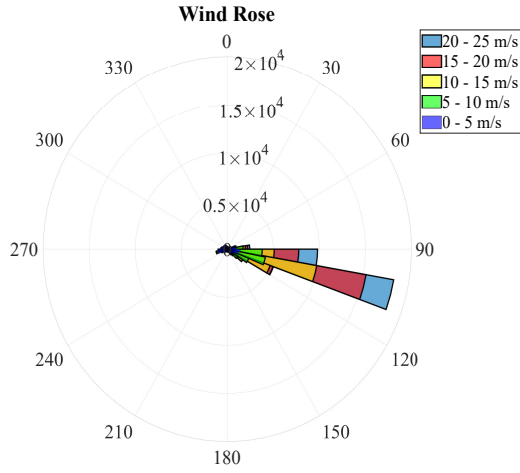
Figure 6.5: Wind rose in tower 2 at 80 m AGL
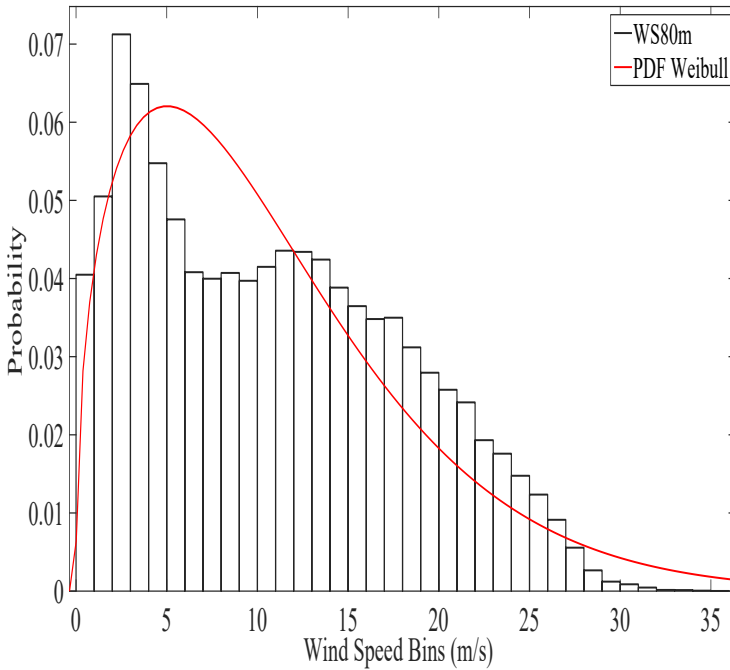
Figure 6.6: Short-term wind speed Weibull distribution in tower 2 at 80 m AGL
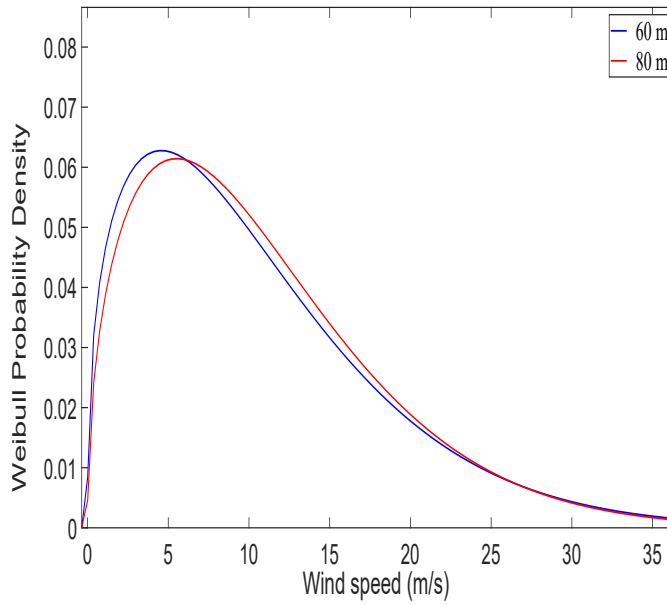
Figure 6.7: Probability Density Function for Weibull
distribution

Table 6.2: Weibull parameters at 30 and 80 m AGL for 2018

Month	30 m		80 m	
	k	**c**	**k**	**c**
January	1.59	8.47	1.61	10.5
February	1.12	4.47	1.31	7.85
March	1.24	6.78	1.51	8.75
April	1.11	5.14	1.41	8.6
May	1.45	6.35	1.61	9.5
June	4.41	9.93	4.71	12.05
July	3.12	10.94	3.31	14.25
August	2.16	10.79	2.41	13.89
September	1.39	8.83	1.51	10.85
October	1.12	4.47	1.31	7.65
November	1.1	4.47	1.31	6.5
December	1.45	7.85	1.81	10.5
Overall	1.68	6.95	1.51	11.87

Figure 6.8: Monthly variation of Wind Shear Coefficient for Tower 1
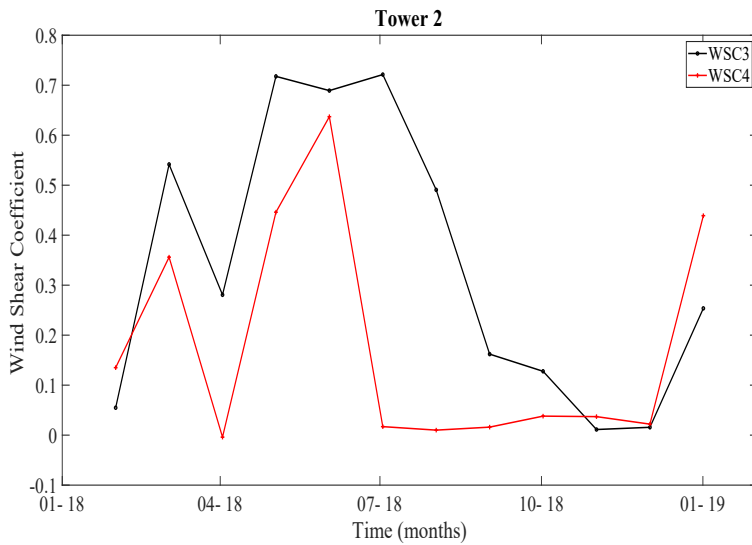
Figure 6.9: Monthly variation of Wind Shear Coefficient for Tower 2

6.2   Wind characteristics

6.2.1   Wind shear profile

The values of WSC were determined using four pairs of wind speeds, two pairs for each tower. The values of WSC_1 and $WSC_{,2}$ were calculated between 10 and 20 m AGL and 20 and 30 m AGL, respectively, using measured data from tower 1. WSC_3 and WSC_4 were calculated between 40 and 60 m AGL, 60 and 80 m AGL by using measured data from tower 2. The monthly variation of WSC values in tower 1 and tower 2 is shown in Fig. 6.8 and Fig. 6.9 respectively. The results indicate that WSC on both towers is variable. In this way, the maximum WSC values appear in winter when WS is low, and the minimum values appear in summer during July and August when WS is high. In addition, one unexpected negative value was observed for WSC_1 in January. Indeed, the WSC is highly influenced by temperature changes and the complex topography of the Sierra region. It should be noted that tower 1 is installed on a plateau, and tower 2 is installed on the top of a hill. Consequently, WSC is affected by wind speed and flow turbulence effects on both towers.

6.2.2   Turbulence Intensity
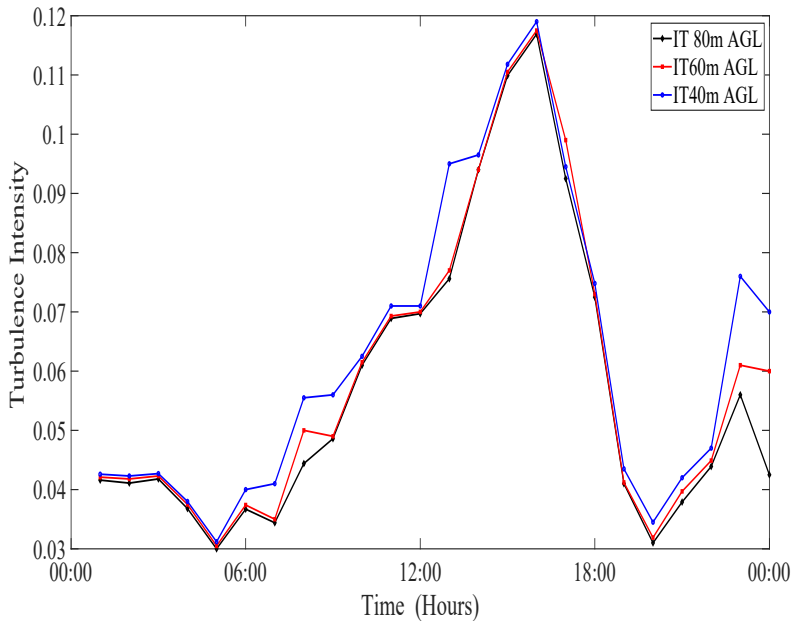
Figure 6.10: Hourly turbulence intensity at 80m AGL for Tower 2

The hourly TI values at 80 m AGL are presented in Fig. 6.10. The higher TI values are observed during the day hours, from 11:00 to 15:00, when the solar radiation reaches its highest value and the wind speed of the anabatic winds is maximum.

The lower values are observed during night hours; when the wind speed of the katabatic winds is lower [15, 57]. Likewise, the monthly TI values at 80 m AGL during 2018 are shown in Fig. 6.11. The TI´s higher values are observed in the winter months when the wind speed is slow. On the other hand, the TI values are observed in the summer months when the wind speed is high. Jeong and Ha [129] stated that wind profile and TI are highly influenced by complex terrain topography such as steeper hills and valleys, which cause wind flow separation. Frost et al. [115] stated that ideal sites for WT sitting are regions with accelerated wind flow, such as mountain passes with high mean wind speed and low TI.
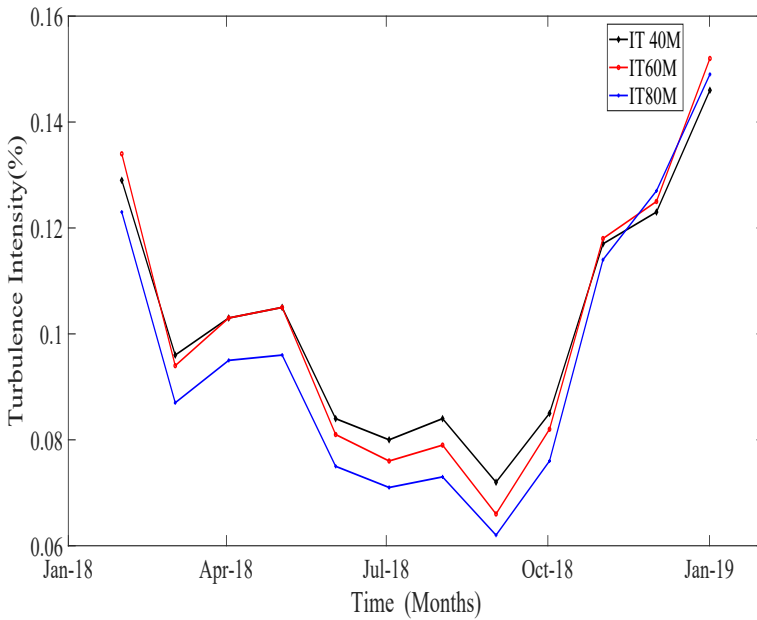
Figure 6.11: Monthly variation of Turbulence Intensity for Tower 2
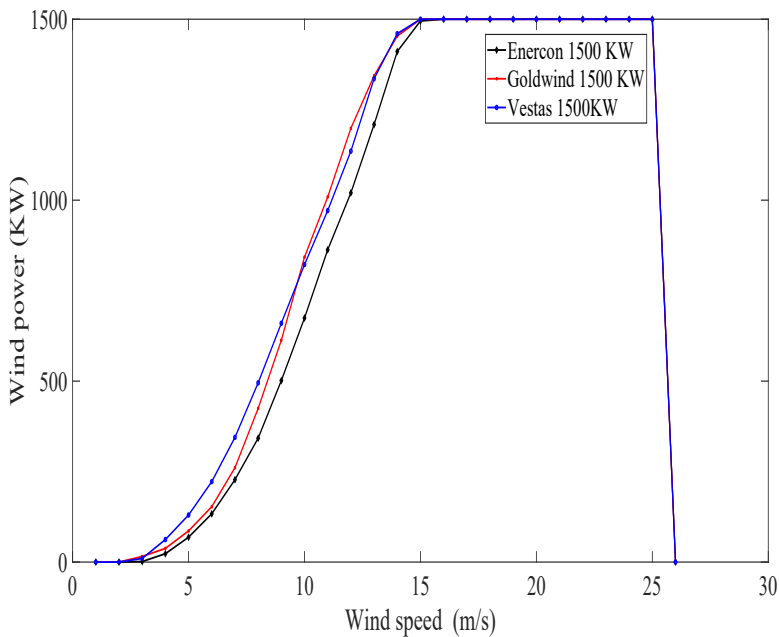
Figure 6.12: Selected wind turbine power curves

6.3 AEP comparison results against Villonaco wind farm

6.3.1 Selection of suitable wind turbines

In this study, the best-suited WT is determined based on annual wind energy production, mean annual WS, and TI class. The selected WT are classified as large-scale and suggested for wind farms in complex terrain [130], which are: Enercon E66/1.5 MW, Goldwind 70/1.5 MW, and Vestas 63/1.5 MW. The selected WT power curves are shown in Fig. 6.12; which were designed from the manufacturers´ web page considering the low air density of the zone of study. In this case, this variable is considered a limitation. It causes a power loss between power start and nominal power compared against power curves obtained with air density at sea level [57]. Table 6.3 summarizes the technical specifications of selected wind turbines. The following aspects were considered when choosing a WT: IEC wind class, power to be installed, hub height, train/generator set, and power output to the grid [19]. Therefore, the comparison of WT power curve results confirms that the best suitable WT for the zone of study is Goldwind 70/1500 suitable choice considered, which is installed at the Villonaco wind farm in Loja, Ecuador [86].

Table 6.3: **Technical data of the 1500 KW class wind turbines**

Wind turbine	Cut-in speed (m/s)	Cut-out speed (m/s)	Rated speed (m/s)	Rated power power (KW)	Rotor diameter (m)	Wind class IEC
Enercon	2.5	25	13	1500	66	IIa
Goldwind	3	25	11.8	1500	70	Ia
Vestas	4	16	25	1500	63.6	Ia

Table 6.4: **Annual energy production and capacity factors**

Wind turbine	Hub height (m)	Nominal power (MW)	Net AEP (GWh/year)	Capacity factor
Enercon	67	1500	6.1	0.46
Goldwind	70	1500	7.24	0.56
Vestas	63	1500	6.2	0.52

6.3.2   AEP and CF estimation

In this work, gross AEP based on PDF Weibull was estimated for three large-scale WT, such as Enercon 66/1500, Goldwind 70/1500, and Vestas 63/1500. The estimated net AEP and its corresponding capacity factors for one selected WT are shown in Table 6.4. Furthermore, the greatest AEP value was achieved with the Goldwind WT. Moreover, the CF analysis for the three types of high-power analyzed wind turbines showed high values. The highest net AEP and CF values were obtained with the WT Goldwind 70/1500 for a hub height of 80 m AGL. A similar pattern of results was obtained for the wind energy assessment for the Villonaco wind farm, located over complex terrain at a high altitude [86].

Then, a hypothetical wind farm with an installed power of 16.5 MW, which is composed of 11 WT Goldwind 70/1500 KW each, with 1.5MW active power achieved values AEP and CF of 42,74 GWh and 0.54, respectively, to compare against the wind energy production of the Villonaco wind farm, which in 2018 supplied 49.73 GWh of gross electric energy and had a capacity factor of 54.95% [86, 131]. The comparison results between real Villonaco AEP and theoretical AEP and CF indicated that theoretical AEP and CF values achieved performances of 85.9% and 98%, respectively.

There are 5 relevant characteristics of the study area to be considered a good wind power area:

1. A high average annual wind speed: the site is located in a wide open valley with no obstructions nearby. It has an annual average wind speed of 10.8 m/s, which is considered excellent for wind turbine operation. Wind turbines generate power proportional to the cube of wind speed.

2. There is at least 10 Km of separation from noise-sensitive neighbors. Furthermore, the selected WT is remarkably quiet, with low noise levels.

3. Reliable grid connection: There is an electric substation located about 30km away to discharge generated energy from the theoretical wind farm to the grid.

4. Easy site access: Because wind turbines of 1.5 MW are large and heavy. The access roads and tracks available are capable of carrying these loads without any risk.

5. No environmental damage or landscape impact: There are now no objections to wind turbine installation because of bird strikes, due to the absence of special bird areas.
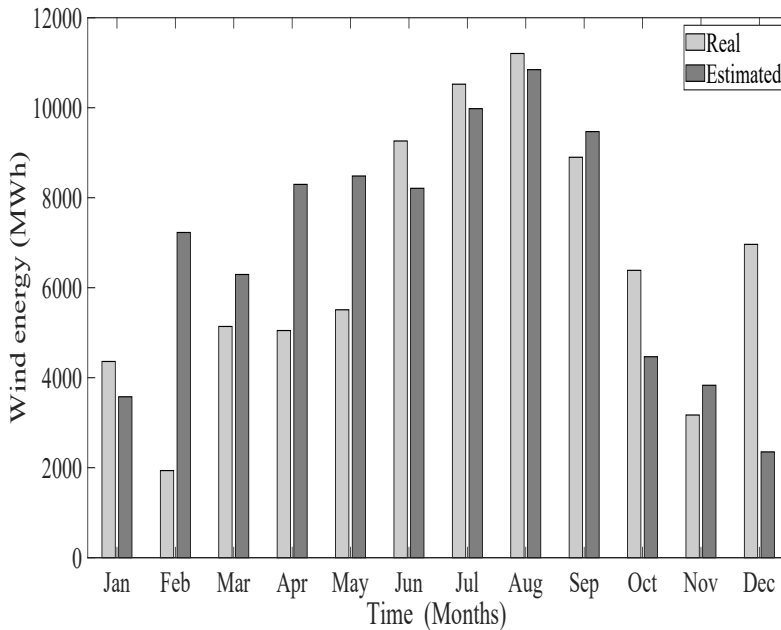
Figure 6.13: Monthly wind energy yield during 2018 using
WT Goldwind 1500

From the above-exposed characteristics, it is clear that the region of study is promising for wind energy projects using high-power wind turbines. Moreover, the evaluation of the feasibility of wind energy projects in the Ecuadorian Highlands must contain an exhaustive economic analysis according to the project requirements accomplish the project requirements, such as estimated AEP, project lifetime, and profitability [37,57].

6.4   Monthly wind energy yield and Capacity Factor estimation

To calculate the monthly estimated wind energy during 2018, it is supposed a hypothetical wind farm of 16.5 MW of installed power. The wind speed at 80 m AGL is considered to estimate monthly gross wind energy; which was compared against monthly net wind energy values from Villonaco wind farm as is shown in Fig. 6.13. The estimated wind energy values were higher than the real values of Villonaco; which were obtained during the winter months. In addition, many factors affect wind farm operation, such as climatic conditions, grid features, and equipment performance [132].
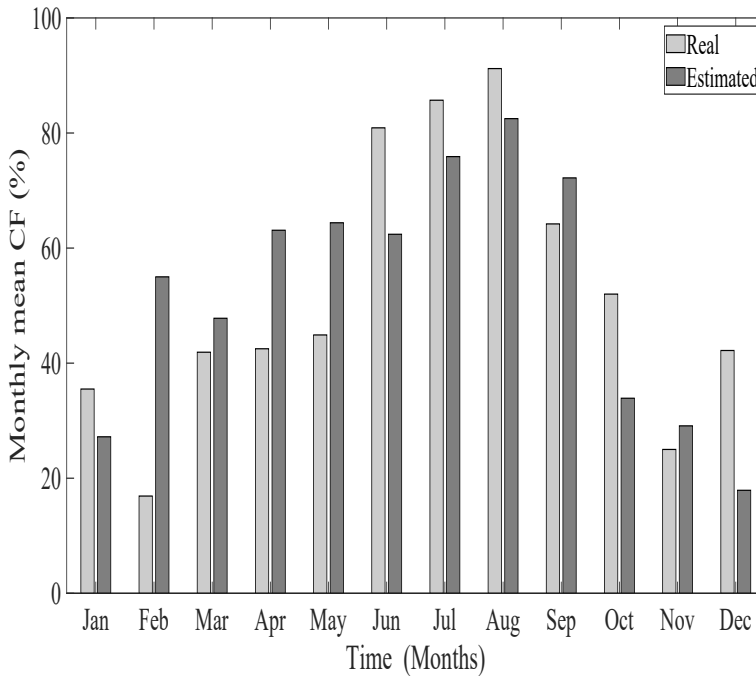
Figure 6.14: Monthly CF during 2018 using WT Goldwind 1500

The mean monthly CFs were calculated by the comparison of the CF Villonaco wind farm against an estimated CF theoretical wind farm, as is observed in Fig. 6.14. The estimated CF is higher than the real CF for the winter months. Furthermore, it is observed that height change increases CF and decreases WSC values at the height of 80 m AGL. A similar pattern of wind energy and higher CF results were obtained by comparing the annual wind energy and CF in 2018 at 80 m AGL against estimated wind energy and CF at an altitude of 2957 m ASL in the Swiss Alps [133].

6.4.1 Conclusions

In this chapter, the results of the evaluation of the wind resource and characteristics of the wind regime in the Ecuadorian Andes have been presented. The following deductions are presented below:

- At 80 meters AGL, the annual wind speed at 80 m AGL is 10.5 m/s due to the wind speed accelerating effects caused by the orography of the complex terrain, and there is low turbulence which is considered A category. The wind speed increases with the change in height, and the TI decreases.

- The monthly wind speed has a high value in summer due to the influence of air masses coming from the Atlantic and the South. In contrast, the monthly wind speed is moderate during winter.

- The monthly WPD value is a function of wind speed; therefore, the highest values are observed in the months of May-August, which correspond to summer. Furthermore, the mean WPD in 2018 in the zone of study is considered high and is equal to 600 W/m^2. Consequently, a hypothetical wind farm of 16.5 MW using 11 WT Goldwind 70/1500 KW was designed to determine the feasibility of wind power generation in this sector. The WT Goldwind 70/ 1500 KW class A, using direct-drive permanent magnet technology, was found to be the best option for these site characteristics.

- Based on the comparison between the estimated AEP and CF of the theoretical wind farm and the actual yields of the Villonaco wind farm in 2018, it can be seen that they achieved ratios close to the actual yields of 77.2% and 94%, respectively. Consequently, the WPD, AEP, and CF of the hypothetical wind farm indicate the feasibility of its construction in the study area in Ecuador's Andes.

Chapter 7

Short-term wind speed, power, and energy forecasting results

This chapter presents the results of the short-term WS, wind power, wind energy over complex terrain in the Ecuadorian Andes, and the cost of forecasted energy in winter and summer are all discussed in four cases. It's worth noting that are reported the results of other studies conducted in similar circumstances worldwide. In the four cases, WS forecasting achieved a lower proportion of forecasting error than other studies worldwide.

7.1 Short-term wind speed forecasting using proposed model

This section presents the results of the short-term prediction of the wind speed in the study area using the proposed hybrid model. For the proposed hybrid model, statistical models served as a baseline for WS forecasting, and DNN-RNN models are used to improve WS forecasting performance.

7.1.1 Comparison of obtained results among forecasting models

The comparison between measured hourly wind speed and forecasted hourly wind speed by using DNN and RNN, such as NARX, NAR, NIO, and LSTM and linear regression models, such as persistence, MA, and ARMA, 12 hours in advance was developed to show the results during the best windy day hours to predict wind speed

for winter and summer at heights of 30m and 80 m AGL. To evaluate the forecasting performance of regressive and DNN models by using four case studies:

7.1.2   Wind speed forecasting in winter

7.1.2.1   Case-study 1 Short-term wind speed forecasting for winter at 30m AGL
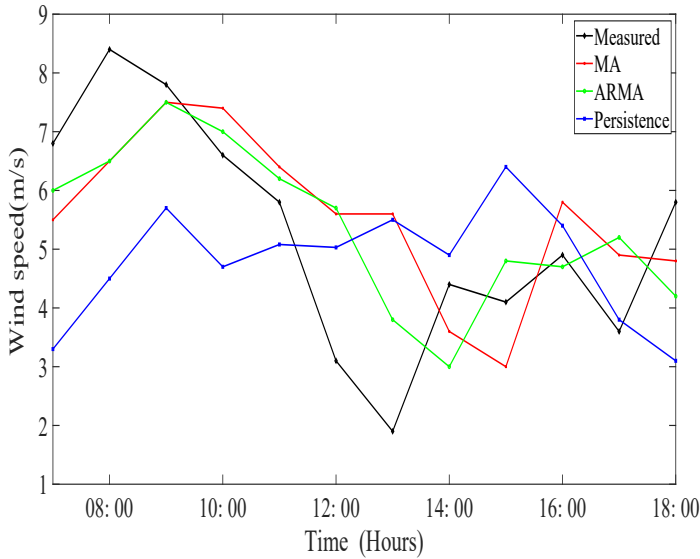
Figure 7.1: Wind speed forecasting in winter on March 05-18 at 30m AGL using linear regression models

     The comparison results for half day in winter at a height of 30m AGL using regressive models and DNN models are presented in Table 7.1; where the highest performance is highlighted in bold and shows that the LSTM network outperforms the other five models reaching a MAPE value of 5.3% during the training phase by using Adam optimizer, learning rate 0.001, and 200 epochs. The graphic sample of the results of linear models is presented in Fig. 7.1; where the ARMA model outperforms better than the other two models by considering p,q values (1,1) and wind speed data from three days ago. Fig. 7.2 indicates a slight improvement in forecasting performance of the LSTM network around 0.9% in MAPE value over the NARX model. These results are beyond previous reports [54], showing a lower RMSE value.
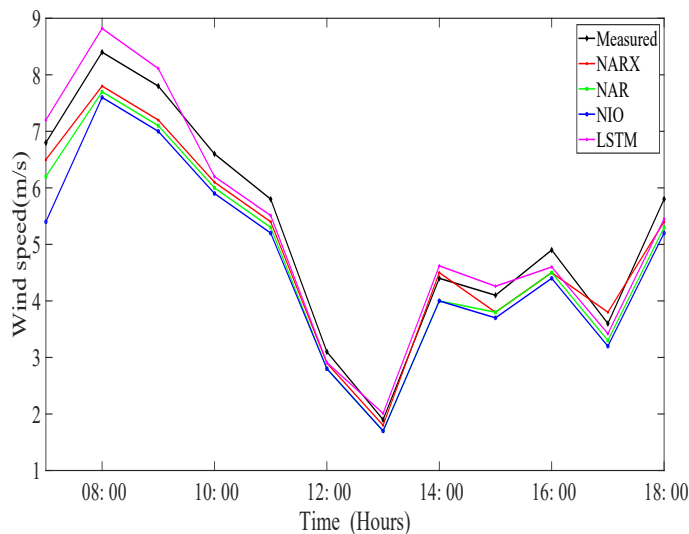
Figure 7.2: Wind speed forecasting in winter on March 05-18 at 30m AGL using DNN models

7.1.2.2 Case-study 2 Short-term wind speed forecasting for winter at 80m AGL

The comparison results for wind speed 12 next hours in winter at a height of 80m AGL using regressive models and DNN models are shown in Table 7.2; where the highest performance is highlighted in bold; which indicates that the LSTM network outperforms the other five models reaching a MAPE value of 4.9% during the training phase by using Adam optimizer, learning rate 0.001, and 300 epochs. The graphic sample of the results of linear regression models is presented in Fig. 7.3; where the ARMA model outperforms better than the other two models by including for (p,q) values (2,1) and wind speed data from three days ago. Figure 7.4 shows a slight improvement in forecasting performance of the LSTM network around 0.9% in MAPE value over the NARX model. A similar pattern of results was obtained by Liu et al. [53].

7.1.3 Wind speed forecasting in Summer

7.1.3.1 Case-study 3 Short-term wind speed forecasting for Summer at 30m AGL

The comparison results for wind speed 12 next hours in summer at a height of 30m AGL using linear regression models and DNN models are shown in Table 7.3; where the

Table 7.1: **Results of simulation process for winter at a height of 30 m AGL**

NN Model	MSE	RMSE	MAPE(%)	R
Persistence	2.5	1.58	41.2	0.52
MA	1.35	1.46	38.3	0.54
ARMA	1.08	1.03	24.9	0.8
LSTM	**0.09**	**0.3**	**5.3**	**0.99**
NARX	0.33	0.61	6.2	0.98
NAR	0.39	0.62	6.4	0.97
NIO	0.4	0.63	6.9	0.98

Table 7.2: **Results of simulation process for winter at a height of 80m AGL**

NN Model	MSE	RMSE	MAPE(%)	R
Persistence	1.5	1.37	25.2	0.55
MA	1.28	1.13	18.3	0.6
ARMA	1.01	1.004	14.9	0.85
LSTM	**0.13**	**0.36**	**4.9**	**0.99**
NARX	0.3	0.3	5.8	0.99
NAR	0.34	0.58	5.9	0.95
NIO	0.65	0.8	8.2	0.98

highest performance is highlighted in bold; where the LSTM network outperforms the other five models reaching a MAPE value of 4.1% during the training phase by using Adam optimizer, learning rate 0.001, and 300 epochs. The graphic sample of the results of linear models is presented in Fig. 7.5; where the ARMA model outperforms better than the other two models by using p,q values (2,1) and wind speed data from three days ago. Fig. 7.6 shows a slight improvement of 0.7% in forecasting the performance of the LSTM network over the NARX model. We found that LSTM networks outperform other models by at least 10% when comparing the results from Wu et al. [134] with our forecasting results.

7.1.3.2 Case-study 4 Short-term wind speed forecasting for summer at 80m AGL

A comparison of linear and RNN models are presented in Table 7.4 for wind speed 12 next hours at an altitude of 80m AGL during winter; the most successful model is highlighted in bold, indicating that with Adam optimizer, the learning rate of 0.001, and 400 epochs. The LSTM network outperformed the other five models, reaching a MAPE value of 4.01% during the training phase. The graphic sample of the results
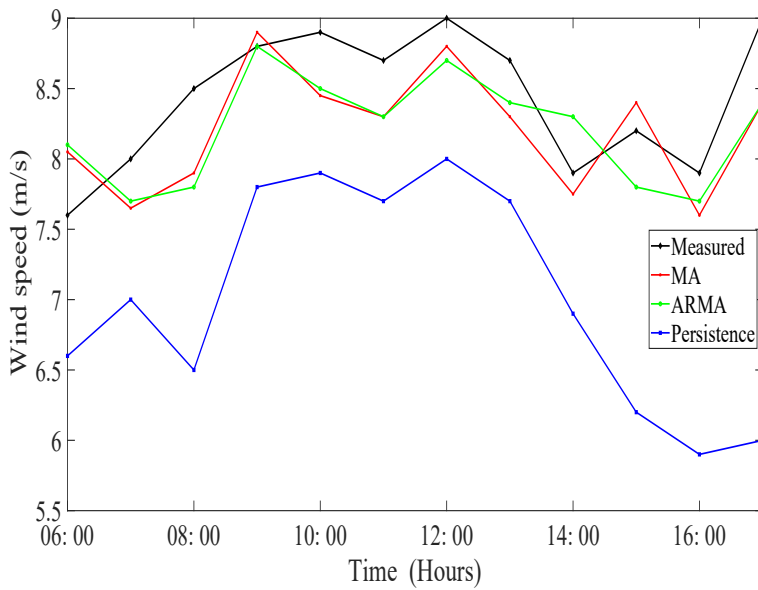
Figure 7.3: Wind speed forecasting in winter on April 05-18 at 80m AGL using regressive models

of linear models is presented in Fig. 7.7, where the ARMA model outperforms better than the other two models by using (p,q) values (2,1) and wind speed data from three days ago. Fig. 7.8 shows a slight improvement of 1.9% in forecasting the performance of the LSTM network over the NARX model. In line with previous studies by Yao et al. [135, 136], where the LSTM network had effective forecasting performance.
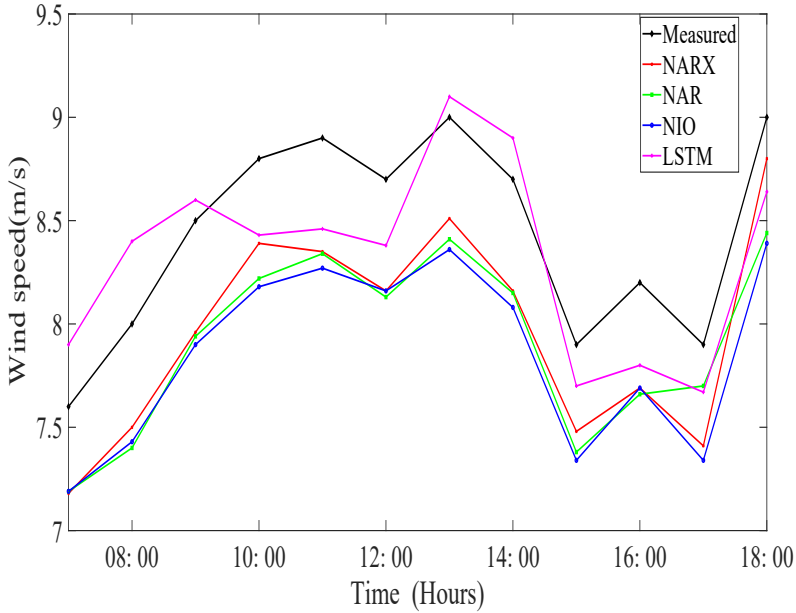
Figure 7.4: Wind speed forecasting in winter on April 05-18 at 80m AGL using DNN models

Table 7.3: **Results of simulation process for summer at a height of 30m AGL**

NN Model	MSE	RMSE	MAPE(%)	R
Persistence	1.9	1.37	23.1	0.55
MA	1.28	1.13	18.3	0.6
ARMA	1.01	1.004	14.9	0.85
LSTM	**0.13**	**0.36**	**4.1**	**0.99**
NARX	0.18	0.33	5.4	0.99
NAR	0.37	0.6	6.1	0.93
NIO	0.37	0.6	6.3	0.94

Figure 7.5: Wind speed forecasting in summer on June 06-18 at 30 m AGL using linear regression models

Table 7.4: **Results of simulation process for summer at a height of 80m AGL**

NN Model	MSE	RMSE	MAPE(%)	R
Persistence	1.5	1.22	20.5	0.57
MA	1.28	1.13	18.3	0.6
ARMA	1.01	1.004	14.9	0.85
LSTM	**0.12**	**0.38**	**3.8**	**0.99**
NARX	0.11	0.56	5.7	0.98
NAR	0.58	0.76	6.6	0.98
NIO	0.41	0.64	7.1	0.97

Figure 7.6: Wind speed forecasting in summer on June 06-18 at 30m AGL using DNN models
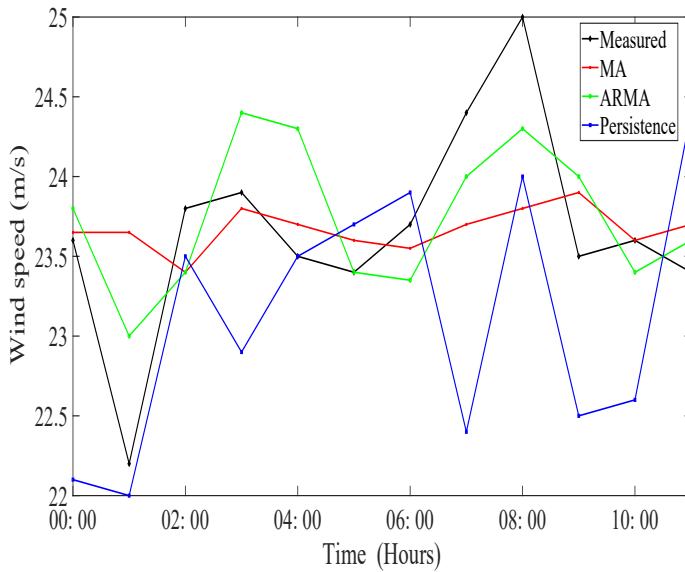
Figure 7.7: Wind speed forecasting in summer on August 08-18 at 80 m AGL using linear regression models

7.2   Short-term wind power and wind energy forecasting

The sixth specific objective of this thesis is to obtain the average hourly wind power and wind energy available for the next 12 hours in the theoretical wind farm for winter and summer.
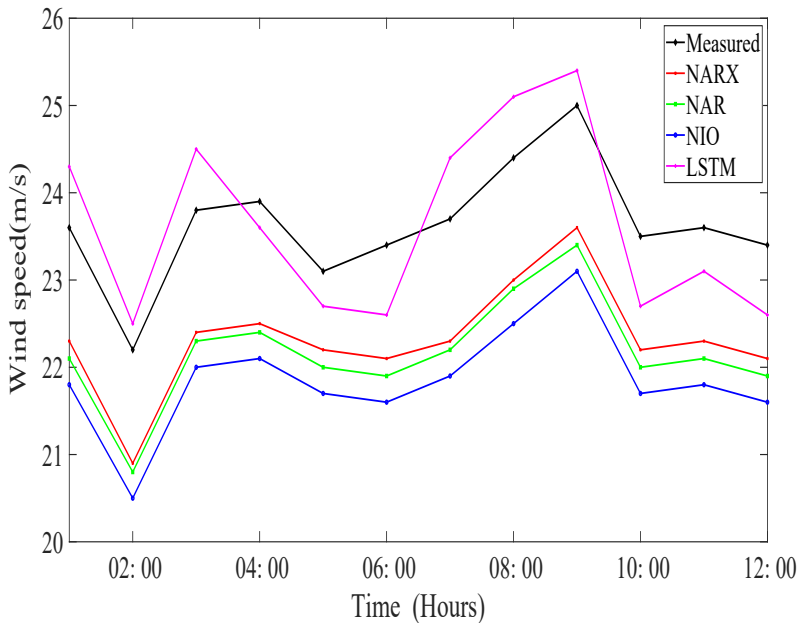
Figure 7.8: Wind speed forecasting in summer on August 08-18 at 80m AGL using DNN models

7.2.1   Forecasting analyzed models

For the prediction of the wind power available at 80 m AGL (hub height) for winter and summer, the following forecasting models were used:

- LSTM

- NARX

- NAR

- NIO

7.2.2   Data available

The data used to make the wind power forecast, considering a horizon of 12 hours in advance for winter and summer. In this case, the wind speed data from the proposed hybrid model at an altitude of 80 m AGL.

7.2.3   Short-term wind power and wind energy forecasting in winter

7.2.3.1   Short-term wind power forecasting

In both cases for winter and summer, 11 WT Goldwind 70/1500 KW were considered in the theoretical wind farm. Their power curve supplied by the manufacturer was adjusted to the air density of the study area as indicated in Figure 6.12, which is used for the conversion of wind speed to gross wind power and by using WS forecasted from Fig. 7.5. The results of the wind power projection for the next 12 hours of the day are shown in Fig. 7.9, with the highest wind speeds corresponding to GSR occurring during this time. These are the real (measured) and DNN model values. The LSTM model predicts values that are better suited to the real value.
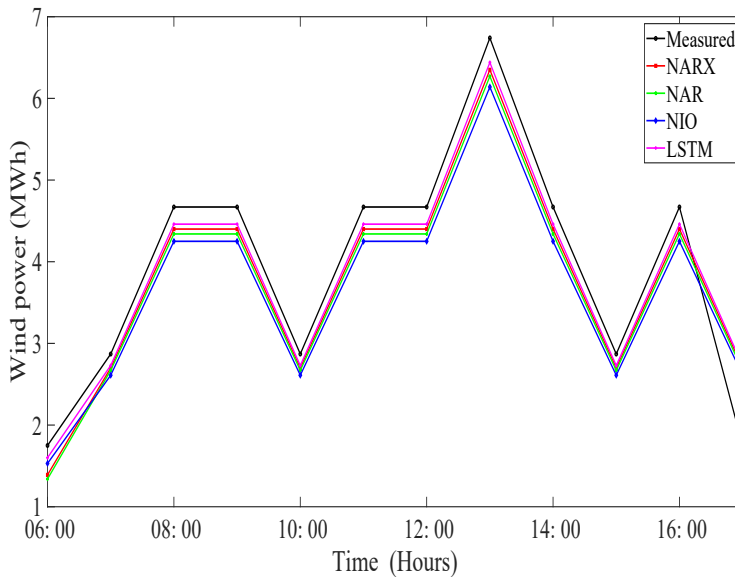
Figure 7.9: Wind power forecasting in winter on April 05-18 at 80m AGL using DNN models

7.2.3.2   Short-term wind energy forecasting

The second proposed goal is to predict electrical energy in a hypothetical wind farm for the next 12 hours. Information on available power and the number of hours of wind speed obtained by the WS bins method from Fig. 7.2. Wind turbine energy generation is determined by the wind turbine's potential and how often the wind blows, or more scientifically, by the wind speed frequency distribution at the site [15,19]. It is possible to calculate the total energy generated over a period of 12 hours in advance by adding up the power generated at all velocities (the actual cut-in speed to the shut-down speed) multiplied by the number of hours where the wind blows at those speeds. For power conversion, the bin method was used to determine the frequency of occurrence of wind speeds within the 12-hour period. The LSTM model has the most predicted gross energy that is closest to the true number as is shown in Fig, 7.10. Table 7.5 outlines the verification of the values used to establish the prediction's accuracy. The LSTM model has reduced RMSE and MSE values of 2.09 and 4.4, respectively.
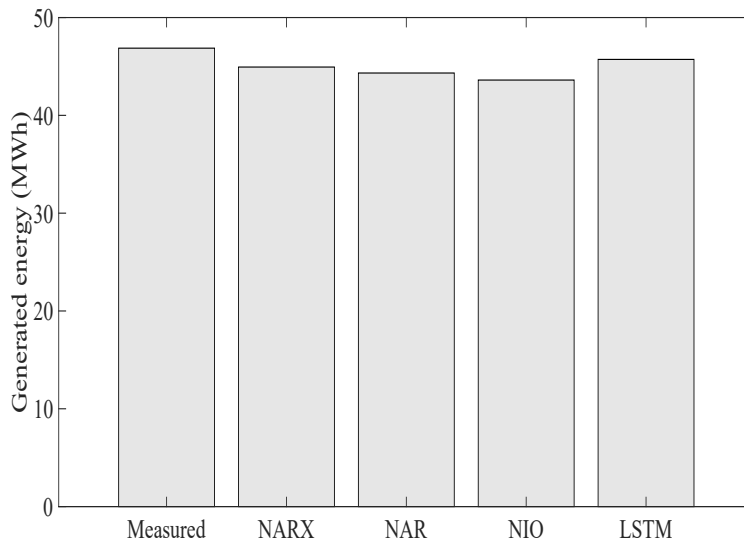
Figure 7.10: Wind energy forecasting in winter on April 05-18 at 80m AGL using DNN models

7.2.3.3   Economic value of electricity forecast

To illustrate the economic benefit of short-term wind energy forecasting for the next 12 hours, we proceed to calculate the cost of wind energy produced on a winter day. Taxes or supplements for reactive power are not considered, nor are the costs for

Table 7.5: **Comparison results among wind energy forecasting for winter at a height of 80 m AGL**

NN Model	MSE	RMSE	Error percentage
LSTM	**4.4**	**2.09**	**6.6**
NARX	7.0	2.6	7.7
NAR	9.4	3.06	8.9
NIO	12	3.46	11.4

secondary regulation as indicated in Fig. 7.11. Where it can be seen that the lowest percentage of error is reached with the LSTM network. Furthermore, CONELEC Regulation 004/11 establishes the energy prices of wind generation at 0.0913 USD/kWh. The validity of the prices will be 15 years from the date of subscription of the qualifying title (2012-12-31) [55].
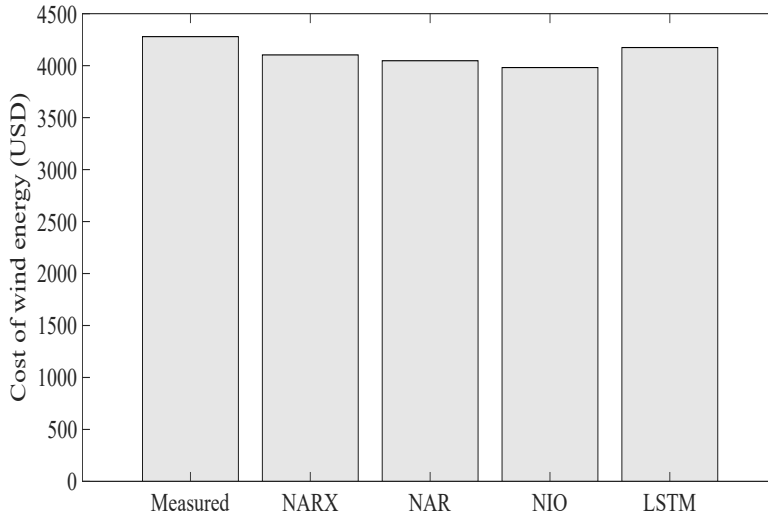
Figure 7.11: Cost of wind energy in winter on April 05-18 at 80m AGL using DNN models

7.2.4 Short-term wind power and wind energy forecasting in summer

7.2.4.1 Short-term wind power forecasting

The power curve adjusted to the air density of the study area, as indicated in Fig. 6.12, was used to convert WS forecasted on August 08-18 at 80m AGL, from 7.8 into wind power. In this particular case, when the nominal power stabilizes, the speeds within the 12 hours are in the range of the nominal speed of 21-25m/s, which is a relevant fact. The maximum power of the WT Goldwind 70/1500 KW is in the region of 15-25 m/s, according to the power curve. After considering the 4 DNN forecasting models, it is estimated that the available power will be a horizontal line with a power of 16.5 MW. By assuming that the 11 WTs Goldwind 70/1500 KW operate at nominal power during the analysis period.

7.2.4.2 Short-term wind energy forecasting

In order to determine the generated wind turbines' energy in summer on August 08-18 at 80 m AGL, from 16.5 MW constant nominal wind power for 11 WTs, which is multiplied by the wind occurrence frequency at the analyzed period of 12 hours. The gross wind energy predicted by each of the 4 models is constant for 4 prediction models reaching a measured and generated energy value of 198 MWh. Based on equal real and predicted electrical energy values. Therefore, the values for RMSE, MSE, and Error percentage in the four prediction models (NARX, NAR, NIO, LSTM) will have a zero value, because there is no difference among them.

7.2.4.3 Economic value of electricity forecast

To demonstrate the economic value of short-term wind energy using the 4 forecasting models over the next 12 hours, we calculate the cost of wind energy produced on a summer day on June 06-18 at 80 m AGL using DNN models, excluding taxes or reactive power supplements, as well as secondary regulation costs. The energy cost will be equal for 4 models considering generated energy (198 MWh), and the cost of wind energy (0.0913 USD/KWh), because the energy value ($ 18.000) is the same for each model.

7.3 Wind characteristics modeling and micro-siting

7.3.1 Wind characteristics on complex terrain

The wind speed map over the computational domain in Zone 1 is shown in Fig. 7.12, which represents the horizontal wind speed of the study area at 80 m AGL, which
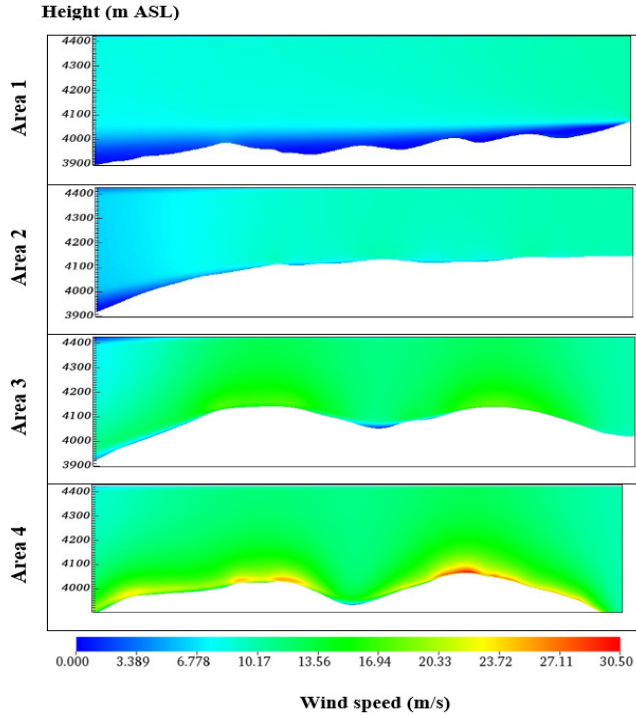
Figure 7.12: Wind speed simulation in zone 1

is similar to the hub height of the selected WT. We determined that the annual mean wind speed (10.8 m/s) at the inlet of the computational domain in four areas of zone 1 would have as an outlet higher WS values on the summit of mountains of 3.3 m/s to 24 m/s due to the wind speed-up effect nearby to measured WS values during 2018. A similar pattern of WS simulation results but with lower WS values was obtained by Solano et al. [137] for the southern mountainous region of Ecuador at heights of 10 and 100 m AGL using the software Surfer 3D.

In this way, it confirms that WS increases and TI decreases with height change [19, 57]. On the other hand, The TI map over the computational domain in Zone 1 is shown in Fig. 7.13, which represents the TI of the study area at 80 m AGL, which is similar to the hub height of the selected WT. TI was simulated values using annual mean WS (10.8 m/s) as WS inlet in four Areas of Zone 1 to have higher TI values on the top of mountains from 0.04 to 0.18 due to the friction of WS against the terrain surface. Consequently, from these results, it is clear that the risks to the WT performance and durability caused by fatigue loads on WT blades could be greatly reduced by assessing the wind characteristics of the WT installation site, such as TI simulation over complex terrain to optimize wind farm layout to keep clear of turbulent flows [129, 138].
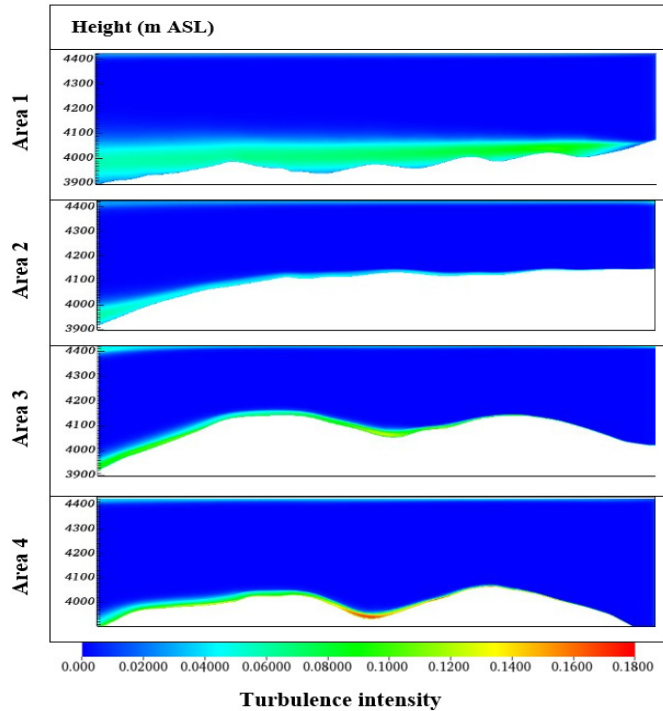
Figure 7.13: TI simulation in Zone 1

7.3.2   Micro-siting of wind turbines of the proposed wind farm

Micro-siting to place 11 WT Goldwind 70/ 1500 KW was performed in three steps for each of the four horizontal areas of Zone 1 as follows: First, we should consider relevant factors such as WT orientation about predominant WD (windward from East), and locating WT on the top of the mountains, considered as wind acceleration areas.

Second, removing WT from highly turbulent flows originated by wakes and vortices from other surrounding terrains of lower height [115, 139].

Third, consider WT row and column separation regulations [119]. Fig. 7.14 shows the layout of the proposed wind farm by considering areas with high active power.

7.3.3   Conclusions

The results of wind speed and wind energy forecasting have been reported in this chapter utilizing the proposed prediction model. Similarly, the results of the wind speed and turbulence modeling have been displayed in a mountain in the study area using the CFD Ansys Fluent software. The main inferences are listed below.
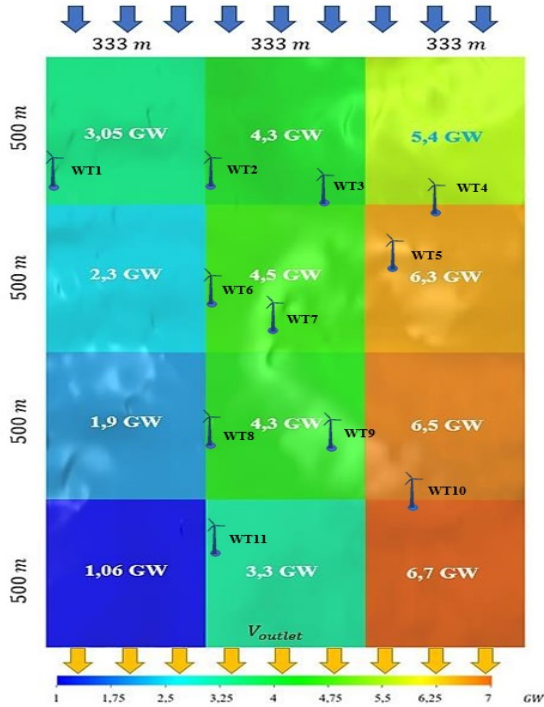
Figure 7.14: WT positions in computational domain Zone 1

- Short-term wind speed prediction was carried out in complex terrain in the Ecuadorian Andes, using the proposed model at heights of 30 m and 80 m AGL. The predictions were developed in 4 cases of study. The prediction results indicate that the lowest values of the MAPE and RMSE indicators were obtained at 80 m AGL using the LSTM recurrent network.

- Short-term wind power prediction was performed in the study area using the WT Goldwind 70/1500 KW, as well as the cost of generated power, using the NARX and LSTM networks at the height of 80 m AGL. The predictions were developed for winter and summer. The results of the predictions with the lowest percentage of error were obtained with the LSTM recurrent network. These results indicate that the most significant amount of energy was produced in summer.

- The simulation of the wind characteristics was carried out using the Ansys Fluent CFD software and the k-epsilon turbulence model. The simulation was performed to determine the micro-siting of the 11 wind turbines. The results indicate that the values of mean speed and intensity of turbulence are very close to the real values.

Chapter 8

Conclusions, main contributions, and future works

8.1 Conclusiones (Spanish)

Esta tesis doctoral ha abordado la Evaluación del Recurso Eólico (WRA), el diseño de parques eólicos con Dinámica de Fluidos Computacional (CFD), y el uso de algoritmos de Redes Neuronales Artificiales (ANN), tales como Redes Neuronales Dinámicas -Redes Neuronales Recurrentes (DNN-RNN), en el contexto de la predicción de la velocidad y potencia del viento en terreno complejo a gran altitud en los Andes Ecuatorianos. La base de datos se basa en las variables climáticas medidas en 2018 por dos torres meteorológicas instalaladas en una zona montañosa de investigación en la Cordillera de los Andes. Los siguientes son los hallazgos más relevantes de este estudio:

1. Las principales características del viento superficial en el paso de viento entre dos volcanes se definen a partir de las variables meteorológicas, la orografía del terreno y el efecto embudo provocado por la aceleración del viento que atraviesa el páramo de El Arenal en los Andes Ecuatorianos. La dinámica atmosférica a gran altura tiene una influencia significativa debido al predominio de una gran cantidad de irradiación solar global (GSR), debido a que el área de estudio se encuentra en la posición geográfica más cercana al Sol, lo que provoca la variabilidad atmosférica en el área.

2. Los valores más altos y más bajos de Velocidad de Viento (WS) corresponden a los meses de verano e invierno, respectivamente. Al hacer una correlación entre la velocidad media anual medida y la estimada en el Atlas Eólico Ecuatoriano,

se obtiene un valor de Raíz del Error Cuadrático Medio (RMSE) de 0,45, lo que representa una variación de 1,5-2 m/s. Por lo tanto, el Atlas Ecuatoriano tiende a subestimar la velocidad del viento en esta región a 80 m sobre el Nivel de la tierra (AGL).

3. El análisis mensual de la velocidad del viento para el 2018 mostró que la velocidad del viento aumenta con el cambio de altura y la Intensidad de Turbulencia (TI) disminuye. Además, los rangos de velocidad del viento fueron más altos en los meses de verano que en los meses de invierno debido a los grandes flujos de aire frío del Sur. De acuerdo con el perfil de la velocidad del viento, el horario de pronóstico debe ser en verano en cualquier momento durante las 24 horas; mientras que en invierno solo durante las horas del día. Cabe señalar que las velocidades de viento disponibles en la zona de estudio para invierno y verano a una altura de 80m AGL pueden ser aprovechadas para generación eólica de alta potencia.

4. La Densidad de Potencia Eólica (WPD) media en 2018 en la zona de estudio se considera alta y es igual a 600 W/m^2. En consecuencia, se diseñó un parque eólico hipotético de 16,5 MW utilizando 11 Aerogeneradores (WT) Goldwind 70/1500 KW para determinar la factibilidad de generación de energía eólica en este sector. El Aerogenerador (WT) Goldwind 70/ 1500 KW clase A, que utiliza tecnología de imanes permanentes de accionamiento directo, resultó ser la mejor opción para estas características del sitio.

5. Se encontró que la Producción Anual de energía (AEP) en 2018 para un parque eólico hipotético que utiliza 11 Aerogeneradores (WT) Goldwind 70/1500 KW tenía alrededor de 75 GWh y un Factor de Capacidad (CF) alto de 0,46, que está más cercano al del parque eólico Villonaco. Por lo tanto, estos valores de AEP son adecuados para la generación de energía eólica a gran escala.

6. El diseño y el posicionado de los 11 aerogeneradores Goldwind 70/1500 KW del parque eólico se desarrollaron utilizando el programa Ansys Fluent CFD. El modelo estándar de Intensidad de Turbulencia (TI) k-ϵ ha sido validado para el flujo de viento sobre terreno complejo a grandes altitudes mediante la comparación de los resultados numéricos obtenidos del programa Ansys Fluent CFD con los datos experimentales disponibles. Los resultados de la comparación entre el modelo de dos ecuaciones k-ϵ y los datos calculados mostraron que el modelo k-ϵ puede predecir la velocidad media y la energía cinética turbulenta están más cerca de los valores medidos.

7. El modelo propuesto para pronosticar la velocidad del viento con seis horas de anticipación, se desarrolló mediante la aplicación de una metodología que incluy el uso de modelos de regresión lineal, como el persistente, Media Móvil (MA) y Auto Regresivo Media Móvil (ARMA) considerados como línea de base para la predicción, en combinación con redes más complejas para mejorar el rendimiento

del pronóstico, como redes con Memoria a Corto Plazo (LSTM) y Redes No lineales con Entradas Exógenas (NARX).

8. Los resultados de la comparación entre los modelos propuestos se desarrollaron utilizando las medidas de pronóstico de errores, como Error Cuadrático Medio (MSE), RMSE, Error Absoluto Medio Porcentual (MAPE) y el coeficiente de correlación (valor R); lo que mostró que el rendimiento del pronóstico de los modelos de regresión lineal utilizados como una línea de base indican valores altos para las medidas de error. Considerando que se alcanzaron mejores resultados de rendimiento de pronóstico utilizando la red LSTM multivariable con una mejora de al menos un 10% sobre la red NARX. Los mejores rendimientos se alcanzaron utilizando el modelo LSTM a una altura de 80 m AGL. Los resultados del MAPE y del coeficiente R para el modelo LSTM indicaron valores para invierno de 4,1 y 99% respectivamente, y para verano de 3,8 y 99% de forma independiente.

9. Se realizó la predicción de la potencia eólica a corto plazo en el área de estudio utilizando el aerogenerador WT Goldwind 70/1500 KW, así como el costo de la potencia generada, utilizando las redes NARX y LSTM a una altura de 80 m AGL. Las predicciones se desarrollaron para invierno y verano. Los resultados de las predicciones con menor porcentaje de error se obtuvieron con la red recurrente LSTM. Estos resultados indican que la mayor cantidad de energía se produjo en verano.

10. El presente estudio es relevante debido a que contribuye a la comunidad científica al brindar resultados novedosos sobre el pronóstico de la velocidad de viento en terrenos complejos en los Andes Ecuatorianos. Las redes multivariable LSTM o NARX utilizadas en esta investigación se pueden aplicar en otros trabajos para pronosticar la velocidad del viento a corto plazo en terrenos complejos. Cabe señalar que hasta el momento no existen trabajos publicados sobre la aplicación de técnicas RNN o DNN para el pronóstico de la velocidad del viento en Ecuador, donde la energía eólica se encuentra en proceso de crecimiento.

8.2 Conclusions, main contributions, and future works

8.2.1 Conclusions

This doctoral thesis has addressed WRA, wind farm design with CFD, and the use of ANN algorithms, such as DNN-RNN, in the context of wind speed and power forecasting over complex terrain at high altitudes in the Ecuadorian Andes. The database is based on climatic variables measured by two meteorological towers installed in a hilly research zone in the Andes Mountains in 2018. The following are the most relevant findings from this study:

1. The main characteristics of the surface wind in the wind pass between two volcanoes are defined based on the meteorological variables, terrain orography, and the funnel effect caused by the acceleration of the wind that crosses the El Arenal moorland in the Ecuadorian Andes. High-altitude atmospheric dynamics have a significant influence due to the predominance of a large amount of GSR because the study area is in the closest geographical position to the Sun, causing atmospheric variability in the area.

2. The higher and lower WS values correspond to the summer and winter months, respectively. By making a correlation between the mean annual speed measured and the one estimated in the Ecuadorian Wind Atlas, an RMSE value of 0.45 is obtained, which represents a variation of 1.5-2 m/s. Therefore, the Ecuadorian Atlas tends to underestimate the wind speed in this region at 80 m AGL.

3. The monthly wind speed analysis for 2018 showed that wind speed increases with the change of height and turbulence decreases. In addition, wind speed ranges were higher in summer months than in winter months because of great cold air flows from the South. According to the wind speed profile, the forecasting schedule should be in summer at any time during 24 hours; whereas in winter for day hours only. It should be noted that the wind speeds available in the zone of study for winter and summer at a height of 80 m AGL can be used for high-power wind generation.

4. The mean WPD in 2018 in the zone of study is considered high and is equal to 600 W/m^2. Consequently, a hypothetical wind farm of 16.5 MW using 11 WT Goldwind 70/1500 KW was designed to determine the feasibility of wind power generation in this sector. The WT Goldwind 70/ 1500 KW class A, using direct-drive permanent magnet technology, was found to be the best option for these site characteristics.

5. The AEP in 2018 for a hypothetical wind farm using 11 WT Goldwind 70/1500 KW was found to have around 75 GWh and a high CF of 0.46, which is closer to the Villonaco wind farm. Therefore, these AEP values are suitable for large-scale wind power generation.

6. The meshing procedure of the two-dimensional CFD numerical simulation.

7. Wind farm design and micrositing were developed using 11 WT Goldwind 70/1500 and Ansys Fluent CFD software. The TI standard k-ϵ model has been validated for wind flow over complex terrain at high altitudes by comparing the numerical results obtained from the Ansys Fluent CFD software with the available experimental data. The comparison results between the k-ϵ two-equation model and calculated data showed that the k-ϵ model can predict the mean velocity and the turbulent kinetic energy that are closer to the measured values.

8. The proposed model to forecast the wind speed six hours in advance was developed by applying a methodology that includes the use of linear regression models,

such as persistent, MA, and ARMA, considered as a baseline for prediction, in combination with more complex networks to improve forecast performance, such as multivariable LSTM and NARX networks.

9. The comparison results among proposed models were developed by using the error forecastings measurements, such as MSE, RMSE, MAPE, and correlation coefficient (R-value); which showed that the forecasting performance of the linear regression models used a baseline indicates high values for error measurements. Whereas, better forecasting performance results were reached using a multivariable LSTM network with at least 10% improvement over the NARX network. The best performances were reached using the LSTM model at a height of 80m AGL. The MAPE and R coefficient results for the LSTM model indicated values for winter of 4.1 and 99% respectively, and for summer of 3.8 and 99% independently.

10. Short-term wind power prediction was performed in the study area using the WT Goldwind 70/1500 KW, as well as the cost of generated power, using the NARX and LSTM networks at a height of 80 m AGL. The predictions were developed for winter and summer. The results of the predictions with the lowest percentage of error were obtained with the LSTM recurrent network. These results indicate that the greatest amount of energy was produced in summer.

11. The present study is relevant due to that contributes to the scientific community by supplying novel results about wind speed forecasting over complex terrain in the Ecuadorian Andes. The multivariable LSTM or NARX networks used in this research can be applied in other works to forecast short-term wind speed over complex terrain. It should be noted that until now there are no published works about the application of RNN or DNN techniques for wind speed forecasting in Ecuador, where wind power is in the growth process.

8.2.2 Main contributions of the thesis

The main outstanding original contributions of the research work carried out in the thesis are the following:

- A novel short-term wind speed prediction model for application to complex high-altitude terrain was developed using regressive models for baseline prediction and DNN-RNN to improve model prediction. The results obtained as wind speed time series for winter and summer allowed the short-term prediction of the following parameters:

  1. Short-term wind power available at hub height 80 m AGL.
  2. Short-term wind power for the proposed wind farm using the wind turbine selected for the study area.

3. Cost of the energy to be produced by the proposed wind farm.

- A novel assessment of wind potential and wind regime characteristics over complex high-altitude terrain in the Ecuadorian Andes was developed using data measured at the site using sensors installed in two meteorological towers located at 30m and 80m AGL. This evaluation allowed us to obtain the error percentage compared to estimates of the wind map of Ecuador developed by NASA using mesoscale and NWP models. The differences between the 2 values are indicated below:

  1. Average annual wind speed at 80 m AGL underestimated by between 1-2m/s.

  2. Average monthly speed in Summer, underestimated by 28.5%, equivalent to a difference of 2 m/s.

  3. WPD at 80 m AGL is undervalued with a 14.2% value corresponding to 100 W/m^2.

  4. WT Golwind 70/1500 power curve adjusted to air density of study area.

- Modeling of wind characteristics in complex high-altitude terrain in the Ecuadorian Andes has been developed for the first time using Ansys Fluent CFD software. To achieve this objective a domain equivalent to the dimensions of a real hill located in the study area has been considered placing as input variables to the computational domain the values of the meteorological variables measured at the site. The results obtained allowed us to obtain simulations of the following wind characteristics:

  1. Accelerating effects of wind speed due to hill effect in summer at 80 m AGL.

  2. Turbulence intensity variation at 80 m AGL.

  3. Micrositing of the 11 WT Goldwind 70/1500 KW that make up the theoretical wind farm on the hill chosen for its high wind potential.

- Improvement in the prediction of short-term wind power obtained at hub height. To achieve this objective, the following alternatives are proposed: Consider the barometric pressure gradient to adjust the power curve to the air density to be used.

- CFD simulations of wind speed and turbulence intensity variations with height on complex terrain have improved. The following options are offered in order to attain this goal: In difficult terrain, take into account atmospheric stability. Consider the temperature difference as a function of altitude. Take into account the terrain's orography.

8.2.3   Future works

Once the wind energy prediction research work on complex terrain at high altitudes is finished, several future lines of research are presented whose main objective is to reduce and improve the prediction of the prediction indicated below:

- Increase the accuracy of the short-term wind speed prediction model over a 6-hour horizon over complex terrain, taking into account the following alternatives:

    1. Using advanced deep learning machine learning algorithms.
    2. Analysis of the influence of atmospheric stability and complex terrain orography on wind speed.

Bibliography

[1] IEA, "Renewables information: Overview," International Energy Agency, 31-35 rue de la Fédération 75739 Paris Cedex 15 France, techreport, Aug. 2019.

[2] GWEC, "Global wind report 2018," Global Wind Energy Council, Rue d'Arlon 80 1040 Brussels, Belgium, techreport, Apr. 2018. [Online]. Available: https://gwec.net/wp-content/uploads/2019/04/GWEC-Global-Wind-Report-2018.pdf

[3] J. Jung and R. P. Broadwater, "Current status and future advances for wind speed and power forecasting," *Renewable and Sustainable Energy Reviews*, vol. 31, pp. 762 – 777, 2014. [Online]. Available: http://www.sciencedirect.com/science/article/pii/S1364032114000094

[4] A. P. Marugán, F. P. G. Márquez, J. M. P. Perez, and D. Ruiz-Hernández, "A survey of artificial neural network in wind energy systems," *Applied Energy*, vol. 228, pp. 1822 – 1836, 2018. [Online]. Available: http://www.sciencedirect.com/science/article/pii/S0306261918311048

[5] G. W. E. C. (GWEC), "Global wind report (annual market update 2017)," Global Wind Energy Council(GWEC), HAMBURG-GERMANY, techreport, 2018.

[6] D. Carvalho, A. Rocha, C. S. Santos, and R. Pereira, "Wind resource modelling in complex terrain using different mesoscale–microscale coupling techniques," *Applied Energy*, vol. 108, pp. 493 – 504, 2013. [Online]. Available: http://www.sciencedirect.com/science/article/pii/S0306261913002705

[7] WWEA, "Global wind installations," Information, Apr. 2020. [Online]. Available: https://wwindea.org/information-2/information/

[8] GWEC, "Global wind report 2019," Global Wind Energy Council, techreport, 2019.

[9] L. Ye, Y. Zhao, C. Zeng, and C. Zhang, "Short-term wind power prediction based on spatial model," *Renewable Energy*, vol. 101, pp. 1067 – 1074, 2017. [Online]. Available: http://www.sciencedirect.com/science/article/pii/S096014811630859X

[10] Y. Noorollahi, M. A. Jokar, and A. Kalhor, "Using artificial neural networks for temporal and spatial wind speed forecasting in iran," *Energy Conversion and Management*, vol. 115, pp. 17 – 25, 2016. [Online]. Available: http://www.sciencedirect.com/science/article/pii/S0196890416300711

[11] T. W. Power, "Vestas v105-3300-datasheet," https://www.thewindpower.net/turbine-es-625-vestas-v105-3300.php, may 2021, accessed 2021-05-02.

[12] G. Sun, C. Jiang, P. Cheng, Y. Liu, X. Wang, Y. Fu, and Y. He, "Short-term wind power forecasts by a synthetical similar time series data mining method," *Renewable Energy*, vol. 115, pp. 575 – 584, 2018. [Online]. Available: http://www.sciencedirect.com/science/article/pii/S0960148117308327

[13] D. Barbosa de Alencar, C. De Mattos Affonso, R. C. Limão de Oliveira, J. L. Moya Rodríguez, J. C. Leite, and J. C. Reston Filho, "Different models for forecasting wind power generation: Case study," *Energies*, vol. 10, no. 12, 2017. [Online]. Available: http://www.mdpi.com/1996-1073/10/12/1976

[14] S. Emeis, *Wind Energy Meteorology Atmospheric Physics for Wind Power Generation*, 1st ed., ser. Green Energy and Technology, Springer, Ed. Institut für Meteorologie und Klimaforschung Karlsruher Institut für Technologie Kreuzeckbahnstr. 19 82467 Garmisch-Partenkirchen Germany: Springer, 2013, iSSN 1865-3537.

[15] L. Landberg, *Meteorology for wind energy*, 1st ed., Wiley, Ed. The Atrium, Southern Gate, Chichester, West Sussex, PO19 8SQ, United Kingdom: John Wiley & Sons Ltd, 2016, iSBN: 9781118913444.

[16] H.-G. Kim, Y.-H. Kang, and J.-Y. Kim, "Evaluation of wind resource potential in mountainous region considering morphometric terrain characteristics," *Wind Engineering*, vol. 41, no. 2, pp. 114–123, 2017. [Online]. Available: http://dx.doi.org/10.1177/0309524X16689445

[17] D. S. Tony Burton, N. Jenkin, and E. Bossanyi, *Wind Energy Handbook*, 1st ed., L. John Wiley & Sons, Ed. John Wiley & Sons, Inc., 605 Third Avenue, New York, NY 10158-0012, USA: John Wiley & Sons, Ltd, 2011.

[18] E. Branlard, *Wind Turbine Aerodynamics and Vorticity-Based Methods*, 1st ed., ser. Research Topics in Wind Energy, J. Peinke, Ed. Gewerbestrasse 11, 6330 Cham, Switzerland: Springer, 2017, vol. 7.

[19] M. C. Brower, *Wind Resource Assessment*, J. W. . S. Inc., Ed. Hoboken, USA: John Wiley & Sons Inc., 2012, vol. 1.

[20] M. Zhang, *Wind resource assessment and micro-sitting*, 1st ed., C. M. PRESS, Ed. John Wiley & Sons, Ltd, 2015, vol. 1.

[21] M. Castro, *Hacia una nueva matriz energética diversificada en Ecuador*, J. Elbers, Ed. Av. Eloy Alfaro N32-650 y Rusia, 3er. Piso. Quito, Ecuador: CEDA, 2011.

[22] MEER, "Plan maestro de electrificación 2012-2021," Av. Naciones Unidas E7-71 y Av. de los Shyris, Quito-Ecuador, Feb. 2013.

[23] G. L. Javier García, Alex Mayorga, "A novel probability density function applied to wind characterization in order to evaluate the wind power potential in tungurahua, ecuador's andean region," *Wind Engineering*, vol. 0, no. 0, pp. 1–24, 2017. [Online]. Available: https://doi.org/10.1177/0309524X18780383

[24] M. Ayala, J. Maldonado, E. Paccha, and C. Riba, "Wind power resource assessment in complex terrain: Villonaco case-study using computational fluid dynamics analysis," *Energy Procedia*, vol. 107, pp. 41 – 48, 2017, 3rd International Conference on Energy and Environment Research, {ICEER} 2016, 7-11 September 2016, Barcelona, Spain. [Online]. Available: http://www.sciencedirect.com/science/article/pii/S1876610216317167

[25] S. T. (Bitsuamlak, A. F, and B. C, "Numerical evaluation of wind flow over complex terrain: review," *Journal of Aerospace Engineering*, vol. 17, no. 4, pp. 135–145, 2004.

[26] S. Ramechecandane and A. R. Gravdahl, "Numerical investigations on wind flow over complex terrain," *Wind engineering*, vol. 36, no. 3, pp. 273–296, 2012.

[27] C. A.-C. Ernesto Arteaga-López and F. Bañuelos-Ruedas, "Advanced methodology for feasibility studies on building-mounted wind turbines installation in urban environment: Applying cfd analysis," *Energy*, vol. 16, pp. 181–188, 2019.

[28] D. Tabas and F. P.-A. Jiannong Fang, "Wind energy prediction in highly complex terrain by computational fluid dynamics," *Energies*, vol. 12, no. 1311, pp. 1–12, 2019. [Online]. Available: https://www.mdpi.com/1996-1073/12/7/1311/pdf

[29] T. Ahmad, H. Zhang, and B. Yan, "A review on renewable energy and electricity requirement forecasting models for smart grid and buildings," *Sustainable Cities and Society*, vol. 55, p. 102052, 2020. [Online]. Available: http://www.sciencedirect.com/science/article/pii/S2210670720300391

[30] I. Colak, S. Sagiroglu, and M. Yesilbudak, "Data mining and wind power prediction: A literature review," *Renewable Energy*, vol. 46, pp. 241 – 247, 2012. [Online]. Available: http://www.sciencedirect.com/science/article/pii/S0960148112001541

[31] K. G. Sheela and S. Deepa, "A review on neural network models for wind speed prediction," *Wind Engineering*, vol. 37, no. 2, pp. 111–123, 2013. [Online]. Available: http://dx.doi.org/10.1260/0309-524X.37.2.111

[32] D. Niu, D. Pu, and S. Dai, "Ultra-short-term wind-power forecasting based on the weighted random forest optimized by the niche immune lion algorithm," *Energies*, vol. 11, no. 5, 2018. [Online]. Available: https://www.mdpi.com/1996-1073/11/5/1098

[33] M. Dadkhah, M. J. Rezaee, and A. Z. Chavoshi, "Short-term power output forecasting of hourly operation in power plant based on climate factors and effects of wind direction and wind speed," *Energy*, vol. 148, pp. 775 – 788, 2018. [Online]. Available: http://www.sciencedirect.com/science/article/pii/S0360544218301919

[34] P. Ramasamy, S. Chandel, and A. K. Yadav, "Wind speed prediction in the mountainous region of india using an artificial neural network model," *Renewable Energy*, vol. 80, pp. 338 – 347, 2015. [Online]. Available: http://www.sciencedirect.com/science/article/pii/S0960148115001342

[35] M. Beccali, M. Cellura, V. L. Brano, and A. Marvuglia, "Short-term prediction of household electricity consumption: Assessing weather sensitivity in a mediterranean area," *Renewable and Sustainable Energy Reviews*, vol. 12, no. 8, pp. 2040 – 2065, 2008. [Online]. Available: http://www.sciencedirect.com/science/article/pii/S1364032107000664

[36] J. Heinermann and O. Kramer, "Machine learning ensembles for wind power prediction," *Renewable Energy*, vol. 89, pp. 671 – 679, 2016. [Online]. Available: http://www.sciencedirect.com/science/article/pii/S0960148115304894

[37] T. M. Letcher, *Wind Energy Engineering*, 1st ed., T. M. Letcher, Ed. 525 B Street, Suite 1800, San Diego, CA 92101-4495, United States: Academic Press, 2017.

[38] L. Lazić, G. Pejanović, and M. Živković, "Wind forecasts for wind power generation using the eta model," *Renewable Energy*, vol. 35, no. 6, pp. 1236 – 1243, 2010. [Online]. Available: http://www.sciencedirect.com/science/article/pii/S0960148109004546

[39] B. Yan and Q. Li, "Coupled on-site measurement/cfd based approach for high-resolution wind resource assessment over complex terrains," *Energy Conversion and Management*, vol. 117, pp. 351 – 366, 2016. [Online]. Available: http://www.sciencedirect.com/science/article/pii/S0196890416301145

[40] O. B. Shukur and M. H. Lee, "Daily wind speed forecasting through hybrid kf-ann model based on {ARIMA}," *Renewable Energy*, vol. 76, pp. 637 – 647, 2015. [Online]. Available: http://www.sciencedirect.com/science/article/pii/S0960148114008155

[41] A. Mosavi, M. Salimi, S. Faizollahzadeh Ardabili, T. Rabczuk, S. Shamshirband, and A. R. Varkonyi-Koczy, "State of the art of machine learning models in

energy systems, a systematic review," *Energies*, vol. 12, no. 7, 2019. [Online]. Available: https://www.mdpi.com/1996-1073/12/7/1301

[42] M. Sharifzadeh, A. Sikinioti-Lock, and N. Shah, "Machine-learning methods for integrated renewable power generation: A comparative study of artificial neural networks, support vector regression, and gaussian process regression," *Renewable and Sustainable Energy Reviews*, vol. 108, pp. 513 – 538, 2019. [Online]. Available: http://www.sciencedirect.com/science/article/pii/S1364032119301807

[43] A. Stetco, F. Dinmohammadi, X. Zhao, V. Robu, D. Flynn, M. Barnes, J. Keane, and G. Nenadic, "Machine learning methods for wind turbine condition monitoring: A review," *Renewable Energy*, vol. 133, pp. 620 – 635, 2019. [Online]. Available: http://www.sciencedirect.com/science/article/pii/S096014811831231X

[44] X. Yuan, Q. Tan, X. Lei, Y. Yuan, and X. Wu, "Wind power prediction using hybrid autoregressive fractionally integrated moving average and least square support vector machine," *Energy*, vol. 129, pp. 122 – 137, 2017. [Online]. Available: http://www.sciencedirect.com/science/article/pii/S0360544217306606

[45] P. Zucatelli, E. Nascimento, G. Aylas, N. Souza, Y. Kitagawa, A. Santos, A. Arce, and D. Moreira, "Short-term wind speed forecasting in uruguay using computational intelligence," *Heliyon*, vol. 5, no. 5, p. e01664, 2019. [Online]. Available: http://www.sciencedirect.com/science/article/pii/S2405844018368087

[46] P. Kim, *MATLAB Deep Learning*, T. Green, Ed. 233 Spring Street, 6th Floor, New York, NY 10013: APRESS, 2017.

[47] K. Philippopoulos and D. Deligiorgi, "Application of artificial neural networks for the spatial estimation of wind speed in a coastal region with complex topography," *Renewable Energy*, vol. 38, no. 1, pp. 75 – 82, 2012. [Online]. Available: http://www.sciencedirect.com/science/article/pii/S0960148111003892

[48] C. M. Matteo Mana, Massimiliano Burlando, "Evaluation of two ann approaches for the wind power forecast in a mountainous site," *INTERNATIONAL JOURNAL of RENEWABLE ENERGY RESEARCH*, vol. 7, no. 4, pp. 1629–1638, 2017. [Online]. Available: https://ijrer.org/ijrer/index.php/ijrer/article/view/6186

[49] E. Cadenas, W. Rivera, and R. C. Rafael Campos-Amezcua, "Wind speed forecasting using the narx model, case: La mata, oaxaca, méxico," *Neural Computing and Applications*, vol. 27, no. 8, p. 2417–2428, 2016, springer. [Online]. Available: https://link.springer.com/article/10.1007/s00521-015-2012-y

[50] Y. Gao and M. J. Er, "Narmax time series model prediction: feedforward and recurrent fuzzy neural network approaches," *Fuzzy Sets and Systems*, vol. 150, no. 2, pp. 331 – 350, 2005. [Online]. Available: http://www.sciencedirect.com/science/article/pii/S0165011404004099

[51] M. Jawad, S. M. Ali, B. Khan, C. A. Mehmood, U. Farid, Z. Ullah, S. Usman, A. Fayyaz, J. Jadoon, N. Tareen, A. Basit, M. A, Rustam, and I. Sami, "Genetic algorithm-based non-linear autoregressive with exogenous inputs neural network short-term and medium-term uncertainty modelling and prediction for electrical load and wind speed," *The Journal of Engineering*, vol. 20, no. 8, pp. 721–729, 2018, eISSN 2051-3305. [Online]. Available: https://ieeexplore.ieee.org/stamp/stamp.jsp?tp=&arnumber=8440878

[52] S. Barja-Martinez, M. Aragüés-Peñalba, Íngrid Munné-Collado, P. Lloret-Gallego, E. Bullich-Massagué, and R. Villafafila-Robles, "Artificial intelligence techniques for enabling big data services in distribution networks: A review," *Renewable and Sustainable Energy Reviews*, vol. 150, p. 111459, 2021. [Online]. Available: https://www.sciencedirect.com/science/article/pii/S1364032121007413

[53] H. Liu, X. wei Mi, and Y. fei Li, "Wind speed forecasting method based on deep learning strategy using empirical wavelet transform, long short term memory neural network and elman neural network," *Energy Conversion and Management*, vol. 156, pp. 498–514, 2018. [Online]. Available: https://www.sciencedirect.com/science/article/pii/S0196890417311056

[54] A. Xie, H. Yang, J. Chen, L. Sheng, and Q. Zhang, "A short-term wind speed forecasting model based on a multi-variable long short-term memory network," *Atmosphere*, vol. 12, no. 5, 2021. [Online]. Available: https://www.mdpi.com/2073-4433/12/5/651

[55] CONELEC, "Resolución 04/11," National Electricity Council (concejo Nacional de Electricidad), techreport, 2011.

[56] Z. Salameh, *Chapter 3 - Wind Energy Conversion Systems*. Academic Press, 2014, pp. 115–199.

[57] J. F. Manwell and J. G. McGowan, *Wind Energy Explained*, 2nd ed., Wiley, Ed. The Atrium, Southern Gate, Chichester, West Sussex, PO19 8SQ, United Kingdom: John Wiley and Sons Ltd., 2009, iSBN 978-0-470-01500-1.

[58] Y. Zhou, M. Wei, Z. Cheng, Y. Ning, and L. Qi, "The wind and temperature information of amdar data applying to the analysis of severe weather nowcasting of airport," in *2013 IEEE Third International Conference on Information Science and Technology (ICIST)*, 2013, pp. 1005–1010.

[59] S. A. G. J.L. Rodríguez Amenedo, J.C. Burgos Díaz, *Sistemas eólicos de producción de energía eléctrica*, 1st ed., F. Rueda, Ed. Porto Cristo, 13, 28294, Madrid-Spain.: Editorial Rueda S.L., 2003, vol. 1.

[60] B. H. Bailey and S. L. McDonald, *Wind resource Assessment Handbook*, 1st ed., NREL, Ed. National Renewable Energy Laboratory 1617 Cole Boulevard Golden, CO 80401: AWS Scientific, Inc., 1997.

[61] R. W. J.J. Sharples, R.H.D. McRae, "Wind characteristics over complex terrain with implications for bushfire risk management," *Environmental Modelling and Software*, vol. 25, pp. 1099–1120, 2010.

[62] S. Pishgar-Komleh, A. Keyhani, and P. Sefeedpari, "Wind speed and power density analysis based on weibull and rayleigh distributions (a case study: Firouzkooh county of iran)," *Renewable and Sustainable Energy Reviews*, vol. 42, pp. 313–322, 2015. [Online]. Available: https://www.sciencedirect.com/science/article/pii/S1364032114008454

[63] T. M. Letcher, *Wind Energy Engineering*, T. M. Letcher, Ed. 125 London Wall, London EC2Y 5AS, United Kingdom: Academic Press, 2017.

[64] S. M., V. C., and V. Kumar, "Current advances and approaches in wind speed and wind power forecasting for improved renewable energy integration: A review." *Engineering Reports*, vol. 12, pp. 1–20, 2020.

[65] G. P. Navarro Diaz, A. C. Saulo, and A. D. Otero, "Full wind rose wind farm simulation including wake and terrain effects for energy yield assessment," *Energy*, vol. 237, p. 121642, 2021. [Online]. Available: https://www.sciencedirect.com/science/article/pii/S0360544221018909

[66] Y. S. R. H. William Corrêa Radünz, A. P. Petry, J. C. Passos, and E. D. Mayara Miqueletti, "Influence of atmospheric stability on wind farm performance in complex terrain," *Applied Energy*, vol. 282, pp. 1–18, 2021.

[67] C. A. . D. M. . L. Michael, "Effect of winds in a mountain pass on turbine performance," *Wind Energy*, vol. 17, pp. 1543–1562, 2014.

[68] B. R. W. William David Lubitz, "Wind-tunnel and field investigation of the effect of local wind direction on speed-up over hills," *Journal of Wind Engineering and Industrial Aerodynamics*, vol. Volume 282, Part A, pp. 639–661, 2007.

[69] M. L. U. Focken, *Physical Approach to Short-Term Wind Power Prediction*, S. verlag, Ed. Springer Berlin Heidelberg: Springer, 2005.

[70] F. Castellani, D. Astolfi, M. Mana, E. Piccioni, M. Becchetti, and L. Terzi, "Investigation of terrain and wake effects on the performance of wind farms in complex terrain using numerical and experimental data," *Wind Energy*, vol. 20, no. 7, pp. 1277–1289, 2017. [Online]. Available: https://onlinelibrary.wiley.com/doi/abs/10.1002/we.2094

[71] K. Murthy and O. Rahi, "A comprehensive review of wind resource assessment," *Renewable and Sustainable Energy Reviews*, vol. 72, pp. 1320–1342, 2017. [Online]. Available: https://www.sciencedirect.com/science/article/pii/S1364032116306918

[72] NRG, "Wind resource assessment," https://www.nrgsystems.com/products/applications/wind-resource-assessment, may 2021, accessed 2021-05-06.

[73] J. S. González, M. B. Payán, and F. G.-L. Jesús Manuel Riquelme Santos, "A review and recent developments in the optimal wind-turbine micro-siting problem," *Renewable and Sustainable Energy Reviews,*, vol. 30, pp. 133–144, 2014.

[74] M. Song, K. Chen, and J. W. Xing Zhang, "Optimization of wind turbine micro-siting for reducing the sensitivity of power generation to wind direction,," *Renewable Energy*, vol. 87, pp. 57–65, 2016.

[75] G. N., *Computational Fluid Dynamics Methods for Wind Turbines Performance Analysis. In: Hu W. (eds)*.   Ithaca, New York, USA: Springer, Cham, 2018.

[76] L. E. B. Cruz and B. S. Carmo, "Wind farm layout optimization based on cfd simulations," *The Brazilian Society of Mechanical Sciences and Engineering*, vol. 42, no. 433, pp. 273–296, 2020.

[77] Y. Yi, G. Ming, and C. S. y J. Xinyang, "New inflow boundary conditions for modelling the neutral equilibrium atmospheric boundary layer in computational wind engineering," *Journal of Wind Engineering and industrial Aerodynamics*, vol. 97, no. 2, pp. 88–99, 2009.

[78] GWEC, "Global wind report 2021," Global Wind Energy Council, Rue Belliard 51-53, 1000 Brussels, Belgium, Tech. Rep., 2021.

[79] WWEA, "World wind energy asociation," 2021. [Online]. Available: https://wwindea.org/worldwide-wind-capacity-reaches-744-gigawatts/

[80] IEA, "Global energy review 2021," International Energy Agency, techreport, 2022. [Online]. Available: https://www.iea.org/reports/global-energy-review-2021

[81] MEER, "Rendición de cuentas 2021," Ministry of Energy and Non-Renewable Natural Resources, techreport, 2022.

[82] M. Ponce-Jara, M. Castro, M. Pelaez-Samaniego, J. Espinoza-Abad, and E. Ruiz, "Electricity sector in ecuador: An overview of the 2007–2017 decade," *Energy Policy*, vol. 113, pp. 513 – 522, 2018. [Online]. Available: http://www.sciencedirect.com/science/article/pii/S0301421517307826

[83] MEER, "Electricity master plan," Ministry of Electricity and Renewable Energy, Quito-Ecuador, techreport ISBN:9789942221537, 2017. [Online]. Available: https://www.celec.gob.ec/hidroagoyan/images/PME%202016-2025.pdf

[84] J. Maldonado-Correa, M. Valdiviezo-Condolo, M. S. Viñan-Ludeña, C. Samaniego-Ojeda, and M. Rojas-Moncayo, "Wind power forecasting for the villonaco wind farm," *Wind Engineering*, vol. 45, no. 5, pp. 1145–1159, 2021. [Online]. Available: https://doi.org/10.1177/0309524X20968817

[85] J. Cevallos-Sierra and J. Ramos-Martin, "Spatial assessment of the potential of renewable energy: The case of ecuador," *Renewable and Sustainable Energy Reviews*, vol. 81, pp. 1154–1165, 2018. [Online]. Available: https://www.sciencedirect.com/science/article/pii/S1364032117311590

[86] CELEC, "Central eólica villonaco (villonaco wind farm)," https://www.celec.gob.ec/gensur/index.php/cev/central-eolica-villonaco-en-cifras-2, May 2019, accessed 2021-06-30.

[87] G. del Ecuador, "Cenace," Operador nacional de Electricidaad, May 2022. [Online]. Available: http://www.cenace.gob.ec

[88] IEA and IRENA, "Wind power technology brief," International Renewable Energy Agency, techreport, Mar. 2016.

[89] A. M. Foley, P. G. Leahy, A. Marvuglia, and E. J. McKeogh, "Current methods and advances in forecasting of wind power generation," *Renewable Energy*, vol. 37, no. 1, pp. 1 – 8, 2012. [Online]. Available: http://www.sciencedirect.com/science/article/pii/S0960148111002850

[90] X. Deng, H. Shao, C. Hu, D. Jiang, and Y. Jiang, "Wind power forecasting methods based on deep learning: A survey," *CMES - Computer Modeling in Engineering and Sciences*, vol. 122, no. 1, pp. 273–301, 2020, cited By 0. [Online]. Available: https://www.scopus.com/inward/record.uri?eid=2-s2.0-85078524155&doi=10.32604%2fcmes.2020.08768&partnerID=40&md5=3f9280a2d77703b9eb365f04ea76a4ec

[91] G. Chang, H. Lu, Y. Chang, and Y. Lee, "An improved neural network-based approach for short-term wind speed and power forecast," *Renewable Energy*, vol. 105, pp. 301 – 311, 2017. [Online]. Available: http://www.sciencedirect.com/science/article/pii/S0960148116311314

[92] J. W. Zack, "Overview of wind energy generation forecasting new york state independent system operator truewind solutions, llc," 2004.

[93] F. Cassola and M. Burlando, "Wind speed and wind energy forecast through kalman filtering of numerical weather prediction model output," *Applied Energy*, vol. 99, pp. 154 – 166, 2012. [Online]. Available: http://www.sciencedirect.com/science/article/pii/S0306261912002747

[94] S. Jung, O. Arda Vanli, and S.-D. Kwon, "Wind energy potential assessment considering the uncertainties due to limited data," *Applied Energy*, vol. 102, pp. 1492–1503, 2013, special Issue on Advances in sustainable biofuel production and

use - XIX International Symposium on Alcohol Fuels - ISAF. [Online]. Available: https://www.sciencedirect.com/science/article/pii/S0306261912006514

[95] O. Rodriguez-Hernandez, O. Jaramillo, J. Andaverde, and J. del Río, "Analysis about sampling, uncertainties and selection of a reliable probabilistic model of wind speed data used on resource assessment," *Renewable Energy*, vol. 50, pp. 244–252, 2013. [Online]. Available: https://www.sciencedirect.com/science/article/pii/S0960148112003540

[96] R. Baker, S. Walker, and J. Wade, "Annual and seasonal variations in mean wind speed and wind turbine energy production," *Solar Energy*, vol. 45, no. 5, pp. 285–289, 1990. [Online]. Available: https://www.sciencedirect.com/science/article/pii/0038092X90900133

[97] S. S. S., Z. Hamidreza, M. Om, and M. Paras, "A review of wind power and wind speed forecasting methods with different time horizons," in *North American Power Symposium 2010*, 2010, pp. 1–8.

[98] P. Jian and J. W. Yun Wang, "Short-term wind speed forecasting using a hybrid model," *Energy*, vol. 119, pp. 561–577, 2019.

[99] L. M. Focken U. and . W. H. P., "Previento-a wind power prediction system with an innovative upscaling algorithm," *In Proceedings of the European Wind Energy Conference,*, vol. 176, 2001.

[100] C. McGowin, "California wind energy forecasting system development and testing. phase 1: Initial testing," *Electric Power Research Institute (EPRI)*, 2003.

[101] M. I., C. E. Cabezón D.and Villanueva J.and Sanisidro M. J.and Loureiro Y., and S. J., "Localpred and regiopred. advanced tools for wind energy prediction in complex terrain." 2003, pp. 16–19.

[102] T. Z. and R. Y. Wang G., "Short-term wind speed forecasting based on autoregressive moving average with echo state network compensation," *Wind Energineering*, vol. 44, pp. 152–167, 2020.

[103] A. K. Palit and D. Popovic, *Computational Intelligence in Time Seies Forecasting: Theory and Engineering Applications*, Springer, Ed.   Springer-Verlag London Limited: Springer, 2005, iSBN 1852339489.

[104] S. Haykin, *Neural Networks*, 2nd ed., P. Education, Ed.   Nueva Delhi 110092 India: Pearson, 2005.

[105] M. Paulescu, E. Paulescu, and V. Badescu, "Chapter 9 - nowcasting solar irradiance for effective solar power plants operation and smart grid management," in *Predictive Modelling for Energy Management and Power Systems Engineering*, R. Deo, P. Samui, and S. S. Roy, Eds.   Elsevier, 2021, pp. 249–270. [Online]. Available: https://www.sciencedirect.com/science/article/pii/B9780128177723000094

[106] P. Gomes and R. Castro, "Wind speed and wind power forecasting using statistical models: Autoregressive moving average (arma) and artificial neural networks (ann)," *International Journal of Sustainable Energy Development*, vol. 1, 12 2012.

[107] H. B. D. Mark Hudson Beale, Martin T. Hagan, *Neural Network Toolbox™ 7 User's Guide*, T. M. Inc., Ed.   MathWorks, 2010.

[108] E. Diaconescu, "The use of narx neural networks to predict chaotic time series," *WSEAS TRANSACTIONS on COMPUTER RESEARCH*, vol. 3, no. 3, pp. 182–191, Mar. 2008, iSSN: 1991-8755. [Online]. Available: https://pdfs.semanticscholar.org/64de/97e26727254d67624c0c92f4d6a3350ae457.pdf

[109] T. Blanchard and B. Samanta, "Wind speed forecasting using neural networks," *Wind Engineering*, vol. 44, no. 1, pp. 33–48, 2020. [Online]. Available: https://doi.org/10.1177/0309524X19849846

[110] E. Loh, S. Ismail, and A. Mustapha, "Bitcoin price forecasting using different artificial neural network and training algorithm," *International Journal of Advanced Trends in Computer Science and Engineering*, vol. 9, pp. 374–378, 01 2020.

[111] S. Hochreiter and J. Schmidhuber, "Long Short-Term Memory," *Neural Computation*, vol. 9, no. 8, pp. 1735–1780, 11 1997. [Online]. Available: https://doi.org/10.1162/neco.1997.9.8.1735

[112] F. R. Ningsih, E. C. Djamal, and A. Najmurrakhman, "Wind speed forecasting using recurrent neural networks and long short term memory," in *2019 6th International Conference on Instrumentation, Control, and Automation (ICA)*, 2019, pp. 137–141.

[113] Metamorf, "Ecuador explorer.com," Ecuador Explorer.com, 1997-2018. [Online]. Available: http://www.ecuadorexplorer.com/html/location_geography_climate.html

[114] MEER, "Atlas eólico del ecuador con fines de generación eléctrica," Ministerio de Electricidad y Energía Renovable, Tech. Rep., 2013. [Online]. Available: https://es.scribd.com/document/355204005/ATLAS-EOLICO-ECUADOR-MEER-2013-pdf

[115] W. Frost and C. F. Shieh, "Wind characteristics over complex terrain relative to wecs siting," *Journal of Energy*, vol. 5, no. 5, pp. 263–269, 1981.

[116] Google, "Google earth," Apr. 2018.

[117] G. D. ECUADOR, "Inamhi," INAMHI2020, May 2017. [Online]. Available: http://www.serviciometeorologico.gob.ec/biblioteca/

[118] G. López and P. Arboleya, "Short-term wind speed forecasting over complex terrain using linear regression models and multivariable lstm and narx networks in the andes range, ecuador," *Renewable Energy*, 2021. [Online]. Available: https://www.sciencedirect.com/science/article/pii/S0960148121015299

[119] IEC, *IEC 61400-12-1*, International Electrotechnical Commission, GENEVA, SWITZERLAND, 2005.

[120] MathWorks, *Mastering Machine Learning, A Step-by-Step Guide with MAT-LAB*, 1st ed., The MathWorks Inc., The MathWorks, Inc. 3 Apple Hill Drive Natick, MA 01760-2098, Sep. 2010. [Online]. Available: https://la.mathworks.com/content/dam/mathworks/tag-team/Objects/m/machine-learning-workflow-ebook.pdf

[121] C. Li, S. Lin, F. Xu, D. Liu, and J. Liu, "Short-term wind power prediction based on data mining technology and improved support vector machine method: A case study in northwest china," *Journal of Cleaner Production*, vol. 205, pp. 909 – 922, 2018. [Online]. Available: http://www.sciencedirect.com/science/article/pii/S095965261832866X

[122] Y. Wang, R. Zou, F. Liu, L. Zhang, and Q. Liu, "A review of wind speed and wind power forecasting with deep neural networks," *Applied Energy*, vol. 304, p. 117766, 2021. [Online]. Available: https://www.sciencedirect.com/science/article/pii/S0306261921011053

[123] C. J. Blocken B, Stathopoulos T, "Cfd simulation of the atmospheric boundary layer: wall function problems," *Atmospheric Environment*, vol. 41, no. 2, pp. 238–252, 2009.

[124] T. A. ATrešnjo Dino and M. M. Torlak Muris, Redzic Elma, *Comparison of CFD and Linear Model When Calculating Maps of Wind Potential at the Location with Complex Topography*. Springer, 2018, vol. 28, pp. 155–169.

[125] J. M. A.D. Griffiths, "Simulations of separated flow over two-dimensional hills," *Journal Of Wind Engineering and Industrial aerodynamics*, vol. 98, no. 3, pp. 155–160, 2010.

[126] R. L. Serra Adalberto, *As Massas de Ar da América do Su*. Río de Janeiro, Brasil: Revista geográfica del Instituto Panamericano de Geografía e Historia, 1960, vol. 51-52.

[127] K. Tar, "Some statistical characteristics of monthly average wind speed at various heights," *Renewable and Sustainable Energy Reviews*, vol. 12, no. 6, pp. 1712–1724, 2008. [Online]. Available: https://www.sciencedirect.com/science/article/pii/S1364032107000342

[128] Gupta, "Weibull parameters for annual and monthly wind speed distributions for five locations in india," *Sol. Energy; (United Kingdom)*, vol. 37:6, 1986.

[129] J.-h. Jeong and K. Ha, "Evaluation of wind flow characteristics by rans-based numerical site calibration (nsc) method with met-tower measurements and its application to a complex terrain," *Energies*, vol. 13, no. 19, 2020. [Online]. Available: https://www.mdpi.com/1996-1073/13/19/5121

[130] IDAE, *Energía Eólica*, Instituto para la Diversificación y Ahorro de la Energía, C/ Madera, 8 , E-28004-Madrid, Sep. 2006.

[131] MEER, "Balance energético nacional 2018," Ministry of Energy and Non-Renewable Natural Resources, techreport, 2018.

[132] M. Abbes and J. Belhadj, "Wind resource estimation and wind park design in el-kef region, tunisia," *Energy*, vol. 40, no. 1, pp. 348 – 357, 2012. [Online]. Available: http://www.sciencedirect.com/science/article/pii/S036054421200076X

[133] B. Kruyt, J. Dujardin, and M. Lehning, "Improvement of wind power assessment in complex terrain: The case of cosmo-1 in the swiss alps," *Frontiers in Energy Research*, vol. 6, p. 102, 2018. [Online]. Available: https://www.frontiersin.org/article/10.3389/fenrg.2018.00102

[134] Y.-X. Wu, Q.-B. Wu, and J.-Q. Zhu, "Data-driven wind speed forecasting using deep feature extraction and lstm," *IET Renewable Power Generation*, vol. 13, no. 12, pp. 2062–2069, 2019, cited By 21. [Online]. Available: https://www.scopus.com/inward/record.uri?eid=2-s2.0-85071246329&doi=10.1049%2fiet-rpg.2018.5917&partnerID=40&md5=480120fba4f04aad25c89decbfb18b18

[135] W. Yao, P. Huang, and Z. Jia, "Multidimensional lstm networks to predict wind speed," vol. 2018-July, 2018, pp. 7493–7497, cited By 20.

[136] G. Abbas, M. Nawaz, and F. Kamran, "Performance comparison of narx amp; rnn-lstm neural networks for lifepo4 battery state of charge estimation," in *2019 16th International Bhurban Conference on Applied Sciences and Technology (IB-CAST)*, 2019, pp. 463–468.

[137] J. Solano, T. Montaño, J. Maldonado-Correa, A. Ordóñez, and M. Pesantez, "Correlation between the wind speed and the elevation to evaluate the wind potential in the southern region of ecuador," *Energy Reports*, vol. 7, pp. 259–268, 2021, 2021 6th International Conference on Advances on Clean Energy Research. [Online]. Available: https://www.sciencedirect.com/science/article/pii/S2352484721004091

[138] L. Roy and D. MacPhee, "Meso-scale cfd simulation for wind resources: A case study of complex mountainous terrain," *Energies*, vol. 11, no. 6, 2018. [Online]. Available: https://www.mdpi.com/1996-1073/11/6/1366

[139] J. W. Qiang Wang, R. Y. Yali Hou, and J. F. Kun Luo, "Simulations of separated flow over two-dimensional hills," *Renewable Energy*, vol. 118, pp. 11 118–1133, 2018.

Appendices

Appendix A

Journal publications

A.1 Short-term wind speed forecasting over complex terrain using linear regression models and multivariable LSTM and NARX networks in the Andes Mountains, Ecuador

Short-term wind speed forecasting over complex terrain using linear regression models and multivariable LSTM and NARX networks in the Andes Mountains, Ecuador

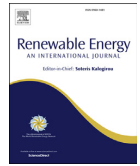Germánico López*, Pablo Arboleya

Department of Electrical Engineering, University of Oviedo, 33203, Gijón, Spain

ARTICLE INFO

ABSTRACT

Wind speed forecasting systems over complex terrain at high altitude are very complex and conventional forecasting systems are unable to be applied due to wind variability. This study proposes an approach developed specifically for this study with application of linear regression models as baseline, and Recurrent Neural Networks (RNN): Long Short Term Memory (LSTM) network, and Dynamic Neural Networks (DNN): Nonlinear Autoregressive Exogenous (NARX) network to perform accurate wind speed forecasting in complex terrain in the Ecuadorian Andes to identify feasible places for wind energy applications. This work starts with the installation of two meteorological stations within of the mountainous zone of study to collect measured variables during 2018. Later on, the measured variables were evaluated by using statistical tools and Pearson Correlation Coefficient (PCC) to determine the input variables. Finally, the proposed forecasting models were trained, validated, and tested by using measured data. The DNN and RNN models were compared to determine the best performance through the statistical error forecast measurements as follows, Mean Absolute Percentage Error (MAPE), Mean Squared Error (MSE), and correlation coefficient. The comparison results of the proposed models indicated that the most precise values were for multivariable LSTM network, suggesting this model as a powerful approach to forecast wind speed over complex terrain, demonstrating the importance by using measured variables. Furthermore, the forecasted wind speed showed high values which are suitable for high wind power generation.

© 2021 Elsevier Ltd. All rights reserved.

1. Introduction

The global demand for energy coming from fossil fuel had a significant annual growth tendency in 2018 [1]. Fuel combustion produces hazard emissions that causes environmental damage as global warming [2,3]. To mitigate this effect and reduce conventional fuel dependence; it is important to use renewable energies available in their different forms. According to Organisation for Economic Co-operation and Development (OECD) the proportion of renewable energy in total primary energy supply for 2018 reached a new high of 10.2% [1]. Wind energy has become one of the most relevant forms of renewable energy [4–6]. By the end of 2019, it reached a global installed wind power capacity of 651 GW, with

60.4 GW of newly installed power, with an increase of 10% compared to 2018 [7,8]. It is expected to reach a total installed power of 840 GW by 2022. The global distribution of wind power in 2017 was as follows: Africa 4.52 GW, Asia 228.6 GW, Europe 177.5 GW, North America 150.3 GW, Pacific Region 5.1 GW, Latin America, and Caribbean 17.2 GW [2,5]. However, it is difficult to integrate renewable generation into the power grid either temporally or spatially [9,10].

Wind energy have have a rapid growth last two decades [2,4,7]. It is growing at exponential rate due to depletion of operation, maintenance costs, and increase of wind turbines reliability [2]. Whereas, the major problem of introducing wind energy into the power grid is the variability and intermittence of the wind; which is one of the main barriers faced by power system operators [3,7]. Accurate forecasting tools are required to solve this problem, directed to principal objectives of planning wind turbine schedule, cut down power system operation cost and reduce its fluctuation [11,12].

* Corresponding author.
E-mail addresses: UO260514@uniovi.es, lopezgermanico51@gmail.com (G. López), arboleyapablo@uniovi.es (P. Arboleya).

In Ecuador renewable energy represents a high percentage of the total installed generation system around 8762 MW. Renewable energy sources are composed the most of hydropower; which represents 53.31% of total installed power, it is expected to become 5100 MW by March 2021 [14,15]. Wind power with a installed power of 21.15 MW holds the lowest proportion around of 0.26% of total installed generation systems [14–16]. In addition, Ecuador has not still exploited its full wind gross potential of around 1670.96 MW. Loja and Galapagos are leading in onshore wind farms [17]. The National Electricity Council (CONELEC) published in 2013 the Ecuadorian Wind Atlas developed by NASA based on Numeric Weather Prediction (NWP) models. This Atlas estimated wind potential around of 1670.8 MW at 80 m above ground level (AGL) [17]. Therefore, wind speed range is from 10 to 25 m/s and wind power density range from 250 to 600 W/m^2, which are classified as superb according to NREL [18].

Wind over complex terrain is mainly influenced by land topography and elevation [18]. In this way, wind flow passing over topographical variations, such as mountain tops, ridges, escarpments, and channel pits in mountain ranges cause wind speed acceleration and turbulence [19,20]. Turbulence are fluctuations in wind speed on a relatively fast time scale, generally less than 10 min. It is generated by two main causes: (1) friction of wind speed with the surface of the earth, which cause wind flow disturbance, (2) thermal effects caused by variations in air temperature and density; which cause vertical movements in the air masses [21,22]. It should be noted that wind speed increases with height above ground and there is a great wind potential in the mountainous regions. In particular, between the Andes volcanoes Chimborazo 6263 m Above Sea Level (ASL) and Carihuayrazo (5116 m ASL); where wind speed increases its speed and reduces pressure named tunnel effect as is shown in Fig. 1 [21,23,24].

The community of Mechahuasca located within of the zone of study, was the selected place because of its high wind potential, which requires to be assessed for wind energy applications [14,17]. Near to this location, García et al. [25] studied the influence of sampling rate on wind power density for these communities in the highlands of the Ecuadorian Andes, and proposed a Probability Density Function (PDF) based on the daily Gaussian average of sinusoidal wave forms. Additionally, Ayala et al. [26] estimated the wind energy in Villonaco wind farm located in complex terrain at high altitude (2700 m ASL). The results were annual wind speed of over 10 m/s, and a capacity factor of 0.53.

Regardless of studies about wind power assessment in complex terrain in the Ecuadorian Andes. Nowadays, there is not a work about wind speed and power forecasting. Consequently, it appears a need to develop an accurate model to forecast wind speed. To reach this objective a technique based on uni-variable regressive models, such as persistence model, MA, and ARMA; which are considered a base line for wind speed prediction; to improve the forecasting performance are employed complex RNN, such as a deep learning algorithm known as multi-variable LSTM network, and DNN models using a NARX model through measured meteorological variables are going to be used. The authors present a novel application of linear regression models, LSTM network and NARX model to predict short-term wind speed in a mountainous region of the Ecuadorian Western Andes to identify feasible places for wind farm installation considering wind shear profile. The main contribution of this paper is twofold: (1) The proposed model sets out to develop one important step further on wind speed behavior over complex terrain using the LSTM and NARX models. (2) The results of the proposed model for wind speed forecasting represents a relevant contribution to the scientific research due to no available previous studies in Ecuador and worldwide. This paper is structured as follows: Section 2; presents a background of wind speed and power forecasting by using Artificial Neural Networks (ANN). Section 3; describes the area of study in the Highlands and used methodology. Section 4; presents the comparison results and discussion of the proposed forecasting models. Section 5; shows the corresponding forecasting results and discussion. Section 6; exposes main conclusions and further directions.

2. Literature review

Nowadays, wind speed forecasting methods are very relevant due to fast propagation of wind power generation worldwide for wind characterization, resource evaluation, and wind power forecasting [27,28]. Accurate wind and power forecasting methods are required to reduce forecasting errors in wind power generation considering wind uncertainty and advances on wind energy conversion systems [3,4]. The accuracy of prediction of wind speed forecasting results are affected by two main aspects as: selection of input variables and forecasting methods [3].

Regarding to input variables selection to be used in wind speed forecasting have reached great relevance because wind power generation and wind farm planning are influenced by wind speed
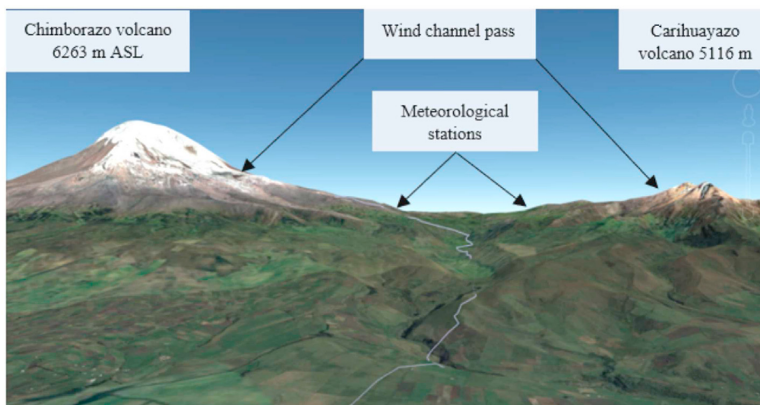

Fig. 1. Area of study in the Andes Range [13].

[7,35]. Wind speed and power forecasting depends on meteorological variables, such as wind direction, barometric pressure, temperature, humidity, and others [12,29,36]. Among climate factors that change according with the geographical position, wind speed is the most relevant [30,37]. Ramasamy et al. [38] proposed an Artificial Neural Networks (ANN) model to predict wind speed using measured wind data of Hamirpur. The MAPE and correlation coefficient achieved in prediction of daily wind speed were 4.55% and 98% respectively. Beccali et al. [39] stated a forecasting model by using Elman network and weather variables for short time household electricity consumption. The forecasting results had an accuracy of 97% and average percentage error of 3.1%.

Respect to forecasting methods by using time horizon, wind power is represented by its instability and intermittence because of the complex physics of the atmosphere [19,22,40]. To integrate variable wind energy into electrical grid are required integrated transmission systems for wind turbines operation and accurate forecasting tools, with weather forecasting included [41–43]. In addition, the expected demand is required in hourly intervals in the energy markets at least one or two days ahead [44]. Wind power forecasting is the estimation of wind conditions based on wind data available, and topographical and meteorological variables of a place [24,45]. Wind speed and power prediction with great quickness and precision, to integrate into the power system are the principal objectives of wind speed and power forecasting [3,44]. The classification of wind speed forecasting according to time horizon and its main applications is listed in Table 1.

The forecasting methods are classified in five groups as follows: wind speed and power forecasting, spatial correlation forecasting, regional forecasting, probabilistic forecasting, and offshore forecasting [3]. To increase accuracy of the forecasting methods have been accomplished various wind speed and power forecasting approaches, including physical, statistical, and artificial intelligence for renewable energy systems [22,46,47]. Moreover, the energy efficiency, energy control and stability in the energy demand prediction in renewable energy systems have been improved with the application of machine learning techniques [48]. These techniques have been used with quick development from many years ago in modelling, design, and prediction of energy systems [35,48]. These approaches have been adopted worldwide to evaluate wind power performance and to acquire relevant information for application in wind power generation systems [49–51]. In wind energy systems are found 10 groups of machine learning algorithms, such as ANN, MLP, ELM, SVM, WNN, ANFIS, decision trees, deep learning, ensembles, and advanced hybrid models with great acceptance in wind energy systems [48]. The ANN models according to the application can be classified in four main categories, such as forecasting and prediction, prediction and control, design optimization, fault detection and diagnosis [4]. In South America, Zucatelli et al. [52] performed a short-term wind speed forecasting model for Colonia Eulacio, Uruguay for one year, by applying an ANN technique. The results showed good accuracy for heights tested and optimal wind speed forecasting with low computational cost. Recent studies show that the forecasting accuracy decreases after 6 h time horizon and the MAPE increases to around 15% [35,37,53]. In recent years, it has occurred a growing interest to research wind

speed, wind power modelling and forecasting in complex terrain because wind speed increases on top of hills and mountains to be exploited by wind turbines [24,46]. For this reason has been developed many research works dedicated to improve wind power forecasting performance. The wind power assessment in complex terrain must be done carefully considering morphological features [6,54], and unstable weather regimes to install wind turbines in a mountainous region [3]. Feed forward Neural Networks (FNN) were used to predict hourly wind speed in a coastal region with complex topography. To increase ANN accuracy was used a wind vector incorporated variability [34]. Mana et al. [55] proposed two models ANN pure and a hybrid ANN-CFD to forecast wind power in very complex terrain in Italy. The two methods had similar performances. However, the hybrid model showed better performance in low and high wind speed range. Tabas et al. [56] analyzed Computational Fluid Dynamics (CFD) technique to forecast wind power in complex terrain. It was stated the combined presence of three complex factors: topography, heterogeneous vegetation, and interactions between wind turbine wakes.

In order to make a more accurate wind speed forecasting using real data measured in complex terrain located at high altitude. This study proposes wind speed forecasting with great accuracy by using NARX network used until now by few researchers as follows: Cadenas et al. [57] generated a model to forecast short term wind speed in Mexico by using NARX model and compared with NAR and persistent models. The results indicated that NARX model had a performance of 4% over the NAR and 11% over the persistence model. Gao and Er [58] proposed a NARMAX time series model prediction using FNN and RNN as approaches to improve the performance of the NARX model. Hence, comparative studies demonstrated that FNN approach can learn complex temporal sequences in a flexible way. Jawad et al. [59] developed a GA-NARX model to predict short term or medium term wind power and electrical load. The results showed good accuracy for short-term wind speed forecasting.

In recent studies, according to technological advances in machine learning. Therefore, new deep learning algorithms have been designed and widely used for times series prediction. Among these algorithms the LSTM networks part of RNN are used for accurate wind speed forecasting results [60]. Liu et al. [61] proposed a deep learning strategy for multistep wind speed forecasting based on EWT to disintegrate original data, LSTM to predict low frequency data, and Elman networks to predict high frequency data. The results of the proposed model indicated good forecasting performance. Xie et al. [62] presented a shor-term wind speed forecasting model based on Auto Regressive Mean Average (ARMA) and multivariable LSTM network by using meteorological variables data in Beijing. The results showed feasibility in forecasting and LSTM superiority over ARMA and simple variable LSTM. These samples of LSTM studies show good feasibility for prediction; as well as to consider in this study this algorithm as a good option to improve the wind speed forecasting performance.

From literature above reviewed it is observed that have not been reported studies about wind speed forecasting by using LSTM or NARX models over complex terrain located at high altitude in the Western Ecuadorian Andes. The present work improves on the

Table 1
Classification of wind speed forecasting [29].

Categories	Time horizon	Applications
Very short term	Few seconds to 30 min	Wind turbine control and load tracking [30]
Short term	30 min to 6 h	Wind speed forecasting and Wind turbines power prediction [12,31]
Medium term	6–24 h	Power system management and energy trading [12,32]
Long term	1–7 days	Wind turbine maintenance program [33,34]

previous ones on the fact that it is the first in predicting wind speed at the highest altitude reported so far (4428 m ASL); as well as using RNN and DNN models in place of hybrid models. The LSTM and NARX networks have been developed using measured data instead of using climatic models. Furthermore, it is validated by using DNN instead of hybrid models using wind speed measurements closer to the hub height of high power wind turbines. From this point of view, this study is unique, and the conclusions obtained of the setup wind speed forecasting method can be useful for other researchers to forecast wind speed in mountainous terrains at high altitude.

3. Methodology

This section presents the characteristics of the area of study, as well as wind speed forecasting features, such as proposed forecasting models, forecasting process, forecasting optimization techniques. Furthermore, the fundamentals of the proposed forecasting models: linear regression, DNN and RNN are given here; in addition forecasting process for each model.

3.1. Area of study

The country of Ecuador is composed of four regions as: Coast, Highlands or Sierra, East or Amazon, and Galapagos Islands. The topography of Highlands is marked by the snow-capped peaks of the Andes mountains [63]. The province of Tungurahua is located within of the highlands between the Eastern and Western Andes

Range; which are traversing the country from North to South in two parallel ranges [Fig. 2] [63]. The zone of study is located in Tungurahua, within a mountainous area in The Andes Western Range [63]. It is composed of valleys, plateaus, hills (3000 m—4500 m ASL) and snow peaks (5000m—6263m ASL), within a mountainous area of 220 Km^2 [13]. This region has two climatic stations winter from December to May; summer from June to November. The high elevation terrain shows moderate snow fall in winter and strong winds in summer. The total annual rainfall varies from 2000 to 2500 mm. The average summer temperature changes from 3°C to 7°C and winter temperature varies from − 3°C to 2°C [64]. The orography of the complex terrain on the western range cause large and temporal variations as mountain and valley breezes which are similar to anabatic and katabatic winds, but smaller in scale [18,21,23].

3.2. Data collection

Two meteorological stations were installed within the zone of study. The station 1 at a height of 30m AGL was installed in the community of Mechahuasca as is shown in Fig. 3 and the station 2 at a height of 80m AGL was installed close to Chimborazo volcano. The geographic coordinates and land elevation of both towers are detailed in Table 2. The main objective of data collection is to save that measured data are available to make data analysis and to protect data from damage or loss [23]. The collected data are from January 15th, 2018 to January 15th, 2019 according to IEC 61400 12-1 [65]. The measured parameters to forecast the future value of
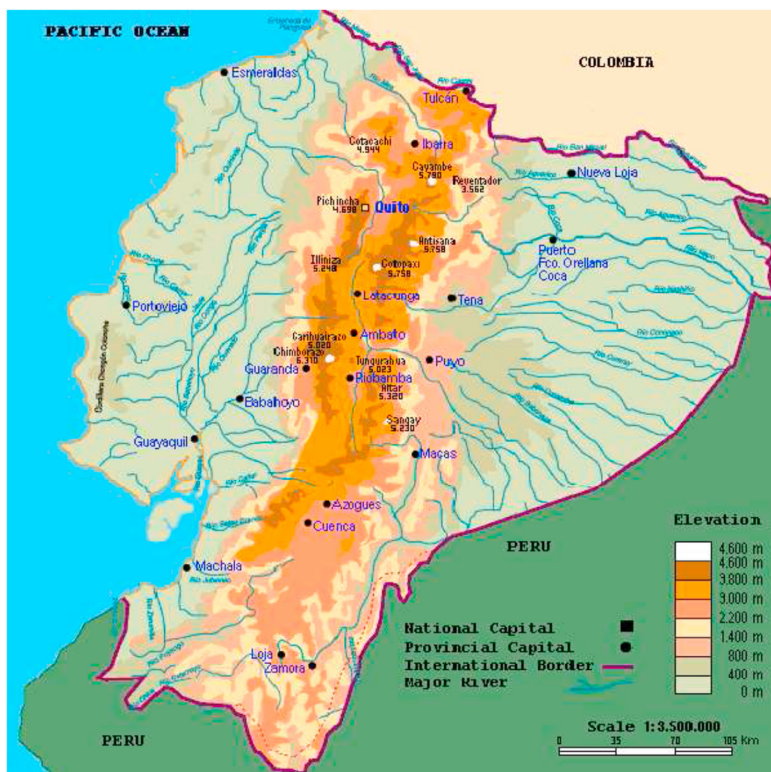

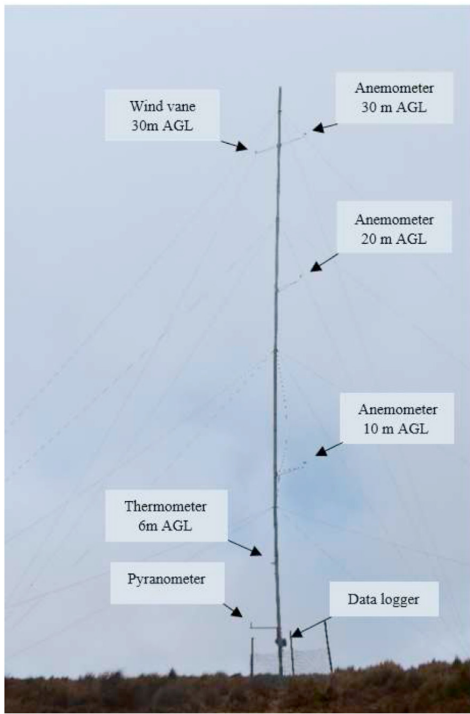**Fig. 2.** Orographic map of Ecuador [63].

Fig. 3. Meteorological station 1 in the community Mechahuasca.

wind speed are the following:

- AVGTEMP Average air temperature (°C)
- ATPRES Atmospheric pressure (millibars)
- GSR Global solar radiation (W/m^2)
- WD wind direction (°)
- WSAVG Wind speed average (m/s)
- WSMAX Wind speed maximum (m/s)
- WSMIN Wind speed minimum (m/s)

This study is focused in wind speed characterization and forecasting in the Ecuadorian Andes. To get this purpose are considered data from two meteorological stations, which are property of the Technical University of Ambato, and Ministry of Electricity and Renewable Energy (MEER) respectively. The meteorological sensors and its features installed on the two stations to measure weather variables are listed on Table 3. The daily variations of wind speed average measured at heights of 30m and 80m AGL during 2018 are shown in Fig. 4. It is observed higher average wind speed in station 2 than station 1; due to that station 2 is installed at a height of 80m AGL. It confirms that wind speed increases with terrain height [23,24].

Table 2
Geographic coordinates of meteorological stations.

Parameter	Station 1	Station 2
Latitude	1°54′S	1°54.8′S
Longitude	79°15′W	78°45.6′W
Elevation	4350 m ASL	4428 m ASL

Table 3
Sensors installed on both meteorological towers.

Type	Model	Range	Deviation
Anemometer	NRG #40C	$1ms^{-1}$-$96ms^{-1}$	± 0.5%
Vane	NRG 200P	0-360°	± 1%
Barometer	NRG BP20	15 KPa-115KPa	± 1.5%
Thermometer	NRG 110S	−40° to 95.5°C	± 1.3%
Pyranometer	LI 200R	400−1100 nm	± <10μV

3.3. Proposed linear regression forecasting models

This subsection presents the fundamentals of the mathematical formulation of the regressive models used as reference in this paper for wind speed forecasting studies, such as persistence, Moving Average (MA), and Auto Regressive Moving Average (ARMA).

3.3.1. Persistence model

The persistence model is considered as the easiest to make a prediction; by considering that the present time will be equal to time forecasted [66]. Furthermore, this model has been widely used by researchers in wind power forecasting as baseline to make comparisons against this model [67]. Moreover, this model has a good performance when the weather variables have a slight variation, and the forecasting time does not exceed more than 1 h [57].

Considering a time series Y_t, knowing its historical data set H_t, forecasting of the future values, through a persistence process is given in Equation (1).

$$H_t = H_t + 1, H_t + 2, ..., H_t + n \qquad (1)$$

Specifically, forecasting of the oncoming value will be shown in Equation 2

$$H_t = Y_t - n \qquad (2)$$

In this study the wind speed at the moment n will be equal to the wind speed 12 similar hours of the previous day.

3.3.2. MA model

This approach is often used to modelate univariate time series. In this model, a certain observation is conditioned by the random impulses of the previous observations. In this way, the current observation is defined as the sum of the current pulse and the previous random pulses with a certain weight. The general form of this model is defined in the Equation (3) [67].
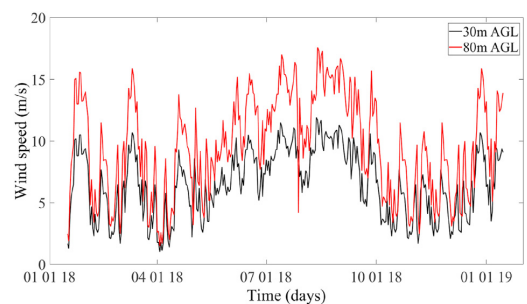

Fig. 4. Daily wind speed average at 30m and 80m AGL for 2018.

$$Y_t = a_t - \Theta_1 a_t - 1 - \Theta_2 a_t - 2 - \Theta_3 a_t - 3 - \ldots - \Theta_q a_t - q \tag{3}$$

Where: Y_t is the time series to be described in terms of unlimited amount of linear a_t; which is the remainder in period t, and $a_t - 1$ the previous values of the error, $(\Theta_1, \Theta_2, \ldots, \Theta_q)$ are the MA process parameters. Introducing the MA parameter of order q as is shown in Equation (4).

$$\theta(B) = 1 - \Theta_1 B - \Theta_2 B^2 - \Theta_3 B^3 - \ldots - \Theta_q B^q \tag{4}$$

The MA model contains (q+2) unknown parameters to be predicted from the observed values [68]. The compact form of this model is expressed as Equation (5):

$$Y_t = \theta(B)a_t \tag{5}$$

3.3.3. ARMA model of order p,q

The ARMA model is a practical tool used to express dynamic behaviour of the time series. The estimation of future values of an independent time series through this model is carried out as a combination of past values as well as by random impulses of past observations [67]. This model is the result of the combination of the AR and MA models. The general form of the ARMA model is expressed in Equation 6.

$$Y_t = \varphi_1 Y_t - 1 + \varphi_2 Y_t - 2 + \cdots + \varphi_p Y_t - p + a_t - \varphi_1 a_t - 1 - \varphi_2 a_t - 2 - \ldots - \varphi_q a_t - q \tag{6}$$

Writing again the model as Equation 7.

$$Y_t = \varphi_1 Y_t - 1 + \varphi_2 Y_t - 2 + \cdots + \varphi_p Y_t - p + a_t - \varphi_1 a_t - 1 - \varphi_2 a_t - 2 - \ldots - \varphi_q a_t - q \tag{7}$$

Ordering again as Equation 8.

$$\left(1 - \varphi_1(B) - \varphi_2(B_2^2) - \ldots - \varphi_p(B^p)\right) Y_t$$
$$= (1 - \Theta_1 B - \Theta B^2 - \ldots - \Theta_q B^q) a_t \tag{8}$$

The compact form of the ARMA model is written as Equation 9.

$$\varphi(B)Y_t = \theta(B)a_t \tag{9}$$

3.4. Proposed forecasting RNN and DNN models

The RNN are a special kind of deep learning technique designed to work with time series. The RNN are characterized by introducing the time dimension to network topology; as well as a short-term memory to acquire information from past states of inputs to have influence on input and output [68]. In this study, will be used DNN and RNN as short-term wind speed forecasters.

3.5. Dynamic Neural Networks

The DNN reply temporally to an input signal applied from output as a feedback; enabling them to obtain a state representation useful for modelling and forecasting of non linear systems [69]. In this study the NARX network is used as forecaster.

3.5.1. NARX model architecture

The NARX (Nonlinear Auto Regressive network with exogenous inputs) model is a type of RNN dynamically driven, with feedback connections enclosing several layers of the network [59,69,70]. The basic architecture of the NARX model with one input only is shown in Fig. 5; which is based in the static Multi Layer Perceptron (MLP) to exploit its mapping capability [57,69]. The single output or predicted variable $y_{(t+1)}$ is feedback to the network input creating a series-parallel architecture; which is one unit of time ahead of the input u_n. The signal vector to input layer is composed of two parts: (1) present and past values of the input or exogenous inputs named $u_{(n)}$, $u_{(n-1)}$, ..., $u_{(n-q+1)}$, and (2) delayed values of the output named, $y_{(n)}$, $y_{(n-1)}$, ..., $y_{(n-q+1)}$. The used equation to define the dynamic behavior of the NARX model is shown in Equation (10).

$$y_{(n+1)} = F(y_{(n)}, \ldots, y_{(n-q+1)}, u_{(n)}, \ldots, u_{(n-q+1)}) \tag{10}$$

Where F is a nonlinear function, n is the number of iterations [69]. In this study, the exogenous variable to be incorporated in the NARX model is wind speed. The representation of this model is shown in equation (11), considering Vav as wind speed forecasted used as feedback from output to input layers.

$$y'_{(n+1)} = F(y_{(n)}, \ldots, y_{(n-q+1)}, Vav_{(n)}, \ldots, Vav_{(n-q+1)}) \tag{11}$$

The general NARX (n_x, N_y) model for prediction considering: on the one hand, y, e, and x as output, noise and input respectively. On the other hand, n_y, n_e, n_x as the maximum lags of input, noise, and input in the order given. In addition, F is an unrevealed smooth function; it supposes a mean value of zero for e(t); which is independent with the past value with a finite variance σ^2 as is represented in Equation (12) [58].
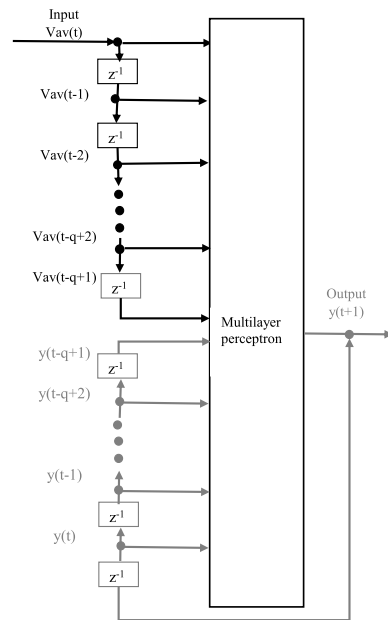

Fig. 5. NARX model architecture [69].

$$y(t) = F(y(t-1), \ldots, y(t-n_y), x(t-1), \ldots, x(t-n_x)) + e(t)$$

$$(12)$$

The optimum prediction theory turns around of reducing the Mean Square Error (MSE) value; considering a finite set of past values dependent of the mean. The lowest MSE predictor dependent of the mean is given by Equation (13).

$$\bar{y}(t) = E[y(t)|y(t-1, y(t-2), \ldots, y(1)]$$

$$(13)$$

Supposing the conditions of zero noise and finite variance given in equation (1). The optimal predictor $NARX(n_x, n_y)$ is shown in Equation (14).

$$\bar{y}(t) = F[y(t-1), \ldots, y(t-n_y), x(t-1), x(t-n_x)]$$

$$(14)$$

3.5.2. NARX model learning algorithms

This network is a two-layer feedforward network, with a tan-sigmoid transfer function in the hidden layer and a linear transfer function in the output layer. This network is created and trained in open loop using true output; which is more accurate and efficient than closed loop. Once training has finished the network may be converted to closed loop for prediction mode [70]. This process is developed using static backpropagation algorithm and decoupled feedback.

The regularization technique is used to solve the training problems regarding to weights and connections contained in the network to prevent overtraining. This technique changes the performance reducing the parameters range. In this way, the performance function for training MSE Eq. (15) is changed by MSE_{reg} as is shown in Equation (17).

$$MSE = \frac{1}{n} \sum_{t=1}^{n} (t_i - t_f)^2$$

$$(15)$$

Considering Mean Square Weight (MSW) as is indicated in Equation (16):

$$MSW = \frac{1}{n} \sum_{j=1}^{n} (W_i)^2$$

$$(16)$$

The MSE_{reg} is shown Equation (17):

$$MSE_{reg} = \xi MSE + (1 - \xi) MSW$$

$$(17)$$

Where t_i is the target, t_f is the predicted value, ξ performance ratio. The new performance ratio generates that the network acquires smaller weights and biases. Furthermore, the network is forced to reply smoother and little chance of overfitting [71].

The main advantage of the NARX model indicates that the similar structure is composed of unlike models and computational intelligence with rational cost [57]. The main feature of NARX model is based on the size of embedded memory of input, output, and number of neurons in the input layer. Furthermore, its generalization and convergence are better than others networks [59,71]. Therefore, the NARX network can be used as a predictor, nonlinear filtering, and modelling of nonlinear dynamic systems [70].

3.5.3. NAR model

The NAR network only has one series involved; in this way the future values of a time series y(t) are predicted from past values. This prediction is named nonlinear autoregressive [70]. The performance comparison of the NARX model can be made using NAR network; which is satisfactory for time series prediction using its delays. The NAR network structure is a combination of MLP with a autoregressive model. In this model the independent variable y(t) is acquired as a nonlinear function from past d values [57]. The used equation to define the NAR model is shown in Equation (18).

$$y_{(t)} = f(y_{(t-1)}, \ldots, y_{(t-d)})$$

$$(18)$$

The architecture of the NAR model is composed by three layers: input, hidden and output as is shown in Fig. 6. The main characteristics of the hidden layer are: feedback delays, number of neurons, weights matrix, bias vector, and nonlinear activation function between hidden layer and output layer for each neuron. Furthermore, the NAR architecture for optimization is reached through trial-and error-testing of the feedback delays and neurons per hidden layer [72]. The algorithm used for NAR network training is Levenberg-Marquardt; which is an approximation to the method of Newton method through backpropagation with descendent gradient technique to determine the second derivative order without considering Hessian matrix. The sum of the difference of squares between the real and the estimated value constitutes the performance function; which allows to determine the gradient as seen in the Equation (19) and the Hessian matrix $\nabla^2 f(x)$ is estimated by the Equation (20).

$$\nabla f(x) = J^T(x) e(x)$$

$$(19)$$

$$\nabla^2 f(x) = J^T(x) J(x) + S(x)$$

$$(20)$$

Where J is the Jacobian matrix of the first derivatives of the network error regarding to weights and biases vectors, e is a network error vector correspondent to each training step. The modification to Gauss-Newton method made by Cigizoglu & Özgur [74] assumes $S(x) = 0$ and uses the following algorithm to estimate Hessian matrix according to Equation (21).

$$\delta(x) = [J^T(x) J(x) + \mu I]^{-} 1 + J^T(x) e(x)$$

$$(21)$$

Where μ is a parameter used to approximate Equation (21) to Gauss-Newton method through an easy modification to the backpropagation algorithm.

3.5.4. NIO model

The Nonlinear Input-Output (NIO) network is similar to the NARX model, where there are two series included an input series x(t) and an output series y(t). This model predicts values of y(t) from past values of x(t), with absence of past values of y(t) [70]. The used equation to define NIO model is Equation (22):

$$y_{(t)} = f(x_{(t-1)}, \ldots, x_{(t-d)})$$

$$(22)$$

3.6. LSTM network

The LSTM network is a special kind of RNN characterized by its stability and great power to solve vanishing gradient problems regarding to long-term and short-term dependency. The LSTM is a cell memory to connect previous data to current neurons. This cell can remember temporal state due to three temporary gates, which can add or delete data to these cells [61]. The problem of vanishing gradient was solved by LSTM network through gate control; which was proposed by Hochreiter [75].

The LSTM network can be trained using gradient descendent algorithm in combination with BPTT (Back Propagation Through Time) to calculate the time required for optimization process to change the network weight in proportion to derivative of the error.
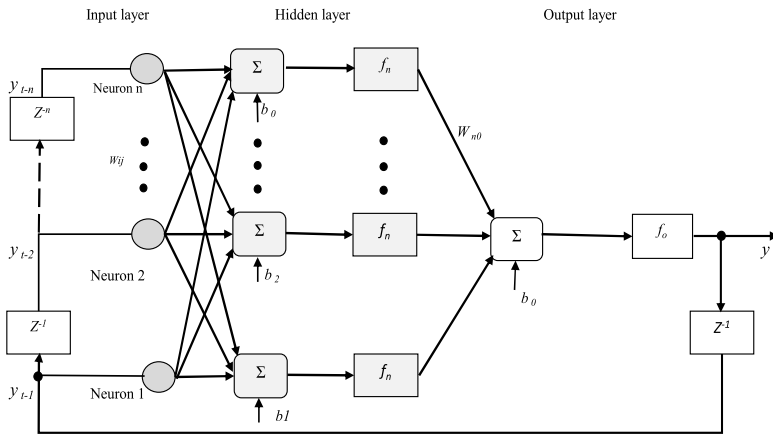
Fig. 6. NAR model architecture [73].

The procedure to find the direct relation between the loss function and the network weights is named unfolding; which is composed of an exact reproduction of hidden layer of the network for each time period to update weights [76]. The LSTM architecture is represented in Fig. 7; which is composed of an input gate i_t, a forgetting gate f_t, an output gate O_t, and a memory cell c. The hidden state is h_t at time point t, the network input at time point t is X_t, the sigmoid activation function is σ [62,76].

1. The forgetting gate is used to select the information to be discarded or retained in the previous cell m_{t-1} according to Equation (23). By entering h_{t-1} and including X_t to sigmoid function as is shown in Equation (24); the output cell designed as c_t [0,1], considering that in zero information will be discarded, and the information will be retained. While W and b are the weights and bias vector respectively [62].

$$f_t = \sigma(W_f[h_{t-1}, X_t] + b_f) \tag{23}$$

$$\sigma_t = \frac{1}{1 - e^-x} \tag{24}$$

2. The input gate decides the new information to be retained in the cell state. By going into the output h_{t-1} and attaching the present input X_t at time point t into Equation (24) (σ function). The generated value [1,0] according to Equation (25) in the cell to select the new information to be retained; the tanh layer accepts simultaneously the selection signal C_t expressed in Equation (26) to keep updated the cell state [62].
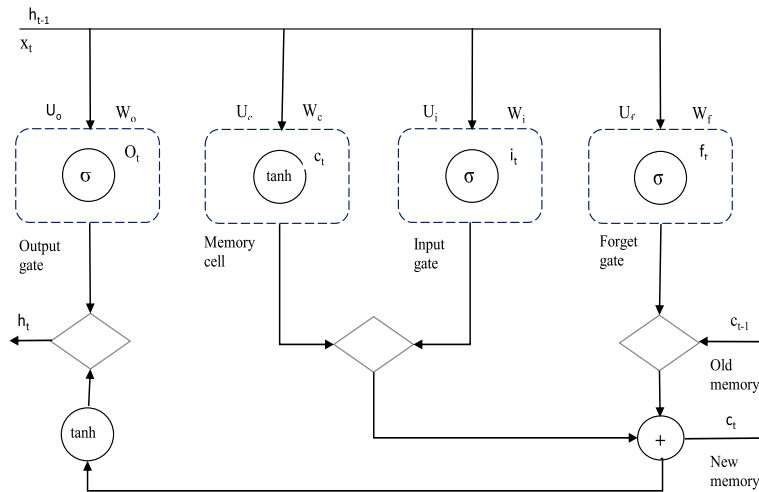
$$i_t = \sigma(W_i[h_{t-1}, X_t] + b_i) \tag{25}$$

Fig. 7. LSTM cell memory architecture [62].

$$c_t = tanh(W_c[h_{t-1}, X_t] + b_c) \qquad (26)$$

3. The output gate decides the information of the cell state will be used as output. The previous state of the output h_{t-1} is entered at the last point time t, and attaching the present input x_t to the sigmoid function generates a signal[1,0] named O_t according to Equation (27) to decide the number of cells are used as output [62]. The output signal h_t can be obtained by sigmoid and tanh using Equation (28).

$$o_t = \sigma(W_o[h_{t-1}, X_t] + b_o) \qquad (27)$$

$$h_t = O_t.tanh(c_t) \qquad (28)$$

4. Application of proposed forecasting models for wind speed forecasting

The particular application of linear regression and DNN models for wind speed forecasting is directioned here.

4.1. Linear regression models

4.1.1. ARMA or MA model
The forecasting methodology employed using ARMA or MA models is performed using three steps [67]:

1. Model definition: Concerning to election of the (p,q) order of the ARMA model, or q for MA model; which is designed as model structure.
2. Model training: Regarding to approximation of the model parameters by way of a reduction process known as least squares.
3. Prediction of the next range: Estimation of the oncoming value of the time series based on past values using measured data from one to three days ago.

4.2. Dynamic Neural Networks models

The forecasting methodology using DNN is performed in five steps:

4.2.1. Data preparation and feature extraction
The data preparation for prediction included five activities, such as data collection, data preprocessing, correlation matrix, data normalization, and structuring of data [68]. Data collected during one year by two meteorological stations, data preprocessing to detect and delete noise due to sensors malfunction. Then, data were validated by using different algorithms [23]. Data normalization of preprocessed data were required to convert data from natural range to operative network range [68]. Structuring of data was used to define a multivariable time series for the ANN toolbox; it were arranged a set of seven variables as input vectors to DNN; which were created according to the number input variables equal to number of neurons. Then, was arranged another set of one time series as output vector into a second cell array. Eight data sets were arranged as follows: two for winter and two for summer, two per 30m and two for 80m AGL. It were taken for each data set 6 h of one day of each month of winter and summer. The output vectors were eight vectors formed by 6 h of average wind speed per one day of each month for winter and summer, four for each season, and four for each height. The total amount for winter were 36 x 7 = 252 (100%), total amount for summer 36 x 5 = 180.

The input and output vectors were randomly divided into three parts as follows: 70% for training set, 15% for validation set, and 15% for testing set [70]. Data used for training in each season were for winter $252 \times 0.7 = 176.4$ (70.0%), for summer 180 x 0.7 = 126 (70%).

The amount for validation to calculate the error value during training were for winter 252 x 0.15 = 37.8, for summer 180 x 0.15 = 27. The amount for testing is for winter 252 x 0.15 = 37.8, for summer 180 x 0.15 = 27.

Feature extraction is considered one of the most important parts of machine learning process because raw data is converted into suitable information for that algorithms can eliminate repetition by overfitting. The features were extracted using statistical tools as mean, median, standard deviation, and frequency domain [77]. The correlation matrix was based on PCC, which showed the correlation between input variables and output variable. In fact, the variables that are not highly correlated can be deleted. PCC is a parametric statistical technique to measure the direction and strength between two variables [78]. In this way, to know if the points of the two variables have a tendency to be placed in a straight line. PCC is defined as the covariance between x and y divided by the product of the standard deviations of each variable [24]. The equation (29) is used to calculate PCC.

$$PCC = \frac{cov(xy)}{\varsigma x \varsigma y} \qquad (29)$$

Where cov is the covariance between variables x and y, ςx is standard deviation of x variable, ς is standard deviation of y variable.

The PCC results between measured weather variables and average wind speed at a height of 80m AGL in 2018 are shown in the Table 4, which indicates that WSAVG had high linear correlation with WSMAX, WSMIN, while the correlation coefficients with AVGTEMP, ATPRES and GSR are very small, and there is an inverse correlation with WD.

4.2.2. Determination of network architecture
In order to achieve this aim were proposed DNN to predict nonlinear time series for representation of systems whose internal state changes with time. They are particularly appropriate for modelling of nonlinear dynamic systems, generally defined by the state-space [68]. The DNN models with feedback, such as NARX and NAR models are good for time series prediction [70]. The following activities were carried out to configure the network architecture as follows: determination of input nodes required as inputs to neural networks; which was realized according to seven selected variables such as, WSAVG, VSMAX, WSMIN, WD, AVGTEMP, ATPRES, GSR. In this way, one neuron per each selected variable. Therefore, the output single node was considered the average wind speed only as is presented in Fig. 8.

4.2.3. Network training strategy
During network training for time series forecasting all main characteristics inserted in the training data of the time series

Table 4
PCC results at 80m AGL.

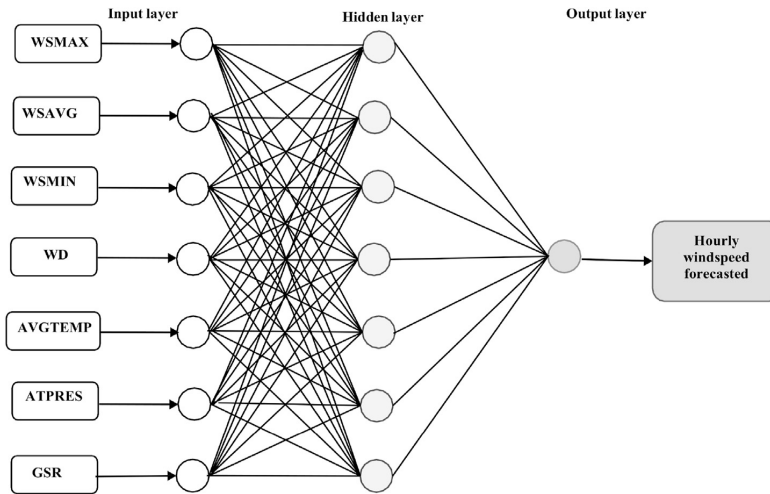| Variables	WSAVG	WSMAX	WSMIN	WD,	AVGTEMP	ATPRES	GSR
WSAVG	1	0.96	0.94	−0.47	0	0.29	0.22
WSMAX	0.96	1	0.97	−0.46	0.03	0.28	0.25
WSMIN	0.94	0.97	1	−0.45	0.02	0.28	0.23
WD	−0.47	−0.46	−0.45	1	0.02	−0.19	0.01
AVGTEMP	0.2	0.03	0.02	0.16	1	−0.12	0.72
ATPRES	0.29	0.28	0.28	−0.19	0.16	1	−0.01
GSR	0.22	0.25	0.23	0.01	−0.01	−0.01	1

Fig. 8. Proposed NARX network architecture.

should be known and learnt [68]. The input selected parameters are used to train DNN, and wind speed as output. Any of the input values had been used for testing and validation purposes. In order to prevent overfitting, the input vectors and target vector were randomly divided into three sets as follows: 70%, 15%, 15% to attribute the data to training, validation and test of network generalization respectively. MLP utilizes an algorithm named Levenberg-Marquardt backpropagation to train the network. The performance of the three DNN models were improved by adjusting the number of neurons in the hidden layers, delay, and number of epochs [70].

4.2.4. Network forecasting

Forecasting of the next value by presenting the network an input vector based in the past observations.

4.2.5. Error parameters

The forecasting performance to minimize uncertainty was evaluated by using Equations: 30, 31, and 32 named as Root Mean Square Error (RMSE), MSE, and MAPE respectively [49].

$$RMSE = \sqrt[2]{\frac{1}{n} \sum_{t=1}^{n} (Ws_f - Ws_m)^2} \tag{30}$$

$$MSE = \frac{1}{n} \sum_{t=1}^{n} (Ws_f - Ws_m)^2 \tag{31}$$

$$MAPE = \frac{1}{n} \sum_{t=1}^{n} \left| \frac{Ws_m - Ws_f}{Ws_m} \right| 100 \tag{32}$$

In the equations (30)–(32) n is the total number of inputs and outputs, Ws_m is measured wind speed, Ws_f is forecasted wind speed.

4.2.6. Software tools

Three kinds of dynamic networks were employed in MATLAB R2020b together with the Neural Network Time Series Tool with graphic interface. In the present study were used three kinds of DNN, such as NARX, NAR, and NIO.

4.3. Forecasting using multivariable LSTM networks

The forecasting process for Multivariable LSTM networks is developed in five stages [62,79] as follows:

4.3.1. Data preprocessing

Multivariable time series means that there are seven meteorological variables for each time step to be used as inputs to LSTM to have one output e,g. wind speed forecasted. The first step to prepare measured variables dataset as a supervised learning to enter LSTM network. Then was developed a PCC analysis using the seven measured meteorological variables and obtained data from Table 4. The multivariable LSTM method contains four data sets; 12 hours of seven meteorological variables each; one set for Winter, and other for Summer, one for 30 m and other for 80m AGL. The data set was divided 80% for training and 20% for testing.

4.3.2. Data normalization

The seven meteorological variables have different measurement units and require a same range. Therefore, the selected variables were normalized to have values between zero and one, by using the highest and lowest values of each variable as is shown in Equation (33).

$$v_n = \frac{v_i - v_{max}}{v_{max} - v_{min}} \tag{33}$$

Where v_n is the normalized value for any variable, v_i is the current value of the variable to be converted, v_{max} is the maximum range for any variable, v_{min} is the minimum range for any variable.

4.3.3. Define and fit LSTM model

This step is to create a LSTM regression network and to define how many neurons will be used in the hidden layer. The training options must be specified, set up the solver Adam to optimize performance. The gradient threshold should be set to prevent gradient exploding. The learn rate is set by default to 0.001 and should drop each 5 epochs.

4.3.4. LSTM network training and optimization

To perfectly memorize data sequence would be used a lower number of neurons in the hidden layer. The RMSE plots the training report from the standardized data, and is employed to measure loss function together with Adam network performance optimizer. The training and validation loss converge after a certain epochs number.

4.3.5. LSTM network forecasting

The future values of multivariable time series are forecasted one at time, and the same are updated after each prediction. The last prediction is used as input for each new prediction. The real wind speed forecasted and RMSE are obtained using an inverse normalization.

4.3.6. LSTM software tools

The simulations were developed using MATLAB R2020b together with the Neural Network Deep Learning Tool.

5. Results and discussion

The wind speed forecasting process was developed in three steps to have good results as follows: First, time series data analysis and feature extraction. Second, the importance of the weather variables used as DNN inputs. Third, optimization capacity of the DNN to forecast wind speed.

5.1. Data analysis and feature extraction

The monthly variation of wind speed average at 30 and 80 m AGL during 2018 from January to December is shown in Fig. 9. The monthly wind speed analysis indicates two strong seasonal variations. The strongest winds appear from June to September because of cold air flows from the East are present in this season added to valley and mountain breezes. Whereas, the weakest winds in winter season from January to April and from October to December [17,64]. García et al. [25] observed similar monthly wind speed average in the wind data analysis for a nearby location. Strong winds could be feasible for a future wind farm installation with high power wind turbines, and could be a good option to forecast short time wind speed for power generation. The Fig. 9 indicates the daily winter and summer wind speed profiles. In the winter profile there is very low wind speed during the night, which is not recommended for wind turbine operation. During day hours there is medium wind speed which could be used to forecast wind speed. In contrast, the daily wind speed profile in summer reached high wind speed during the day and night; it is excellent to forecast wind speed anytime. Therefore, in summer showed variable wind speed higher than annual mean wind speed value of 10,2 m/s. It should be
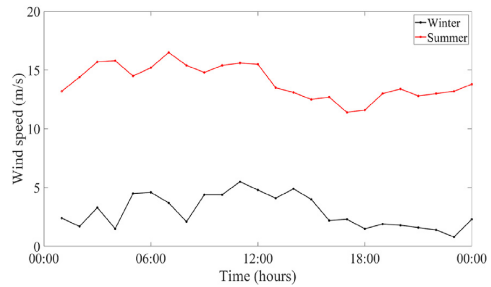

Fig. 10. Daily wind speed profile for winter and summer 2018 at 80 m AGL.

noted that the ideal wind speed range for wind turbine operation to reach maximum power generated is from 12 to 15 m/s [21,23] (see Fig. 10).

5.2. Importance of input variables

The relative importance of input variables were found from the highest to the lowest importance in the following order: WSMAX, WSMIN, GSR, ATPRES, AVGTEMP, and WD, as is shown in Table 4. It is observed that the importance of WSMAX and WSMIN are almost equal because both variables are wind speed control limits. The variables ATPRES and GSR have low importance because both are in direct relation with altitude and hour of the day; there is an inverse relation between WD and WSAVG.

5.3. Wind speed forecasting optimization

In order to evaluate the forecasting performance employing DNN architecture; twenty one simulations per each model were developed using the NARX, NAR, NIO models varying the number of neurons in the hidden layer from 5 to 25, and delay number from 1 to 4. The best performance for DNN models was developed considering the lowest values of MSE, RMSE, MAPE, and R coefficient of the test set. The lowest results for MSE, RMSE, MAPE and the highest PCC with the lowest MSE of the test set for winter were reached with 1 network defined by and 1 delay, 13 neurons in the hidden layer, 1 output at a height of 80m AGL. The NARX model with the best performance for summer had seven neurons in the input layer, 13 neurons in the hidden layers, one neuron in the output layer by using Log-Sigmoid transfer as activation function and feedforward connection between hidden layers between the input layer and the hidden layer, and the linear transfer function in the output layer [69,70].

The best performance results for summer at 80m AGL were reached with 1 network defined by 1 delay, 11 neurons in the hidden layer, 1 output. The results with the best performance are shown in the Table 6 and Table 8 respectively. The MAPE and R coefficient results indicated that the NARX model had values for Winter at a height of 80m AGL of 5.8% and 98% respectively, and for summer 5.7% and 98% respectively. It should be noted that the best NARX performances were gotten at a height of 80m AGL due to that the wind speed increases with height and the turbulence decreases. Therefore, wind speed is not affected by terrain roughness [19].

The performance plot of NARX model for training, validation, and testing sets, for winter and summer at a height of 80m AGL are shown in Fig. 13 and Fig. 14 respectively. These figures indicate that when the number of epochs increases the MSE reaches the lowest value. This action is known as early stopping, which is realized at the point where the network has reached maximum generalization.
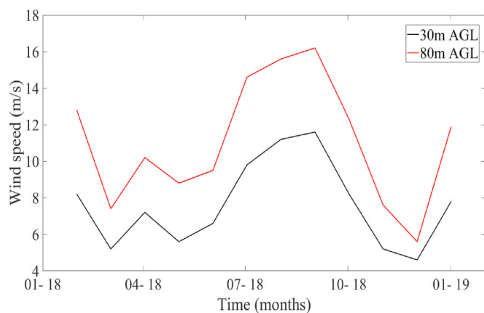

Fig. 9. Monthly wind speed for 2018 at 30m and 80m AGL.

Hence, if the training continues past this point could occur the network overfitting [68]. One epoch is defined as one complete pass of data set through the learning algorithm to update the weights [68]. The test set error and validation set error shows different features and the best validation performance had occurred at the epoch 5 and epoch 6 as are shown in the Fig. 11 and Fig. 12 respectively.

The regression analysis performed by NARX model for winter and summer in weather station 2 at a height of 80m AGL shows the correlation coefficient, which measures the correlation between output and target. The R value takes values from one to zero, which indicates a strong and weak relation respectively [69].

The R value reached for training data set in winter is 0.96 is represented in Fig. 13(a). The R value is 0.99 in validation data set as is displayed in Fig. 13(b). The R value is 0.98 in test data set as is described in Fig. 13(c). The R value in whole data set is 0.97 as is illustrated in Fig. 13(d). The R value reached for training data set in summer is 0.99 is represented in Fig. 14(a). The R value is 0.99 in validation data set as is presented in Fig. 14(b). The R value is 0.85 in test data set as is displayed in Fig. 14(c). The R value in whole data set is 0.97 as is showed in Fig. 14(d). The R values represented in the last two figures indicate good forecasting accuracy in complex terrain located at high altitude showing that wind speed forecasted for winter and summer at a height of 80m AGL is close to measured values.

5.4. Comparison and analysis of the proposed models for short-term wind speed forecasting

The comparison between measured hourly wind speed and forecasted hourly wind speed by using DNN and RNN, such as NARX, NAR, NIO, and LSTM and linear regression models, such as persistence, MA, and ARMA, 12 hours in advance was developed to show the results during the best windy day hours to predict wind speed for winter and summer at heights of 30m and 80 m AGL. In order to evaluate the forecasting performance of regressive and DNN models by using four case-studies as follows:

5.4.1. Case-study 1 short-term wind speed forecasting for winter at 30m AGL

The comparison results for half day in winter at height of 30m AGL using regressive models and DNN models are shown in Table 5; where the best performance is highlighted in bold and shows that the LSTM network outperforms the other five models reaching a MAPE value of 5.3% during training phase by using Adam optimizer, learning rate 0.001, and 200 epochs. The graphic sample of the
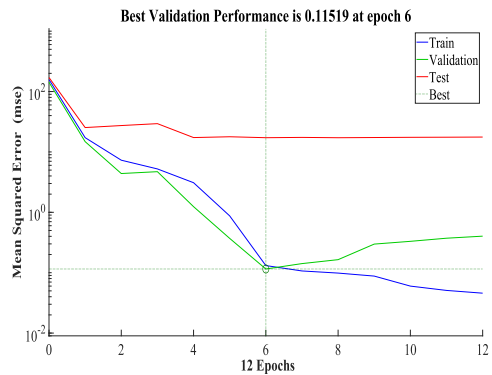

Fig. 12. NARX model performance plot for summer at 80m AGL.

results of linear models are presented in Fig. 15; where the ARMA model outperforms better than other two models by using p,q values (1,1) and wind speed data of three days ago. The Fig. 16 shows a slight improvement on forecasting performance of the LSTM network around 0.9% in MAPE value over NARX model. These results go beyond previous reports [62], showing a lower RMSE value.

5.4.2. Case-study 2 short-term wind speed forecasting for winter at 80m AGL

The comparison results for wind speed 12 next hours in winter at a height of 80m AGL using regressive models and DNN models are shown in Table 6; where the best performance is highlighted in bold; which indicates that the LSTM network outperforms the other five models reaching a MAPE value of 4.9% during training phase by using Adam optimizer, learning rate 0.001, and 300 epochs. The graphic sample of the results of linear regression models are presented in Fig. 17; where the ARMA model outperforms better than other two models by using for (p,q) values (2,1) and wind speed data of three days ago. The Fig. 18 shows a slight improvement on forecasting performance of the LSTM network around 0.9% in MAPE value over NARX model. A similar pattern of results was obtained by Liu te al [61].

5.4.3. Case-study 3 short-term wind speed forecasting for summer at 30m AGL

The comparison results for wind speed 12 next hours in summer at a height of 80m AGL using linear regression models and DNN models are shown in Table 7; where the best performance is highlighted in bold; where the LSTM network outperforms the other five models reaching a MAPE value of 4.1% during training phase by using Adam optimizer, learning rate 0.001, and 300 epochs. The graphic sample of the results of linear models are presented in Fig. 19; where the ARMA model outperforms better than other two models by using p,q values (2,1) and wind speed data of three days ago. The Fig. 20 shows a slight improvement of 0.7% on forecasting performance of the LSTM network over NARX model. By comparing the results from Wu et al. [80] against our forecasting results, we determined that LSTM networks outperforms over other models at least 10%.

5.4.4. Case-study 4 short-term wind speed forecasting for summer at 80m AGL

The comparison results for wind speed 12 next hours in winter at a height of 80m AGL using linear models and RNN models are
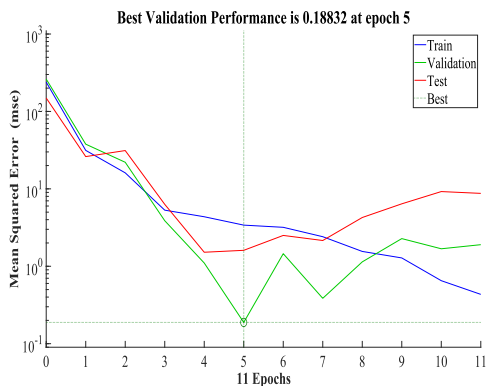

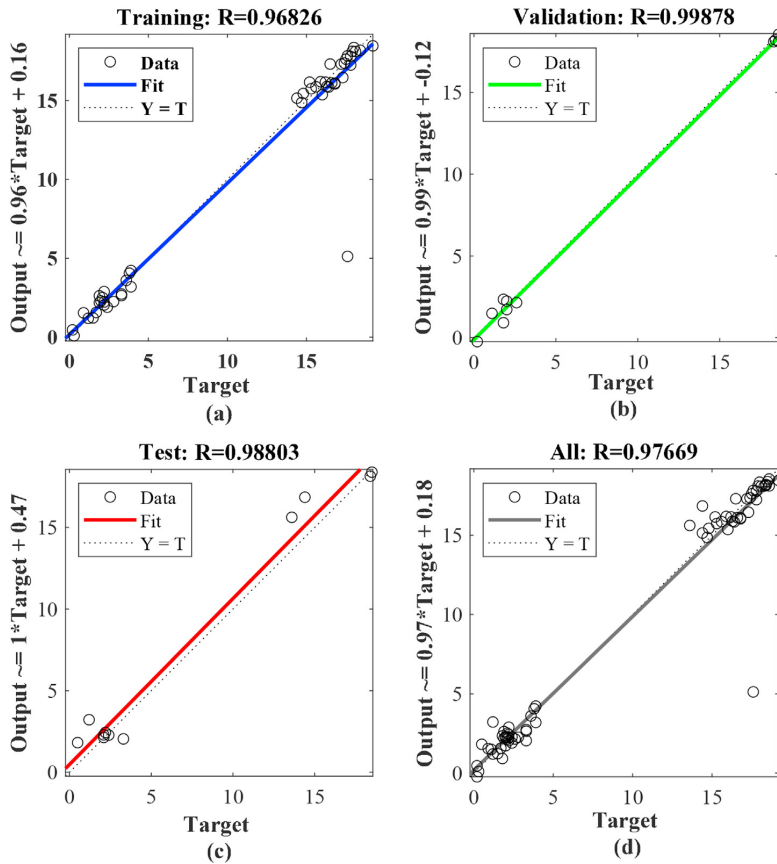**Fig. 11.** NARX model performance plot for winter at 80m AGL.

Fig. 13. Results of NARX model performance regression plot for winter at a height of 80m AGL. (a) Training dataset. (b) Validation dataset. (c) Testing dataset. (d) All datset.

shown in Table 8; where the best performance is highlighted in bold and indicates that the LSTM network outperforms the other five models reaching a MAPE value of 4.01% during training phase by using Adam optimizer, learning rate 0.001, and 400 epochs. The graphic sample of the results of linear models are presented in Fig. 21; where the ARMA model outperforms better than other two models by using (p,q) values (2,1) and wind speed data of three days ago. The Fig. 22 shows a slight improvement of 1.9% on fore-casting performance of the LSTM network over NARX model. In line with previous studies developed by Yao el al. [81,82]; where LSTM network has good forecasting performance.

5.4.5. Deductive arguments

This section highlights the important findings obtained through comparison of statistical analysis as follows:

5.4.5.1. Wind shear profile and turbulence. In this work to observe the change of height effect on wind speed is considered forecasting performance by using measured data at heights of 30 m and 80m AGL for training, validation and testing of the DNN realized by comparison between measured and forecasted values. The best MAPE values 5.7%, and 5.8% for winter and summer respectively, were for NARX model at a height of 80m AGL, which are better to previous results (11%) [57] and (16%) [55]. These concrete results

are mainly because NARX model has computational intelligence with with embedded memory to forecast future values from past at this height wind is more stable with lower turbulence. Therefore, wind speed is not affected by topography of complex terrain [23]. Based on the indicated results, it is inferred that the wind speed at a height of 30m AGL is significantly affected by surface roughness and topography. Furthermore, it is observed that wind speed values reach higher values in summer at a height of 80m AGL than at a height of 30m AGL due to that wind speed increases with height and turbulence decreases [22,23]. The turbulence decreasing cau-ses wind more stable, which is used to reach stability in wind po-wer generation [4,24]. The forecasting results of LSTM and NARX models presents a better adjustment than NAR and NIO models, for both heights in winter and summer due to the embedded which is used to retain past values of wind speed. Moreover, it is suggested that the LSTM or NARX approaches can be used for other studies about wind speed forecasting at high altitude to exploit its great wind potential available, and to promote wind energy development in Ecuador.

5.4.5.2. Influence of number of epochs and amount of data over forecasting performance. The forecasting results MAPE and MSE values indicate that if the number of epochs, data quantity are increased the forecasting performance is increased at least 10% of
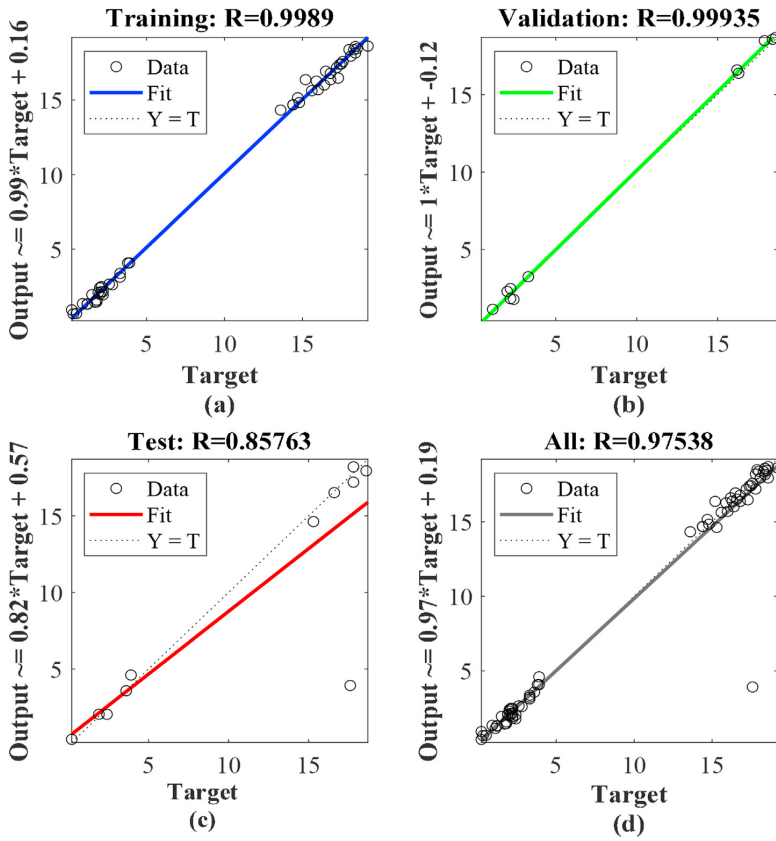
Fig. 14. Results of NARX model performance regression plot for summer at a height of 80m AGL. (a) Training dataset. (b) Validation dataset. (c) Testing dataset. (d) All datset.

Table 5
Results of simulation process for winter at a height of 30 m AGL.

NN Model	MSE	RMSE	MAPE(%)	R
Persistence	2.5	1.58	41.2	0.52
MA	1.35	1.46	38.3	0.54
ARMA	1.08	1.03	24.9	0.8
LSTM	**0.09**	**0.3**	**5.3**	**0.99**
NARX	0.33	0.61	6.2	0.98
NAR	0.39	0.62	6.4	0.97
NIO	0.4	0.63	6.9	0.98

the remaining value between NARX forecasting values and measured value using a multivariable LSTM networks. In other words there is a direct proportion between both parameters.

5.4.6. Research limitation

The limitations of the present study during research period naturally include the following aspects:

•• Time measurement constraint for weather variables

The minimum time for wind speed assessment is one year according to IEC 61400-12-1. However, to reach more accurate results is suggested by using measured data from more than one year.
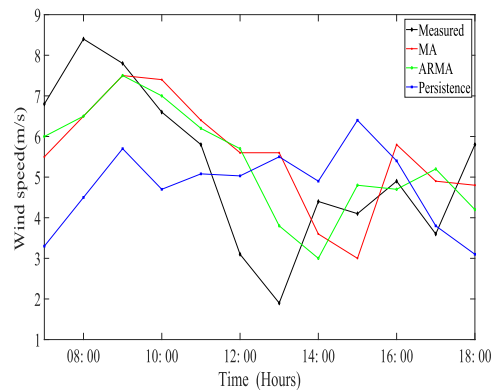

Fig. 15. Wind speed forecasting in winter on March 05–18 at 30m AGL using linear regression models.

• Lack of previous studies in research area

The absence of previous studies in complex terrain at high altitude have been one lackness in this research to be considered as a baseline to improve our results; considering that is the first wind
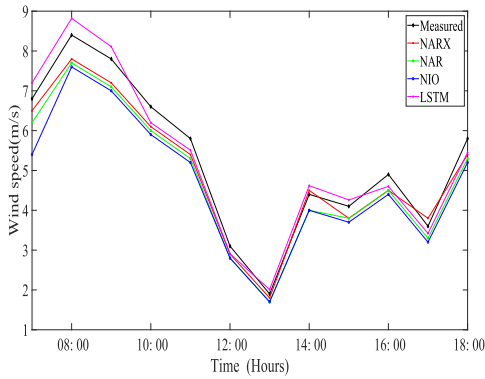
Fig. 16. Wind speed forecasting in winter on March 05−18 at 30m AGL using DNN models.
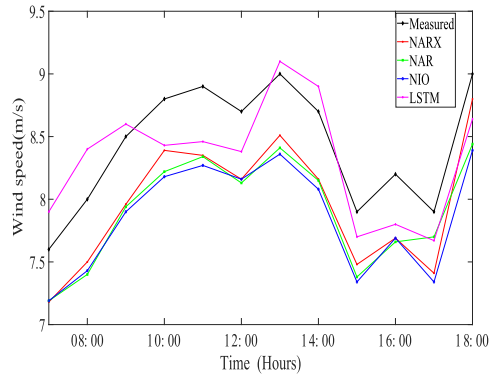

Fig. 18. Wind speed forecasting in winter on April 05−18 at 80m AGL using DNN models.

Table 6
Results of simulation process for winter at a height of 80m AGL.

NN Model	MSE	RMSE	MAPE(%)	R
Persistence	1.5	1.37	25.2	0.55
MA	1.28	1.13	18.3	0.6
ARMA	1.01	1.004	14.9	0.85
LSTM	**0.13**	**0.36**	**4.9**	**0.99**
NARX	0.3	0.3	5.8	0.99
NAR	0.34	0.58	5.9	0.95
NIO	0.65	0.8	8.2	0.98

Table 7
Results of simulation process for summer at a height of 30m AGL.

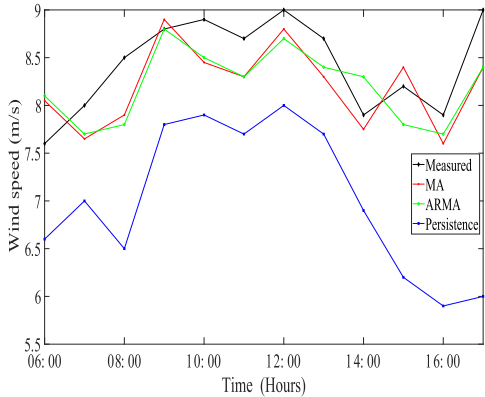| NN Model	MSE	RMSE	MAPE(%)	R
Persistence	1.9	1.37	23.1	0.55
MA	1.28	1.13	18.3	0.6
ARMA	1.01	1.004	14.9	0.85
LSTM	**0.13**	**0.36**	**4.1**	**0.99**
NARX	0.18	0.33	5.4	0.99
NAR	0.37	0.6	6.1	0.93
NIO	0.37	0.6	6.3	0.94

Fig. 17. Wind speed forecasting in winter on April 05−18 at 80m AGL using regressive models.
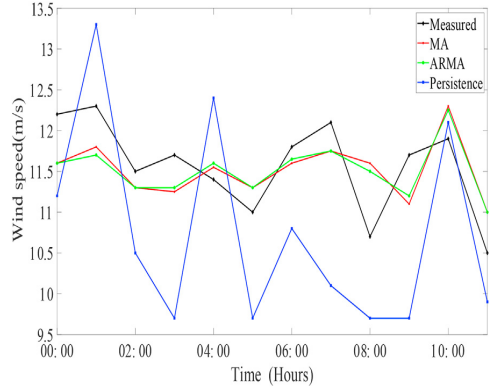

Fig. 19. Wind speed forecasting in summer on June 06−18 at 30m AGL using linear regression models.

speed forecasting at the highest altitude reported until now.

6. Conclusions and future works

In the present study, the hourly average wind speed over complex terrain was modeled and forecasted 12 hours in advance by using linear regression models, such as persistence, MA, and ARMA considered as a baseline for prediction, in combination with more complex networks to improve forecasting performance, such as multivariable LSTM, and NARX networks. Database is based on measured meteorological variables during 2018 by two meteorological towers installed within mountainous zone of study in the

Andes Range. The most important results about this work can be summarized as follows:

- The results of correlation analysis among measured variables by using PCC tool to determine the contribution of each measured variables to obtain as output average wind speed indicated that the wind speed is highly dependent of atmospheric variables, mainly wind speed maximum and minimum values.
- The monthly wind speed analysis for 2018 showed that wind speed increases with change of height and turbulence decreases. In addition, wind speed ranges were higher in summer months than in winter months because of great cold air flows
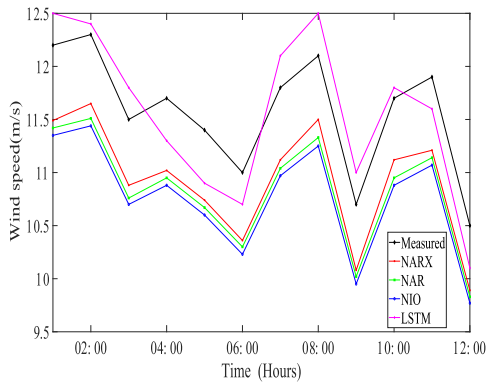
Fig. 20. Wind speed forecasting in summer on June 06–18 at 30m AGL using DNN models.
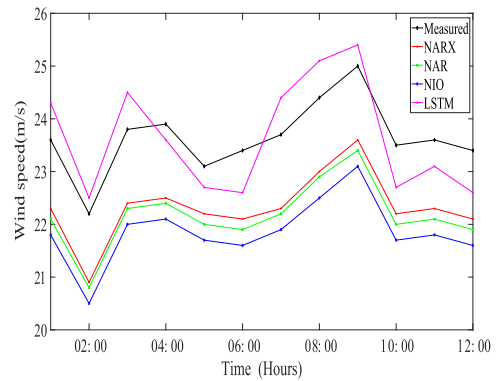
Table 8
Results of simulation process for summer at a height of 80m AGL.

NN Model	MSE	RMSE	MAPE(%)	R
Persistence	1.5	1.22	20.5	0.57
MA	1.28	1.13	18.3	0.6
ARMA	1.01	1.004	14.9	0.85
LSTM	**0.12**	**0.38**	**3.8**	**0.99**
NARX	0.11	0.56	5.7	0.98
NAR	0.58	0.76	6.6	0.98
NIO	0.41	0.64	7.1	0.97

Fig. 21. Wind speed forecasting in summer on August 08–18 at 80m AGL using linear regression models.

from the East. According to wind speed profile the forecasting schedule should be in summer at anytime during 24 hours; whereas in winter for day hours only. It should be noted that the wind speeds available in the zone of study for winter and summer at a height of 80m AGL can be used for high power wind generation.

- The comparison results among proposed models were developed by using the error forecasting measurements, such as MSE, RMSE, MAPE, and correlation coefficient (R-value); which showed that the forecasting performance of the linear regression models used a base line indicate high values for error measurements. Whereas, better forecasting performance results

Fig. 22. Wind speed forecasting in summer on August 08–18 at 80m AGL using DNN models.

were reached using multivariable LSTM network at least 10% improvement over the NARX network. The best performances were reached using NARX model at a height of 80m AGL. The MAPE and R coefficient results for LSTM model indicated values for winter of 4.1 and 99% respectively, and for summer of 3.8 and 99% independently.

- The present study is relevant due to that contributes to the scientific community by supplying novel results about wind speed forecasting over complex terrain in the Ecuadorian Highlands. The multivariable LSTM or NARX networks used in this research can be applied in other works to forecast short term wind speed over complex terrain. It should be noted that until now there are no published works about application of RNN or DNN techniques for wind speed forecasting in Ecuador, where wind power is in growth process. Future works will be focused on the analysis of orography in complex terrain and the application of other deep learning algorithms to forecast wind speed with better accuracy.
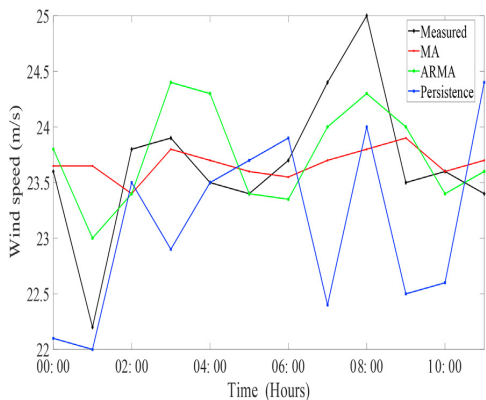
Data availability

Datasets related to this article can be found at LOPEZ, GERMA-NICO (2021), "Meteorological variables 2018 at 80m AGL", Mendeley Data, V1, https://doi.org/10.17632/wfvk5k34rs.1.

CRediT authorship contribution statement

Germánico López: Conceptualization, Investigation, Methodology, Writing – original draft, preparation, Data curation, Formal analysis. **Pablo Arboleya:** Visualization, Supervision, Software, Resources, Writing – review & editing.

Declaration of competing interest

The authors declare that they have no known competing financial interests or personal relationships that could have appeared to influence the work reported in this paper.

Acknowledgment

References

[1] IEA, Renewables Information: Overview. Tech. rep. 31-35 rue de la Fédération 75739 Paris Cedex 15 France, International Energy Agency, Aug. 2019.

[2] GWEC, Global Wind Energy Report 2018, Global Wind Energy Council, Rue d'Arlon 80 1040 Brussels, Belgium, 2018. https://tureb.com.tr/eng/lib/uploads/12288d020bbbcd29.pdf.

[3] Jaesung Jung, P. Broadwater, Current status and future advances for wind speed and power forecasting, Renew. Sustain. Energy Rev. 31 (2014) 762–777, https://doi.org/10.1016/j.rser.2013.12.054. ISSN: 1364-0321.

[4] Alberto Marugán, et al., A survey of artificial neural network in wind energy systems, Appl. Energy 228 (2018) 1822–1836, https://doi.org/10.1016/j.apenergy.2018.07.084. ISSN: 0306-2619.

[5] Global Wind Energy Council (GWEC), Global Wind Report (Annual Market Update 2017), Tech. Rep., Global Wind Energy Council(GWEC), Hamburg-Germany, 2018 https://gwec.net/global-wind-report-2017/.

[6] D. Carvalho, et al., Wind resource modelling in complex terrain using different mesoscale–microscale coupling techniques, Appl. Energy 108 (2013) 493–504, https://doi.org/10.1016/j.apenergy.2013.03.074. ISSN: 0306-2619.

[7] WWEA, Global wind installations. Information, Apr. 2020. URL: https://wwindea.org/information-2/information/.

[8] GWEC, Global Wind Report 2019. Tech. Rep, Global Wind Energy Council, 2019. https://gwec.net/wp-content/uploads/2020/08/Annual-Wind-Report_2019_digital_final_2r.pdf.

[9] Lin Ye, et al., Short-term wind power prediction based on spatial model, Renew. Energy 101 (2017) 1067–1074, https://doi.org/10.1016/j.renene.2016.09.069. ISSN: 0960-1481. DOI.

[10] Younes Noorollahi, et al., Using artificial neural networks for temporal and spatial wind speed forecasting in Iran, Energy Convers. Manag. 115 (2016) 17–25, https://doi.org/10.1016/j.enconman.2016.02.041. ISSN: 0196-8904. DOI.

[11] Gaiping Sun, et al., Short-term wind power forecasts by a synthetical similar time series data mining method, Renew. Energy 115 (2018) 575–584, https://doi.org/10.1016/j.renene.2017.08.071. ISSN: 0960-1481. DOI.

[12] David Barbosa de Alencar, et al., Different models for forecasting wind power generation: case study, Energies 10 (12) (2017), https://doi.org/10.3390/en10121976. ISSN: 1996-1073.

[13] Google, Google Earth, Apr. 2018.

[14] Miguel Castro, Hacia una nueva matriz energética diversificada en Ecuador, in: Joerg Elbers (Ed.), 2011, ISBN 978-9942-9998-5-6. Av. Eloy Alfaro N32-650 y Rusia, 3er. Piso. Quito, Ecuador: CEDA.

[15] M.A. Ponce-Jara, et al., Electricity sector in Ecuador: an overview of the 2007–2017 decade, Energy Pol. 113 (2018) 513–522, https://doi.org/10.1016/j.enpol.2017.11.036. ISSN: 0301-4215. DOI.

[16] MEER, *Plan Maestro de Electrificación 2012-2021*. Av. Naciones Unidas E7-71 y Av. de los Shyris, MEER, Feb. 2013. Quito-Ecuador, https://www.regulacionelectrica.gob.ec/plan-maestro-de-electrificacion-2012-2021/.

[17] MEER, Atlas Eólico del Ecuador con fines de Generación Eléctrica. Tech. rep. Ministerio de Electricidad y Energía Renovable, 2013. URL: https://es.scribd.com/document/355204005/ATLAS-EOLICO-ECUADOR-MEER-2013-pdf.

[18] Stefan Emeis, Wind energy meteorology atmospheric physics for wind power generation, in: Green Energy and Technology. ISSN 1865-3537. Institut für Meteorologie und Klimaforschung Karlsruher Institut für Technologie Kreuzeckbahnstr. 19 82467 Garmisch-Partenkirchen Germany, first ed., Springer, 2013. Springer.

[19] Lars Landberg, Meteorology for wind energy, in: The Atrium Southern Gate Chichester West Sussex PO19 8SQ, first ed., John Wiley & Sons Ltd, United Kingdom, 2016, ISBN 9781118913444. Wiley.

[20] Hyun-Goo Kim, et al., Evaluation of wind resource potential in mountainous region considering morphometric terrain characteristics, Wind Eng. 41 (2) (2017) 114–123, https://doi.org/10.1177/0309524X16689445.

[21] Tony Burton, et al., Wind Energy Handbook, Ltd John Wiley & Sons. 1st. John Wiley & Sons Inc. 605 Third Avenue New York NY 10158-0012, John Wiley & Sons, Ltd, USA, 2011, ISBN 978-1-119-99272-1. E-PDF.

[22] Emmanuel Branlard, Wind turbine aerodynamics and vorticity-based methods, in: Joachim Peinke (Ed.), Research Topics in Wind Energy. Gewerbestrasse 11, vol. 7, Springer, Cham, Switzerland, 2017, ISBN 978-3-319-55163-0, p. 6330, https://doi.org/10.1007/978-3-319-55164-7.

[23] C. Brower Michael, Wind Resource Assessment, Ed., vol. 1, John Wiley & Sons Inc., Hoboken, USA, 2012. John Wiley & Sons Inc.

[24] Matthew Zhang, Wind Resource Assessment and Micro-sitting, China Machine Press, 2015, 1st. Vol. 1. John Wiley & Sons, Ltd.

[25] Javier García, et al., A novel probability density function applied to wind characterization in order to evaluate the wind power potential in Tungurahua, Ecuador's Andean region, 0.0, Wind Eng. (2017) 1–24, https://doi.org/10.1177/0309524X18780383.

[26] M. Ayala et al. "Wind Power Resource Assessment in Complex Terrain: Villonaco Case-study Using Computational Fluid Dynamics Analysis". In: *Energy Procedia* 107 (2017). 3rd International Conference on Energy and Environment Research, {ICEER} 2016, 7-11 September 2016, Barcelona, Spain, pp. 41–48. ISSN: 1876-6102. DOI: https://doi.org/10.1016/j.egypro.2016.12.127.

[27] Wen-Yeau Chang, A literature review of wind forecasting methods, J. Power Energy Eng. 2 (2014) 161–168, https://doi.org/10.4236/jpee.2014.24023.

[28] Francesco Castellani, et al., Investigation of terrain and wake effects on the

[29] Ilhami Colak, et al., Data mining and wind power prediction: a literature review, Renew. Energy 46 (2012) 241–247, https://doi.org/10.1016/j.renene.2012.02.015. ISSN: 0960-1481. DOI.

[30] Dongxiao Niu, et al., Ultra-short-term wind-power forecasting based on the weighted random forest optimized by the Niche Immune lion algorithm, Energies 11 (5) (2018), https://doi.org/10.3390/en11051098. ISSN: 1996-1073.

[31] G.W. Chang, et al., An improved neural network-based approach for short-term wind speed and power forecast, Renew. Energy 105 (2017) 301–311, https://doi.org/10.1016/j.renene.2016.12.071. ISSN: 0960-1481. DOI.

[32] John W. Zack, Overview of Wind Energy Generation Forecasting New York State Independent System Operator Truewind Solutions, Truewind Solutions LLc, 2004. https://www.semanticscholar.org/paper/Overview-of-Wind-Energy-Generation-Forecasting-New-Zack/c8fa884998e5e9f231a73abff092691bd87c1757.

[33] Federico Cassola, Massimiliano Burlando, Wind speed and wind energy forecast through Kalman filtering of Numerical Weather Prediction model output, Appl. Energy 99 (2012) 154–166, https://doi.org/10.1016/j.apenergy.2012.03.054. ISSN: 0306-2619. DOI.

[34] Kostas Philippopoulos, Despina Deligiorgi, Application of artificial neural networks for the spatial estimation of wind speed in a coastal region with complex topography, Renew. Energy 38 (1) (2012) 75–82, https://doi.org/10.1016/j.renene.2011.07.007. ISSN: 0960-1481. DOI.

[35] Tanveer Ahmad, et al., A review on renewable energy and electricity requirement forecasting models for smart grid and buildings, Sustainable Cities and Society 55 (2020) 102052, https://doi.org/10.1016/j.scs.2020.102052. ISSN: 2210-6707. DOI.

[36] K. Gnana Sheela, S.N. Deepa, A review on neural network models for wind speed prediction, Wind Eng. 37 (2) (2013) 111–123, https://doi.org/10.1260/0309-524X.37.2.111.

[37] Mojtaba Dadkhah, et al., Short-term power output forecasting of hourly operation in power plant based on climate factors and effects of wind direction and wind speed, Energy 148 (2018) 775–788, https://doi.org/10.1016/j.energy.2018.01.163. ISSN: 0360-5442. DOI.

[38] P. Ramasamy, et al., Wind speed prediction in the mountainous region of India using an artificial neural network model, Renew. Energy 80 (2015) 338–347, https://doi.org/10.1016/j.renene.2015.02.034. ISSN: 0960-1481.

[39] M. Beccali, et al., Short-term prediction of household electricity consumption: assessing weather sensitivity in a Mediterranean area, Renew. Sustain. Energy Rev. 12 (8) (2008) 2040–2065, https://doi.org/10.1016/j.rser.2007.04.010. ISSN: 1364-0321.

[40] Justin Heinermann, Oliver Kramer, Machine learning ensembles for wind power prediction, Renew. Energy 89 (2016) 671–679, https://doi.org/10.1016/j.renene.2015.11.073. ISSN: 0960-1481.

[41] IRENA, *Wind Power Technology Brief*. Tech. Rep, International Renewable Energy Agency, Mar. 2016. https://irena.org/publications/2016/Mar/Wind-Power.

[42] M. Foley, et al., Current methods and advances in forecasting of wind power generation, Renew. Energy 37 (1) (2012) 1–8. ISSN: 0960-1481. DOI: http://doi.org/10.1016/j.renene.2011.05.033.

[43] X. Deng, et al., Wind power forecasting methods based on deep learning: a survey, 1, in: CMES - Computer Modeling in Engineering and Sciences, vol. 122, 2020, pp. 273–301, https://doi.org/10.32604/cmes.2020.08768. cited By 0.

[44] Lazić, et al., Wind forecasts for wind power generation using the Eta model, Renew. Energy 35 (6) (2010) 1236–1243, https://doi.org/10.1016/j.renene.2009.10.028. ISSN: 0960-1481.

[45] Trevor M. Letcher, in: Science direct (Ed.), Wind Energy Engineering, Academic Press, 1st. 525 B Street Suite 1800 San Diego CA ,92101-4495, United States, 2017. https://www.elsevier.com/books/wind-energy-engineering/letcher/978-0-12-809451-8.

[46] B.W. Yan, Q.S. Li, Coupled on-site measurement/CFD approach for high-resolution wind resource assessment over complex terrains, Energy Convers. Manag. 117 (2016) 351–366, https://doi.org/10.1016/j.enconman.2016.02.076. ISSN: 0196-8904, http://www.sciencedirect.com/science/article/pii/S0196890416301145.

[47] Osamah Shukur, Muhammad Lee, Daily wind speed forecasting through hybrid KF-ANN model based on {ARIMA, Renew. Energy 76 (2015) 637–647, https://doi.org/10.1016/j.renene.2014.11.084. ISSN: 0960-1481.

[48] Amir Mosavi, et al., State of the art of machine learning models in energy systems, a systematic review, Energies 12 (7) (2019), https://doi.org/10.3390/en12071301. ISSN: 1996-1073.

[49] Mahdi Sharifzadeh, Alexandra Sikinioti-Lock, Nilay Shah, Machine-learning methods for integrated renewable power generation: a comparative study of artificial neural networks, support vector regression, and Gaussian Process Regression, in: Renewable and Sustainable Energy Reviews, vol. 108, 2019, pp. 513–538, https://doi.org/10.1016/j.rser.2019.03.040. ISSN: 1364-0321.

[50] Stetco Adrian, et al., Machine learning methods for wind turbine condition monitoring: a review, Renew. Energy 133 (2019) 620–635, https://doi.org/10.1016/j.renene.2018.10.047. ISSN: 0960-1481.

[51] Xiaohui Yuan, et al., Wind power prediction using hybrid autoregressive fractionally integrated moving average and least square support vector

machine, Energy 129 (2017) 122—137, https://doi.org/10.1016/j.energy.2017.04.094. ISSN: 0360-5442.

[52] P. Zucatelli, et al., Short-term wind speed forecasting in Uruguay using computational intelligence, Heliyon 5 (5) (2019), e01664, https://doi.org/10.1016/j.heliyon.2019.e01664. ISSN: 2405-8440.

[53] Inci Okumus, Dinler Ali, Current status of wind energy forecasting and a hybrid method for hourly predictions, Energy Convers. Manag. 123 (2016) 362—371, https://doi.org/10.1016/j.enconman.2016.06.053. ISSN: 0196-8904.

[54] Phil Kim, Matlab deep learning, in: Tood Green. 233 Spring Street 6th Floor, APRESS, New York, NY 10013, 2017, https://doi.org/10.1007/978-1-4842-2456-6.

[55] Catherine Meißner, Matteo Mana, Massimiliano Burlando, Evaluation of two ANN approaches for the wind power forecast in a mountainous site, Int. J. Renew. Energy Resour. 7 (4) (2017) 1629—1638.

[56] Jiannong Fang, et al., Wind energy prediction in highly complex terrain by computational Fluid dynamics, Energies 12 (1311) (2019) 1—12, https://doi.org/10.3390/en12071311.

[57] Erasmo Cadenas, et al., Wind speed forecasting using the NARX model, case: La Mata, Oaxaca, México, Neural Comput. Appl. 27 (8) (2016) 2417—2428, https://doi.org/10.1007/s00521-015-2012-y. Springer.

[58] Yang Gao, Joo Meng, NARMAX time series model prediction: feedforward and recurrent fuzzy neural network approaches, Fuzzy Set Syst. 150 (2) (2005) 331—350, https://doi.org/10.1016/j.fss.2004.09.015. ISSN: 0165-0114.

[59] Muhammad Jawad, et al., Genetic algorithm-based non-linear autoregressive with exogenous inputs neural network short-term and medium-term uncertainty modelling and prediction for electrical load and wind speed, J. Eng. 20 (8) (2018) 721—729, https://doi.org/10.1049/joe.2017.0873, eISSN 2051-3305.

[60] Sara Barja-Martinez, et al., Artificial intelligence techniques for enabling Big Data services in distribution networks: a review, in: Renewable and Sustainable Energy Reviews, vol. 150, 2021, p. 111459, https://doi.org/10.1016/j.rser.2021.111459. ISSN: 1364-0321. DOI.

[61] Hui Liu, Xi wei Mi, Yan fei Li, Wind speed forecasting method based on deep learning strategy using empirical wavelet transform, long short term memory neural network and Elman neural network, in: Energy Conversion and Management, vol. 156, 2018, pp. 498—514, https://doi.org/10.1016/j.enconman.2017.11.053. ISSN: 0196-8904.

[62] Anqi Xie, et al., A short-term wind speed forecasting model based on a multivariable long short-term memory network, Atmosphere 12 (5) (2021), https://doi.org/10.3390/atmos12050651. ISSN: 2073-4433.

[63] Metamorf. *Ecuador Explorer.Com.* Ecuador Explorer.Com. 1997-2018. URL: http://www.ecuadorexplorer.com/html/location_geography_climate.html..

[64] Gobierno del Ecuador, *INAMHI.* INAMHI2020, May 2017. URL: http://www.serviciometeorologico.gob.ec/biblioteca/.

[65] IEC, IEC 61400-61412-1, International Electrotechnical Commission, Geneva, Switzerland, 2005. https://webstore.iec.ch/publication/26603.

[66] Marius Paulescu, et al., Chapter 9 - Nowcasting solar irradiance for effective solar power plants operation and smart grid management, in: Ravinesh Deo (Ed.), Predictive Modelling for Energy Management and Power Systems Engineering, Elsevier, 2021, pp. 249—270.

[67] Pedro Gomes, Ruiz Castro, Wind speed and wind power forecasting using statistical models: AutoRegressive moving average (ARMA) and artificial neural networks (ANN), in: International Journal of Sustainable Energy Development vol. 1, Dec. 2012, https://doi.org/10.20533/ijsed.2046.3707.2012.0007.

[68] Ajoy K. Palit, Dobrivoje Popovic, Computational Intelligence in Time Series Forecasting: Theory and Engineering Applications, Springer, 2005, ISBN 1852339489. Springer-Verlag London Limited: Springer.

[69] Haykin Simon, in: Pearson (Ed.), Neural Networks, Second, Pearson Education, Nueva Delhi 110092 India, 2005.

[70] Howard B. Demuth, et al. *Neural Network Toolbox^{TM} 7 User's Guide*, The MathWorks Inc. on line. MathWorks, 2010.

[71] Eugen Diaconescu, The use of NARX neural networks to predict chaotic time series, in: WSEAS Transactions on Computer Rerearch 3.3, Mar. 2008, pp. 182—191. ISSN: 1991-8755.

[72] Tyler Blanchard, Biswanath Samanta, Wind speed forecasting using neural networks, Wind Eng. 44 (1) (2020) 33—48. https://doi.org/10.1177/0309524X19849846.

[73] Eng Loh, et al., Bitcoin price forecasting using different artificial neural network and training algorithm, in: International Journal of Advanced Trends in Computer Science and Engineering 9, Warse, 2020, pp. 374—378. https://www.researchgate.net/publication/345694892_Bitcoin_Price_Forecasting_using_Different_Artificial_Neural_Network_and_Training_Algorithm.

[74] Kerem. Cigizoglu, Özgür Kişi, Flow prediction by three back propagation techniques using k-fold partitioning of neural network training data, ISSN: 0029-1277, Nord. Hydrol 36 (1) (Feb. 2005) 49—64, https://doi.org/10.2166/nh.2005.0005. eprint.

[75] Sepp Hochreiter, Jürgen Schmidhuber, Long short-term memory, ISSN: 0899-7667, Neural Comput. 9 (8) (Nov. 1997) 1735—1780, https://doi.org/10.1162/neco.1997.9.8.1735. eprint.

[76] Fitriana R. Ningsih, et al., Wind speed forecasting using recurrent neural networks and long short term memory, in: 2019 6th International Conference on Instrumentation, Control, and Automation (ICA), IEEE, 2019, pp. 137—141.

[77] MathWorks, Mastering Machine Learning, A Step-by-step Guide with MATLAB, 1st, The MathWorks Inc. The MathWorks, Inc. 3 Apple Hill Drive Natick, MA, Sept. 2010, 01760-2098, https://www.mathworks.com/campaigns/offers/mastering-machine-learning-with-matlab.html.

[78] Cunbin Li, et al., Short-term wind power prediction based on data mining technology and improved support vector machine method: a case study in Northwest China, J. Clean. Prod. 205 (2018) 909—922, https://doi.org/10.1016/j.jclepro.2018.09.143. ISSN: 0959-6526.

[79] Yun Wang, et al., A review of wind speed and wind power forecasting with deep neural networks, Appl. Energy 304 (2021) 117766, https://doi.org/10.1016/j.apenergy.2021.117766. ISSN: 0306-2619.

[80] Y.-X. Wu, et al., Data-driven wind speed forecasting using deep feature extraction and LSTM, 12, in: IET (Ed.) 13,IET Renewable Power Generation, 2019, pp. 2062—2069. cited By 21.

[81] W. Yao, et al., Multidimensional LSTM Networks to Predict Wind Speed, IEEE, 2018, pp. 7493—7497.

[82] Ghulam Abbas, Menaa Nawaz, Farrukh Kamran, Performance comparison of NARX amp; RNN-LSTM neural networks for LiFePO4 battery state of charge estimation, in: 2019 16th International Bhurban Conference on Applied Sciences and Technology (IBCAST), 2019, pp. 463—468, https://doi.org/10.1109/IBCAST.2019.8667172.

Germánico López received his Master degree (2013) in Renewable Energy in Electrical Systems from University Carlos III of Madrid, Spain. Nowadays, he is pursuing his PhD at LEMUR Research Group at University of Oviedo. His main research interests have to do with the wind speed and power forecasting over complex terrain at high altitude, distribution networks, networks analysis and simulation and failures detection. His areas of interest are high wind power system modeling, and high scale integration of renewable energy into power system.

Pablo Arboleya (SM'13) received the M.Sc. and Ph.D. (with distinction) degrees from the University of Oviedo, Gijón, Spain, in 2001 and 2005, respectively, both in Electrical Engineering. Nowadays, he works as Associate Professor in the Department of Electrical Engineering at the University of Oviedo, he is Managing Editor of the International Journal of Electrical Power and Energy Systems and holder of the Gijón Smart Cities Chair at the University of Oviedo. Presently his main research interests are focused in the micro-grid and smart-grid modeling and operation techniques, Internet of the Energy applications, railway traction networks simulation and combined AC/DC power flow algorithms.

A.2   A novel probability density function applied to wind characterization in order to evaluate the wind power potential in Tungurahua, Ecuador's Andean region.

A novel probability density function applied to wind characterization in order to evaluate the wind power potential in Tungurahua, Ecuador's Andean region

Javier García del Valle, Alex Mayorga and Germánico López

Abstract

In this investigation, the measured wind characteristics over the span of a year is reported for a location in the highlands of the Ecuadorian Andes. The first part of the article has been devoted to study the influence of the sampling rate on the annual power density by means of a number of techniques, namely the ensemble of means, aliasing, and Fourier low-pass filters. A byproduct of this analysis, once the wind frequency pattern was identified, has been the proposal of a new probability density function based on a daily Gaussian-weighted average of sinusoidal waveforms. The second part of the article thoroughly develops the proposed model along with a comparison with the measured data. The model proposed herein was found appropriate for describing poor class wind locations, as the one portrayed here, due to its ability of predict a zero wind probability.

Keywords

Probability density function, Fourier analysis, truncated Gauss distribution, remote electrification, high altitude

Introduction

Wind energy has played a residual role in Ecuador's national electric grid. Aside from the recent publication of a nation-wide wind map (MEER, 2013), publicly available experimental wind measurements are altogether missed, with the exception of Villonaco wind farm (Ollague and Crespo, 2014). The contribution from neighboring regions is also discrete. Encinas et al. (2015) and Forero et al. (2009) measured the wind potential for the Bolivian altiplano and a site close to Bogotá, respectively and concluded a poor annual average wind speed. In this investigation, experimental wind measurements over a year in the Ecuadorian highlands are introduced. Frequency-domain analysis as well as wind characterization through probability density functions (PDFs) will be applied to the experimental data set.

Frequency-domain analysis is two-fold. In the lower frequency range, its application is directed toward the determination of seasonal or yearly wind patterns (Bett et al., 2017). Such analysis is excluded in the present investigation due to the limited measured range. On the contrary, in the higher frequency range, power spectrum analysis has been used to determine the sampling time to be employed in data-loggers in meteorological stations (Van der Hoven, 1957). The current industry standard 10-min time averages (International Electrotechnical Commission (IEC), 2005) have been recently challenged by Rodriguez-Hernandez et al. (2016), where 1-min time averages are suggested to accurately capture the actual energy pattern for small wind turbine simulations. Provided the majority of data-loggers store signal time averages, the question arises whether other averaging methods could provide better signal fidelity. This remark has been largely overlooked in the literature and will be explored in this investigation.

Área de Energía, Facultad de Ingeniería Civil y Mecánica, Universidad Técnica de Ambato, Ambato, Ecuador

Corresponding author:

Javier García del Valle, Área de Energía, Facultad de Ingeniería Civil y Mecánica, Universidad Técnica de Ambato, Avd Los Chasquis y Río Payamino, Ambato, CP 180206, Ecuador.
Email: jav.garcia@uta.edu.ec

Wind characterization is usually described by means of a PDF, which fully suppresses any time information. As suggested by the IEC (2005) standard, Weibull and Rayleigh PDFs have been repeatedly used for this purpose (Bilir et al., 2015; Pishgar-Komleh et al., 2015). Furthermore, the goodness of fit of the Weibull distribution for a number of algorithms has been studied by Dorvlo (2002), Bhattacharya and Bhattacharjee (2009), and Mohammadi et al. (2016). The results show no agreement due to the fact that not all algorithms, neither the fitting tests were uniform among these investigations. The performance of a number of well-known, non-symmetrical PDFs have been examined by Tar (2008) and Ouarda et al. (2015). The Weibull distribution did not excel in any of the cases studied. The mathematical derivation of a PDF is a more complex subject often associated with a number of simplified hypothesis, as it is the case for the Rayleigh distribution (Davenport, 1967). Harris and Cook (2014) extended the model by assuming non-zero mean velocity vector and different variance for each of the x and y wind components. They concluded that the Weibull distribution is a especial case of their model. However, there are two scenarios where the aforementioned PDFs fail to correctly predict wind behavior. The first is when calms are present and the second is when long periods are considered.

When calms are a predominant site feature, either the Weibull or Rayleigh PDF fail due to its property of assigning zero probability to zero wind velocity. A mathematical artifact was introduced by Takle and Brown (1978) and later used by Torrielli et al. (2013) to modify this behavior. A joint PDF consisting of a Weibull and a Dirac delta function was used, being the latter responsible for modeling the calms. If long periods are considered, seasonal effects substantially modify the wind histogram, usually producing a curve with local maximums associated with each season (Kumaravel et al., 2014). Again, a joint probability function, that is, a weighted average of simple PDFs, is used in these cases (Cook, 2015).

This investigation is focused on two areas. The first one, taking as starting point the work of Rodriguez-Hernandez et al. (2016), studies the influence of data-averaging procedures on the power density. Three techniques have been considered, the industry standard signal time averages, Fourier-based low-pass filters, and random signal undersampling. The second one deals with the characterization of the wind measurements by means of a PDF. The selected site presents calms and seasonal variations. The latter have been minimized by a monthly analysis of the wind. In order to account for the calms, rather than a joint PDF, a new two-parameter PDF based on the truncated Gaussian distribution of a sinusoidal daily wind pattern has been derived and applied to the measured data. To the best of the authors knowledge, this PDF has not been used before to describe the wind characteristics. Provided the resulting fitting error was below than that of the Weibull distribution, a number of two-parameter PDFs were evaluated in order to see the extent of the validity of the proposed algorithm.

Site selection and measurement station

The orography of the equatorial Andes is characterized for two ranges running alongside in north to south direction. The valley in between is home to major cities, from Quito to Cuenca. Tungurahua province is also located in this valley, spanning from the east to west range. The criteria established in order to place the meteorological tower included a socio economical constraint, that is proximity to remote communities as portrayed by EEASA (2014) and an orography constraint that is to favor local prominent locations (Kim et al., 2017).

After visual inspection of six potential sites, a location close to the community of Rioblanco was considered the best option as the former criteria were met. The actual location is detailed in the Table 1. The place is a high plateau bordering the Chimborazo volcano (6263 MASL).

The sensors used in the meteorological tower are specified in Table 2. The wind speed was measured at heights of 10, 20, and 30 m. The remaining properties were measured at a height of 5 m. A data logger model "NRG Symphony Plus 3" was used to collect the data. The sampling frequency is 1 Hz, averaging the readings in 10 min intervals. The average, standard deviation, and extreme values are stored in the data logger memory. The system has run continuously from October 2015 to September 2016. No data error was detected in the whole data set.

Due to the bias introduced in the wind velocity analysis due to the wind direction, it has been preferred to provide a short account of the vane measurements in this section. The wind rose, represented in plane mode, has been included in Figure 1. An east blowing wind is predominant in this site, feature which indicates a site effect due to the complex range-valley-range structure described earlier. Usually, the PDF for each direction is included, but, since the dispersion is low,

Table 1. Location of the meteorological tower.

Latitude	1°21'22.0799" S
Longitude	78°49'3.1689" Q
Altitude	4016.5 MASL

Table 2. Relevant measure sensors used in the meteorological tower.

Type	Model	Full scale	Deviation
Anemometer	NRG #40C	1 ms⁻¹ 96 ms⁻¹	±0.5% F.S.
Vane	NRG #200P	360°	±1% F.S.
Barometer	NRG BP20	15–115 kPa	±1.5% F.S.
Temperature	NRG 110S	−40° to 52.5°C	±1.3% F.S.
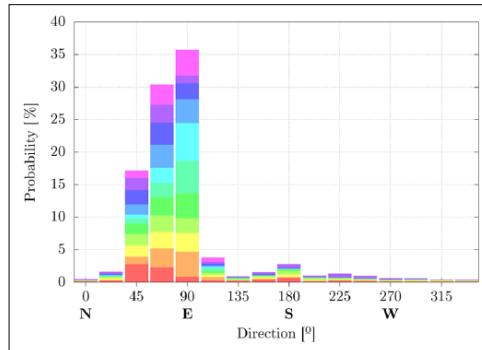
Figure 1. Wind direction probability. Each bin represents the monthly contribution to each direction.

this would merely be the PDF of the wind series itself. Therefore, the monthly contribution to each direction has been preferred. It can be seen that monthly contributions are uniform for each direction.

Part 1: effect of averaging techniques into the power density

Methodology

As discussed in "Introduction," this section explores the adequacy of wind speed time averaging commonly used in commercial data-loggers (Rodriguez-Hernandez et al., 2016) in relation with other averaging techniques. The final goal of this section is to apply three different averaging procedures to the measured data and compare the mismatch between the actual and the signal-averaged wind power density. In order to standardize the nomenclature, simple time averaging is referred to as the mean ensemble, meaning the average of the measured velocity over a span of time. Its application is largely due to a legacy byproduct of the dawn of the personal computer, as discussed by Griffith et al. (1956). The mathematics behind its analysis are an adaptation of that used in electrical signal processing (Blackman and Tukey, 1958). Little though has been devoted to the fact that while in electrical engineering the signal squared (either the voltage or intensity) is a direct measurement of the power, in fluid dynamics is not, and it rather should be called a variance spectrum analysis instead of power spectrum. The wind power density can be computed by means of equation (1), (Safari and Gasore, 2010), for either a discrete or a continuous sample.

$$\frac{P}{A} = \frac{1}{n}\sum_{i=1}^{n}\frac{1}{2}\cdot\rho\cdot v_i^3 = \frac{1}{2}\cdot\rho\cdot\int_0^\infty v^3\cdot f(v)\cdot dv \tag{1}$$

The mean ensemble technique applied to the wind speed will result in an underestimation of the power density due to the fact that the cube of the mean is lower than the mean of the cubes. A simple case may be devised to test this statement. For the sake of discussion, if a dipole with values "$\mu+\sigma$" and "$\mu-\sigma$" is considered, where "μ" is the mean value and "σ^2" is the variance, the mean power relative error for the averaged power density $\bar{P}$ may be easily computed, equation (2)

$$\frac{P - \overline{P}}{\overline{P}} = \frac{\frac{1}{2} \cdot \left((\mu + \sigma)^3 + (\mu - \sigma)^3 \right) - \mu^3}{\mu^3} = 3 \cdot \left(\frac{\sigma}{\mu} \right)^2 \tag{2}$$

Furthermore if "i" poles "$(\mu + \sigma_i)$" are considered, equation (3) may be derived

$$\frac{P - \overline{P}}{\overline{P}} = \frac{\frac{1}{n} \cdot \sum_{i}^{n} (\mu + \sigma_i)^3 - \mu^3}{\mu^3} = \frac{3 \cdot \mu \cdot \sum_{i}^{n} \sigma_i^2 + \sum_{i}^{n} \sigma_i^3}{n \cdot \mu^3} \tag{3}$$

The first term in the numerator is the variance and the second term is the skewness. Since typical wind distributions have negative skewness, the first term may be considered as the upper bound for the mismatch between the actual power density and that obtained by the mean ensemble technique. If a periodic symmetric function, "$g(t)$," as define in equation (4) is considered, an expression may be derived for the power density mismatch, equation (5)

$$g(t) = \mu + h(t), \quad \text{where,} \quad h(t) = -h(t + \tau) = h(t + 2 \cdot \tau) \tag{4}$$

$$\frac{P - \overline{P}}{\overline{P}} = \frac{\frac{\int_{0}^{2 \cdot \tau} \left(\mu + h(t) \right)^3 \cdot dt}{2 \cdot \tau} - \mu^3}{\mu^3} =$$

$$\frac{\left(\frac{\int_{0}^{2 \cdot \tau} \left(\mu^3 + 3 \cdot \mu^2 \cdot h(t) + 3 \cdot \mu \cdot h(t)^2 + h(t)^3 \right) \cdot dt}{2 \cdot \tau} \right) - \mu^3}{\mu^3} = \tag{5}$$

$$\frac{\left(\mu^3 + 3 \cdot \mu \cdot \frac{\int_{0}^{2 \cdot \tau} h(t)^2 \cdot dt}{2 \cdot \tau} \right) - \mu^3}{\mu^3} = 3 \cdot \left(\frac{\sigma}{\mu} \right)^2$$

Being the dipole, a particular case of equation (4), the latter result, not only includes but is equal to the former. The implications of equation (5) may be further extended. Provided the equation (1) is commutative, the data series order may be altered. If the wind were to be derived from a symmetrical PDF, the data could be rearranged in a way equation (4) applies. The result of equation (3) together with equation (5) suggests that not only the upper limit for the power density mismatch is a function of the variance over the mean squared but also that this bound is related with a symmetric distribution. Thus, it can be inferred that the quotient of the actual power relative error, to that computed with equation (5) is a direct measurement of the symmetry of the wind distribution. A long discussion related with the non-Gaussian wind behavior and its implications applied to structural aerodynamic loads may be found in Gurley et al. (1997).

Along with the mean ensemble technique, a low-pass Fourier-based filter and undersampling the original data set have been considered as alternative averaging procedures. The latter is related to the notion of signal aliasing in electrical engineering. Its behavior is well defined (Griffith et al., 1956), there is mainly a shift of energy from a higher frequency to a lower frequency. The former is based on the fast Fourier transform (FFT) of the data set, it then nulls higher frequencies and transforms back the filtered data.

As stated earlier, this three methods have been applied to the measured data. Given the 10-min average mean velocity provided by the data logger, "v_i," the algorithms to compute the upper bound, mean ensemble, and aliasing curves are shown in equations (6) to (8), respectively. The function "INV" refers to the inverse gate (INV) function, equation (9).
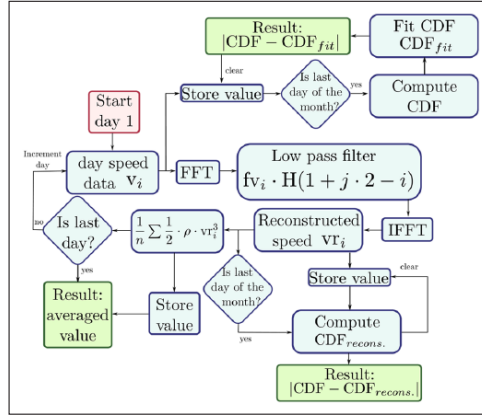
Figure 2. Programed flow diagram for computing the power density by means of a Fourier-based low-pass filter.

The operator "%" computes the remainder of a division. In each of the three cases, the data is clustered in "j" elements. The artificial sample rate is thus reduced by a factor of "j" The upper bound term requires further explanation. Both the mean and the variance are computed in an interval ranging from the "$i \cdot j$" to the "$(i \cdot (j+1)-1)$" index, that is the "j" elements considered for each interval

$$\frac{P}{A}\text{upper bound} = 3 \cdot \left(\frac{\sigma}{\mu}\right)^2 = \frac{3}{n}\sum_{i=1}^{\frac{n}{j}}\left(\frac{\sigma\left(\mathbf{v}_{[(i \cdot j):(i \cdot (j+1)-1)]}\right)}{\mu\left(\mathbf{v}_{[(i \cdot j):(i \cdot (j+1)-1)]}\right)}\right)^2 \tag{6}$$

$$\frac{\overline{P}_{\text{ensemble}}(j)}{A} = \frac{1}{n}\sum_{i=1}^{\frac{n}{j}}\frac{1}{2} \cdot \rho \cdot \left(\sum_{k=1}^{j}v_{(i \cdot j+k)}\right)^3 \tag{7}$$

$$\frac{\overline{P}_{\text{aliasing}}(j)}{A} = \frac{1}{n}\sum_{i=1}^{n}\frac{1}{2} \cdot \rho \cdot v_i^3 \cdot \text{INV}(i\%j) \tag{8}$$

$$\text{INV}(x) = \begin{cases} 0 & \text{if } x \neq 0 \\ 1 & \text{if } x=0 \end{cases} \tag{9}$$

Regarding the FFT, it takes an "n" length vector "v" and returns another "n" length vector "fv," where the first element is the averaged value and the "$1+2 \cdot j$" and "$2+2 \cdot j$" are the cosine and sine component of the "j_{th}" harmonic, respectively. The flow diagram of the computer program implemented to solved the low-pass filter procedure has been detailed in Figure 2 and will be used in the following section, so only the central branch will be considered here. The Heaviside function $H(x)$, used in Figure 2, is defined in equation (10)

$$\text{H}(x) = \begin{cases} 0 & \text{if } x \leq 0 \\ 1 & \text{if } x>0 \end{cases} \tag{10}$$

Furthermore, the density "ρ" in equations 7 and 8 is considered constant and equal to 0.824. It is computed by the ideal gas law based on the year average pressure, 658.2 Pa, and temperature, 5.3ºC. It is assumed that the density variation plays
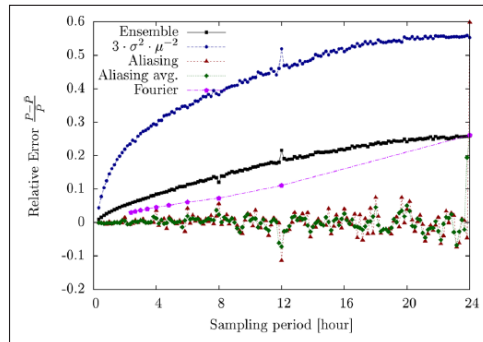
Figure 3. Relative power density error for the mean ensemble and undersample techniques.

but a residual role in the former equations. All the data processing was programed in C++, using, when necessary, the mathematical library GNU-GSL (GSL, 2017). For simplicity and readability of the figures, only the wind speed at 30 m has been considered throughout the manuscript unless explicitly noted.

Results

The results for the three different averaging procedures considered has been plotted in Figure 3, with a maximum averaged period of 1 day.

The following remarks can be made regarding Figure 3: (1) the mean ensemble technique power density underestimation grows proportionally to the averaged window considered; (2) the upper limit term follows the same pattern, being its value approximately doubled in relation with the former for whole window considered; this fact clearly demonstrate the non-symmetry of the wind speed as discussed earlier; (3) the undersample technique error is always below than that of the mean ensemble, confirming the shifting energy behavior mentioned earlier. The result of the aliasing curve is remarkable, since with only three measurements a day (8 h interval), the power density error would be within $\pm$ 3%; (4) although it may seem unnoticeable, three peaks are clearly visible at 6, 12, and 24 h. The third peak induce a massive error in the aliasing curve. The 12-h peak error is predominant in all curves; (5) trying to smooth out the aliasing curve, the moving average of two elements was introduced as "Aliasing avg." It does smooth the curve, diminishing the error for every point, but the peaks are still clearly visible; (6) from the aliasing curve results, it is clear than the day is the key temporal unit to measure wind power potential; (7) for the Fourier-based low-pass filter, as expected, the result for a 24-h period, which is simply the average of the data, is the same as that obtained by the mean ensemble technique; and (8) the error falls almost linearly with the sampling period considered and is almost halved for each point in relation with the mean ensemble technique, inferring that the Fourier transform is a more suitable procedure than the former.

Based on the former results, a prediction concerning the power leakage due to the averaging procedure of 1 Hz signals to obtain the 10-min mean ensemble output produced by the data logger, may be accomplished. Since both the value of the standard deviation and the average are directly provided by the data logger, the upper limit bound term for the measured data is straightforward computed by means of the equation (11), obtaining a value of 0.146

$$\frac{P}{A} \text{upper bound} = 3 \cdot \left(\frac{\sigma}{\mu}\right)^2 = \frac{3}{n} \sum_{i=1}^{n} \left(\frac{\sigma_i}{\mu_i}\right)^2 \tag{11}$$

It is theorized that the rule 2:1 found for the macro time scale also applies to the micro time scale. Thus, a theoretical extra 7.3% power would be available for the selected site. However, this enhancement is quite unlikely to be realized by an actual machine, since the inertia of the system would rather prevent or at least attenuate this high-frequency power resource as mentioned by Rodriguez-Hernandez et al. (2016). It is beyond the scope of this investigation the dynamic time response of wind turbines. A last remark concerning equation (11), since the quotient "σ / μ" is commonly portrayed as the turbulence intensity, this parameter might be thought as the upper limit high-frequency power potential hindered by wind turbines dynamic response.

As a summary of this section, three methods have been studied, the aim of which is to represent a set of data by means of a smaller subset. Provided that ultimately for each and every point in Figure 3, each method uses a reduced subset of the same length, it must be concluded that the aliasing method excels in utilizing scarce data. It is followed by the Fourier analysis and the mean ensemble technique in that order.

Part 2: wind characterization based on PDFs

Methodology

PDFs are a convenient way of summarizing wind characteristics, since a reduced number of parameters, namely those of the distribution, are needed. As discussed in the preceding section, the wind is largely a non-symmetric phenomenon, such as the PDF traditionally used to represent it. Instead of working with the PDF, its integral or cumulative density function (CDF) is preferred, since the dependence of the bin velocity size used to compute the discrete PDF is eliminated. The algorithm to compute the experimental CDF is shown in equation (12) in terms of the Heaviside function, equation (10). The mean absolute deviation (MABD) is proposed to compare any two CDFs, equation (13). The bin velocity size used in this investigation is $0.25\,ms^{-1}$.

$$CDF(v) = \frac{1}{n}\sum_{i=1}^{n} H(v - v_i) \tag{12}$$

$$MABD\,(CDF_1, CDF_2) = \frac{1}{n}\sum_{i=1}^{n}\left|CDF_2(bin \cdot i) - CDF_1(bin \cdot i)\right| \tag{13}$$

After considering the results obtained so far and after plotting the combination of the daily averaged speed together with the cloud of points which originated it, Figure 4(a), the concept of new way of obtaining a PDF arose based on the daily wind velocity profile.

From Figure 4(a), it can be seen that the daily wind pattern is characterized by the existence of a night calm, and a half-sine like velocity profile during light hours. This behavior is found in other locations (Buflasa et al., 2008; Cook, 2015). Thus, instead of a timeless PDF, the information provided by the daily wind velocity profile may be used as the base for the construction a daily-based PDF. The idea is to assume a daily velocity curve and apply to that curve a PDF. The assumed daily velocity has been taken as a sinusoidal wave and the PDF as a truncated Gaussian distribution. Provided the velocities cannot be negative, the left Gaussian tail producing such negatives values are clustered at zero, thus the truncated distribution. The outcome of this arrangement is two-fold, first it produces a non-symmetric PDF, and second, it assigns a non-zero value probability to zero velocity, a feature of paramount importance in poor wind resource sites.

The use of a sine function for the day velocity profile is not random. If the Fourier filter described in the preceding section is used, the experimental CDF may be compared against the CDF obtained by the Fourier-filtered data. The numerical procedure follows the lower branch of the flow diagram shown in Figure 2. The results are shown in Figure 5, where the dependence of the MABD in terms of the number of Fourier harmonics is illustrated. As expected, the error rapidly falls with the numbers of terms. However, the bulk of the error reduction appears at the transition between the zeroth harmonic (mean ensemble) and the first harmonic. A slow error reduction rate is found afterwards. Based on this results, the sinusoidal waveform was taken as the base function for the proposed PDF.

The parameters of the proposed PDF are three, the mean (μ_s) and amplitude ("θ") of the sinusoidal waveform, "$\mu_s - \theta \cdot sin(((2 \cdot \pi) / T) \cdot t)$," and the standard deviation of the Gauss distribution ("σ"). The CDF of such waveform may be computed according to equation (14). For simplicity, this function will be called "$CDF_{sin}(A, B, v)$". The proposed CDF is simply the Gaussian-weighted average of the sinusoidal waveform. To fully understand the concepts put forth herein, Figure 4(b) has been included. This figure is a bitmap representing the probability of having a given speed at a given time. The sinusoidal period has been set to 24 h. Furthermore, the maximum probability has been scaled to one in order to improve the readability of the figure.

In the continuum, this function may be written as in equation (15). The following remarks apply: (1) the mean value of the sinusoidal wave must not be negative, thus the first integral term starts at 0; (2) the tail probability for mean values lower than zero is assigned to zero (second integral term); (3) consequently, there are two non-symmetrical sources, the second integral term and the fact that the speed v cannot be negative.
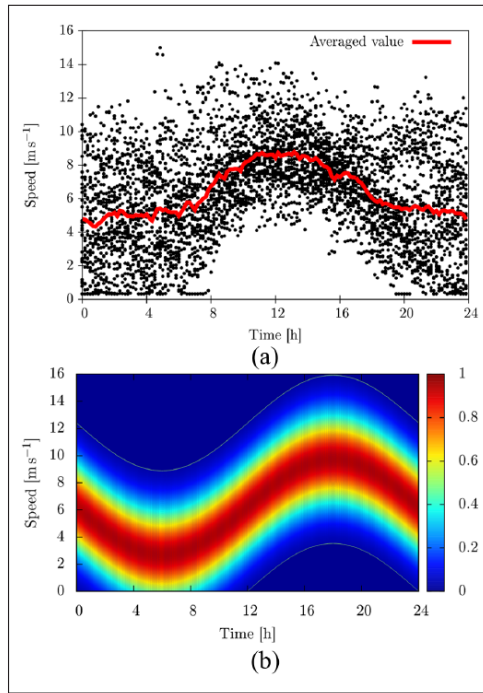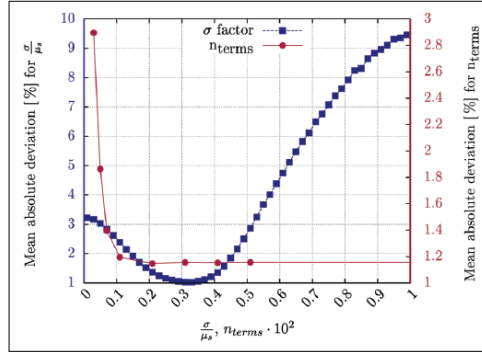
Figure 4. Wind speed values for the month of May at a height of 30 m: (a) daily mean velocity together with measured values and (b) daily probability of the proposed PDF, computed with $\mu_s = 6.36\,\text{ms}^{-1}$, $\theta = 3.72\,\text{ms}^{-1}$, and $\sigma = 2.37\,\text{ms}^{-1}$.
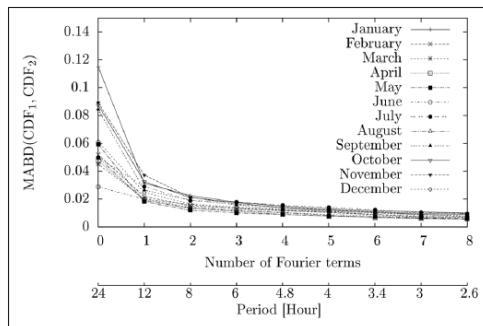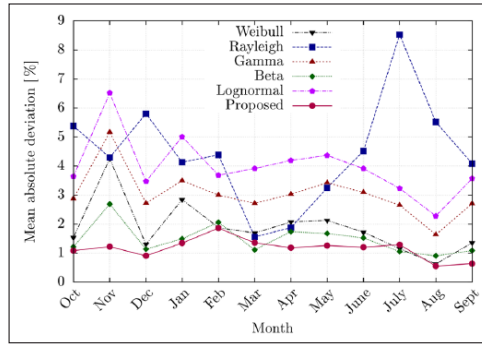

Figure 5. Mean absolute deviation between the original CDF and the CDF obtained from the Fourier-filtered data as a function of the terms of Fourier harmonics.

The equation (15) has been discretized in order to be implemented in a computer program. The second integral may be computed explicitly. The trapezoidal rule with "*n*" steps was used for the first one. The integral extents up to $2 \cdot \mu_s$, being the right tail probability assigned to this value

$$\text{CDF}_{sin}(\mu_s, \theta, v) = \begin{cases} 0 & \text{if } v \le (\mu_s - \theta) \\ \dfrac{1}{2} - \dfrac{1}{\pi} \cdot \arcsin\left(\dfrac{\mu_s - v}{\theta}\right) & \text{if } (\mu_s - \theta) < v < (\mu_s + \theta) \\ 1 & \text{if } v \ge (\mu_s + \theta) \end{cases} \tag{14}$$

Figure 6. Influence of the Gaussian σ and of the number of terms used in the integration equation (15), on the mean absolute deviation in regards of the experimental data.

Figure 7. Mean absolute deviation between the original and fitted CDF.

$$\mathrm{CDF}(\mu_s,\theta,\sigma,\mathrm{v}) = \int_0^\infty G(x-\mu_s,\sigma)\cdot CDF_{sin}(x,\theta,\mathrm{v})\cdot dx + CDF_{sin}(0,\theta,\mathrm{v})\cdot \int_{-\infty}^0 G(x-\mu_s,\sigma)\cdot dx \qquad (15)$$

Before this procedure is applied to the measured data, it is worth exploring the meaning of the three parameters of the proposed distribution. Is theorized that "μ_s" should be close to the mean value of the wind speed in the considered period. The parameter "θ" should be related with an estimator of the width of the distribution. In this case, either the variance $(\theta = \sqrt{2}\cdot\sigma)$ or the MABD $(\theta = \mathrm{MABD}\cdot(\pi/2))$ of the measured data in the considered period could be used. A subtle detail should be considered for the Gaussian standard deviation "σ". This parameter is related with the mean of the variance of the data for each time rather than the variance of the whole data set. Since the former two parameters are directly related with a visible shape feature and the latter is not, it has been considered useful to independently study its influence on the distribution fitting error. For that purpose, the CDF proposed herein has been fitted to the measured data in a monthly basis, as illustrated in the flow diagram introduced in the preceding section, Figure 2. The least square fitting procedure has been used for that purpose. The details of the algorithm can be found in the GSL library documentation (GSL, 2017).

After any calculation was performed, the influence of the number of terms used for the integral shown in equation (15) was explored. If was found, Figure 6, that after 200 terms, the error variation is minimal. The value of "σ" amounted to $0.25\cdot\mu_s$, thus the fitting algorithm only has to compute two parameters, namely those related with the underlaid sinusoidal wave. For the remaining calculations, the number of terms was set to 500.

In order to find a dimensionless parameter, the quotient "σ/μ_s" was introduced. This quantity was sequentially varied from 0 to 1 and the subsequent two-parameter fitting performed. The resulting year-averaged MABD is shown in Figure 6. There is a minimum at a ratio of approximately 0.3, being the error moderate in the range from 0.2 to 0.4. Based on these results, for

Table 3. General wind speed statistics along with fitted parameters for selected PDF at a height of 30m. For the measured variables, the units are μ, σ, MABD (ms^{-1}), and Power (Wm^{-2}). The fitting coefficients are based on speeds with units (ms^{-1}).

	Measured			Proposed PDF		Weibull		Gamma		Beta		Log-normal	
	μ	σ	Power	μ_s	θ	k	c	α	c	α	c	ζ	σ
Jan	4.17	2.28	69.3	3.97	3.42	1.46	4.66	1.86	2.29	1.18	2.44	1.24	0.73
Feb	6.36	2.13	163.4	6.28	2.74	2.73	7.16	6.10	1.06	3.28	4.52	1.81	0.39
Mar	5.38	2.41	124.0	5.18	3.48	1.87	6.07	2.97	1.85	1.81	3.33	1.57	0.57
Apr	5.19	2.38	112.8	5.00	3.48	1.83	5.88	2.84	1.87	1.85	4.10	1.53	0.58
May	6.36	2.37	171.4	6.27	3.28	2.38	7.22	4.64	1.41	2.45	3.29	1.79	0.46
Jun	7.26	2.42	235.3	7.21	3.17	2.72	8.21	6.05	1.23	3.05	3.71	1.94	0.40
Jul	7.66	1.91	236.5	7.64	1.90	3.72	8.46	10.95	0.71	4.65	3.97	2.01	0.30
Aug	7.08	1.98	200.0	6.94	2.33	3.20	7.78	8.12	0.87	4.81	7.47	1.91	0.35
Sep	5.92	1.97	127.4	5.83	2.63	2.65	6.64	5.75	1.05	3.00	3.83	1.72	0.41
Oct	5.53	1.70	97.9	5.46	2.16	2.93	6.17	6.97	0.80	3.31	3.56	1.67	0.37
Nov	4.44	2.22	72.9	4.29	3.36	1.69	5.10	2.35	1.97	1.29	1.96	1.37	0.65
Dec	6.55	1.94	160.6	6.488	2.411	3.039	7.307	7.439	0.893	3.672	4.150	1.840	0.362
Year	5.99	2.14	147.6	MABD=1.2%		MABD=1.9%		MABD=3.0%		MABD=1.5%		MABD=4.0%	

PDF: probability density function; MABD: mean absolute deviation.

Table 4. Selected probability density function for wind speed characterization.

Type	PDF	Range
Rayleigh	$$f(x) = \frac{x}{c^2} \cdot e^{\left(-\frac{x^2}{2 \cdot c^2}\right)}$$	$x > 0$
Weibull	$$f(x) = \frac{k}{c^k} \cdot x^{k-1} \cdot e^{\left[-\left(\frac{x}{c}\right)^k\right]}$$	$x > 0$
Gamma	$$f(x) = \frac{1}{\Gamma(a) \cdot b^a} \cdot x^{a-1} \cdot e^{-\frac{x}{b}}$$	$x > 0$
Beta	$$f(x) = \frac{\Gamma(a+b)}{\Gamma(a) \cdot \Gamma(b)} \cdot x^{a-1} \cdot (1-x)^{b-1}$$	$0 \leq x \leq 1$
Log-normal	$$f(x) = \frac{1}{x \cdot \sqrt{2\pi\sigma^2}} \cdot e^{-\frac{(ln(x)-\zeta)^2}{2\sigma^2}}$$	$x > 0$

PDF: probability density function.

the remaining calculations "σ" was taken as "$0.3 \cdot \mu_s$." It shall be noted that, according the description given earlier, the year average of the quotient "σ / μ" for each of the 10-min interval is 0.42, relatively close to the minimum error value.

Results

The proposed two-parameter PDF has been fitted to the experimental CDF in a monthly basis following the procedure shown in the upper branch of Figure 2. The absolute deviation for the fitting is shown in Figure 7. Furthermore, the numerical values for the parameters "μ_s" and "θ" have been included in Table 3 along with other wind statistics. The following comments follows: (1) the fitting error is approximately 1% for all months; (2) the fitting coefficients "μ_s" and "θ," from Table 3, are in accordance with the detail provided earlier, namely they are closely related with the monthly mean and absolute deviation, respectively; (3) the month analysis is justified by the strong seasonal variation, as can be seen by the mean power density in Table 3. The best months in terms of power density are June, July, and August. This is also the case for Villonaco wind farm (Ollague and Crespo, 2014); and (4) an average wind speed of 5.99 and power density of 147 show a low-grade wind class completely out of reach from commercial exploitation. However, mini eolic could by feasible with such moderate resource.

Provided the fitting error was small, it was decided to test a number of commonly used PDF (Ouarda et al., 2015). The list of selected one- and two-parameter PDFs are included in Table 4. Any further detail about these distributions may be found in most statistics books (Montgomery and Runger, 2014). Since the range of Beta distribution is right bounded, the data velocity has been scaled by dividing the month data set by the maximum value. The least square fitting algorithm has been chosen for all cases. Moreover, the maximum likelihood method, as suggested by Safari and Gasore (2010), has also been used for the Weibull distribution.

Since all the proposed PDFs are readily available in the GSL library, the numerical implementation of such routines is straightforward. The results have been included in Figure 7, albeit the Weibull maximum likelihood case due to its proximity with the Weibull least squared one, depicted in the aforementioned plot; the MABD was 2.03% and 1.88%, respectively, slightly favoring the least square method. Both the fitting coefficients and year-averaged deviations, but for the Rayleigh case, alongside with basic wind speed statistics have been included in Table 3. Based on the former information, the following comments may be derived as follows: (1) the Rayleigh distribution underperformed globally, as was found by Tar (2008). This result may be related with the fact the Rayleigh distribution assumes zero mean velocity vector, feature distant from the actual velocity vector. (2) Log-normal, Gamma, and Weibull distributions behave quite similar although the error decrease in the mentioned order; (3) the Beta distribution, not frequently used for this application, is second best only after the distribution proposed herein; (4) another error estimators were tested, namely the autocorrelation parameter R^2 and the variance. They do not alter the discussion so far.

The distributions behavior for the best and worst fitted months deserves further attention in order to fully identify the reasons behind the proposed model low-error estimations. From Figure 7, it is clear that November and August are the worst and best months in that regard, respectively. From Table 3, it is verified that the same is true for either the mean
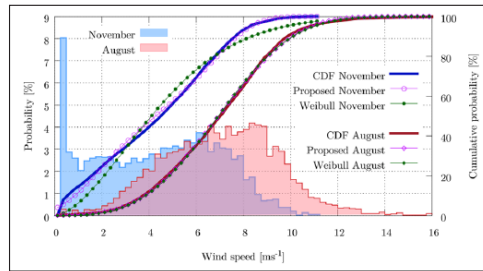
Figure 8. Probability density function and its cumulative for the months of August and November. Predicted values for the CDF by the Weibull distribution and the proposed model have also been included. The bin speed has been set to $0.25\,ms^{-1}$.

speed or power density. To further enhance this discussion, the PDF and its cumulative for the measured data have been included in Figure 8. Moreover, the CDF reconstruction based on the Weibull and the proposed distribution have been included.

The difference between both months is clear. A visual inspection shows that August closely resembles a Weibull-type distribution. On the contrary, the appearance of probability assigned to zero (it is not actually zero due to the offset of the anemometer) wind speed clearly distort the distribution in November. Translated to the CDF, the initial step increase of the curve cannot be met by the Weibull distribution. However, the proposed model shows, as noted before, cumulative probability at zero speed. By extension, any PDF which lacks the feature of non-zero probability assigned to zero would likely underperform in this case. This gap is filled by the model proposed herein. On the contrary, a smooth cumulative curve near the origin is found for August. In this case, both models capture appropriately the cumulative curve profile.

A final thought regarding the distribution proposed here is related with its application to high windy locations. As the average value "μ_s" increases, the non-symmetry fades away since low cumulative probability will be left in the underlaid Gauss distribution lower tail. Thus, is theorized that for high-grade winds this method shall underperform in relation with the results presented here.

Conclusion

In the present investigation, the wind resource for a location in the highlands of the Equatorial Andes has been studied. The year-round available experimental wind speed and direction data have been but a vehicle to provide further insights into wind characterization techniques. In Part I, the influence on the wind power density of techniques aimed at lowering the experimental sampling rate has been lengthly discussed. An upper limit for the power density error for any of these procedures was derived. Furthermore, it was proposed that the non-symmetry characteristic of the wind is closely related to the disagreement between this theoretical upper limit and the actual computed value. The aliasing method provide an extraordinary accuracy, being able to closely match wind power density with sampling intervals up to a day. The worst method of clustering information was found to be the mean ensemble technique.

Based on those results, a new time-based PDF, derived as the Gaussian dispersion of a daily wind curve of sinusoidal waveform, was proposed. The non-symmetry obtained by tail probability shifting to zero wind speed has proved useful when dealing with poor wind potential sites, as is the present case, with an average year wind speed of $5.99\,ms^{-1}$ and power density of $147\,W\,m^{-1}$. This feature is missed in commonly used distributions, namely Rayleigh, Weibull, Beta, Gamma, and Log-normal, which showed inferior prediction performance for the measured data. Furthermore, the wind direction shows consistent east-facing alignment, which is a positive factor if a small eolic turbine were to be fitted into place.

References

Bett PE, Thornton HE and Clark RT (2017) Using the twentieth century reanalysis to assess climate variability for the European wind industry. *Theoretical and Applied Climatology* 127: 61–80.

Bhattacharya P and Bhattacharjee R (2009) A study on Weibull distribution for estimating the parameters. *Wind Engineering* 5: 469–476.

Bilir L, Imir M, Devrim Y, et al. (2015) Seasonal and yearly wind speed distribution and wind power density analysis based on Weibull distribution function. *International Journal of Hydrogen Energy* 40: 15301–15310.

Blackman R and Tukey J (1958) *The Measurement of the Power Spectra from the Point of View of Communications Engineering*. Mineola, NY: Dover Publications.

Buflasa HA, Infield D, Watson S, et al. (2008) Wind resource assessment for the kingdom of Bahrain. *Wind Engineering* 32: 439–448.

Cook NJ (2015) A statistical model of the seasonal-diurnal wind climate at Adelaide. *Australian Meteorological and Oceanographic Journal* 65(2): 206–232.

Davenport AG (1967) The dependence of wind loads on meteorological parameters. In: *Proceedings of the second international conference on wind effects*, Ottawa, ON, Canada, 11–15 September. Toronto, ON, Canada: University of Toronto Press.

Dorvlo AS (2002) Estimating wind speed distribution. *Energy Conversion and Management* 43: 2311–2318.

EEASA (2014) Electrification Program for Rural and Marginal Urban Areas-II, Project Number EC-L1128, Inter-American Development Bank. Available at: https://www.iadb.org/en/project/EC-L1128

Encinas J, Torrez R, Ghezzi F, et al. (2015) Caracteristicas del viento y del potencial eólico del altiplano central. *Revista Boliviana de Física* 27: 20–24.

Forero NL, Caicedo LM and Gordillo G (2009) Análisis del desempeo de una estación autónoma de medición y monitoreo y evaluación estadística de las medidas de las variables ambientales adquiridas. *Revista Colombiana de Física* 2: 349–355.

Griffith H, Panofsky H and van der Hoven I (1956) Power spectrum analysis over large ranges of frequency. *Journal of Meteorology* 13: 279–282.

GSL (2017) GSL—GNU Scientific Library, v 1.16. Available at: https://www.gnu.org/software/gsl/

Gurley KR, Tognarelli MA and Kareen A (1997) Analysis and simulation tools for wind engineering. *Probabilistic Engineering Mechanics* 12: 9–31.

Harris RI and Cook NJ (2014) The parent wind speed distribution: Why Weibull? *Journal of Wind Engineering and Industrial Aerodynamics* 131: 72–87.

International Electrotechnical Commission (IEC) (2005) TC 88: Wind energy generation systems—Part 12-1: Power performance measurements of electricity producing wind turbines.

Kim HG, Kang YH and Kim JY (2017) Evaluation of wind resource potential in mountainous region considering morphometric terrain characteristics. *Wind Engineering* 41: 114–123.

Kumaravel R, Varun C and Sarfudeen M (2014) Mixed Weibull distribution: A case study on Ichanda, India. *Wind Engineering* 6: 613–620.

MEER (2013) Ministerio de Electricidad y Energía Renovable, atlas eólico del ecuador con fines de generación eléctrica. Available at: http://www.energia.gob.ec/biblioteca/

Mohammadi K, Alavi O, Mostafaeipour A, et al. (2016) Assessing different parameters estimation methods of Weibull distribution to compute wind power density. *Energy Conversion and Management* 108: 322–335.

Montgomery DC and Runger GC (2014) *Applied Statistics and Probability for Engineers* (6th edn). Hoboken, NJ: John Wiley & Sons.

Ollague HG and Crespo HE (2014) *Estudio y evaluación de los parámetros de operación del proyecto eólico Villonaco de la proviencia de Loja-Ecuador*. MSc Thesis, Universidad Politécnica Salesiana, Sede Cuenca, Cuenca, Ecuador.

Ouarda T, Charron C, Shin JY, et al. (2015) Probability distributions of wind speed in the UAE. *Energy Conversion and Management* 93: 414–434.

Pishgar-Komleh S, Keyhani A and Sefeedpari P (2015) Wind speed and power density analysis based on Weibull and Rayleigh distributions (a case study: Firouzkooh county of Iran). *Renewable and Sustainable Energy Reviews* 42: 313–322.

Rodriguez-Hernandez O, del Río J and Jaramillo O (2016) The importance of mean time in power resource assessment for small wind turbine applications. *Energy for Sustainable Development* 30: 32–38.

Safari B and Gasore J (2010) A statistical investigation of wind characteristics and wind energy potential based on the Weibull and Rayleigh models in Rwanda. *Renewable Energy* 35: 2874–2880.

Takle ES and Brown JM (1978) Note on the use of Weibull statistics to characterize wind speed data. *Journal of Applied Meteorology* 17: 559–559.

Tar K (2008) Some statistical characteristics of monthly average wind speed at various heights. *Renewable and Sustainable Energy Reviews* 12: 1712–1724.

Torrielli A, Repetto MP and Solari G (2013) Extreme wind speeds from long-term synthetic records. *Journal of Wind Engineering and Industrial Aerodynamics* 115: 22–38.

Van der Hoven I (1957) Power spectrum of horizontal wind speed in the frequency range from 0.0007 to 900 cycles per hour. *Journal of Meteorology* 14: 160–164.

Appendix 1

Notation

$f(\mathrm{v})$	probability density function
$f\nu$	Fourier transform result
v	wind speed (m s^{-1})
vr	reconstructed wind speed (m s^{-1})
A	area (m^2)
$\mathrm{G}(x,\sigma)$	Gauss PDF with zero mean
$\mathrm{H}(x)$	Heaviside function
P	wind power (W)
$\bar{P}$	mean wind power (W)
%	percentage, modulus operator
α	wind shear coefficient
θ	sinusoidal amplitude (m s^{-1})
$\propto$	mean value
ρ	density (kgm^{-3})
σ^2	variance

Appendix B

Submitted paper

B.1 Wind power assessment and wind farm design using CFD in the Andes Mountains, Ecuador

Germánico López, Pablo Arboleya, Diego Núñez, Andrés Freire, "Wind power assessment and wind farm design using Computational Fluid Dynamics in the Andes Mountains, Ecuador" Submitted to Energy Conversion and Management on 2022-11-25.

Wind resource assessment and wind farm design using Computational Fluid Dynamics in the Andes Mountains, Ecuador

Germánico López [1], Pablo Arboleya [2] *Senior Member IEEE, Diego Núñez* [3], *Andrés Freire* [4]

[1−2] University of Oviedo, 33203, Gijón, Spain

[3−4] Technical University of Ambato, Faculty of Civil and Mechanical Engineering, 180103, Ambato, Ecuador

Abstract

In recent years, research has revealed that hydropower designs in Ecuador have not adequately considered sensitivity to climate change. In addition, variations in rainfall patterns cause a drought from July to October. Therefore, it would decrease the flow of the rivers that feed the dams for hydroelectric generation, which would result in a significant reduction of its generating capacity.

To prevent this inconvenience from occurring, it is necessary to promote the use of wind energy to diversify the Ecuadorian energy matrix. This matrix is made up of 70% hydropower and 0.26% wind power. Moreover, the Ecuadorian Andes has significant untapped wind potential due to their complex orography. Currently, there are no detailed studies on wind potential or wind energy prediction in the Andes. As a result, wind resource characterization is necessary. In order to address the challenges mentioned above, promote wind energy development, assess wind potential, and diminish the need for thermal generators, this article describes a methodology for wind resource characterization over complex terrain in the Ecuadorian Andes using measured data from two meteorological towers installed in the mountainous zone of study and wind characteristics modeling through the Ansys Computational Fluid Dynamics (CFD) software for the positioning of 11 Goldwind 70/1500 KW wind turbines to optimize the Annual Energy Production (AEP) of a hypothetical wind farm.

The study's main findings indicate that the wind passing between two volcanoes has a high wind potential. This potential is dependent on meteorological variables, orography, and the accelerating effect of wind speed. These favorable conditions make it possible to install a wind farm in this area with 11 high-power wind turbines. Furthermore, the wind farm design using Ansys CFD showed that the K-epsilon model can model the profile of wind speeds and Turbulence Intensity (TI) over a simulated mountain with great precision.

Index Terms

Ecuadorian Andes; Wind power; Wind characteristics; Ansys CFD; Weibull wind distribution

Nomenclature

ABL Atmospheric Boundary Layer
AGL Above Ground Level
ASL Above Sea Level
CDF Cumulative Density Function
$CONELEC$ National Electricity Council
GSR Global Solar Radiation
$MEER$ Ministry of Electricity and Non-Renewable Resources
$NREL$ National Renewable Energy Laboratory
PDF Probability Density Function
$RANS$ Reynolds Average Navier-Stokes
$RMSE$ Root Mean Square Error
WD Wind Direction
WRA Wind Resource Assessment
WS Wind Speed
WSC Wind Shear Coefficient

I. Introduction

In the last two decades, renewable energies for electricity generation including wind, solar, biomass, hydropower, and others have had rapid growth to reach an energy transition more sustainable with lower fuel fossil consumption and fewer greenhouse gases emissions [1]. Wind energy is a clean and mature technology with rapid growth in the past 20 years [2, 3]. Wind power generation worldwide reached during 2020 a total installed power of 743 GW, adding 93 GW in new installations, and showing a record increase of 53% compared to 2019. Some countries set up new installations around Asia, America, and Europe with a growing tendency to increase wind power generation [4, 5].

Germánico López (corresponding author) is with Lemur Research Oviedo, Spain, email: UO260514@uniovi.es
Pablo Arboleya is with LEMUR Research Group at the Electrical Engineering Department at University of Oviedo, Spain

In recent years, research has revealed that hydroelectric power designs in Ecuador have not appropriately considered climate change sensitivity. Furthermore, climatic conditions determine the variations in the electrical generation of this renewable energy source. As a result, variations in rainfall patterns, in turn, causing the drought that occurs from July to October of each year due to the absence of rainfall, could reduce the flow of rivers that feed the dams for hydroelectric generation in Ecuador, could have a significant effect on hydroelectric generation capacity. Drought concerns in prior years compelled an increase in heat generation utilizing diesel engines, resulting in millions of tons of greenhouse gas emissions [6]. To prevent this inconvenience from occurring, it is necessary to promote the use of wind energy to diversify the Ecuadorian energy matrix. This matrix is made up of 70% hydropower, 28% thermal, and 2% renewable energies.

In Ecuador, wind power reached 21.5 MW in 2013, which represents around 0.26% of total installed power systems [7, 8]. Ecuadorian wind power is composed of two wind power investments. The first is the Villonaco wind farm, which is installed at the highest altitude worldwide (2720 m ASL), and holds an installed power of 16.5 MW supplied by 11 WT Goldwind 70/1500 KW each [9]. This wind farm operates under particular conditions, such as annual mean wind speed of over 10 m/s, low air density around of 0.89 kg/m^3, and TI of 0.15 considered as A-class [10]. The second wind farm is located in the Galapagos Islands with a capacity of 4.6 MW [7, 11]. Nowadays, the MEER has approved the construction of the projects Villonaco II and Villonaco III with an installed power of 110 MW to increase wind generation [9]. The wind Atlas published by CONELEC estimates the feasible wind potential at around 884.2 MW. Most wind potential is in the mountainous region of the Andes Highlands [7]. The full wind gross potential in Ecuador is around 1670 MW, and annual wind energy production estimated at 80 m AGL, can reach 2868.98 GWh/year [9]. In Ecuador, wind power reached 21.5 MW in 2013, which represents around 0.26% of total installed power systems [7, 8]. Ecuadorian wind power is composed of two wind power investments. The first is the Villonaco wind farm, which is installed at the highest altitude worldwide (2720 m ASL), and holds an installed power of 16.5 MW supplied by 11 WT Goldwind 70/1500 KW each [9]. This wind farm operates under particular conditions, such as an annual mean wind speed of over 10 m/s, low air density around 0.89 kg/m^3, and TI of 0.15 considered as A-class [10]. The second wind farm is located in the Galapagos Islands with a capacity of 4.6 MW [7, 11]. Nowadays, the MEER has approved the construction of the projects Villonaco II and Villonaco III with an installed power of 110 MW to increase wind generation [9]. The wind Atlas published by CONELEC estimates the feasible wind potential at around 884.2 MW. Most wind potential is in the mountainous region of the Andes Highlands [7].

The full wind gross potential in Ecuador is around 1670 MW, and annual wind energy production estimated at 80 m AGL, can reach 2868.98 GWh/year [9]. The influence of the complex terrain on the wind flow in the highlands tends to decrease with height above ground level [12]. On the other hand, the wind speed blowing over mountains increases its value due to speed-up effects [13]. Because of these effects, most wind turbines are sited on the summits of mountains due to their high wind potential [14, 15]. Many research studies have been developed in this field to exploit wind potential. Tabas et al. [16] stated that the complex site study features promote the combination of three complicated parameters: topography, heterogeneous vegetation, and interactivities among turbine wake. Solano et al. [17] proposed a regression model by using correlation between average wind speed and terrain elevation in the southern region of Ecuador. The results showed good correlation between both magnitudes and 83% accuracy rate for wind speed prediction. Other studies showed that wind potential over complex terrain in the Andes Highlands is an encouraging region for wind power generation projects [18, 19]. López and Arboleya [20] presented a multivariable LSTM network for short-term wind speed forecasting in the Andes Mountains. The forecasting results showed good performance at 80 m AGL and high wind speed values, which are feasible for large scale wind power generation. However, the integration of wind energy into the electrical grid produced by high-power wind farms located in mountainous areas is a difficult task due to the variability of the wind. Moreover, the Ecuadorian Andes has significant untapped wind potential due to their complex orography. Currently, there are no detailed studies on wind potential or wind energy prediction in the Andes. As a result, wind resource characterization is necessary. In this work, a two-dimensional-2D CFD modeling was carried out using RANS and k-ϵ turbulence model equations to evaluate wind flow characteristics over a location in the Ecuadorian Andes complex terrain, and to validate with similar calculated values.

This paper aims to promote wind energy development over complex terrain through a WRA and wind farm design using Ansys CFD software in the Ecuadorian Andes for the potential installation of a wind farm. By providing novel and relevant information for wind farm investors, researchers, and grid operators. First, we presented a detailed study of wind characteristics; furthermore, local values of the WSC and air density were calculated based on data from 2 meteorological stations installed in the study zone. Then, wind speed frequency distribution was described by the Weibull Probability Density Function (PDF) for daily, hourly, and 10-minute WS intervals. Next, we estimate the Wind Power Density (WPD) for the location at the height of 80 m AGL, using logarithmic wind profiles at each station and wind duration curves. After that, we calculated the AEP and the corresponding CF, which we compared with the historical values of the Villonaco wind farm. The CF of three wind turbine configurations was calculated to select the best-fit technology. Finally, a micro-siting study was performed using Ansys CFD software to optimize the AEP of the proposed wind farm. The present paper is structured as follows: Section 2 describes the site and measurement equipment. Section 3 presents the methodology. Section 4 shows the results and discussion. Section 5 outlines the main conclusions and future studies

II. Literature review

A. 2.1 Wind characteristics modelling using CFD

Specifically, the wind energy industry in recent years has used the CFD software for WRA and predictions. The evolution of computational wind engineering makes very accuracy the evaluation of wind speed over complex terrain. Significant progress was made in the CFD application for specific cases of wind flow evaluation over escarpments, single and multiple hills, and valleys [21]. Many decades ago, CFD emerged as a reliable tool for simulating several engineering problems [22]. It consists in solving a set of Navier-Stokes differential equations to describe the flow in a particular domain. These equations accompanied by the TI models have been able to characterize with high precision the wind behavior on the top of the mountains. In recent studies, Ayala et al. [19] used the Meteodyn CFD tool based on a nonlinear flow model to compare the actual AEP of the Villonaco wind farm with the estimated AEP by Meteodyn. The simulation results indicated that the CFD modeling is adequate for complex terrain, which site measurements should validate. Arteaga-López et al. proposed a CFD methodology to improve wind resource assessment for urban environments. The CFD results showed the efficacy of the suggested method to implement small wind turbines in urban and rural areas [23]. Tabas et al. [16] analyzed the Windsim CFD software to perform accurate wind power prediction in wind farms over complex terrain. The CFD results showed that Windsim on the company of a proper combination of TI patterns could predict wind farm performance with high accuracy.

Over the last two decades, CFD models have been used to improve the accuracy of wind speed forecasting and to assess wind resource in complex terrain. Numerical solving of Navier-Stokes equations provides a more accurate and feasible method to model wind fields with more detailed configurations. Research has explored many advanced CFD models, including large-eddy simulations (LES). However, there is still a high computational cost associated [24]. Yuan and Li [25]presented a coupled on-site measurement/CFD-based approach to replicate the spatial variability of wind speed over complicated terrain to be used for future wind turbine micro-siting. The coupled on-site measurement/CFD approach is anticipated to promote the growth of wind energy and enable reliable WRA. By integrating CFD with data from various masts, Correa-Radunz proposed a framework for creating maps of wind resources and estimating energy output in challenging terrain. The framework made a significant contribution to the mapping of wind resources in difficult terrain and was more sensitive to the number of simulated wind directions. Bilal et al. [26]used a set of mesoscale winds that were modelled with WRF and CFD to take into account the actual topographical effects on wind flow over difficult terrain. The findings show that the quality of mesoscale winds used as input determines how well microscale models work.Specifically, the wind energy industry in recent years has used the CFD software for WRA and predictions. The evolution of computational wind engineering makes very attractive the evaluation of wind speed over complex terrain. In fact, significant progress has been made in the CFD application for specific cases of the evaluation of wind flow over escarpments, single and multiple hills, as well as valleys [21]. Many decades ago, CFD has emerged as a reliable tool for simulating several engineering problems [22]. It consists in solving a set of Navier-Stokes differential equations, to describe the flow in a particular domain. These equations accompanied with the turbulence models have been able to characterize with an acceptable precision the wind behavior on the top of the mountains. In recent study, Tang et al. [27] presented a novel method for assessing wind resources at high resolution. It combined sequential wind velocities at any point within the wind farm. CFD simulations and on-site measurements from multiple meteorological masts. Dynamic sequential velocity at the desired location has been successfully estimated with high accuracy, using the CFD-measurement coupled method.

According to the literature review above, there have been no published studies of WRA and wind characteristics modeling over complex terrain in the Western Ecuadorian Andes using CFD. The present work is the first to assess wind characteristics at the highest altitude reported so far (4350 m ASL). Furthermore, mean WS and TI are modeled using Ansys CFD software to select the most suitable WT for this region. From this point of view, this study is relevant. The conclusions obtained in the wind power assessment method can be valuable for other researchers to forecast wind speed in mountainous terrains at high altitudes.

III. 3. Methodology

This chapter describes the methodology used for WRA, short-term wind speed, and power forecasting considered in the proposed model composed of the following approaches: linear regression models, DNN and RNN networks, and wind farm design using CFD in the Ecuadorian Andes

A. 3.1 Area of study

The study area is located in the Sierra region of the Ecuadorian Andes, among the provinces of Tungurahua, Chimborazo, and Bolívar, as is shown in Figure 1. Hence, there are a few people in this region. The majority of land, which is a natural reserve is owned by the state. According to the Ecuadorian Atlas, El Arenal valley is considered a windy sector within the Ecuadorian Andes [28]. This 10 Km wide valley is located at a natural mountain pass between the volcanoes Chimborazo (6263 m ASL), and Carihuayrazo (5116 m ASL) as is presented in Figure 2. This wind channel pass causes a wind speed-up effect due to the Venturi effect. This particular site with high wind potential was selected after a preliminary assessment; which is considered the first phase in WRA [29]. Therefore, this site is classified as a region with accelerated wind flow [30].
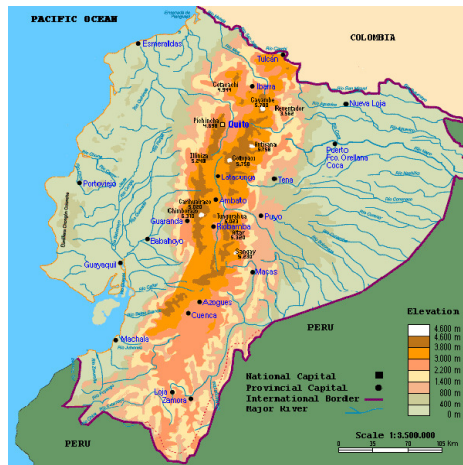
Figure 1: Geographic map of Ecuador [31]

Ecuador is traversed from North to South in the Sierra region by the Andes Mountains, which are composed of East and West mountain ranges. The topography of the Andes Mountains is characterized by complex terrain at high altitude, which is composed of hills, plateaus, mountains (3000-4500 m ASL), and volcanoes (> 5000 m ASL) [31]. In the mountains, during the day, the sun heats air masses, and hot air rises on the sides of the mountains, creating flow circulation and anabatic winds. Katabatic winds occur at night when air parcels descend on the sides of the mountains [12, 32]. Two climatic stations are predominant in this region, such as winter from December to June and summer from July to November [31, 33].
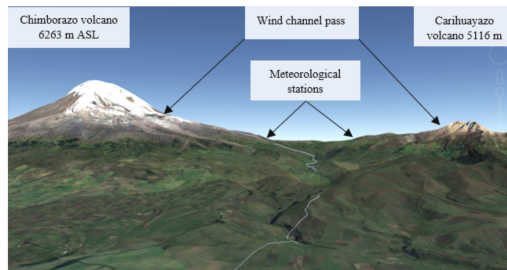
Figure 2: Area of study in the Andes Mountains [34]

Table I: **Geographic coordinates of meteorological stations [20]**

Parameter	Station 1	Station 2
Latitude	$1°54'S$	$1°54.8'S$
Longitude	$79°15'W$	$78°45.6'W$
Elevation	4260m ASL	4428m ASL

B. 3.2 Equipment and data

The collected data were obtained using sensors mounted on two tubular towers at 30 m and 80 m AGL respectively installed in the moorland of the zone of study in accordance with international guidelines [35]. Furthermore, this region is suitable for wind power assessment and development, which does not represent a risk to environmental care [20]. The measured data is formed of 10-minute intervals with average, maximum, minimum, and standard deviation values of the following weather variables: wind speed, wind direction, air temperature, barometric pressure, and GSR. The geographical coordinates of the position of the towers are shown in Table I. Given that wind data set is a parameter very important for WRA, and is required at least wind data of one year to predict WPP [36]. The data was gathered from January 1st to December 31st, 2018. The 40 m-tall-tower was installed on a large plateau. In addition, the tower of 80 m-tall-tower was installed on a round hill in the El Arenal desert close to the Chimborazo volcano. The equipment, sensors, and their characteristics installed on each tower to measure meteorological variables are listed in Table II. One data logger, NRG Symphony Plus 3, for each tower, was used to store data in memory during 2018, and to enable remote communication. Readings are averaged at 10-minute intervals. The sampling frequency is 1 Hz [37].

Table II: **Sensors installed on meteorological towers [20]**

Type	Model	Range	Deviation
Anemometer	NRG #40C	$1ms^{-1}$-$96ms^{-1}$	0.5 %
Vane	NRG 200P	0-360°	1%
Barometer	NRG BP20	15KPa-115KPa	1.5%
Thermometer	NRG 110S	-40° to 95.5°C	1.3 %
Pyranometer	LI 200R	400 to 1100 nm	<10µV

Wind speed was measured in the tower 1 at heights of 10, 20, and 30 m AGL and labeled "WS_1", "WS_2", "WS_3" respectively. For tower 2, at heights of 40, 60, 80 m AGL and designated "WS_4", "WS_5", "WS_6" respectively. The statistical summary of weather variables is stated in Table III. The percentage of measured values is over 99%; which represents a reliable data set. The mean wind speed measured at six heights from 10 m to 80 m AGL shows an increase in wind speed with height variation, [13] as is shown in Figure 3 where WS at 80 m AGL is higher than at 30 m AGL. Moreover, it is observed that WS increases during the summer months due to the influence of the Atlantic equatorial mass composed of the East and Southeast winds that are of greater pressure than the North trade winds [38].
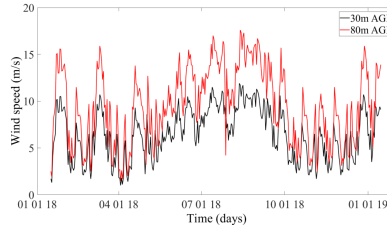

Figure 3: Monthly WS values at 30 m and 80 m AGL in 2018

The WPD was calculated for each height from 10 m to 80 m AGL. It observes an increase in WPD with wind speed variation. The air temperature varies from 1.5 ºC to 9 ºC. Similarly, the barometric pressure reached a mean value of 611.3 millibars due to the high altitude terrain. On the other hand, GSR reaches the highest value of 1245.5 W/m^2 close to the solar constant due to the proximity of the land to the sun because the zone of study is on the Equator. Furthermore, solar radiation outside the Earth's atmosphere is referred to as the solar constant, with a value of approximately 1,361W/m^2 [39, 40].

Table III: **Weather variables statistics for the zone of study**

Variable	Units	Minimum	Average	Maximum	Percentage
Wind speed ($WS_1 at 10mAGL$)	m/s	0.2	6.02	23.1	99.68
Wind speed ($WS_2 at 20mAGL$)	m/s	0.2	6.92	23.5	99.58
Wind speed ($WS_3 at 30mAGL$)	m/s	0.2	7.02	24.2	99.81
Wind speed ($WS_4 at 40mAGL$)	m/s	0.2	9.15	41.4	99.86
Wind speed ($WS_5 at 60mAGL$)	m/s	0.2	10.8	41.5	99.68
Wind speed ($WS_6 at 80mAGL$)	m/s	0.2	11.02	41.6	99.56
Wind Power Density (WPD_1)	W/m^2	0	135	4678	99.4
Wind Power Density (WPD_2)	W/m^2	0	250	4990	99.35
Wind Power Density (WPD_3)	W/m^2	0	351	5450	99.65
Wind Power Density (WPD_4)	W/m^2	0	511	26500	99.61
Wind Power Density (WPD_5)	W/m^2	0	584	27482	99.48
Wind Power Density (WPD_6)	W/m^2	0	647	28690	99.75
Wind direction (from East)	Degrees	0	10	350	99.45
Air temperature (3.0 m AGL)	Celsius degrees	-1.5	2.7	9.5	99.7 5
Barometric pressure	millibars	0	135	746.0	99.75
Global Solar Radiation	W/m^2	606.2	610.9	615.1	98.85

C. 3.3 Roughness class and length

In the ABL lower than 1 Km AGL, wind speeds are affected by friction with the earth's surface. In the wind industry, a difference is made between the terrain roughness, the influence of obstacles, and the terrain contour influence also named the orography of the area. The roughness class from the roughness length (Z_o) is the height AGL where the wind speed is theoretically zero. When the wind profile moves towards lower speeds as we approach ground level is often named wind shear. The friction speed is related to the shear stress of the terrain with the density of the fluid and is represented by Equation 1

$$\mu_* = \sqrt{\frac{\tau_\omega}{\rho}} \tag{1}$$

Where:

μ_* Friction speed

τ_ω Wind shear stress

ρ Air density

Theodore von Kárman stated on 1930 that in a turbulent flow, its mean speed at any point becomes proportional to the logarithm of the distance between any place to the wall [41]. Equation 2 represents the average horizontal speed located at the height of z.

$$\mu_z = \frac{\mu_*}{k}.ln\frac{Z}{Z_o}; Z \geq Z_o \tag{2}$$

Where:

k von Karman's constant equals to 0.4

Z Wall height

Z_o Surface roughness length

The horizontal average velocity μ_z is known as the logarithmic wall law, and only is used for flows that are closer to the wall. This method has been put into practice to estimate the average velocity profile generated in the surface layer, but it is valid up to 150 meters in height as long as there are strong winds.

The term z_o indicates the size of the eddies generated on the surface of the ground while the ground has a greater roughness; the eddies will be directly proportional to the roughness of the surface. Table IV shows the roughness values of different rough obstacles on uniform study surfaces.

Table IV: **Roughness and length for some types of terrain [42]**

Terrain description	Roughness class	Roughness length (m)
Ice or mud	0	0.001
Outdoors, grass, airport lands	0.5	0.24
Agricultural land with scattered buildings	1	0.03
Agricultural land with fences up to 8 meters height and some houses separated by more than 1 km.	1.5	0.055
Cities, villages, agricultural land with high fences, and forests	3	0.4
Centers of cities with tall buildings	4	1.6

D. 3.4 Wind shear profile

Wind shear is defined as the horizontal or vertical variation in WS or WD with a height change in a small portion of the atmosphere [43]. These variations are due to some variables such as, elevation, atmospheric stability, the hour of the day, surface roughness, and terrain shape [14, 42]. Furthermore, it is also known as wind profile [13, 44]. In this work, the vertical wind speed profile was realized using the power law. Its basic equation is shown in Equation 3:

$$\frac{V_2}{V_1} = \left(\frac{Z_2}{Z_1}\right)^{\alpha} \tag{3}$$

Where :
V_2 = the projected speed at the desired height h_2
V_1 = the observed speed at the measurement height h_1
α = a non-dimensional power law exponent

The power-law exponent is very variable from 0.1 to 0.35 due to many parameters, such as terrain elevation, the hour of the day, terrain classification, wind speed value, atmospheric stability, and other thermal and mechanical factors[42]. This exponent increases its value during the night hours, causing a stable atmosphere, and decreases during the day hours, originating a neutral and unstable atmosphere [45] α can be calculated from Equation 3 as is shown in Equation 4. This work was developed while considering a neutral atmosphere.

$$\alpha = \frac{\ln V_2 - \ln V_1}{\ln Z_2 - \ln Z_1} \tag{4}$$

E. 3.5 Air density

This variable is in proportion to air temperature and air pressure, which decreases with height and temperature increases [42]. Wind power output decreases with lower air density values [46]. The air density for the site of the study was calculated using the ideal gas law is shown in Equation 5.

$$\rho = \frac{P}{RxT}(kg/m^3) \tag{5}$$

Where P is air pressure expressed in KPa, air temperature in Kelvin degrees, and R is the universal constant for gases (287 KPa/JxKg).

F. 3.6 Turbulence Intensity

Wind turbulence is the rapid disturbance in the wind speed, direction, and vertical component. Normally, the duration time is from ten minutes to one hour, and the range is from 0.1 to 0.4. TI is defined in the Equation 6, and is an important site characteristic that depends on the surface roughness, thermal behavior, height above the surface, and topographical features [42, 44]. High turbulence levels may decrease power output and cause extreme loading on WT components.

$$TI = \frac{\sigma}{V} \tag{6}$$

Where σ is the standard deviation of wind speed, V is the mean wind speed.

G. 3.7 Weibull probability density function

The Weibull distribution based on k and c parameters has been widely used for short-term and long-term wind data studies to represent the probability of occurrence of mean wind speed over a period of one year [42, 44, 47]. The PDF Weibull is given for Equation 7.

$$f(V) = k\left(\frac{V^{k-1}}{c^k}\right)exp\left[-\left(\frac{V}{c}\right)^k\right] \tag{7}$$

Where k is the shape parameter dimensionless, which describes the wind speed distribution, and c is the scale parameter measured in m/s.

There are numerous approximations to calculate Weibull parameters k and c; one of them is the analytical model based on mean wind speed $\overline{V}$, and standard deviation σ, which are shown in Equation 8 and Equation 9 respectively [46].

For $1 \leq k < 10$

$$k = \left(\frac{\sigma v}{\overline{V}}\right)^{-1.086} \tag{8}$$

$$c = \left[\frac{\overline{V}}{\gamma(1 + \frac{1}{k})}\right] \tag{9}$$

Where γ is the gamma function.

The annual mean wind speed $\overline{V}$ expressed in Equation 10 can be calculated from Equation 7.

$$\overline{V} = c\gamma\left[1 + \frac{1}{k}\right] \tag{10}$$

The CDF is the interval of time or probability that wind speed may be smaller or equal to a determined wind speed value. CDF is given in Equation 11 [42].

$$F(V) = 1 - exp\left[-\left(\frac{V}{c}\right)^k\right] \tag{11}$$

H. 3.8 Wind power density

It is known as wind energy flux according to Equation 12. Furthermore, wind power resources are compared using WPD, which is independent of wind turbine size, according to NREL and is considered as the quantitative basis of wind standard classification [46].

$$WPD = \left[\frac{P}{A}\right] = \left[\frac{1}{2}\right] * \rho * V^3 (W/m^2) \tag{12}$$

I. 3.6 Annual Energy Production and Capacity Factor

The AEP is composed of gross and net energy production. The gross energy production is considered the wind farm production without losses, as is shown in Equation 13.

$$GEP = \sum_{i=1}^{Nd} \sum_{i=1}^{Ns} P_{ijk} F_{ijk} 8760 \tag{13}$$

Where Nd is the number of direction steps, and Ns is wind speed bins, P_{ijk} is the wind power output for each direction from sector i, to wind speed, bin j, F_{ijk} is the frequency of occurrence of wind speed.

Furthermore, wind resource assessment is influenced by the estimation of wind power losses. Consequently, annual net energy production is estimated considering the following losses: plant availability (2-4%), electrical losses (2-4%), turbine performance (1.5-5%), environmental (1-3%), and curtailment (1-3%). Other losses, such as the site climate and the project location, were considered to be 12% [46].

The CF prediction of a wind farm using data from a measurement campaign is considered a complicated work [48]. In this work, the CF is estimated for one year according to Equation 14.

$$CF = \frac{actual energy production}{energy at rated speed}.100 \tag{14}$$

J. 3.9 Measurement uncertainty

Wind resource estimates present an uncertainty percentage due to many factors, such as wind speed measurements (1.0-2.5%), historical wind records (1.6-4%), future wind resource (1.4-2.2%), wind shear (0.0-6.3%), wind flow modelling (2.0-10%) for a total uncertainty of 3-13% [13]. Wind´s nature and variability causes uncertainty in wind power assessment and forecasting; for this reason, it is difficult to integrate wind energy into the power grid [49, 50]. Jung et al.[51] proposed a Bayesian approach considering uncertainties, such as the limited amount of data, wind speed, air density, surface roughness, and WT performance. In order to estimate the AEP of a site for a hypothetical WT of 3 MW, wind speed data from a nearby weather station is used. The proposed model showed good performance for uncertainty modeling due to the limited amount of data. Rodríguez-Hernández et al.[52] developed a methodology based on a probabilistic model considering different possibilities in the Weibull PDF associated with wind speed to analyze the uncertainty of measurement equipment for wind resource assessment. The developed methodology is indicated to be a useful approach to estimate wind energy production. Baker et al. estimated $\pm$ 10% uncertainty and a confidence level of 90% for wind data collected on-site for one or three years.

K. 3.10 Wind speed modelling using CFD

1) 3.10.1 Mathematical formulation: The Navier-Stokes equations allow us to predict the flow of fluids. These equations are not solvable analytically, except for specific cases, and it is complex to analyze the fluid behavior. For this reason, numerical and experimental models are used to obtain a solution close to reality.

• Mass or continuity conservation equation according to Equation 15

$$\frac{\partial \rho}{\partial t} + \frac{\partial}{\partial x_i}(\rho.U_i) = 0 \tag{15}$$

• Equation for the conservation of momentum as is shown in Equation 16

$$\rho \left(\frac{\partial \rho}{\partial t} + \frac{\partial}{dx_i}(U_i.U_j) \right) = \frac{\partial P}{\partial t} + \frac{\partial \tau ij}{\partial x_j} \tag{16}$$

• Energy conservation equation according to Equation 17

$$\rho \left(\frac{\partial E}{\partial t} + \frac{\partial.U_{jH}}{\partial x_j} \right) = \frac{\partial}{\partial t}.(U_i \tau ij) + \frac{\partial}{\partial x_j} + \left(k \frac{\partial T}{\partial x_j} \right) \tag{17}$$

Where:
ρ flow density
Components that make up the viscous tensor stress
μ_i Cartesian speed components to direction Xi
μ_j Cartesian speed components to direction Xj
P Fluid pressure
τij Components that make up the viscous tensor stress
E Total energy
H Total entalphy
k Thermal conductivity coefficient
T Absolute temperature

2) 3.10.2 Turbulence model k-ε: The discretization techniques and turbulence model selection represents an important function in the simulation accuracy of turbulent air flows [53]. The RANS turbulence selected model contains transport equations that work with mean velocities and scalar variables ϕ, which are turbulent flows, so the Reynolds stress is represented by the Equation 18

$$Reynolds stress = \overline{\mu_i \mu_j} \tag{18}$$

The turbulent transport equation originates with the addition and subtraction of different terms such as production P_{ij}), which is obtained from the gradient of average velocities. Another term is dissipation ϵ_{ij}, to originate from real-time viscosity acting on fluctuating speeds. Finally, we have a redistribution term ϕ_{ij}, which facilitates the energy transfer using pressure and fluctuations caused by the fluid current as is shown in Equation 19.

$$Net energy = Produced energy(P_{ij}) + Redistribute energy(\epsilon ij) - Dissipated energy(\phi ij) \tag{19}$$

External terms must be considered the convective and diffusive that go from one point to another of the created domain, so this turbulence model is the most practical and used, consisting of two equations that represent the turbulent properties of a flow according to Equation 20 [54].

$$C_\mu = \mu_t \rho \frac{k^2}{\epsilon} \tag{20}$$

Where:
C_μ Constant Turbulent kinetic energy
k Dissipation rate of turbulent kinetic energy
μ_t Turbulent viscosity

The equations of the described model are
• Kinetic turbulence according to Equation 21

$$\frac{\partial}{\partial t}(\rho k) + \frac{\partial}{\partial x_i}(\rho k \mu_i) = \frac{\partial}{\partial x_j} \left[\left(\mu + \frac{\partial \mu_t}{\partial \sigma_k}.\frac{\partial k}{\partial x_j} \right) \right] + G_k + G_b - \rho_\epsilon - Y_m - S_k \tag{21}$$

• Turbulence dissipation as is shown in Equation 22

$$\frac{\partial}{\partial t}(\rho \epsilon) + \frac{\partial}{\partial x_i}(\rho \epsilon \mu_i) = \frac{\partial}{\partial x_j} \left[\left(\mu + \frac{\partial \mu_t}{\partial \sigma \epsilon}.\frac{\partial \epsilon}{\partial x_j} \right) \right] + G_1 \epsilon \frac{\partial \epsilon}{k}.(G_k + C_3 \epsilon G m_b) - C_{2\epsilon} \rho \frac{\epsilon^2}{K} + S_\epsilon \tag{22}$$

Where:

G_k Generation of the kinetic energy of the mean speeds gradients

G_b Kinetic power generation by buoyancy

Y_m Contribution of fluctuating expansion on compressible turbulence

$C_{1\epsilon}$,$C_{2\epsilon}$, $C_{3\epsilon}$, σ_t Experimental constants

μ_t Turbulent viscosity

σ_k Prandtl number as a function of k

σ_ϵ Prandtl number as a function of ϵ

The diffusivities represented in the expression of molecular and turbulent viscosities of the turbulence model :

$$r^k = \mu \frac{\mu_t}{\rho_K} \tag{23}$$

$$r^\epsilon = \mu \frac{\mu_t}{\rho_\epsilon} \tag{24}$$

The identification constants $C_{1\epsilon}$,$C_{2\epsilon}$, C_μ, σ_k, σ_ϵ were defined by Launder and Spalding for standard models [53, 55] and their values are:

$C_{1\epsilon}$ = 1.44

$C_{2\epsilon}$ = 1.92

C_μ = 0.09

σ_k = 1

σ_ϵ = 1.3

L. 3.11 Wind characteristics modeling using Ansys CFD software

This section exposes the process to create a computational domain and results of wind characteristics modeling over a simulated mountain complex terrain using Ansys CFD software.

M. 3.11.1 Process to create computational domain

It is well-known that the accuracy of CFD simulations relies mainly on the size and shape mesh generated, the boundaries and initial conditions applied, the turbulence model chosen, and the used wall functions [56]. Therefore, it is reasonable to work based on previous research that has worked and shown acceptable results. The following sections show the conditions under which the simulation was carried out. The numerical methods design is developed in three phases to prevent the effects of possible hiding where variables are subordinated as follows [57]:
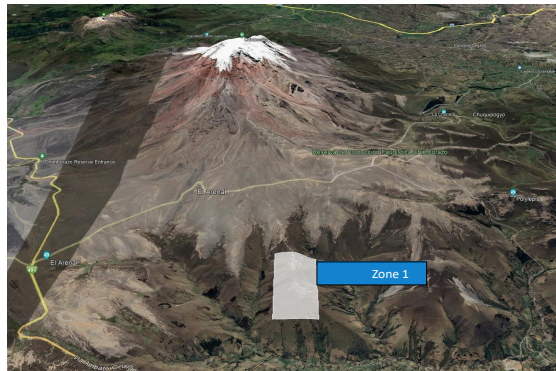

Figure 4: Study area located in Chimborazo National Park

- In the preprocessing phase, the input data already suitable to be treated are defined by Ansys Fluent, determining the geometry, the domains, the grid, and the selection of the physical and chemical phenomena.
- In the calculation stage, the solution of the algebraic equations resulting from the discretization of the physical model for a volume defined by the numerical grid is performed using 100 iterations.
- In the processing, the visible solution of the calculation is presented, transforming it into a suitable form for its subsequent analysis, data post-processing, and interpretation.
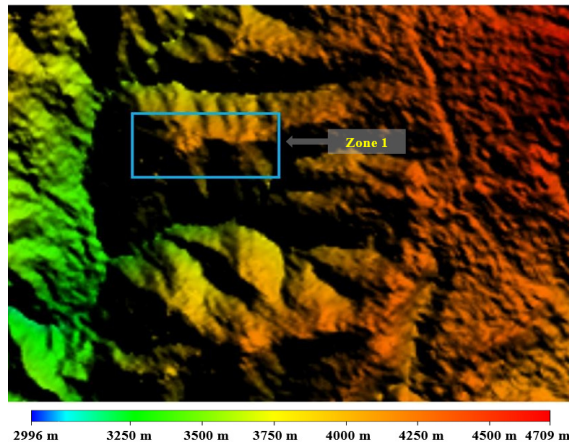
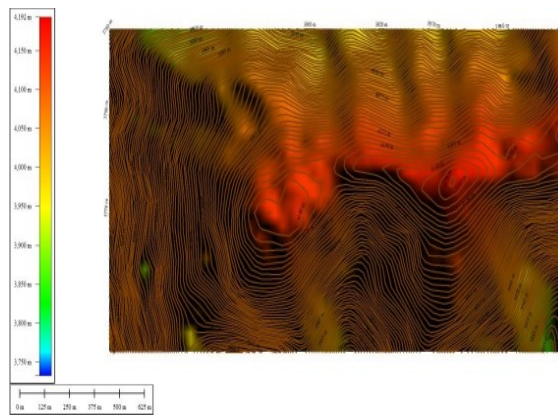Figure 5: Altitude map of the terrain in the study area

Figure 6: Contour lines in Global Mapper Zone 1

The preprocessing phase is developed in three stages as follows:

1) Domain identification The computational domain to be created must be large enough to reduce the uncertainties that may be generated in the boundary conditions so that the analysis generates the so-called wake effect. But the domain should not be too large due to can affect the computational simulation time. Through the Google Earth software, the location was made using the generate polygon tool and thus finally locating the study area, to generate a kmz format file with the selected study area as is shown in Figure 4.

   By using the file generated in Google Earth Pro, we proceed to create the contour lines in this Global Mapper software, where you can determine the maximum and minimum height at sea level of the study areas as is shown in Figure 5. With this, pressure output data were obtained with the help of a pressure-height graph, data necessary for the (Boundary Conditions) for further analysis. Global Mapper also allows generating the contour lines in the study areas as is presented in Figure 6, which the results were exported in DWG format for the next procedure.

   The post-processing of the contour lines was developed using AutoCAD Civil 3D and then transformed to the surface, performing several procedures. Rhinoceros 6 allowed completing the design and modeling of the surface to determine the number of areas required per area of study as is presented in Figure 7.

   The computational domain was determined, based on the predominant WD from the east, and the diameter of the rotor of the WT Goldwind 70/1500 kW, which diameter is 70 meters, In this way, the length on the X-axis is 28D, on the Y-axis is 14D, and the height of 3D is shown in Fig. 8. In the preprocessing of the computational domain of the study area, which is segmented into four surfaces separated by 333 meters from each other and thus obtains a total of 4 contours for the study area as is indicated in Figure 9.
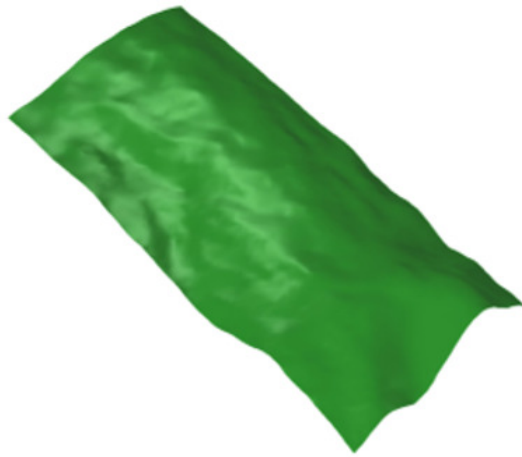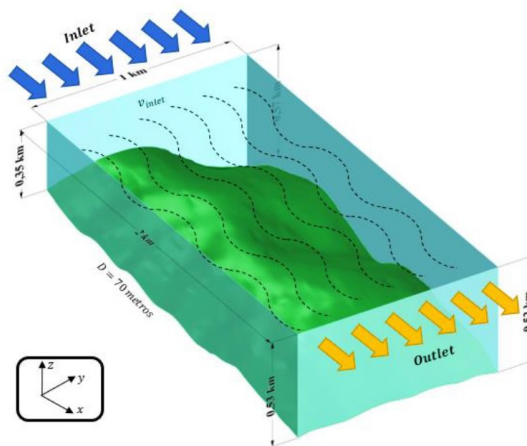
Figure 7: Domain surface generated in Rhinoceros 6

Figure 8: Computational domain of Zone 1

2) Grid generation The grid process consists of dividing the object of study into several sections, the most relevant within a CFD simulation is the type of mesh since it is where the wind data that already have been defined in its specific coordinates, in the inlet of the computational domain to interpolate the values for each cell until reaching the outlet of the computational domain.

Based on the topological relationship, we started by meshing each of the surfaces. In this method, was created the 2D hybrid meshing of the 4 areas using the Ansys Mechanical meshing tool as indicated in Fig.10, which combines structured and unstructured meshing. This allows a better adaptation of the surface to be analyzed. Through the use of skewness in the mesh quality-metric section, meshing asymmetry can be determined if the mesh performed has a high-quality mesh structure through the asymmetry value. Using triangular and quadrilateral shapes to mesh, an equilateral triangle would be the ideal shape for triangular meshes. The same angular and quadrilateral form would be the ideal shape for quadrilateral meshing. This is because highly skewed faces and cells are unacceptable because the equations start to solve assuming the cells are in their correct form. The mesh for study area 1, is excellent for the solution of the equations that describe the model to be analyzed. The average skewness values are in the range of $(0 - 0.25)$ indicating excellent mesh quality.

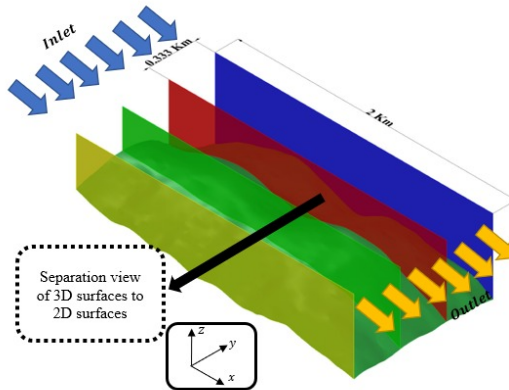3) Setting boundary conditions
   Set up:

Figure 9: Division of the 2D computational domains of Zone 1

Figure 10: Hybrid meshing in zone 1

It configures general data of the terrain, such as air temperature, air density, space 2D planar, and the elevation of the location wind farm location by considering a stable atmosphere. In addition, the initial wind speed values of the wind speed, roughness class and length, air density, and turbulence models are established, which is the most used for the sites in CFD is the k-ϵ model, which is part of the RANS models of the Navier-Stokes equations.

Edge conditions:

Inlet: The inlet was configured to input values of mean wind flow inlet speed and pressure. Also, the calculated monthly values of TI.

Outlet: The outlet was configured so that values of outlet pressure of the wind flow are entered, where the respective calculated value of TI was assigned.

Wall-down: The roughness class of the ground surface was considered, which allows the generation of eddies, thus directly affecting the turbulence and the roughness length. The assigned values are as follows:

Roughness class: 0.5 Landscape with smooth surfaces

Roughness length (Z_0): 0.0024 m corresponding to uninhabited areas with grass

Wall-up: This boundary condition represents the atmospheric boundary layer where it does not present roughness by placing zero values.

Trim: It is considered the interior of the study zone. This element of a cell zone determines the type of fluid to be analyzed, by considering air density.

Table V: Weibull parameters at 30 and 80 m AGL for 2018

Month	30 m		80 m	
	k	c	k	c
January	1.59	8.47	1.61	10.5
February	1.12	4.47	1.31	7.85
March	1.24	6.78	1.51	8.75
April	1.11	5.14	1.41	8.6
May	1.45	6.35	1.61	9.5
June	4.41	9.93	4.71	12.05
July	3.12	10.94	3.31	14.25
August	2.16	10.79	2.41	13.89
September	1.39	8.83	1.51	10.85
October	1.12	4.47	1.31	7.65
November	1.1	4.47	1.31	6.5
December	1.45	7.85	1.81	10.5
Overall	1.68	6.95	1.51	11.87

Table VI: **Technical data of the 1500 KW class wind turbines**

Wind turbine turbine	Cut-in speed (m/s)	Cut-out speed (m/s)	Rated speed (m/s)	Generator	Rated power power (KW)	Rotor diameter (m)	Wind class IEC
Enercon	2.5	25	13	1500	Synchronous	66	IIa
Goldwind	3	25	11.8	1500	Synchronous	70	Ia
Vestas	4	16	25	1500	Asynchronus	63.6	Ia

IV. 4. RESULTS AND DISCUSSION

This chapter presents the results of the short-term WS, wind power, wind energy over complex terrain in the Ecuadorian Andes, and the cost of forecasted energy in winter and summer are all discussed in four cases. It's worth noting that are reported the results of other studies conducted in similar circumstances worldwide. In the four cases, WS forecasting achieved a lower proportion of forecasting error than other studies worldwide.
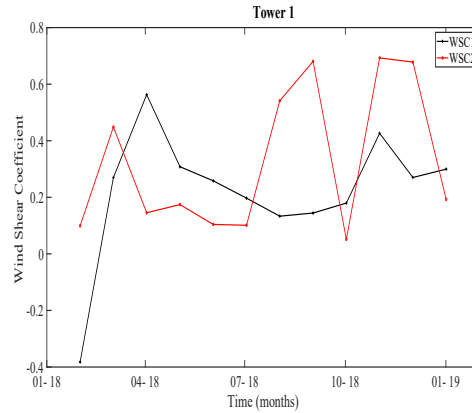

Figure 11: Monthly variation of Wind Shear Coefficient for Tower 1

A. 4.1 Wind shear profile

The values of WSC were determined using four pairs of wind speeds, two pairs for each tower. The values of WSC_1 and $WSC_{,2}$ were calculated between 10 and 20 m AGL and 20 and 30 m AGL, respectively, using measured data from tower 1. WSC_3 and WSC_4 were calculated between 40 and 60 m AGL, 60 and 80 m AGL by using measured data from tower 2. The monthly variation of WSC values in tower 1 and tower 2 is shown in Figure 11 and Figure 12 respectively. The results indicate that WSC on both towers is variable. In this way, the maximum WSC values appear in winter when WS is low, and the minimum values appear in summer during July and August when WS is high. In addition, one unexpected negative value was observed for WSC_1 in January. Indeed, the WSC is highly influenced by temperature changes and the complex topography

Table VII: **Annual energy production and capacity factors**

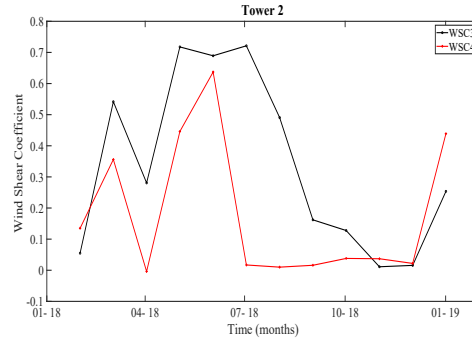| Wind turbine	Hub height (m)	Nominal power (MW)	Net AEP (GWh/year)	Capacity factor
Enercon 1.5	67	1500	6.1	0.46
Goldwind 1.5	70	1500	7.24	0.56
Vestas 1.5	63	1500	6.2	0.52

Figure 12: Monthly variation of Wind Shear Coefficient for Tower 2

of the Sierra region. It should be noted that tower 1 is installed on a plateau, and tower 2 is installed on the top of a hill. Consequently, WSC is affected by wind speed and flow turbulence effects on both towers.

B. 4.2 Air density

Monthly values of air pressure were based on collected data by a barometer on each tower. There is a slight change in monthly values of air density . The minimum and maximum values were found to be 0.768 Kg/m^3 to 0.773 kg/m^3 which were observed in February and June. These air density results are considered lower due to high altitude terrain, and air pressure decreases with height according to the statement indicated by Emeis [12]. Low air density is considered a weakness in this research, which is compensated for high wind speed values.

C. 4.3 Turbulence Intensity

The hourly TI values at 80 m AGL are presented in Figure 13. The higher TI values are observed during the day hours from 11:00 to 15:00; when the solar radiation reaches its highest value and the wind speed of the anabatic winds is maximum. The lower values are observed during night hours; when the wind speed of the katabatic winds is lower [32, 42]. Likewise, the monthly TI values at 80 m AGL during 2018 are shown in Figure 14. The TI´s higher values are observed in the winter months when the wind speed is slow. On the other hand, the TI values are observed in the summer months when the wind speed is high. Jeong and Ha [58] stated that wind profile and TI are highly influenced by complex terrain topography such as steeper hills and valleys, which cause wind flow separation. Frost et al. [30] stated that ideal sites for WT sitting are regions with accelerated wind flow, such as mountain passes with high mean wind speed and low TI.

D. 4.4 Wind rose and Weibull probability function

The prevalent wind speed direction is shown by using a wind rose diagram to indicate useful information through wind speed bins. The wind rose was represented through the software Matlab 2020b, by using ten-minute intervals for wind speed measurements of tower 2, and their corresponding wind directions at 80 m AGL are shown in Figure 15. The prevalent wind speed direction anytime is the wind blowing from an azimuth of 90° (East) varying slightly to 105° due to the zone of study being located within a mountain pass between two volcanoes. A similar pattern of wind behavior was found in a nearby location [18]. In addition, the identical wind direction was observed in another region of the Ecuadorian Andes [19]. Moreover, the prevalent wind direction from East because during summer and winter months

The Weibull PDF for tower 2 at 80 m AGL is shown in Figure 16, and the estimated wind speed distribution parameters for each tower are presented in Table IV; which summarizes the k and c Weibull parameters. Furthermore, the k parameter for both heights is variable due to the influence of the complex topography of the region over eastern winds. Moreover, the annual mean WS is 10.9 m/s. The shape parameter k and scale parameter c overall in 2018 at 80 m AGL have values of 1.5 and 11,8 m/s, respectively. Besides, k is considered a lower value, and c is close to the mean WS. Therefore, according
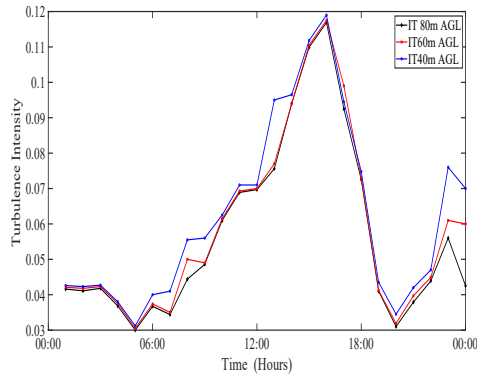
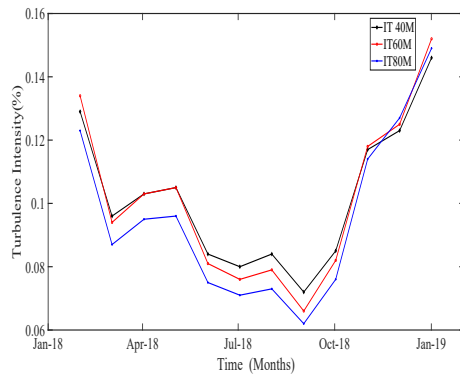Figure 13: Hourly turbulence intensity at 80m AGL for Tower 2

Figure 14: Monthly variation of Turbulence Intensity for Tower 2

to the results of the Weibull parameters, the area of study has great wind variability with less dispersion with respect to the average wind speed and a high availability of wind speed to obtain a large production of wind energy [45]. A similar pattern of Weibull parameters k and c was obtained by Károly Tar [59] to generate monthly average wind speed at different altitudes. In addition, B.K. Gupta [60] attained a variable pattern for k and c monthly values for five locations in India; which is useful to estimate annual and monthly wind energy production.

In addition, according to CDF curves from 10 m to 80 m AGL, the maximum probability of wind speed of 15m/s is 4.1% at 80 m AGL for 2018, and the maximum probability of wind speed of 3 m/s at 40 m AGL is 6.2% as is shown in Figure 17. Fig. 18 shows WPD variability at 80 m AGL for 2018 based on available WS; where higher values are observed in summer months due to the influence of Atlantic equatorial mass and lower values in winter months [38].

E. 4.5 Selection of suitable wind turbines

In this study, the best-suited WT is selected based on annual wind energy production, mean annual WS, and TI class. The selected WT are classified as large-scale and suggested for wind farms in complex terrain [61], which are: Enercon E66/1.5 MW, Goldwind 70/1.5 MW, and Vestas 63/1.5 MW. The selected WT power curves are shown in Figure 19; which were designed from the manufacturers´ web page considering the low air density of the zone of study. This variable is contemplated as one limitation found in this case and causes a power loss between power start and nominal power compared against power curves obtained with air density at sea level [42]. Table VI summarizes the technical specifications of selected wind turbines. The following aspects were considered when selecting a WT: IEC wind class, power to be installed, hub height, train/generator set, power output to the grid [13]. Therefore, the comparison of WT power curve results confirms that the best suitable WT for the zone of study is Goldwind 70/1500 as a good choice to consider, which is installed at the Villonaco wind farm in Loja, Ecuador [62].
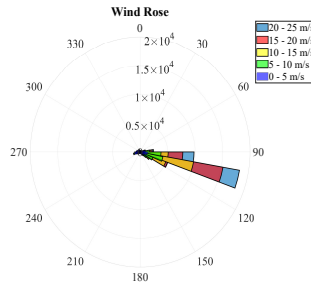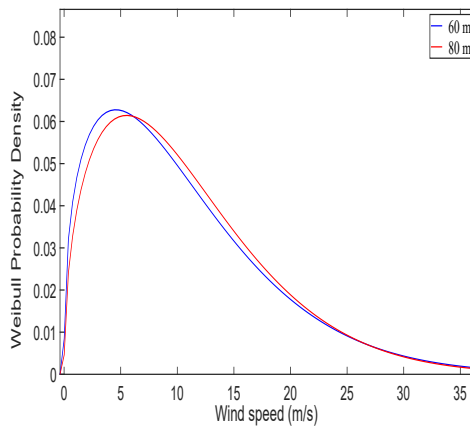
Figure 15: Wind rose in tower 2 at 80 m AGL

Figure 16: PDF for Weibull distribution

F. 4.6 Estimation of wind energy production and capacity factor

In this work, net AEP based on PDF Weibull was estimated for three large scale WT, such as Enercon 66/1500, Goldwind 70/1500, and Vestas 63/1500. The estimated net AEP and its corresponding capacity factors for selected WT are shown in Table VII. Furthermore, the highest AEP value was obtained with the Goldwind WT. Moreover, the CF analysis for the three types of high power analyzed wind turbines showed high values. The highest CF value was 56% obtained with WT Goldwind 70/1500. The best net AEP and CF values were obtained with the WT Goldwind 70/1500 for a hub height of 80 m AGL. A similar pattern of results was obtained for the wind energy assessment for the Villonaco wind farm, located over complex terrain at a high altitude[62].

Then, a hypothetical wind farm with an installed power of 16.5 MW was designed to compare against the wind energy production of the Villonaco wind farm; which in 2015 supplied 94.5 GWh of net wind energy, and reached a higher capacity factor of 63.46% [62].

From the results, it is clear that the region of study is promising for wind energy projects by using high power wind turbines. Moreover, the evaluation of the feasibility of wind energy projects in the Ecuadorian Highlands must contain an exhaustive economic analysis according to the project requirements to accomplish the project requirements such as, estimated AEP, project lifetime, and profitability [42, 46].

There are 5 relevant characteristics of the study area to be considered a good wind power area:

1) A high average annual wind speed: the site is located in a wide open valley with no obstructions nearby. It has an annual average wind speed of 10.8 m/s, which is considered excellent for wind turbine operation. Wind turbines generate power proportional to the cube of wind speed.

2) There is at least 10 Km of separation from noise-sensitive neighbors. Furthermore, the selected WT is remarkably quiet, with low noise levels.

3) Reliable grid connection: There is an electric substation located about 30km away to discharge generated energy from the theoretical wind farm to the grid.
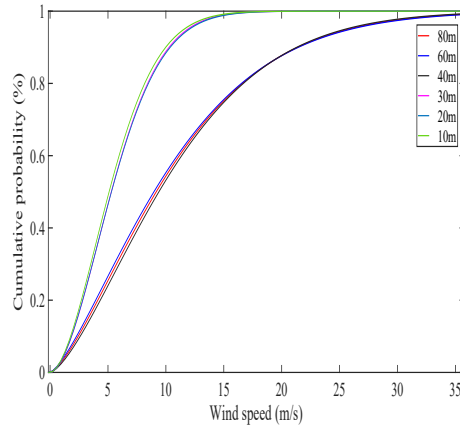
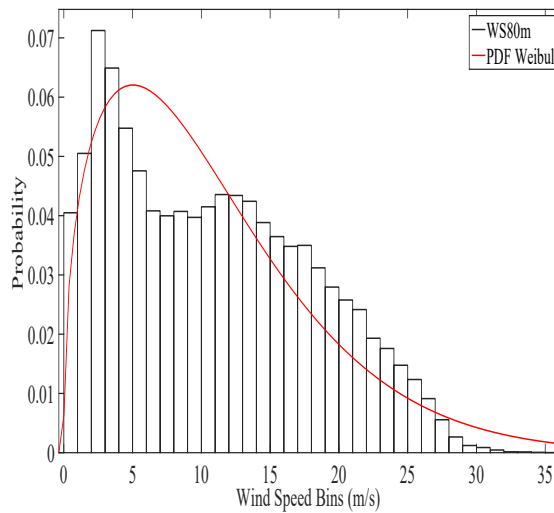Figure 17: Cumulative Density Function for Weibull distribution

Figure 18: Monthly average wind power density at 80m AGL for 2018

4) Easy site access: Because wind turbines of 1.5 MW are large and heavy. The access roads and tracks available are capable of carrying these loads without any risk.
5) No environmental damage or landscape impact: There are now no objections to wind turbine installation because of bird strikes, due to the absence of special bird areas.

G. 4.7 Monthly wind energy yield and Capacity Factor estimation

To calculate the monthly estimated wind energy during 2018, it is supposed a hypothetical wind farm of 16.5 MW of installed power; which is composed of 11 WT Goldwind 70/1500 KW, each with an active power of 1.5 MW. The wind speed at 80 m AGL is considered to estimate monthly net wind energy; which was compared against monthly net wind energy values from Villonaco wind farm as is shown in Figure 20. The estimated wind energy values were higher than the real values of Villonaco; which were obtained during the winter months. In addition, there are many factors that affect wind farm operation, such as climatic conditions, grid features, and equipment performance [63].
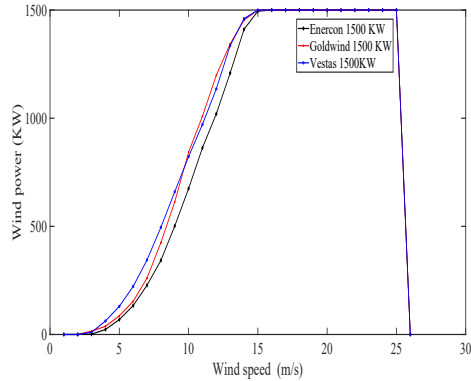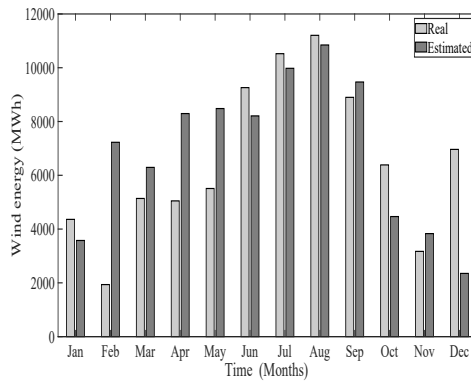
Figure 19: Selected wind turbine power curves

Figure 20: Monthly wind energy yield during 2018 using WT Goldwind 1500

The mean monthly CFs were calculated by the comparison of the CF Villonaco wind farm against an estimated CF theoretical wind farm as is observed in Figure 21. The estimated CF is higher than the real CF for the winter months. Furthermore, it is observed that height change increases CF and decreases WSC values at a height of 80 m AGL. A similar pattern of wind energy and higher CF results were obtained by comparing the annual wind energy and CF in 2018 at 80 m AGL against estimated wind energy and CF at an altitude of 2957 m ASL in the Swiss Alps [64].

H. 4.8 Wind characteristics modeling using CFD

The wind speed map over the computational domain in Zone 1 is shown in Figure 22, which represents the horizontal wind speed of the area of study at 80 m AGL, which is similar to the hub height of selected WT. Wind speed simulated values using annual mean WS (10.8 m/s) as WS inlet to computational domain in four Areas of Zone 1 to have as WS outlet higher WS values on the summit of mountains from 3.3 m/s to 24 m/s due to the wind speed-up effect. A similar pattern of WS simulation results but with lower WS values were obtained by Solano et al. [17] for the southern mountainous region of Ecuador at heights of 10 and 100 m AGL using software Surfer 3D. In this way it confirms that WS increases. and TI decreases with height change [13, 42]. On the other hand, The TI map over the computational domain in the Zone 1 is shown in Figure 23 which represents the TI of the area of study at 80 m AGL, which is similar to the hub height of selected WT. TI was simulated values using annual mean WS (10.8 m/s) as WS inlet in four Areas of Zone 1 to have higher IT values on the top of mountains from 0.04 to 0.18 due to the friction of WS against terrain surface. From these results it is clear that the risks to the WT performance and durability caused by fatigue loads on WT blades could be highly reduced by assessing the wind characteristics of the WT installation site, such as TI simulation over complex terrain to optimize wind farm layout keep way WT of turbulent flows [58, 65].
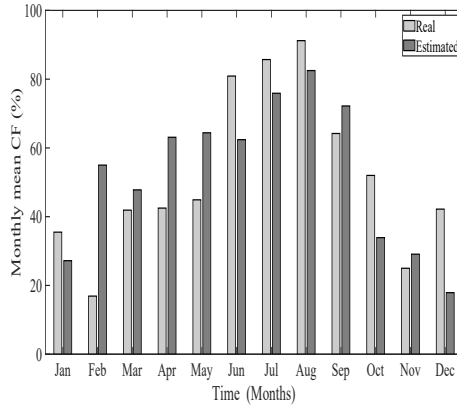
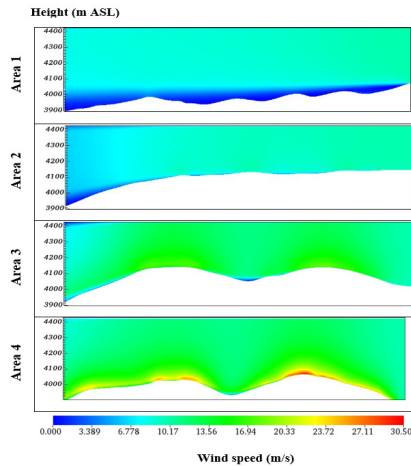Figure 21: Monthly CF during 2018 using WT Goldwind 1500

Figure 22: Wind speed simulation in zone 1

Next, WT micro-siting to place 11 WT Goldwind 70/ 1500 KW was performed in three steps for each of the four horizontal areas of Zone 1 as follows:

First, taking into consideration important factors, such as WT orientation to prevalent WD (windward from East), the most net power sectors, locating WT on the top of the mountains considered as wind acceleration areas.

Second, removing WT from highly turbulent flows originated by wakes and vortices from other surrounding terrains of lower height [30, 66]. Third, considering regulations for separation between WT rows and WT columns [35]. The wind farm layout is obtained as is depicted in Fig. 24.

I. 4.9 Discussion

This study has presented a structured methodology to assess with great precision WPP and develop a wind farm design using CFD in the Ecuadorian Andes by showing novel and relevant findings.

  a) First, in terms of mean WS, this study discovered the highest values during the summer months of June to August, when WS increased due to the presence of large air masses coming from the east and south, reaching more than 25 m/s in some 10-minute periods.

  b) Second, regarding the TI, it is found that the areas with the lowest values were at 80 m AGL, with values ranging from 0.14 to 0.16 between 10 a.m. and 2 p.m., which is considered a TI A class.
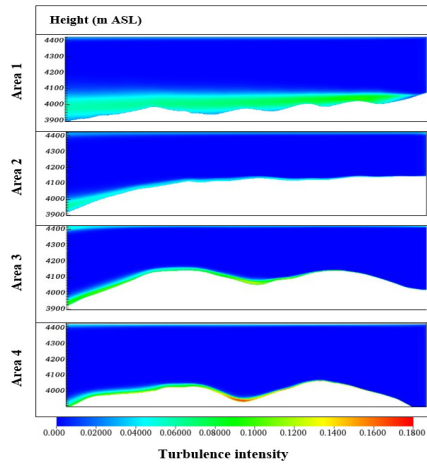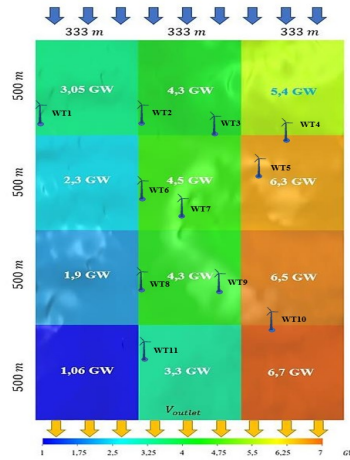
Figure 23: TI simulation in Zone 1

Figure 24: WT positions in computational domain Zone 1

c) Third, WPD reached the highest values during the summer months, between 10 a.m. and 2 p.m., reaching values of up to 800 W/m^2 because of the existence of higher WS provoked by wind speed-up effects, orography, and climatic conditions.

d) Fourth, according to the results of the PDF Weibull parameters, the area of study has great wind variability due to the influence of complex terrain orography, with less dispersion concerning the annual mean WS of 10.9 m/s, which is a high availability of wind speed to obtain a large production of wind energy.

e) Fifth, the comparison results of the AEP and CF of the theoretical wind farm found that the estimated wind energy values were higher than the real values, which were obtained during the winter months. The estimated CF is higher than the real CF for the winter months. Furthermore, it is observed that height change increases CF and decreases at a height of 80 m AGL. In addition, climatic conditions affect durectly to wind farm operations.

f) Sixth, with respect to the best suitable WT for this site, WT power curve results confirm that the best suitable WT for the zone of study is Goldwind 70/1500 KW, which is a good choice to consider.

g) Seventh, this research found that it is clear that the risks to WT performance and durability caused by fatigue loads on WT blades could be highly reduced by assessing the wind characteristics of the WT installation site, such as through TI simulation over complex terrain to optimize wind farm layout and keep WT out of turbulent flows.

h) Eight, The TI standard k-ϵ model has been validated for wind flow over complex terrain at high altitudes by

comparing the numerical results obtained from the Ansys Fluent CFD software with the available experimental data.

This study used and validated WRA methodology to assess WPP in the Ecuadorian Andes. The methodology combines WRA and wind farm design using Ansys CFD. This study provides key drivers for wind energy development in Ecuador's renewable energy sector to increase wind energy's percentage in the Ecuadorian energy matrix. Before coming to any conclusions, it is important to highlight several limitations affecting the above-discussed results. It should be noted that the methods used in this research were compared with other studies, but the lack of information on WRA in the study area from Ecuadorian government sources or other particular sources has restricted the possibility of high-accuracy comparisons. To address this limitation, a wind measurement campaign was launched in 2018 based on data collected from two meteorological towers installed in the study area. The mean WS and WPD values provided by the Ecuadorian Wind Atlas were compared against the WS-measured values, indicating an underestimation of about 2 m/s. In the case of GSR, the comparison results show a difference of about 300 W/m^2. Another key problem to address in future research with the wind characteristics modeling presented in this study is the use of atmospheric variability over complex terrain at high altitudes.

V. 5. CONCLUSIONS

In this study, a novel assessment of wind characteristics and wind potential in the Andes Mountains of Ecuador is performed using measured data from two meteorological towers installed on the site. Furthermore, the study of the airflow over a hill considered a complex terrain has also been carried out; through two-dimensional numerical simulations using the Ansys CFD software; to describe the behavior of the field of speeds and turbulence corresponding to the site of study. The obtained results are useful for researchers, and wind power investors interested in developing wind farm projects in this region. Based on the wind analysis, the following conclusions are drawn:

- The annual mean WS was found at 10.9 m/s at 80 m AGL and the predominant wind direction was from East to West due to the influence of Atlantic equatorial mass. The higher and lower WS values correspond to the summer and winter months, respectively. By making a correlation between the mean annual speed measured and the one estimated in the Ecuadorian Wind Atlas, an RMSE value of 0.45 is obtained, which represents a variation of 1.5-2 m/s. Therefore, the Ecuadorian Atlas tends to underestimate the wind speed in this region at 80 m AGL .

- In the zone of study, the TI at 80 m AGL is low, corresponding to the A-class, which reached lower values between 0.07-0.14. These values were in the winter months and the higher values were in summer, when the wind speed is low and high, respectively. Thus, it confirms that wind speed increases and TI decreases with a change in height. In consequence, this site is ideal for wind farm projects because is a natural mountain pass between two volcanoes with an accelerated wind flow with high mean wind speed and low turbulence.
- The mean WPD in 2018 in the zone of study is considered high and is equal to 600 W/m^2. Consequently, a hypothetical wind farm of 16.5 MW was designed to determine the feasibility of wind power generation in this sector. The WT Goldwind 70/ 1500 KW class A, using direct-drive permanent magnet technology, was found to be the best option for these site characteristics.
- The AEP 2018 by using 11 WT Goldwind 70/1500 KW was found to have around 75 GWh and a high CF of 0.46, which is closer to the Villonaco wind farm. Therefore, these AEP values obtained in the zone of study are suitable for large-scale wind power generation.
- The meshing procedure of the two-dimensional CFD numerical simulation process applied to the computational domain of the analysed hill used a hybrid topological structure, to guarantee the accuracy of the results obtained for the turbulent velocity and kinetic energy fields.
- The TI standard k-ϵ model has been validated for wind flow over complex terrain at high altitudes by comparing the numerical results obtained from the Ansys Fluent CFD software with the available experimental data.The comparison results between the k-ϵ two-equation model and calculated data show that the k-ϵ model can predict the mean velocity and the turbulent kinetic energy that are closer to the measured values. The simulation was performed to determine the micro-siting of the 11 selected wind turbines.
- Future research will consider atmospheric stability on the complex terrain in the CFD approach.

CREDIT AUTHOR STATEMENT

Germánico López: Formal analysis, Methodology, Writing- Original draft preparation. **Pablo Arboleya**: Conceptualization, Supervision, Resources. **Diego Núñez**: Visualization, Investigation, Data curation. **Andrés Freire**: Software, Validation, Writing- Reviewing and Editing.

ACKNOWLEDGMENTS

Data Availability

Datasets related to this article can be found at LOPEZ, GERMANICO (2021), "Meteorological variables 2018 at 80m AGL", Mendeley Data, V2, doi: 10.17632/wfvk5k34rs.2

References

[1] IEA. *World Energy Outlook 2020*. Tech. rep. International Energy Agency, 2020. URL: https://iea.blob.core.windows.net/assets/a72d8abf-de08-4385-8711-b8a062d6124a/WEO2020.pdf.

[2] IEA. *Renewables Information: Overview*. Tech. rep. 31-35 rue de la Fédération 75739 Paris Cedex 15 France: International Energy Agency, Aug. 2019.

[3] David Barbosa de Alencar et al. "Different Models for Forecasting Wind Power Generation: Case Study". In: *Energies* 10.12 (2017). ISSN: 1996-1073. DOI: 10.3390/en10121976.

[4] GWEC. *Global Wind Report 2021*. Tech. rep. Rue Belliard 51-53, 1000 Brussels, Belgium: Global Wind Energy Council, 2021.

[5] WWEA. *World Wind Energy Asociation*. 2021. URL: https://wwindea.org/worldwide-wind-capacity-reaches-744-gigawatts/.

[6] Miguel Castro. *Hacia una nueva matriz energética diversificada en Ecuador*. Ed. by Joerg Elbers. Av. Eloy Alfaro N32-650 y Rusia, 3er. Piso. Quito, Ecuador: CEDA, 2011. ISBN: 978-9942-9998-5-6.

[7] MEER. *Plan Maestro de Electrificación 2012-2021*. Av. Naciones Unidas E7-71 y Av. de los Shyris, Quito-Ecuador, Feb. 2013.

[8] M.A. Ponce-Jara et al. "Electricity sector in Ecuador: An overview of the 2007–2017 decade". In: *Energy Policy* 113 (2018), pp. 513 –522. ISSN: 0301-4215.

[9] MEER. *Electricity Master Plan*. Tech. rep. ISBN:9789942221537. Quito-Ecuador: Ministry of Electricity and Renewable Energy, 2017.

[10] Jorge Maldonado-Correa et al. "Wind power forecasting for the Villonaco wind farm". In: *Wind Engineering* 45.5 (2021), pp. 1145–1159. DOI: 10.1177/0309524X20968817. eprint: https://doi.org/10.1177/0309524X20968817.

[11] Jaime Cevallos-Sierra and Jesús Ramos-Martin. "Spatial assessment of the potential of renewable energy: The case of Ecuador". In: *Renewable and Sustainable Energy Reviews* 81 (2018), pp. 1154–1165. ISSN: 1364-0321. DOI: https://doi.org/10.1016/j.rser.2017.08.015. URL: https://www.sciencedirect.com/science/article/pii/S1364032117311590.

[12] Stefan Emeis. *Wind Energy Meteorology Atmospheric Physics for Wind Power Generation*. Ed. by Springer. 1st ed. Green Energy and Technology. ISSN 1865-3537. Institut für Meteorologie und Klimaforschung Karlsruher Institut für Technologie Kreuzeckbahnstr. 19 82467 Garmisch-Partenkirchen Germany: Springer, 2013.

[13] Michael C. Brower. *Wind Resource Assessment*. Ed. by John Wiley & Sons Inc. Vol. 1. Hoboken, USA: John Wiley & Sons Inc., 2012.

[14] Matthew Zhang. *Wind resource assessment and micro-siting*. Ed. by CHINA MACHINE PRESS. 1st. Vol. 1. John Wiley & Sons, Ltd, 2015.

[15] Hyun-Goo Kim, Yong-Heack Kang, and Jin-Young Kim. "Evaluation of wind resource potential in mountainous region considering morphometric terrain characteristics". In: *Wind Engineering* 41.2 (2017), pp. 114–123. DOI: 10.1177/0309524X16689445. eprint: http://dx.doi.org/10.1177/0309524X16689445.

[16] Jiannong Fang Daniel Tabas and Fernando Porté-Agel. "Wind Energy Prediction in Highly Complex Terrain by Computational Fluid Dynamics". In: *Energies* 12.1311 (2019), pp. 1–12. DOI: doi:10.3390/en12071311.

[17] J.C. Solano et al. "Correlation between the wind speed and the elevation to evaluate the wind potential in the southern region of Ecuador". In: *Energy Reports* 7 (2021). 2021 6th International Conference on Advances on Clean Energy Research, pp. 259–268. ISSN: 2352-4847. DOI: https://doi.org/10.1016/j.egyr.2021.06.044.

[18] Germánico López Javier García Alex Mayorga. "A novel probability density function applied to wind characterization in order to evaluate the wind power potential in Tungurahua, Ecuador's Andean region". In: *Wind Engineering* 0.0 (2017), pp. 1–24. eprint: https://doi.org/10.1177/0309524X18780383.

[19] M. Ayala et al. "Wind Power Resource Assessment in Complex Terrain: Villonaco Case-study Using Computational Fluid Dynamics Analysis". In: *Energy Procedia* 107 (2017). 3rd International Conference on Energy and Environment Research, {ICEER} 2016, 7-11 September 2016, Barcelona, Spain, pp. 41 –48. ISSN: 1876-6102.

[20] Germánico López and Pablo Arboleya. "Short-term wind speed forecasting over complex terrain using linear regression models and multivariable LSTM and NARX networks in the Andes Range, Ecuador". In: *Renewable Energy* (2021). ISSN: 0960-1481. DOI: https://doi.org/10.1016/j.renene.2021.10.070.

[21] Stathopoulos T. (Bitsuamlak, ASCE F, and Bedard C. "Numerical evaluation of wind flow over complex terrain: review". In: *Journal of Aerospace Engineering* 17.4 (2004), pp. 135–145. DOI: https://doi.org/10.1016/0038-092X(90)90013-3.

[22] S. Ramechecandane and Arne Reidar Gravdahl. "Numerical Investigations on Wind Flow over Complex Terrain". In: *Wind engineering* 36.3 (2012), pp. 273–296. DOI: https://doi.org/10.1016/0038-092X(90)90013-3.

[23] César Angeles-Caamacho Ernesto Arteaga-López and Francisco Bañuelos-Ruedas. "Advanced methodology for feasibility studies on building-mounted wind turbines installation in urban environment: Applying CFD analysis". In: *Energy* 16 (2019), pp. 181–188. DOI: https://doi.org/10.1016/j.energy.2018.10.191.

[24] Michael C. Brower Philippe Beaucage and Jeremy Tensen. "Evaluation of four numerical windflow models for windresource mapping". In: *Wind Energy* 17 (2014), pp. 197–208. DOI: DOI : 10 . 1002 / we . 1568CopyrightÂl´2012JohnWiley&Sons,Ltd.197..

[25] Q.S. Li B.W. Yan. "Coupled on-site measurement/CFD based approach for high-resolution wind resource assessment over complex terrains". In: *Energy Conversion and Management* 117 (2016), pp. 351–366. DOI: https://doi.org/10.1016/j.enconman.2016.02.076..

[26] Y. Birkelund M. Bilal and M. Virk M. Homola. "Wind over complex terrain e microscale modelling with two types of mesoscale winds at Nygardsfjell". In: *Renewable Energy* 99 (2016), pp. 647–653. DOI: https://doi.org/10.1016/j.renene.2016.07.042.

[27] Xiao-Yu Tang, Shumian Zhao, and Bernhard Stoevesandt Bo Fan Joachim Peinke. "Micro-scale wind resource assessment in complex terrain based on CFD coupled measurement from multiple masts". In: *Applied Energy* 238 (2019), pp. 806–815. DOI: https://doi.org/10.1016/j.apenergy.2019.01.129..

[28] MEER. *Atlas Eólico del Ecuador con fines de Generación Eléctrica*. Tech. rep. Ministerio de Electricidad y Energía Renovable, 2013. URL: https://es.scribd.com/document/355204005/ATLAS-EOLICO-ECUADOR-MEER-2013-pdf.

[29] Bruce H. Bailey and Scott L. McDonald. *Wind resource Assessment Handbook*. Ed. by NREL. 1st. National Renewable Energy Laboratory 1617 Cole Boulevard Golden, CO 80401: AWS Scientific, Inc., 1997.

[30] Walter Frost and Chih Fang Shieh. "Wind Characteristics Over Complex Terrain Relative to WECS Siting". In: *Journal of Energy* 5.5 (1981), pp. 263–269. DOI: 10.2514/3.62539.

[31] Metamorf. *Ecuador Explorer.com*. Ecuador Explorer.com. 1997-2018. URL: http://www.ecuadorexplorer.com/html/location_geography_climate.html.

[32] Lars Landberg. *Meteorology for wind energy*. Ed. by Wiley. 1st ed. ISBN: 9781118913444. The Atrium Southern Gate Chichester West Sussex, PO19 8SQ, United Kingdom: John Wiley & Sons Ltd, 2016.

[33] Gobierno del Ecuador. *INAMHI*. INAMHI2020. 2017. URL: http://www.serviciometeorologico.gob.ec/biblioteca/.

[34] Google. *Google Earth*. Apr. 2018.

[35] IEC. *IEC 61400-12-1*. International Electrotechnical Commission. Geneva, Switzerland, 2005.

[36] K.S.R. Murthy and O.P. Rahi. "A comprehensive review of wind resource assessment". In: *Renewable and Sustainable Energy Reviews* 72 (2017), pp. 1320–1342. ISSN: 1364-0321. DOI: https://doi.org/10.1016/j.rser.2016.10.038.

[37] NRG. *Wind resource assessment*. https://www.nrgsystems.com/products/applications/wind-resource-assessment. Accessed 2021-05-06. 2021.

[38] Ratisbona Leandro Serra Adalberto. *As Massas de Ar da América do Su*. Vol. 51-52. Río de Janeiro, Brasil: Revista geográfica del Instituto Panamericano de Geografía e Historia, 1960.

[39] Arvind Tiwari G.N. Tiwari. *Handbook of solar energy*. 1st. Springer, 2016. ISBN: 978-981-10-0807-8 (eBook). DOI: 10.1007/978-981-10-0807-8.

[40] Arno HM Smets et al. *Solar Energy*. 1st. Vol. 1. Delft, Netherlands: UIT Cambridge, 2015.

[41] Francesco Castellani et al. "Investigation of terrain and wake effects on the performance of wind farms in complex terrain using numerical and experimental data". In: *Wind Energy* 20.7 (2017), pp. 1277–1289. DOI: https://doi.org/10.1002/we.2094. eprint: https://onlinelibrary.wiley.com/doi/pdf/10.1002/we.2094.

[42] J. F. Manwell and J. G. McGowan. *Wind Energy Explained*. Ed. by Wiley. 2nd. ISBN 978-0-470-01500-1. The Atrium Southern Gate Chichester West Sussex PO19 8SQ, United Kingdom: John Wiley and Sons Ltd., 2009.

[43] Yuan Zhou et al. "The wind and temperature information of AMDAR data applying to the analysis of severe weather nowcasting of airport". In: *2013 IEEE Third International Conference on Information Science and Technology (ICIST)*. 2013, pp. 1005–1010. DOI: 10.1109/ICIST.2013.6747706.

[44] Tony Burton et al. *Wind Energy Handbook*. Ed. by Ltd John Wiley & Sons. 1st. John Wiley & Sons, Inc. 605 Third Avenue New York NY 10158-0012, USA: John Wiley & Sons, Ltd, 2011. ISBN: E-PDF ISBN: 978-1-119-99272-1.

[45] S. Arnalte Gómez J.L. Rodríguez Amenedo J.C. Burgos Díaz. *Sistemas eílicos de producción de energía eléctrica*. 1st. Vol. 1. Porto Cristo 13, 28294, Madrid-Spain: Editorial Rueda S.L., 2003. ISBN: 84-7207-139-1.

[46] Trevor M. Letcher. *Wind Energy Engineering*. Ed. by Trevor M. Letcher. 1st. 525 B Street Suite 1800 San Diego, CA 92101-4495, United States: Academic Press, 2017. ISBN: ISBN: 978-0-12-809451-8.

[47] S.H. Pishgar-Komleh, A. Keyhani, and P. Sefeedpari. "Wind speed and power density analysis based on Weibull and Rayleigh distributions (a case study: Firouzkooh county of Iran)". In: *Renewable and Sustainable Energy Reviews* 42 (2015), pp. 313–322. ISSN: 1364-0321. DOI: https://doi.org/10.1016/j.rser.2014.10.028.

[48] Gonzalo P. Navarro Diaz, A. Celeste Saulo, and Alejandro D. Otero. "Full wind rose wind farm simulation including wake and terrain effects for energy yield assessment". In: *Energy* 237 (2021), p. 121642. ISSN: 0360-5442. DOI: https://doi.org/10.1016/j.energy.2021.121642.

[49] Younes Noorollahi, Mohammad Ali Jokar, and Ahmad Kalhor. "Using artificial neural networks for temporal and spatial wind speed forecasting in Iran". In: *Energy Conversion and Management* 115 (2016), pp. 17 –25. ISSN: 0196-8904. DOI: https://doi.org/10.1016/j.enconman.2016.02.041. URL: http://www.sciencedirect.com/science/article/pii/S0196890416300711.

[50] Lin Ye et al. "Short-term wind power prediction based on spatial model". In: *Renewable Energy* 101 (2017), pp. 1067 –1074. ISSN: 0960-1481. DOI: https://doi.org/10.1016/j.renene.2016.09.069.

[51] Sungmoon Jung, O. Arda Vanli, and Soon-Duck Kwon. "Wind energy potential assessment considering the uncertainties due to limited data". In: *Applied Energy* 102 (2013). Special Issue on Advances in sustainable biofuel production and use - XIX International Symposium on Alcohol Fuels - ISAF, pp. 1492–1503. ISSN: 0306-2619. DOI: https://doi.org/10.1016/j.apenergy.2012.09.011.

[52] O. Rodriguez-Hernandez et al. "Analysis about sampling, uncertainties and selection of a reliable probabilistic model of wind speed data used on resource assessment". In: *Renewable Energy* 50 (2013), pp. 244–252. ISSN: 0960-1481. DOI: https://doi.org/10.1016/j.renene.2012.06.004.

[53] Goudarzi N. "Computational Fluid Dynamics Methods for Wind Turbines Performance Analysis. In: Hu W. (eds)". In: *In: Hu W. (eds) Advanced Wind Turbine Technology*. Ithaca, New York, USA: Springer, Cham, 2018. DOI: https://doi.org/10.1007/978-3-319-78166-2_2.

[54] L. E. Boni Cruz and B. Souza Carmo. "Wind farm layout optimization based on CFD simulations". In: *The Brazilian Society of Mechanical Sciences and Engineering* 42.433 (2020), pp. 273–296. DOI: http://dx.doi.org/10.26678/ABCM.COBEM2017.COB17-1723.

[55] Y. Yi, G. Ming, and C. Suqin y J. Xinyang. "New inflow boundary conditions for modelling the neutral equilibrium atmospheric boundary layer in computational wind engineering". In: *Journal of Wind Engineering and industrial Aerodynamics* 97.2 (2009), pp. 88–99. DOI: https://doi.org/10.1016/j.jweia.2008.12.001.

[56] Carmeliet J Blocken B Stathopoulos T. "CFD Simulation of the atmospheric boundary layer: wall function problems". In: *Atmospheric Environment* 41.2 (2009), pp. 238–252. DOI: https://doi.org/10.1016/j.atmosenv.2006.08.019.

[57] Tahirović Alma ATrešnjo Dino and Music Mustafa Torlak Muris Redzic Elma. "Comparison of CFD and Linear Model When Calculating Maps of Wind Potential at the Location with Complex Topography". In: *Advanced Technologies, Systems, and Applications II*. Vol. 28. Springer, 2018, pp. 155–169. DOI: 10.1007/978-3-319-71321-2_13..

[58] Jae-ho Jeong and Kwangtae Ha. "Evaluation of Wind Flow Characteristics by RANS-Based Numerical Site Calibration (NSC) Method with Met-Tower Measurements and Its Application to a Complex Terrain". In: *Energies* 13.19 (2020). ISSN: 1996-1073. DOI: 10.3390/en13195121. URL: https://www.mdpi.com/1996-1073/13/19/5121.

[59] Károly Tar. "Some statistical characteristics of monthly average wind speed at various heights". In: *Renewable and Sustainable Energy Reviews* 12.6 (2008), pp. 1712–1724. ISSN: 1364-0321. DOI: https://doi.org/10.1016/j.rser.2007.01.014.

[60] Gupta. "Weibull parameters for annual and monthly wind speed distributions for five locations in India". In: *Sol. Energy; (United Kingdom)* 37:6 (1986). DOI: 10.1016/0038-092X(86)90039-3.

[61] IDAE. *Energía Eólica*. Instituto para la Diversificación y Ahorro de la Energía. C/ Madera, 8 , E-28004-Madrid, 2006.

[62] CELEC. *Central Eólica Villonaco (Villonaco Wind Farm)*. https://www.celec.gob.ec/gensur/index.php/cev/central-eolica-villonaco-en-cifras-2. Accessed 2021-06-30. 2019.

[63] Mohamed Abbes and Jamel Belhadj. "Wind resource estimation and wind park design in El-Kef region, Tunisia". In: *Energy* 40.1 (2012), pp. 348 –357. ISSN: 0360-5442. DOI: https://doi.org/10.1016/j.energy.2012.01.061.

[64] Bert Kruyt, Jérôme Dujardin, and Michael Lehning. "Improvement of Wind Power Assessment in Complex Terrain: The Case of COSMO-1 in the Swiss Alps". In: *Frontiers in Energy Research* 6 (2018), p. 102. ISSN: 2296-598X. DOI: 10.3389/fenrg.2018.00102.

[65] Lalit Roy and David MacPhee. "Meso-Scale CFD Simulation for Wind Resources: A Case Study of Complex Mountainous Terrain". In: *Energies* 11.6 (2018). ISSN: 1996-1073. DOI: 10.3390/en11061366.

[66] Jianwen Wan Qiang Wang, Renyu Yuan Yali Hou, and Jianren Fan Kun Luo. "Simulations of separated flow over two-dimensional hills". In: *Renewable Energy* 118 (2018), pp. 11118–1133. DOI: https://doi.org/10.1016/j.renene.2017.09.045.

Germánico López received his Master degree (2013) in Renewable Energy in Electrical Systems from University Carlos III of Madrid, Spain. Nowadays, he is pursuing his Ph.D. at LEMUR Research Group at the University of Oviedo. His main research interests have to do with the smart operation of terminal distribution networks, networks analysis and simulation and failures detection. His areas of interest are distribution system modeling, and large-scale integration of renewable resources.

Pablo Arboleya (SM'13) received the M.Sc. and Ph.D. (with distinction) degrees from the University of Oviedo, Gijón, Spain, in 2001 and 2005, respectively, both in Electrical Engineering. Nowadays, he works as an Associate Professor in the Department of Electrical Engineering at the University of Oviedo, he is Managing Editor of the ELSEVIER's International Journal of Electrical Power & Energy Systems and holder of the Gijón Smart Cities Chair at the University of Oviedo. Presently his main research interests are focused in micro-grid, and smart-grid modeling and operation techniques, Energy Internet applications and railway traction networks modeling and simulation.

Diego Núñez received his Master degree (2013) in Mechanical Engineering: Design and Manufacturing from University of the Basque Country, Spain. Nowadays, he works as an Aggregate Professor in the Technical University of Ambato, Faculty of Civil and Mechanical Engineering. His main research interests are focused in Mechanics Design, Structural Analysis, Computational Fluid Analysis and Simulation and Green Machining of metals using nanofluids and cryo-machining.

Andrés Freire received his Bachelor degree (2022) in Mechanical Engineering from Technical University of Ambato, Ecuador. Nowadays, he works as an Aggregate Professor in the Bautista School of Ambato. His main research interests are focused in Mechanics Design, Structural Analysis and Computational Fluid Analysis.